Search for heavy resonances in the X→WW→e$\nu\mu\nu$ channel with the ATLAS detector at the LHC

Yongke Zhao

NNT : 2018SACLS103

Recherche d'une résonance lourde dans le canal $X \to WW \to e\nu\mu\nu$ avec le détecteur ATLAS au LHC

Search for heavy resonances in the $X \to WW \to e\nu\mu\nu$ channel with the ATLAS detector at the LHC

Thèse de doctorat de Shandong University et de l'Université Paris-Saclay, préparée à l'Université Paris-Sud

École doctorale n°576 Particules, Hadrons, Énergie, Noyau, Instrumentation, Image, Cosmos et Simulation (PHÉNIICS)
SCHOOL of PHYSICS
Spécialité de doctorat : Physique des particules

Thèse présentée et soutenue à Jinan, le 3 Juin 2018, par

M. Yongke ZHAO

Composition du Jury :

M. Liang HAN	
Professeur, University of Science and Technology of China	Président
M. Shenjian CHEN	
Professeur, Nanjing University	Rapporteur
M. Emmanuel PEREZ	
Docteur, CERN	Rapporteur
M. Chunhui CHEN	
Professeur associé, Iowa State University	Examinateur
Mme Rosy NIKOLAIDOU	
Directrice de recherche, IRFU, CEA-Saclay	Examinatrice
M. Lianliang MA	
Professeur, Shandong University	Directeur de thèse
M. Xueyao ZHANG	
Professeur, Shandong University	Directeur de thèse
M. Zhiqing ZHANG	
Directeur de recherche, Laboratoire de l'Accélérateur Linéaire	Directeur de thèse

LAL 18-007

Thèse de doctorat

Résumé

Une recherche de résonance neutre et lourde X est effectuée dans le canal $X \to WW \to e\nu\mu\nu$ en utilisant les données en collision pp correspondant à une luminosité intégrée d'environ 36,1 fb^{-1}, prises à une énergie dans le centre-de-masse de 13 TeV par le détecteur ATLAS au LHC. La résonance peut être soit un boson de Higgs scalaire lourd soit d'autres résonances lourdes aux spins différents. Deux scénarios de largeur sont étudis pour un boson de Higgs lourd dans les modes de fusion gluon-gluon et de fusion vecteur-boson; une largeur soit étroite soit grande. Plusieurs hypothèses sont utilisées pour rechercher d'autres résonances, comme le modèle avec deux doublets de Higgs, le modèle de Georgi-Machacek, le modèle avec un triplet vectoriel en mode d'annihilation quark-antiquark, le modèle de Randall-Sundrum avec un graviton de spin 2 correspondant à un paramètre d'échelle de courbure $k/\bar{M}_{\mathrm{Pl}}$ de 1 ou 0,5 et un signal de spin 2 dans le mode de fusion vecteur-boson. Trois catégories d'événements indépendantes sont définies dans l'analyse: une catégorie inclusive où les espaces de phase en fusion vecteur-boson sont exclus et deux autres catégories qui sont optimisées pour les signaux produits en mode de fusion vecteur-boson avec un jet ou au moins deux jets. Aucun excès significatif d'événements au-delà de la prédiction du bruit de fond du Modèle Standard ne se trouve dans la gamme de masse comprise entre 200 GeV et 5 TeV. Les limites supérieures sont obtenues sur le produit de la section efficace de la production de la résonance et du rapport de branchement $X \to WW$. Pour les signaux de bosons de Higgs lourds, les valeurs supérieures à 6,4 pb et 1,3 pb à $m_H = 200$ GeV et supérieures à 0,008 pb et 0,005 pb à 4 TeV sont exclues à un niveau de confiance de 95% pour la fusion gluon-gluon et la fusion vecteur-boson, respectivement. Pour les signaux prédits par le modèle avec un triplet vectoriel, les valeurs de masse inférieures à 1,3 TeV sont exclues. De la même manière, pour les signaux prédits par le modèle de Randall-Sundrum, les valeurs de masse inférieures à 1,1 TeV et 850 GeV sont exclues pour $k/\bar{M}_{\mathrm{Pl}} = 1$ et $k/\bar{M}_{\mathrm{Pl}} = 0.5$, respectivement.

Mots-clés: Résonance lourde; WW; boson de Higgs; au-delà du Modèle Standard

Abstract

A search for a heavy neutral resonance X is performed in the $X \to WW \to e\nu\mu\nu$ decay channel using pp collision data corresponding to an integrated luminosity of 36.1 fb^{-1}, collected at a centre-of-mass energy of 13 TeV by the ATLAS detector at the Large Hadron Collider. The resonance can be either a heavy scalar Higgs boson or other heavy resonances with different spins. Two scenarios are considered for the heavy Higgs boson hypothesis with different decay widths in both the gluon-gluon fusion and the vector-boson fusion production modes, namely a narrow-width approximation and a large width assumption. Several hypotheses are used for the interpretation to search for other resonances, like two Higgs doublet models, Georgi-Machacek model, heavy vector triplet model in the quark-antiquark annihilation mode, a bulk Randall-Sundrum graviton model with a spin-2 Graviton with a curvature scale parameter $k/\bar{M}_{\text{Pl}}$ of either 1 or 0.5 and a spin-2 signal in the vector-boson fusion mode. Three orthogonal event categories are defined in the analysis: two vector-boson fusion categories which are optimised for the signals produced in the vector-boson fusion mode with one jet or at least two jets and one quasi-inclusive gluon-gluon fusion category where the vector-boson fusion phase spaces defined by the two vector-boson fusion categories are excluded. No significant excess of events beyond the Standard Model background prediction is found in the mass range between 200 GeV and up to 5 TeV. Upper limits are set on the product of the production cross section of the resonance and the $X \to WW$ branching fraction. For heavy Higgs boson signals, values above 6.4 pb and 1.3 pb at $m_H = 200$ GeV and above 0.008 pb and 0.005 pb at 4 TeV are excluded at 95% confidence level for the gluon-gluon fusion and the vector-boson fusion production modes, respectively. For signals predicted by the heavy vector triplet model, mass values below 1.3 TeV are excluded. Similarly, for signals predicted by the bulk Randall-Sundrum graviton model, mass values below 1.1 TeV and 850 GeV are excluded for $k/\bar{M}_{\text{Pl}} = 1$ and $k/\bar{M}_{\text{Pl}} = 0.5$, respectively.

Keywords: Heavy resonance; WW; Higgs boson; beyond the Standard Model

Synthèse

Introduction

Le boson de Higgs, en tant que particule élémentaire prédite par le modèle standard (SM) au début des années 1960, a été découvert en 2012 par les collaborations ATLAS et CMS au Large Hadron Collider (LHC). Par conséquent, l'existence du champ de Higgs, dont on pensait qu'il donnait des masses aux particules et produisait le boson de Higgs par une brisure spontanée de symétrie, a été confirmée. Les propriétés mesurées du boson de Higgs sont, dans les incertitudes expérimentales, en accord avec les prédictions du SM.

Néanmoins, le SM est considéré comme une théorie incomplète et de nombreux scénarios au-delà du SM (BSM) prédisent une extension du secteur de Higgs. Des résonances de spin 1 ou 2 sont également prédites dans plusieurs autres extensions du SM, comme dans les modèles composites de Higgs et les modèles de dimensions supplémentaires "déformées".

Dans cette thèse, une recherche d'un boson de Higgs lourd et neutre ou d'autres résonances lourdes, se désintégrant en WW, est présentée. La recherche utilise les données collectées en 2015 et 2016 par le détecteur ATLAS au LHC à partir des collisions pp à une énergie $\sqrt{s} = 13$ TeV dans le centre de masse, correspondant à une luminosité intégrée de 36,1 fb^{-1}.

Les résultats sont interprétés en termes de différents modèles de référence. Dans le cas d'une résonance scalaire produite par fusion gluon-gluon (ggF) ou par fusion de vecteur-bosons (VBF), deux scénarios avec différentes largeurs intrinsèques sont considérés. Des contraintes sur le scalaire neutre lourd dans les modèles à deux doublets de Higgs (2HDM) sont également obtenues. Le membre neutre du quintuplet du modèle de Georgi-Machacek (GM) sert également de modèle de référence dans le mode de production VBF. Le paramétrage lagrangien du triplet vectoriel lourd (HVT) permet l'interprétation des recherches de résonances de spin 1 d'une manière générique. Le modèle de Randall-Sundrum (RS) présente une excitation gravitationnelle de Kaluza-Klein (KK) de spin 2

(G_{KK}), tandis qu'un signal de résonance tensorielle dans le mode de production VBF est basé sur un modèle lagrangien effectif (ELM).

Une recherche antérieure d'un boson de Higgs lourd dans l'état final $\ell\nu\ell\nu(\ell = e, \mu)$ a été effectuée par ATLAS sur un échantillon de données avec une luminosité intégrée de 20,3 fb^{-1} à $\sqrt{s} = 8$ TeV. La collaboration CMS a également publié une recherche d'un scalaire lourd qui se désintègre en deux bosons W dans l'état final leptonique, en utilisant l'ensemble de données à $\sqrt{s} = 7$ et 8 TeV avec des luminosités intégrées de 5.1 fb^{-1} et 19.5 fb^{-1}, respectivement. Une recherche de résonances lourdes dans les modèles RS dans les modes de désintégrations leptoniques du canal WW, en utilisant l'ensemble de données de 4,7 fb^{-1} à 7 TeV, a été réalisée par la collaboration ATLAS. Les collaborations ATLAS et CMS ont obtenu des contraintes sur les modèles HVT et RS, basées sur d'autres modes de désintégration des canaux VV, V étant soit un boson W soit un boson Z. La recherche dans le mode de désintégration $e\nu\mu\nu$ est complémentaire aux recherches effectuées dans d'autres modes de désintégration. En particulier, la sensibilité aux résonances à basses masses est plus élevée dans l'état final entièrement leptonique que dans les états finals qui incluent les jets, du fait du bruit de fond inhérent à la production de jet.

Mes contributions personnelles à l'analyse sont principalement résumées comme suit: optimisation de la sélection d'événements dans la région de signal (SR); évaluation des incertitudes systématiques expérimentales et théoriques sur les deux processus du bruit de fond dominants de production du quark top et de WW; l'analyse des données, qui inclut entre autres l'estimation du bruit de fond et la comparaison entre les données et la prédiction de Monte Carlo (MC); l'optimisation du binning de la variable discriminante des distributions de la masse transverse et la préparation des données pour l'analyse statistique.

Le modèle standard et le détecteur ATLAS

Le SM de la physique des particules est la théorie qui décrit trois des quatre forces fondamentales connues dans l'univers - les interactions électromagnétique, faible et forte. Toutes les particules élémentaires connues peuvent être classées selon le SM. Le SM a été développé au cours du siècle dernier dans le contexte des théories des champs quantiques. La matière et les forces sont décrites au moyen d'un nombre raisonnablement limité de champs. Les quanta de ces champs sont des particules qui sont actuellement considérées comme fondamentales. Le SM a eu un énorme succès en expliquant quasiment tous les phénomènes observés. Une

partie fondamentale du SM est le mécanisme de brisure spontanée de symétrie responsable de la génération de la masse des particules - le mécanisme de Higgs. Une prédiction clé du SM en conséquence de l'introduction de ce mécanisme est l'existence d'un boson scalaire massif - le boson de Higgs. Cette prédiction a été confirmée en 2012 - 2013 par la découverte et la mesure d'une nouvelle particule réalisée par les expériences ATLAS et CMS. Les caractéristiques de la nouvelle particule sont compatibles avec celles prédites pour le boson de Higgs du SM.

Les bosons scalaires sont des bosons qui ont un spin nul. Jusqu'à présent, le seul boson scalaire qui a été découvert est le boson de Higgs, avec une masse d'environ 125 GeV, sans charge électrique ou de couleur. Le boson de Higgs est une excitation quantique de l'une des quatre composantes du champ de Higgs. Et c'est une particule très instable se désintégrant en d'autres particules presque immédiatement.

Dans le SM, le mode de plus grande section efficace pour produire un boson de Higgs est la ggF qui implique une boucle de quarks virtuels avec leur couplage au boson de Higgs proportionnel à leur masse. Le prochain mode de production important est la VBF dans laquelle le boson de Higgs est émis par un boson virtuel W ou Z échangé entre deux (anti-)fermions en collision. Les autres modes de production sont le Higgs Strahlung (VH) lorsqu'un fermion interagit avec un anti-fermion fournissant un boson virtuel W ou Z qui émet un boson de Higgs, et le mode ttH, dans lequel une paire top-antitop est produite et un Higgs est radié par un des tops, réel ou virtuel.

Le LHC du CERN (Centre Européen de Recherches Nucléaires) est le plus grand et le plus puissant, mais aussi le plus complexe, collisionneur du monde jamais construit par l'homme, dans un tunnel circulaire de 27 km de circonférence, creusé à 100 m sous terre. Il y a sept expériences au LHC - ALICE, ATLAS, CMS, LHCb, LHCf, MoEDAL et TOTEM. Deux d'entre elles, ATLAS et CMS, sont de grands détecteurs polyvalents, principalement destinés à la recherche du boson de Higgs et de la nouvelle physique. À l'intérieur de l'accélérateur, deux faisceaux de particules (protons ou ions lourds) de haute énergie se déplacent à une vitesse proche de celle de la lumière en directions opposées dans des tuyaux de faisceau séparés avant d'être amenés à entrer en collision. Ils sont guidés autour de l'anneau d'accélérateur par un puissant champ magnétique maintenu par les aimants dipôles supraconducteurs. Des aimants quadripolaires supplémentaires sont utilisés pour maintenir les faisceaux focalisés, avec des aimants quadrupolaires plus forts proches des points d'intersection pour maximiser les chances d'interaction des deux faisceaux. Les aimants d'ordres multipolaires supérieurs

sont utilisés pour corriger les petites imperfections dans la géométrie du champ. Le programme de physique du LHC est principalement basé sur des collisions proton-proton.

Le détecteur ATLAS est un détecteur de particules à usage général utilisé pour étudier un grand nombre de processus physiques. Il comprend un détecteur de trace interne (ID) entouré d'un solénoïde supraconducteur mince, des calorimètres électromagnétique et hadronique et un spectromètre à muons (MS) incorporant trois grands aimants toroïdaux supraconducteurs à huit bobines chacun. L'ID est constitué de détecteurs de pixels et de microstrips à granularité fine et d'un décterteur constitué de nombreux tubes à dérive (TRT). Il est immergé dans un champ magnétique axial de 2 Tesla produit par le solénoïde et assure un suivi précis des particules chargées dans la gamme $|\eta| < 2{,}5$, où η est la pseudorapidité de la particule. Le TRT fournit également des mesures de rayonnement de transition pour l'identification des électrons. Le système calorimétrique couvre la plage de pseudorapidité $|\eta| < 4{,}9$. Il est composé de calorimètres d'échantillonnage avec de l'argon liquide (LAr) ou des tuiles de scintillateur comme milieu actif, et du plomb, de l'acier, du cuivre ou du tungstène comme matériau absorbant. Le MS fournit des mesures d'identification et d'impulsion de muons pour $|\eta| < 2,7$. Le détecteur ATLAS dispose d'un système de déclenchement à deux niveaux pour sélectionner les événements à analyser.

Modèles de signaux et échantillons de données

Un des scénarios étudiés pour le scalaire lourd suppose que celui-ci a une largeur beaucoup plus petite que la résolution du détecteur. Ceci est appelé l'approximation de largeur étroite (NWA). Des largeurs plus grandes (hypothèse de grande largeur, LWA) de 5%, 10% et 15% de la masse du boson de Higgs lourd, sont également considérées. Le choix de la plage de largeur pour le boson de Higgs lourd est motivé par le fait que, pour plusieurs modèles BSM les plus pertinents, les largeurs supérieures à 15% de la masse sont déjà exclues par des limites indirectes.

Différents types de modèles 2HDM existent, définis par des hypothèses sur les couplages de chacun des doublets de Higgs et les symétries discrètes imposées. Cette analyse considère le type I, où un doublet de Higgs se couple aux bosons vecteurs tandis que l'autre couple aux fermions, et le type II du modèle supersymétrique minimal (SUSY) dans lequel un doublet de Higgs se couple aux quarks de type up et l'autre aux quarks de type down et aux leptons chargés. Cette anal-

yse utilise les 2HDM génériques qui conservent la charge et la parité (et donc CP) avec une symétrie Z_2 légèrement brisée. Les modèles ont plusieurs paramètres libres: (i) cinq masses m_h, m_H, m_A et $m_{H^\pm}$ pour deux états neutres scalaires, un état pseudo-scalaire et deux états chargées, respectivement, (ii) un angle de mélange α entre les champs des deux scalaires, et (iii) le rapport des valeurs moyennes dans le vide des deux doublets de Higgs $\tan\beta = v_2/v_1$. Le point de référence est défini en fixant $m_h = 125$ GeV et les masses des particules supersymétriques sont suffisamment lourdes pour que les désintégrations du boson de Higgs en particules de SUSY soient strictement interdites. Les sections efficaces et les rapports d'embranchement sont calculées avec SusHi et 2HDMC.

Le modèle GM étend le secteur de Higgs avec l'addition d'un triplet de $\mathrm{SU(2)_L}$ d'une manière qui préserve la valeur du SM de $\rho = M_W^2/(M_Z^2 cos^2\theta_W) = 1$ à l'ordre zero, m_W, m_Z et θ_W étant respectivement la masse de bosons W et Z et l'angle de mélange faible. Les états physiques comprennent un quintuplet fermiophobique, H_5^0, $H_5^\pm$ et $H_5^{\pm\pm}$, de symétrie SU(2) custodiale qui se couple préférentiellement aux bosons vecteurs. Pour cette raison, le modèle GM est moins contraint, lorsqu'il est produit par le processus VBF, que d'autres modèles de référence standards d'un champ de Higgs triplet, tels que le modèle "little Higgs" ou le modèle avec la symétrie gauche-droite. Le modèle a de nombreux paramètres, mais si les autres nouveaux bosons de Higgs sont plus lourds que ceux du multiplet H_5, le seul mode de production est via le processus VBF. La section efficace et la largeur de désintégration en VV sont alors proportionnelles à un seul paramètre, $\sin^2\theta_H$, qui caractérise la fraction de masse des bosons de jauge qui est générée par les champs de Higgs triplets.

Le lagrangien HVT paramétrise les couplages de nouveaux bosons lourds de spin 1 aux particules SM d'une manière générique et permet leur mélange avec les bosons de jauge du SM. Le mécanisme de production en voie s des bosons lourds est principalement via annihilation une $q\bar{q}$ (qqA). Les bosons HVT se couplent au boson de Higgs et aux bosons de jauge du SM avec un couplage $c_h g_V$ et aux fermions avec un couplage $g^2 c_F/g_V$, où g est le couplage de jauge SM $\mathrm{SU(2)_L}$, c_h et c_F sont des facteurs multiplicatifs qui modifient les couplages au boson de Higgs et au fermions, et g_V représente sa force de couplage aux bosons W et Z. Pour le cas de VBF, on suppose qu'il n'y a pas de couplage aux fermions tel que les processus de production non-VBF sont supprimés.

Le G_{KK} de spin 2 est la première excitation de Kaluza-Klein du graviton dans le modèle RS avec une dimension supplémentaire déformée. Ce modèle est caractérisé par la constante de couplage sans dimension $k/\bar{M}_{\mathrm{Pl}} \sim \mathcal{O}(1)$ où k détermine la

courbure de l'espace, et $\bar{M}_{\rm Pl} = M_{\rm Pl}/\sqrt{8\pi}$ est l'échelle réduite de Planck.

Pour le mode de production VBF, le signal de spin 2 est basé sur une approche lagrangienne effective, où Λ est une échelle d'énergie caractéristique de la nouvelle physique sous-jacente,

$$\mathcal{L} = \frac{1}{\Lambda} T_{\mu\nu} \left(f_1 B^{\alpha\nu} B^{\mu}_{\alpha} + f_2 W_i^{\alpha\nu} W_{\alpha}^{i,\mu} + 2 f_5 (D^{\mu}\Phi)^{\dagger} (D^{\nu}\Phi) \right) .$$

Ici, f_i sont des paramètres de couplage variables, $T_{\mu\nu}$ est le champ singlet de spin 2, $B^{\alpha\nu}$ et $W_i^{\alpha\nu}$ sont les tenseurs de champ électrofaible, et Φ est le champ de Higgs scalaire. La dérivée covariante D^{μ} est $D^{\mu} = \partial^{\mu} - igW_i^{\mu}\sigma^i/2 - ig'YB^{\mu}$, où σ^i sont les matrices de Pauli, Y l'hypercharge faible, et g et g' les constantes de couplage de jauge correspondantes. Le modèle diffère du modèle RS en ce que les couplages aux fermions ou aux gluons ne sont pas inclus dans le lagrangien. De plus, l'amplitude BSM est multipliée par un facteur de forme qui est fonction d'une échelle de coupure Λ_{ff} et d'une puissance de suppression n_{ff} afin de préserver l'unitarité à haute énergie:

$$f(p_1^2, p_2^2, k_{\rm sp2}^2) = \left(\frac{\Lambda_{ff}^2}{|p_1^2| + \Lambda_{ff}^2} \cdot \frac{\Lambda_{ff}^2}{|p_2^2| + \Lambda_{ff}^2} \cdot \frac{\Lambda_{ff}^2}{|k_{\rm sp2}^2| + \Lambda_{ff}^2} \right)^{n_{ff}} ,$$

où p_1 et p_2 sont les quadri-impulsions des boson électrofaibles entrants et $k_{\rm sp2}^2$ est le carré de la somme des moments des bosons initiaux, équivalent à la masse invariante d'une particule de spin 2 dans la voie s.

Les données utilisées dans cette analyse ont été déclenchées par un seul lepton (électron ou muon). Ces déclencheurs ont un seuil d'énergie ou d'impulsion transverse, $E_{\rm T}$ ou $p_{\rm T}$, qui dépend de la période de prise de données, le seuil le plus bas variant entre 20 GeV et 26 GeV. L'efficacité du déclenchement pour les événements WW après la sélection d'événements est supérieure à 99%. Des critères de qualité des données sont appliqués pour garantir que les événements sont enregistrés avec des conditions de faisceau stables et que tous les sous-détecteurs concernés sont opérationnels.

Des échantillons d'événements simulés de signal et de bruits de fond sont utilisés pour optimiser la sélection d'événements et pour estimer l'accepance du signal et les taux des bruits de fond de divers processus du SM.

L'échantillon pour le signal de boson de Higgs lourd NWA a été produit avec Powheg-Box 2.0 qui calcule séparément les mécanismes de production ggF et VBF avec des éléments de matrice jusqu'à l'ordre suivant (NLO) de la chromodynamique quantique (QCD). Il utilise la fonction de distribution des partons (PDF)

CT10 NLO et est interfacé avec PYTHIA 8.186 pour les désintégrations $H \to WW$ et pour les gerbes partoniques. Un ensemble de paramètres appelé AZNLO est utilisé pour décrire l'événement sous-jacent. Le boson de Higgs NWA est généré avec une largeur de 4 MeV. Cet échantillon d'événements est également utilisé pour contraindre les modèles 2HDM. Le signal de boson de Higgs lourd LWA a été simulé au NLO en utilisant le générateur d'événements MADGRAPH5_AMC@NLO 2.3.2 avec la PDF NNPDF23LO. Les particules générées au niveau de l'élément de matrice sont complétées par PYTHIA 8.186 avec A14 pour l'événement sous-jacent. La masse des signaux de boson de Higgs lourd considérés dans cette analyse couvre la plage entre 200 GeV et 4 (3) TeV pour les signaux induits par la ggF (VBF). Les échantillons de NWA et de LWA ont été générés par pas de 100 GeV jusqu'à 1 TeV, puis par pas de 200 GeV.

Des échantillons de référence pour les modèles GM, HVT et RS ont été générés au LO en utilisant MADGRAPH5_AMC@NLO interfacé à PYTHIA 8.186 avec la PDF NNPDF23LO. Une valeur de $\sin\theta_H = 0{,}4$ est choisie pour le modèle de référence GM. Pour l'interprétation HVT en mode d'annihilation $q\bar{q}$, des échantillons ont été générés selon le "modèle A" à symétrie de jauge étendue avec $g_V = 1$. En mode VBF, des échantillons ont été générés en utilisant la même valeur de g_V mais en fixant les couplages aux fermions à zéro pour que le nouveau boson vectoriel ne se couple qu'aux bosons vecteurs du SM et aux bosons de Higgs. Pour le modèle RS, un paramètre d'échelle de courbure $k/\bar{M}_{\mathrm{Pl}}$ de 0,5 ou 1 est considéré. Les signaux de spin 2 ELM VBF ont été générés au LO avec VBFNLO3.0.0 beta 2 avec la PDF NNPDF30LO et en utilisant le paramètre suivant: $\Lambda_{ff} = 3$ TeV, $n_{ff} = 4$, $\Lambda = 1{,}5$ TeV et $f_1 = f_2 = f_5 = 1$. La gamme de masse considérée est comprise entre 200 GeV et 5 TeV pour le signal KK graviton, entre 250 GeV et 5 TeV pour le signal HVT qqA, entre 200 GeV et 1 TeV pour le GM et les signaux VBF ELM, et entre 300 GeV et 1 TeV pour le signal VBF HVT.

Les principales sources de fond du SM comprennent les événements de production d'un seul quark top, $t\bar{t}$, dibosons (WW, WZ et ZZ), les Z/γ^*+jets et W+jets. Des événements simulés à un seul quark top ont été générés avec POWHEG-BOX 2.0 en utilisant la PDF CT10 NLO interfacé avec PYTHIA 6.428 pour les gerbes partoniques, avec PERUGIA2012 et CTEQ6L1 PDF pour décrire l'événement sous-jacent. Les événements $t\bar{t}$ ont été générés avec POWHEG-BOX 2.0 en utilisant la PDF NNPDF30NLO interfacé avec PYTHIA 8.186 pour les gerbes partoniques, avec A14 et la PDF CTEQ6L1 pour décrire l'événement sous-jacent. Des échantillons de dibosons ont été générés avec SHERPA 2.1.1 pour les processus de production gg et SHERPA 2.2.1 pour les processus de production $q\bar{q}$, en utilisant

respectivement les PDF CT10 NLO et NNPDF30NNLO. La production de bosons W et Z en association avec des jets a également été simulée en utilisant SHERPA 2.1.1 avec la PDF CT10 NLO, où les quarks b et c sont traités comme des particules massives. La production de $gg \to WW$ comprend également la contribution du boson de Higgs SM à 125 GeV et les effets d'interférence entre le continuum et les processus de résonance de Higgs. La partie VBF de la production de boson de Higgs SM a été générée avec POWHEG-BOX interfacé avec PYTHIA 8.186 pour les gerbes partoniques.

L'effet de multiples interactions pp dans les mêmes croisements de paquets et les voisins (empilement) a été inclus en superposant des collisions à biais minimum, simulées avec PYTHIA 8.186, sur chaque événement généré de signal ou de bruit de fond. Le nombre de collisions superposées est tel que la distribution du nombre moyen d'interactions par croisement de paquets pp dans la simulation correspond aux conditions d'empilement observées dans les données, soit environ 25 interactions en moyenne. Les échantillons générés ont été traités par une simulation de détecteur basée sur GEANT4, suivie du logiciel de reconstruction ATLAS standard utilisé pour les données de collision.

Reconstruction d'événements

Les événements utilisés dans cette analyse doivent avoir un vertex primaire, défini comme étant celui ayant les traces associées de plus haut p_{T}.

Les électrons sont reconstruits à partir d'amas de dépôts d'énergie dans le calorimètre électromagnétique correspondant à une trace reconstruite dans l'ID. Ils sont identifiés en utilisant des critères d'identification basés sur une méthode de maximum de vraisemblance. Les électrons doivent passer la sélection "MediumLH" pour $p_{\mathrm{T}} > 25\,\mathrm{GeV}$ ou la sélection "TightLH" pour $p_{\mathrm{T}} < 25\,\mathrm{GeV}$ et être dans $|\eta| < 2{,}47$, à l'exclusion de la région de transition, $1{,}37 < |\eta| < 1{,}52$, entre la partie centrale et les embouts du calorimètre.

Les muons sont reconstruits en combinant les traces ID et MS qui ont des trajectoires et courbures compatibles. Les candidats muons doivent requis d'avoir $|\eta| < 2{,}5$ et passer la sélection "Medium" pour $p_{\mathrm{T}} > 25\,\mathrm{GeV}$ ou la sélection "Tight" pour $p_{\mathrm{T}} < 25\,\mathrm{GeV}$, définie sur la base de la qualité de reconstruction et identification.

Pour s'assurer que les leptons proviennent du point d'interaction, une condition $|d_0|/\sigma_{d_0} < 5(3)$ est imposée aux électrons (muons) et $|z_0 \sin\theta| < 0{,}5\,\mathrm{mm}$ est appliqué aux deux types de leptons. Ici d_0 et z_0 sont les paramètres transverse et

longitudinal d'impact du lepton par rapport au vertex primaire, respectivement, et σ_{d_0} est l'incertitude de la valeur mesurée de d_0. De plus, les électrons et les muons doivent être isolés des autres traces et des activités calorimétriques en appliquant des critères d'isolation qui dépendent de p_{T} et $|\eta|$.

Les jets sont reconstruits à partir de dépôts d'énergie tridimensionnel dans les calorimètres électromagnétique et hadronique utilisant l'algorithme anti-k_t avec un paramètre de rayon de $R = 0{,}4$ implémenté dans le package FastJet. Les jets sont corrigés de l'énergie de l'empilement. Les jets doivent avoir $p_{\mathrm{T}} > 30\,\mathrm{GeV}$ et $|\eta| < 4{,}5$.

Pour les jets avec $p_{\mathrm{T}} < 60\,\mathrm{GeV}$ et $|\eta| < 2{,}5$, l'algorithme multivarié "tagger vertex" est utilisé pour supprimer les jets des interactions d'empilement. Pour éviter le double comptage, les jets de toute impulsion transverse sont rejetés s'ils sont dans un cône de taille $\Delta R = 0{,}2$ autour d'un candidat électron ou s'ils ont moins de trois traces associées et sont dans un cône de taille $\Delta R = 0{,}2$ autour d'un candidat muon. Cependant, si un jet avec trois traces ou plus est dans un cône de $\Delta R < 0{,}4$ autour d'un candidat muon, ou si la séparation entre un électron et un jet est de $0{,}2 < \Delta R < 0{,}4$, le candidat muon ou électron correspondant est rejeté.

Pour estimer le nombre de b étiquetés dans l'événement, les jets avec $p_{\mathrm{T}} > 20\,\mathrm{GeV}$ et au sein de $|\eta| < 2{,}5$ sont considérés comme contenant un hadron b si la variable discriminante de l'algorithme MV2c10 a une valeur dépassant un seuil, qui correspond au point de référence de 85% d'efficacité d'étiquetage de b, estimé à partir de b-jets dans des événements $t\bar{t}$ simulés.

Le moment transverse manquant, avec pour magnitude $E_{\mathrm{T}}^{\mathrm{miss}}$, est calculé comme étant l'opposé de la somme vectorielle des impulsions transverses des électrons, muons, et des jets calibrés provenant du vertex primaire, ainsi que des traces avec $p_{\mathrm{T}} > 500\,\mathrm{MeV}$ compatibles avec le vertex primaire et non associées à l'un de ces objets.

Sélection d'événements

Dans un premier temps, les événements candidats WW sont sélectionnés en demandant deux leptons avec des charges opposées et saveurs différentes (e ou μ). Les deux leptons doivent satisfaire les critères de qualité discutés ci-dessus. Lorsqu'ils sont ordonnés en p_{T}, ces leptons sont appelés leptons "leading" et "sub-leading", $p_{\mathrm{T}}^{\ell,(\mathrm{sub})\mathrm{lead}}$. Afin de supprimer le bruit de fond des processus de diboson, un veto est imposé sur les événements ayant un lepton supplémentaire avec $p_{\mathrm{T}}^{\ell,\mathrm{other}} > 15\,\mathrm{GeV}$.

Les variables utilisées dans les sélections sont les plus discriminantes choisies par un arbre de décision boosté (BDT), basé sur les échantillons de signal NWA. Ceux-ci sont $p_{\mathrm{T}}^{\ell,\mathrm{lead}}$, $m_{\ell\ell}$, la masse invariante de deux leptons, et $\Delta\eta_{\ell\ell}$, leur différence de pseudorapidité. Les deux premières variables fournissent une bonne séparation entre un signal de résonance lourde et les bruits de fond WW et quark top. La séparation entre le signal et le bruit de fond basée sur la distribution $\Delta\eta_{\ell\ell}$ s'avère avoir une efficacité raisonnable et permet, en même temps, de définir une région de contrôle pour le bruit de fond WW. Pour chaque variable sélectionnée, le critère de sélection est défini en maximisant la signification du signal en présence de bruit de fond. Les sélections ainsi obtenues sont $p_{\mathrm{T}}^{\ell,\mathrm{lead}} > 45\,\mathrm{GeV}$, $m_{\ell\ell} > 55\,\mathrm{GeV}$ et $|\Delta\eta| < 1{,}8$. Ces sélections optimisées conviennent également pour les signaux LWA.

Afin de supprimer davantage le bruit de fond quark top, des événements avec au moins un jet b étiqueté ($N_{b\text{-tag}} \geq 1$) est rejeté des régions de signal. Pour réduire la contribution du bruit de fond Z+jets et W+jets, deux autres variables sont utilisées: $p_{\mathrm{T}}^{\ell,\mathrm{sublead}}$, satisfaisant $p_{\mathrm{T}}^{\ell,\mathrm{sublead}} > 30\,\mathrm{GeV}$ et m_{T}^{W}, la valeur maximale de la masse transverse calculée avec l'un des deux leptons et l'impulsion transverse manquante, satisfaisant $\max(m_{\mathrm{T}}^{W}) > 50\,\mathrm{GeV}$. La dernière variable est définie comme: $m_{\mathrm{T}}^{W} = \sqrt{2p_{\mathrm{T}}^{\ell}E_{\mathrm{T}}^{\mathrm{miss}}\left[1-\cos(\phi^{\ell}-\phi^{E_{\mathrm{T}}^{\mathrm{miss}}})\right]}$, où p_{T}^{ℓ} et ϕ^{ℓ} sont l'impulsion transverse et l'angle azimutal d'un lepton et $\phi^{E_{\mathrm{T}}^{\mathrm{miss}}}$ est l'angle azimutal du vecteur de moment transverse manquant.

Trois catégories d'événements sont définies: deux catégories disjointes sont optimisées pour la production VBF, VBF $N_{\mathrm{jet}} = 1$ et VBF $N_{\mathrm{jet}} \geq 2$ (SRVBF1J et SRVBF2J), et une catégorie quasi-inclusive (à l'exclusion de l'espace de phase VBF) dédiée au signal ggF ou qqA (SRggF). Pour la catégorie VBF $N_{\mathrm{jet}} = 1$, deux variables discriminantes sont utilisées pour minimiser la contribution du signal ggF: la pseudorapidité du jet, η_j, et la valeur minimale de la différence de pseudorapidité entre le jet et l'un des leptons, $\min(|\Delta\eta_{j\ell}|)$. Ils sont tenus de satisfaire $|\eta_j| > 2{,}4$ et $\min(|\Delta\eta_{j\ell}|) > 1{,}75$, qui s'appelle l'espace de phase VBF1J. Pour la catégorie VBF $N_{\mathrm{jet}} \geq 2$, la masse invariante, m_{jj}, et la différence de rapidité, Δy_{jj}, des deux jets principaux sont utilisées pour sélectionner le signal VBF. Ils doivent satisfaire $m_{jj} > 500\,\mathrm{GeV}$ et $|\Delta y_{jj}| > 4$, qui s'appelle l'espace de phase VBF2J.

L'efficacité des signaux NWA et le LWA, après la sélection complète pour un signal ggF de 700 GeV, est d'environ 50% dans la catégorie quasi-inclusive ggF et 5% ou moins dans les catégories VBF $N_{\mathrm{jet}} = 1$ et $N_{\mathrm{jet}} \geq 2$. Pour un signal VBF de 700 GeV, elle est comprise entre 15% et 25% pour les trois catégories d'événements.

Pour les échantillons avec des masses de résonance inférieures, l'efficacité est plus faible parce que les leptons sont plus mous. C'est aussi la raison pour laquelle la recherche est limitée à des valeurs de masse de signal supérieures à environ 200 GeV. La même sélection est appliquée à tous les modèles et les différentes efficacités de sélection entre les modèles sont principalement dues aux différentes distributions $\Delta\eta_{\ell\ell}$ pour les différents états de spin.

La variable discriminante utilisée pour l'analyse statistique dans cette recherche est la masse transverse définie comme $m_{\mathrm{T}} = \sqrt{\left(E_{\mathrm{T}}^{\ell\ell} + E_{\mathrm{T}}^{\mathrm{miss}}\right)^2 + \left|\mathbf{p}_{\mathrm{T}}^{\ell\ell} + \mathbf{E}_{\mathrm{T}}^{\mathrm{miss}}\right|^2}$ où $E_{\mathrm{T}}^{\ell\ell} = \sqrt{|\mathbf{p}_{\mathrm{T}}^{\ell\ell}|^2 + m_{\ell\ell}^2}$ et $\mathbf{p}_{\mathrm{T}}^{\ell\ell}$ est le vecteur d'impulsion transverse de deux leptons.

Estimation du bruit de fond

Le bruit de fond dominant de l'état final $e\nu\mu\nu$ est dû aux événements quark top et WW du SM. Les autres bruits de fond proviennent des processus V+jets et diboson VZ, $V\gamma$ et $V\gamma^*$. Puisque la variable discriminante utilisée pour cette recherche est la masse transverse, m_{T}, la normalisation et la forme de la distribution de m_{T} des bruits de fond doivent être estimées. La forme des bruits de fond est modélisée en utilisant des événements simulés tandis que les normalisations des bruits de fond quark top et WW sont déterminées par un ajustement simultané aux données utilisant les distributions en m_{T} dans les régions de signal et les taux d'événements totaux dans les régions de contrôle. Les facteurs de normalisation de l'ajustement, appelés ci-dessous facteurs de normalisation "post-ajustement", fournissent la meilleure correspondance globale entre le nombre d'événements de données observés et les attentes des bruits de fond SM correspondantes dans toutes les régions de signal et de contrôle. Les régions de contrôle sont définies par des critères similaires à ceux utilisés pour les régions de signal, mais avec certaines exigences relâchées ou inversées pour obtenir des échantillons appauvris en signaux, enrichis en bruits de fond.

Les événements avec un boson W produit en association avec des jets peuvent entrer dans la SR lorsqu'un jet est identifié comme étant un lepton. En raison des difficultés de modélisation précise du processus d'identification erronée dans la simulation, la contribution du bruit fond W+jets est estimée à l'aide d'une méthode basée sur les données. Un échantillon d'événements est utilisé qui satisfait tous les critères de la sélection d'événements, sauf que l'un des deux candidats leptons ne répond pas aux critères de qualité pour être un lepton identifié mais satisfait à une sélection moins restrictive, appelée "anti-identifié". A partir de cet échantillon de données, la contribution de non-W+jets, dominée par les processus

quark top et WW, est soustraite sur la base des prédictions MC. La contamination des W+jets dans la région du signal est ensuite déterminée en multipliant le nombre d'événements dans l'échantillon de données soustraites de bruit de fond par un facteur d'extrapolation, qui est le rapport entre le nombre de leptons identifiés et le nombre de leptons anti-identifiés obtenu dans un échantillon de données des événements de dijet en fonction de p_{T} et η du lepton.

La contribution des bruits de fond Z/γ^* et diboson non-WW est faible. Les échantillons MC Z/γ^*+jets sont normalisés en utilisant les sections efficaces NNLO et les non-WW avec les sections efficaces NLO calculées par le générateur d'événements Sherpa. Le petit bruit de fond de la résonance du boson de Higgs $m_h \simeq 125\,\mathrm{GeV}$ et de sa composante hors-couche de masse est inclus et son interférence avec le bruit de fond continuum WW est pris en compte.

Incertitudes systématiques

Les sources dominantes d'incertitude expérimentale dans les taux de signal et des bruits de fond sont l'échelle et la résolution de l'énergie du jet, l'efficacité de l'étiquetage de b et la modélisation de l'empilement. Les autres incertitudes systématiques telles que celles associées aux efficacités de déclenchement, aux reconstructions du lepton et aux résolutions, la reconstruction de l'impulsion transverse manquante et le taggeur de vertex sont également prises en compte lors de l'évaluation des effets systématiques sur la forme et la normalisation des bruits de fond, la forme et l'efficacité de la sélection du signal. L'incertitude sur la luminosité intégrée totale de 2015 et 2016 est de 2,1%.

L'estimation du bruit de fond W+jets est sujette à plusieurs sources d'incertitude systématique. La soustraction des processus électrofaibles sous-dominants a un impact significatif sur le calcul du facteur d'extrapolation à grand p_{T} du lepton. L'incertitude correspondante sur le nombre d'événements dans la région de signal est obtenue en faisant varier cette soustraction. La méthode suppose que les facteurs d'extrapolation des échantillons de dijet et de W+jets sont égaux. Les différences dans la composition de la saveur des jets entre les événements dijet et W+jets introduisent une incertitude systématique supplémentaire. Ceci est évalué comme la somme en quadrature de deux contributions: les différences entre les facteurs d'extrapolation calculés avec les échantillons dijet et les échantillons de Z+jets dans les données, et les différences entre les facteurs d'extrapolation évalués avec les échantillons MC de W+jets et Z+jets. Enfin, les incertitudes statistiques des différents échantillons de données et de

MC utilisés pour évaluer les facteurs d'extrapolation sont considérées comme une source supplémentaire d'incertitude systématique.

Pour les sources des bruits de fond qui sont normalisés en utilisant des régions de contrôle, les incertitudes théoriques sont évaluées pour l'extrapolation de la région de contrôle à la région de signal selon la prescription du groupe de travail de section efficace du Higgs au LHC. Les incertitudes incluent l'impact des corrections d'ordre supérieur manquantes, des variations PDFs et d'autres modélisations MC.

Les incertitudes théoriques dans l'acceptance du signal incluent les effets dus au choix des échelles de renormalisation et de factorisation de la QCD, les PDFs ainsi que la modélisation sous-jacente et le modèle de parton. Ces incertitudes sont évaluées séparément dans chacune des trois catégories d'événements en fonction de la masse de résonance et indépendamment pour les résonances induites par la ggF et la VBF.

Résultats

Une fonction de vraisemblance $\mathcal{L}$ est définie comme le produit des probabilités de Poisson associées au nombre d'événements dans les bins des distributions m_{T} dans les régions du signal et des nombres totaux d'événements dans les régions de contrôle. Chaque source d'incertitude systématique est paramétrée par un paramètre de nuisance correspondant θ contraint par une fonction gaussienne.

Les distributions m_{T} dans les régions de signal sont divisées en 18 (8) pour la catégorie quasi-inclusive ggF (chacune de VBF $N_{\mathrm{jet}} = 1$ et ≥ 2). Les bins sont de taille variable pour refléter la largeur croissante de la distribution m_{T} du signal attendu avec une masse croissante, tout en gardant une précision statistique suffisamment élevée sur les contributions de bruits de fond dans chaque bin.

Les nombres d'événements sont obtenus à partir d'un ajustement simultané aux données dans toutes les SRs et CRs. Celui du signal ajusté est compatible avec zéro. Les compositions de bruits de fond dépendent fortement des catégories d'événements: le quark top et les processus WW sont comparables dans les SRs de ggF et VBF $N_{\mathrm{jet}} = 1$ tandis que les événements de quark top dominent dans la SR de VBF $N_{\mathrm{jet}} \geq 2$. Comme aucun excès par rapport à la prédiction de bruit fond n'est observé, des limites supérieures à 95% de niveau de confiance (CL) sont définies sur le produit de la section efficace de la production et le rapport d'embranchement, $\sigma_X \times B(X \to WW)$, pour les signaux dans chaque modèle de référence.

Les limites supérieures à 95% de CL sont calculées en utilisant la méthode

fréquentiste modifiée connue comme CL_s, avec l'approximation asymptotique de la distribution d'un test statistique, q_μ, une fonction de l'importance du signal μ, où μ est défini comme le rapport de $\sigma_X \times B(X \to WW)$ à la valeur du modèle:

$$q_\mu = -2 \ln \left(\frac{\mathcal{L}(\mu; \hat{\boldsymbol{\theta}}_\mu)}{\mathcal{L}(\hat{\mu}; \hat{\boldsymbol{\theta}})} \right) .$$

Les quantitiés $\hat{\mu}$ et $\hat{\boldsymbol{\theta}}$ sont les paramètres qui maximisent la vraisemblance et $\hat{\boldsymbol{\theta}}_\mu$ sont les valeurs de paramètres de nuisance qui maximisent la vraisemblance pour un μ donné.

Les limites sont obtenues séparément pour la production de ggF et de VBF pour des hypothèses de signaux NWA et LWA. Pour dériver les limites attendues sur le mode de production ggF (VBF), la section efficace de la production de VBF (ggF) est mise à zéro pour que les limites attendues correspondent seulement à l'hypothèse de bruit de fond. Pour dériver les limites observées sur le mode de production de ggF (VBF), la section efficace de la production de VBF (ggF) est traitée comme un paramètre de nuisance dans l'ajustement et profilé, de la même manière que de traiter les facteurs de normalisation des différents processus des bruits de fond. Cette approche évite de faire des suppositions sur la présence ou l'absence du signal dans l'un de ces modes de production.

Des valeurs de $\sigma_H \times B(H \to WW)$ au-dessus de 6,4 pb (1,3 pb) à $m_H = 200$ GeV et au-dessus de 0,008 pb (0,006 pb) à 4 (3) TeV sont exclues à 95% de CL pour le signal NWA dans le mode de production ggF (VBF). Les principales incertitudes systématiques affectant les limites sont celle liée à la correction p_{T} pour le premier lepton dans le bruit fond du quark top, l'incertitude théorique sur la contribution manquante d'ordre supérieur pour le même bruit de fond, l'incertitude sur la modélisation des gerbes partoniques de la production WW, et les incertitudes sur l'échelle d'énergie et la résolution de jet. Les limites sont compatibles avec celles attendues en l'absence d'un signal sur la gamme de masse étudiée.

L'analyse peut être étendue à un cas plus général où la fraction relative de la section efficace de la production de ggF varie sur celle de la production totale de ggF et de VBF. Les valeurs de limite pour une fraction ggF de 0 et 1 sont comparables aux limites VBF et ggF données ci-dessus à la même valeur de masse. Les limites VBF sont plus strictes que celles de ggF puisque la région de signal VBF $N_{\mathrm{jet}} \geq 2$ a le meilleur rapport du signal sur le bruit de fond et est donc la plus sensible.

La limite d'exclusion de la NWA indiquée ci-dessus peut être aussi traduite en contours d'exclusion dans le 2HDM pour l'espace de phase où l'approximation à faible largeur est valable. Les contours d'exclusion à 95% de CL pour les types I et II dans le plan de $\tan\beta$ et $\cos(\beta-\alpha)$ pour trois valeurs de masse de 200 GeV, 300 GeV et 500 GeV sont obtenues. Pour une valeur fixe de $\cos(\beta-\alpha) = -0{,}1$, on obtient également des limites d'exclusion à 95% de CL sur $\tan\beta$ en fonction de la masse du boson de Higgs lourd. Le couplage du boson de Higgs le plus lourd de CP-pair aux bosons vecteurs est proportionnel à $\cos(\beta-\alpha)$ et dans la limite de découplage $\cos(\beta-\alpha) \to 0$, le boson de Higgs de CP-pair est indiscernable du boson de Higgs SM avec la même masse. La gamme de $\cos(\beta-\alpha)$ et $\tan\beta$ explorée est limitée à la région où l'hypothèse d'un boson lourd de Higgs à largeur étroite avec interférence négligeable est valide. Lors du calcul des limites à un choix donné de $\cos(\beta-\alpha)$ et de $\tan\beta$, le taux relatif de production de ggF et de VBF dans l'ajustement est fixé à la prédiction du 2HDM pour ce choix de paramètre.

Pour le scénario LWA, les effets d'interférence entre le boson lourd, le boson de Higgs à 125GeV et le continuum WW SM ont été étudiés et ont montré un impact négligeable sur les limites d'exclusion. Les limites pour les largeurs de signal de 5%, 10% et 15% de leur masse sont comparables à celles du scénario NWA pour le signal VBF tandis que pour le signal ggF, les limites s'affaiblissent légèrement aux masses élevées lorsque la largeur augmente. Pour le cas LWA 15%, la limite d'exclusion supérieure est comprise entre 5,2 pb (1,3 627 pb) à $m_H = 200$ GeV et 0,02 pb (0,006 pb) à 4 (3) TeV pour le signal ggF (VBF).

Les limites sur le produit de la section efficace de la production de résonance et le rapport d'embranchement $\sigma_X \times B(X \to WW)$ et sur $\sin\theta_H$ pour un signal scalaire GM avec des masses comprises entre 200 GeV et 1 TeV sont obtenues. À la limite observée, la largeur est plus étroite que la résolution expérimentale. La sensibilité actuelle n'est pas suffisante pour exclure le modèle de référence avec $\sin\theta_H = 0{,}4$.

Les limites sont dérivées dans la gamme de masse de 250 GeV à 5 TeV et de 300 GeV à 1 TeV pour un signal HVT avec le mode de production qqA et VBF, respectivement. Pour la production de qqA, les signaux de masse inférieure à environ 1,3 TeV sont exclus à 95% de CL. Aucune limite ne peut être définie pour le mode de production VBF dans le modèle de référence qui suppose une force de couplage aux bosons de jauge $g_V = 1$ et un couplage aux fermions $c_F = 0$. Le modèle a une largeur intrinsèque beaucoup plus étroite que la résolution du détecteur.

Les limites d'un signal $G_{\mathrm{KK}} \to WW$ sont dérivées pour deux couplages

différents: $k/\bar{M}_{\mathrm{Pl}} = 1$ et $k/\bar{M}_{\mathrm{Pl}} = 0{,}5$, pour des masses comprises entre 200 GeV et 5 TeV, et pour un signal ELM spin 2 en mode de production VBF pour des masses comprises entre 200 GeV et 1 TeV. Les limites observées excluent un signal de graviton KK plus léger que 1,1 TeV (750 GeV) avec le grand (faible) couplage, tandis que la sensibilité actuelle n'est pas suffisante pour exclure le signal ELM spin 2 en mode de production VBF.

Conclusion

Cette thèse présente une recherche de résonances neutres et lourdes se désintègrant en une paire de bosons WW dans le canal $e\nu\mu\nu$. La recherche, réalisée par la collaboration ATLAS au LHC, utilise des données de collision proton-proton à une énergie dans le centre de masse de 13 TeV correspondant à une luminosité intégrée de 36,1 fb^{-1}. Mes contributions à cette analyse couvrent essentiellement toutes les parties de l'analyse, y compris l'optimisation de la sélection des événements dans différentes régions du signal et de la taille des bins pour les distributions de la masse transverse utilisées pour l'analyse statistique, les définitions des différentes régions de contrôle et l'estimation de contributions des bruits de fond SM correspondants, l'évaluation des incertitudes systématiques expérimentales et théoriques pour les bruits de fond principaux, l'analyse des données et la production d'intrants pour l'analyse statistique.

Aucun excès significatif d'événements au-delà de la prédiction des bruits de fond du modèle standard ne se trouve dans la gamme de masse comprise entre 200 GeV et jusqu'à 5 TeV. Des limites supérieures sont obtenues sur le produit de la section efficace de production et le rapport d'embranchement $X \to WW$ dans plusieurs scénarios: un boson de Higgs lourd avec une largeur étroite ou avec des largeurs intermédiaires (de 5%, 10%, 15% de la masse du boson de Higgs lourd), ainsi que d'autres signaux scalaires, vectoriels et de spin 2. Pour les signaux lourds de boson de Higgs à largeur étroite, des valeurs supérieures à 6,4 pb (1,3 pb) à $m_H = 200$ GeV et supérieures à 0,008 pb (0,005 pb) à 4 (3) TeV sont exclues avec un niveau de confiance de 95% pour le mode de production en fusion gluon-gluon (vecteur-boson). Pour les signaux du triplet vecteur lourd dans le modèle A, produit par l'annihilation quark-antiquarks, et pour le graviton du modèle Randall-Sundrum avec $k/\bar{M}_{\mathrm{Pl}} = 1$ (0,5), des valeurs de masse inférieures à 1,3 TeV et 1,1 TeV (750 GeV) sont exclues, respectivement.

Pour certains des modèles spécifiques considérés dans cette thèse, les limites d'exclusion actuelles sont toujours supérieures aux prédictions correspondantes des

modèles. Donc là il y aura une bonne perspective pour de futures améliorations. À faible masse ou faible m_{T} où la contribution de bruits de fond du SM est importante, la principale amélioration devrait venir d'une réduction de bruit de fond et des incertitudes systématiques. À des masses plus élevées où la sensibilité actuelle est limitée par la faible statistique des données, la forte augmentation attendue de la luminosité intégrée de la future prise de données au LHC améliorera grandement la sensibilité de la recherche.

Acknowledgements

First, I would like to take this opportunity to thank my Ph.D supervisor from LAL in France, Dr. Zhiqing Zhang, for his guidance on my Ph.D thesis, his help on my study and life and his excellent leadership in our analysis team. I'm very grateful for the convenience obtained from him in my life, especially given the fact that I don't really speak French and always seek for his help. I feel fortunate and honoured to know him and to work together with him under his supervision during the last three years. I enjoy discussing my work with him, because I always learn something new, especially the way of thinking to solve problems and to work efficiently. He is a very outstanding and respectable scientist who devotes his life to exploring the nature of universe and particles. And he is a reputable and considerate supervisor who always has critical comments on my work, experienced leadership of the research project and proper arrangements for me to proceed with my study abroad. He is also a very amiable person who is always willing to respect, believe and help me.

It gives me immense pleasure to thank my Ph.D supervisors from Shandong University in China, Prof. Lianliang Ma and Prof. Xueyao Zhang, for the opportunities they provided to me to join the ATLAS experiment and to study abroad, their continuous financial and sentimental support of my Ph.D study and related researches, their constructive suggestions on my work and their enthusiastic concern about my personal life. Lianliang is a diligent scientist, a conscientious advisor and also a very admirable person. He has also edified me a lot on my work and personality. He told me to be honest when it comes to something that is out of my knowledge, and it really helped me to know myself better and keep away from many troubles. He also gave many judicious comments on my work which helped me solve a lot of problems. Xueyao is a very kind person, a very patient advisor and a hard-working scientist. He has been continually provided me with not only financial support but also a lot of help which allows me to finish my university studies. Without their support and guidance, it would not be possible for me to conduct my researches and my Ph.D study.

I would also like to express my sincere gratitude to thank my master supervisor during the first year of my graduate education in Shandong University, Prof. Xingtao Huang, who directed my bachelor's thesis and took me to the world of particle physics experiments, accepted me as a graduate student after my undergraduate education and supervised my work on the Daya Bay experiment.

I would also like to thank Caterina Pizio and Sofia Maria Consonni from Italy,

who supervised my qualification task together with Lianliang when I was studying in University of Milan as a short-term exchange student. They also helped me a lot to get familiar with the life there and working on the ATLAS experiment, and moreover with Linux shell and C++ programming languages.

Apart from my supervisors, I would like to thank all the rest members of my thesis committee not only for their insightful comments and encouragement, but also for the hard questions that incented me to broaden my research from various perspectives.

I appreciate the effective scientific coopreration with all my fellow workmates from the ATLAS collaboration, the beneficial and stimulating academic discussions with the colleagues and friends from LAL and Shandong University and all the fun we have had in the last three years. Without their help and advice, it would be very hard for me to carry on my research project.

I would also like to thank all the professors and other lecturers in Shandong University and University of Paris-Sud, from whose comprehensive and impressive courses, I acquired immense knowledge about physics, experiments and statistics, which have been proved to be essential and helpful for my research project throughout my entire Ph.D study.

My sincere thanks also goes to all the administrator staff from LAL, CERN and Shandong University for their good work that makes my life much easier and guarantees the completeness of my registrations, travels and reimbursement, routine affairs and so on.

Last but not the least, I would like to thank my family: my parents and grandparents, as well as my grandgrandfather who passed away some years ago, for their understanding, financial and sentimental support and their persistent love. And a special thanks to my girlfriend, for her permanent love and company.

Contents

Chapter 1

Introduction

The Higgs boson, as an elementary particle predicted by the Standard Model (SM) in the early 1960s, was discovered in 2012 by the ATLAS [1] and CMS [2] Collaborations at the Large Hadron Collider (LHC) for the first time in the history of particle physics. Therefore the existence of the Higgs field, which was thought to give a particle mass and produce the Higgs boson through spontaneous symmetry breaking, was confirmed. The measured properties [3–6] of the Higgs boson are within experimental uncertainties, consistent with the SM predictions.

Nevertheless, the SM is still thought to be an incomplete theory. Many scenarios beyond the SM (BSM) are proposed with an extended Higgs sector [7, 8]. In several other extensions to the SM, such as the composite Higgs models [9, 10] and the warped extra dimensions models [11–14], diboson vector and tensor resonances are also predicted.

In this thesis, a search for a neutral heavy Higgs boson or other heavy resonances is presented, motivated by the statement mentioned above. The search uses the data collected by the ATLAS detector at the LHC from the pp collisions at the center-of-mass energy $\sqrt{s} = 13\,\text{TeV}$, corresponding to an integrated luminosity of $36.1\,\text{fb}^{-1}$.

A previous search for a heavy Higgs boson in the $H \to WW \to \ell\nu\ell\nu$ ($\ell = e, \mu$) decay channel was performed by the ATLAS [15] experiment based on a data sample with an integrated luminosity of $20.3\,\text{fb}^{-1}$ at $\sqrt{s} = 8\,\text{TeV}$. No excess of events beyond the SM background prediction was found. Upper limits were set on the product of the production cross section and the $H \to WW$ branching ratio in three different scenarios: a high-mass Higgs boson with a complex-pole scheme (CPS) lineshape and the width predicted for a SM Higgs boson, one with a narrow width approximation (NWA), and one with an intermediate width. The search was also performed in the $H \to WW \to \ell\nu qq$ decay channel in the same

study [15]. A combination of the $\ell\nu\ell\nu$ and $\ell\nu qq$ final states gave stronger upper limits. The CMS experiment also published a search for a high-mass scalar decaying into two W bosons or two Z bosons, including the fully leptonic final state [16], using datasets at $\sqrt{s} = 7$ and 8 TeV of 5.1 fb^{-1} and up to 19.7 fb^{-1} of integrated luminosity, respectively. The search was performed in the Higgs boson mass range 145–1000 GeV. Except for the SM Higgs boson with $m_H = 125$ GeV which was considered as a background process, addtional Higgs bosons with SM-like properties are excluded in the entire search range at the 95% confidence level (CL). A search for heavy resonances in the (bulk) Randall-Sundrum (RS) models in the fully leptonic decays of the WW channel, using a dataset of 4.7 fb^{-1} at 7 TeV [17], was reported by the ATLAS experiment. No significant excess of events was observed and upper limits on the production cross-section times branching ratio were set for two benchmark models: a spin-2 RS graviton G^* and the bulk RS graviton G^*_{bulk}. The observed lower limits at 95% CL on the masses of the two models are: 1.23 TeV for G^* and 0.84 TeV for G^*_{bulk}, assuming the coupling strength $k/\bar{M}_{\text{Pl}} = 0.1$ and $k/\bar{M}_{\text{Pl}} = 1.0$, respectively, where k is the curvature of the warped fifth dimension and $\bar{M}_{\text{Pl}} = \frac{M_{\text{Pl}}}{\sqrt{8\pi}}$ is the reduced Planck mass. The ATLAS and CMS experiments have obtained limits in the heavy vector triplet (HVT), the bulk RS and some other exotic models, based on other decay modes of the VV channels, V being either a W or a Z boson [18–27].

For the sake of a complete description of the analysis and results that are presented in this thesis, not only my own work but also the work from everyone in the working group are discussed. My personal contributions to the analysis are mainly listed as follows:

1. Optimisation of event selection in signal region (SR).

2. Analysis of data, which includes background estimation and making cut-flows, comparison between data and Monte Carlo (MC) prediction.

3. Estimation of experimental systematic uncertainty and theoretical systematic uncertainty on top and WW backgrounds.

4. Production of input for the statistical treatment.

5. Optimisation of the binning of transverse mass distributions for the statistical analysis.

The main body of the thesis is organised as follows. Chapter 2 gives an introduction to the SM, BSM physics and the signal models that are used in the

analysis to interpret the results. Chapter 3 presents briefly the LHC and the ATLAS detector, as well as the event reconstruction. Chapter 4 describes the data and MC samples that are used in the analysis. Chapter 5 introduces the definition of the objects or variables that are used in the analysis. Chapter 6 discusses the event selection in the SRs, including the optimisation strategy. Chapter 7 shows the backgrounds estimation. Chapter 8 discusses the systematic uncertainties. Chapter 9 presents the results. Chapter 10 provides a conclusion and an outlook of the analysis.

Chapter 2

Theoretical models

In this chapter, an introduction to the SM is presented, as well as some BSM theories. Signal models used in the analysis are also discussed in this chapter.

2.1 The Standard Model

The SM [28] of particle physics is the theory that describes three of the four known fundamental forces in the universe — the electromagnetic, weak and strong interactions. All known elementary particles can be well classified according to the SM. The SM has been developed during the last century within the context of gauge quantum field theories. Matter and forces are described by means of a reasonably limited number of fields. The quanta of these fields are particles, which at present are believed to be fundamental. The SM has had an enormous success in explaining several phenomena. A fundamental part of the SM is the spontaneous symmetry breaking mechanism responsible for the generation of masses of particles — the Higgs mechanism. A key prediction of the SM as a consequence of the introduction of this mechanism is the existence of a massive scalar boson — the Higgs boson. This prediction has been proved in 2012 - 2013 by the discovery and measurements of a new boson particle performed by the ATLAS and CMS experiments. The characteristics of the new particle are compatible with those predicted for the SM Higgs boson.

2.1.1 Elementary particles

In the SM, the elementary particles are grouped into 4 parts: quarks, leptons, gauge bosons and the scalar Higgs boson. There are three basic properties that are used to describe an elementary particle: mass, charge and spin. Each property

is assigned a number value, which can not be changed. Figure 2.1 shows these elementary particles in the SM. An elementary particle can be a fermion or a boson. Fermions are the building blocks of matter and have mass, while bosons behave as force carriers for fermion interactions. Fermions all have spin $\frac{1}{2}$, in unit of $\hbar$, and can be grouped into two types: leptons and quarks. Bosons can also be divided into two types: gauge bosons and scalar bosons. Every elementary particle has its own antiparticle. An antiparticle usually has the same mass, opposite electric charge and the same spin state with the elementary particle. For some particles, their antiparticles are themselves, like the Z boson and the photon.

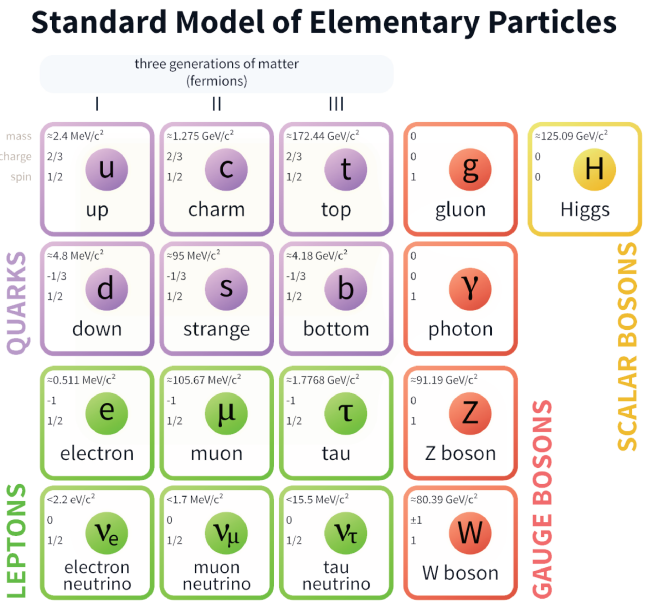

Figure 2.1: Elementary particles in the SM.

Leptons interact only through the electromagnetic interaction if they are charged and the weak interaction no matter whether they are charged or not. There are three generations of leptons that have been found so far. The first generation of leptons is composed of the electron (e^-) and electron neutrino (ν_e), and it is the lightest generation. The second generation of leptons includes the muon (μ^-) and muon neutrino (ν_μ) while the third generation includes the tau (τ^-) and tau neutrino (ν_τ) and it is the heaviest generation. Neutrinos have much smaller mass than the charged leptons in each generation of leptons. And neutrinos are believed to oscillate between different flavours in flight. For example, an electron neutrino that is produced in a beta decay [29] reaction may interact in a distant detector as a muon or tau neutrino. Usually in high energy collision physics experiments, when we talk about leptons, neutrinos are commonly not counted, due to

the fact that they are not observable in the detectors, and they are reconstructed in form of missing energy (more discussion about this can be seen in Section 5.5).

Quarks interact through the electromagnetic and weak interactions and also the strong interactions, and quarks have also six flavours that are also grouped into three generations. Similar to leptons, the first generation is the lightest and the third one is the heaviest. The first generation is composed of the up quark (u) and the down quark (d). The second generation includes the charm quark (c) and the strange quark (s). And the third generation is made up of the top quark (t) and the bottom quark (b). Quarks u, c and t all carry $\frac{2}{3}$ charge, while d, s and b quarks have $-\frac{1}{3}$ charge. A hadron is a composite particle that is usually made of 2 or 3 quarks bounded together by the strong force. And hadrons can be grouped into baryons (made of three quarks) and mesons (made of a quark and an antiquark). For example, protons and neutrons are both hadrons, and a proton is composed of two u quarks and a d quark, while a neutron is formed by udd quarks. Pions ($\pi^+ : u\bar{d}$, $\pi^0 : u\bar{u}$ or $d\bar{d}$, $\pi^- : d\bar{u}$) are an example of mesons.

Gauge bosons include the W boson, the Z boson, gluons and photons. The W boson can be either a W^- or a W^+ and they are each other's antiparticles. The Z boson carries no charge and is its own antiparticle. The W and Z bosons are known as the intermediate vector bosons for the weak interaction. A W boson can decay leptonically to a charged lepton and a neutrino or hadronically to a quark and an antiquark. A Z boson can decay to a fermion and its antiparticle. The decay can be either leptonic or hadronic. Gluons and photons both have no mass and carry no charge, and they are also regarded as antiparticles to themselves. In quantum chromodynamics (QCD) [30], gluons act as the exchange particles between quarks in the form of the strong interaction. In QCD, quarks carry three types of color charge (red: r, green: g and blue: b), while antiquarks carry three types of anticolor charge ($\bar{r}$, $\bar{g}$ and $\bar{b}$). There are eight independent types of gluon, known as the eight gluon colors, that are eight mixed states of the colors and anticolors. Photons are the force carrier for the electromagnetic force, massless and always travels at the speed of light within a vacuum.

In the SM, scalar bosons are bosons that have zero spin. So far, the only scalar boson that has been found is the Higgs boson, with a mass around 125 GeV, in the SM, with no electric or color charge. The Higgs boson is a quantum excitation of one of the four components of the Higgs field (see Section 2.1.3). And it is a very unstable particle decaying into other particles almost immediately. The decay branching ratios of the Higgs boson are shown in Figure 2.2.

According to the SM, the most important processes for the production of the

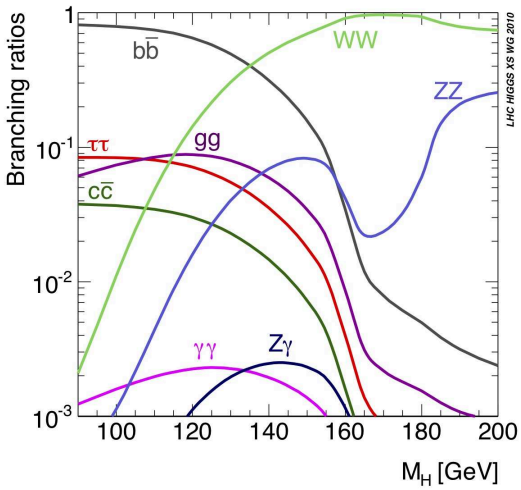

Figure 2.2: Standard Model Higgs boson decay branching ratios at different mass points.

Higgs boson are as follows:

Gluon gluon fusion (ggF): the easiest way to produce a Higgs boson, since there is a loop of virtual quarks (especially for heavy quarks t and b) in the production and the coupling of them to the Higgs boson is proportional to their masses.

Vector boson fusion (VBF): the Higgs boson is emitted by a virtual W or Z boson that is exchanged between two colliding (anti-)fermions.

Higgs Strahlung (VH): when a fermion collides with an anti-fermion, they are supposed to merge into a virtual W or Z boson that afterwards can emit a Higgs boson.

Top fusion (ttH): two gluons collide and both decay into a quark-antiquark pair, and from each pair a quark and an antiquark can then combine to form a Higgs boson.

The Feynman diagrams for these production modes are summarised in Figure 2.3. At the LHC, the ggF process is dominant in the production of Higgs bosons, and the VBF process is the second most important. VH is the third largest process and ttH is the smallest. The cross section of the processes for Higgs production at $\sqrt{s} = 13\,\text{TeV}$ is shown in Figure 2.4. The cross section for the ggF production mode is shown in blue color, and the VBF, VH and ttH modes are shown in red, green and purple, respectively.

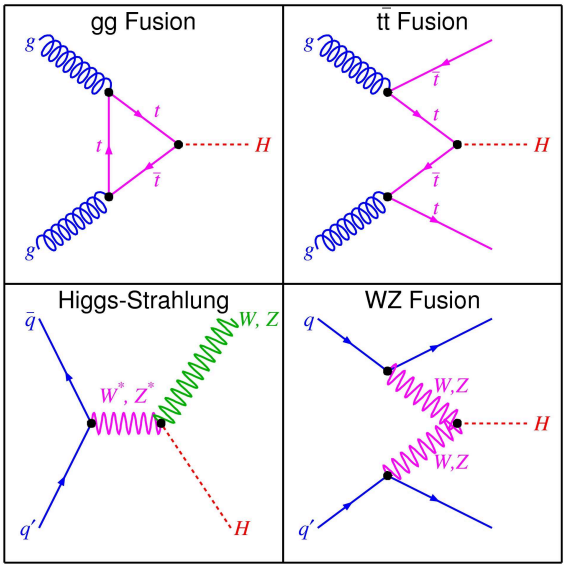

Figure 2.3: Feynman diagrams for the production of the Standard Model Higgs boson: ggF (top left), ttH (top right), VH (bottom left) and VBF (bottom right).

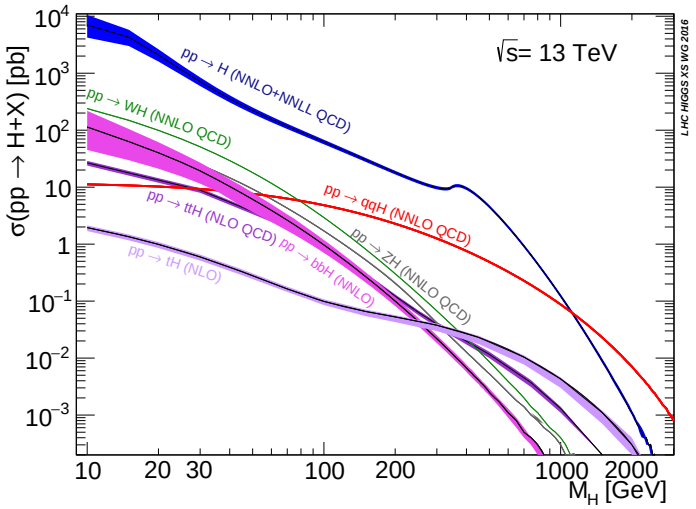

Figure 2.4: SM-like Higgs boson production cross sections as a function of mass. "NLO QCD" and "NNLO QCD" refer to next-to-leading order and next-to-next-to-leading order QCD calculations, respectively. "NNLO+NNLL" means that the logarithmically enhanced contributions due to multiple soft emissions have been resummed up to next-to-next-to-leading logarithmic accuracy and the result has been consistently matched to the fixed order NNLO result[31].

2.1.2 Fundamental interactions

There are four types of fundamental interactions that have been distinguished so far in nature. On the scales of particle physics, gravitional forces are insignificant, and usually neglected in the SM. Nevertheless the four forces are described briefly as follows:

Electromagnetic interaction: photons are the quanta of this force field and force carriers between charged fermions.

Weak interaction: W and Z bosons are the quanta of this force field. Based on the uncertainty principle, it is a short ranged force, with a range of approximately 10^{-3} fm.

Strong interaction: the quanta are gluons. It also has a short interaction range, approximately 1 fm, due to the fact that the gluon fields are always confining.

Gravitional force: known as gravity, which is the weakest in the four fundamental forces, and has no significant effect at the level of particle physics. The range of interaction is infinite, but the force becomes weaker as the range increases.

2.1.3 The Higgs mechanism

The central question of electroweak physics is: "Why are the W and Z boson masses non-zero?". To express this mathematically, a $U(1)$ gauge theory with a single gauge field is considered [32], known as the *Abelian Higgs Model*. The Lagrangian is simply

$$\mathcal{L} = -\frac{1}{4} F_{\mu\nu} F^{\mu\nu} \,, \tag{2.1}$$

where

$$F_{\mu\nu} = \partial_\nu A_\mu - \partial_\mu A_\nu \,. \tag{2.2}$$

The statement of local $U(1)$ gauge invariance is that the Lagrangian is invariant under the transformation:$A_\mu(x) \to A_\mu(x) - \partial_\mu \eta(x)$ for any η and x. Suppose we now add a mass term for the gauge boson to the Lagrangian,

$$\mathcal{L} = -\frac{1}{4} F_{\mu\nu} F^{\mu\nu} + \frac{1}{2} m^2 A_\mu A^\mu \,. \tag{2.3}$$

It is easy to see that the mass term violates the local gauge invariance. It is thus $U(1)$ gauge invariance which requires the gauge boson to be massless.

We now extend the model by adding a single complex scalar field with charge $-e$ which couples to the gauge boson. The Lagrangian is now,

$$\mathcal{L} = -\frac{1}{4}F_{\mu\nu}F^{\mu\nu} + |D_\mu\phi|^2 - V(\phi)\,, \tag{2.4}$$

where

$$\begin{aligned} D_\mu &= \partial_\mu - ieA_\mu \\ V(\phi) &= \mu^2|\phi|^2 + \lambda(|\phi|^2)^2\,. \end{aligned} \tag{2.5}$$

$V(\phi)$ is the most general renormalizable potential allowed by the $U(1)$ gauge invariance.

This Lagrangian is invariant under global $U(1)$ rotations, $\phi \to e^{i\theta}\phi$, and also under local gauge transformations:

$$\begin{aligned} A_{\mu(x)} &\to A_\mu(x) - \partial_\mu\eta(x) \\ \phi(x) &\to e^{-ie\eta(x)}\phi(x)\,. \end{aligned} \tag{2.6}$$

There are two possibilities for the theory[1]. If $\mu^2 > 0$ the potential has the shape shown in Figure 2.5 and preserves the symmetries of the Lagrangian. The state of lowest energy is that within $\phi = 0$, the vacuum state. The theory is simply quantum electrodynamics with a massless gauge boson and a charged scalar field ϕ with mass μ.

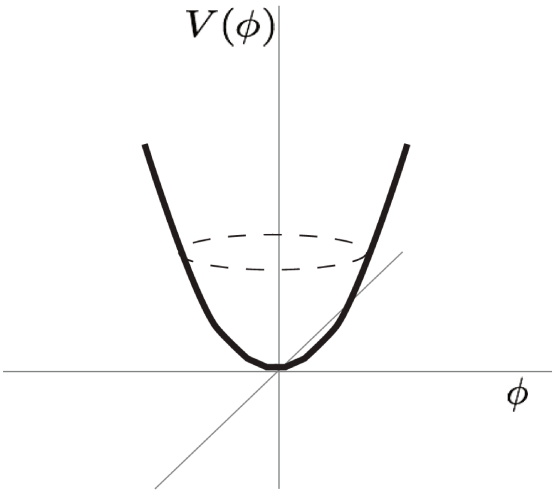

Figure 2.5: Scalar potential with $\mu^2 < 0$.

[1]We assume $\lambda > 0$. If $\lambda < 0$, the potential is unbounded from below and has no state of minimum energy.

In the alternative case $\mu^2 < 0$ and the potential can be written as,

$$V(\phi) = -|\mu^2||\phi|^2 + \lambda(|\phi|^2)^2\,, \tag{2.7}$$

which has the Mexican hat shape shown in Figure 2.6. In this case the minimum energy state is not at $\phi = 0$ but rather at

$$\langle\phi\rangle = \sqrt{-\frac{\mu^2}{2\lambda}} \equiv \frac{v}{\sqrt{2}}\,. \tag{2.8}$$

$\langle\phi\rangle$ is called the vacuum expectation value (VEV) of ϕ. Note that the direction in which the vacuum is chosen is arbitrary, but it is conventional to choose it to lie along the direction of the real part of ϕ. The VEV then clearly breaks the global $U(1)$ symmetry.

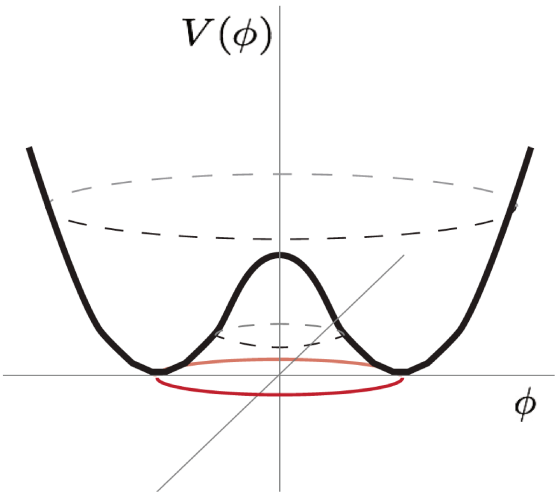

Figure 2.6: Scalar potential with $\mu^2 < 0$.

It is convenient to rewrite ϕ as

$$\phi \equiv \frac{1}{\sqrt{2}} e^{i\frac{\chi}{v}}(v + h)\,, \tag{2.9}$$

where χ and h are real fields which have no VEVs. If we substitute Equation 2.9 back into the original Lagrangian, the interactions in terms of the fields with no

VEVs can be found,

$$\begin{aligned}\mathcal{L} = & -\frac{1}{4}F_{\mu\nu}F^{\mu\nu} - ev A_\mu \partial^\mu \chi + \frac{e^2 v^2}{2} A_\mu A^\mu \\ & + \frac{1}{2}(\partial_\mu h \partial^\mu h + 2\mu^2 h^2) + \frac{1}{2}\partial_\mu \chi \partial^\mu \chi \\ & + (h, \chi\text{interactions})\,.\end{aligned} \tag{2.10}$$

Equation 2.10 describes a theory with a gauge boson of mass $M_A = ev$, a scalar field h with mass-squared $-2\mu^2 > 0$ and a massless scalar field χ. The mixed $\chi - A$ term is confusing, however, this term can be removed by making a gauge transformation:

$$A'_\mu \equiv A_\mu - \frac{1}{ev}\partial_\mu \chi\,. \tag{2.11}$$

After making the gauge transformation of Equation 2.11, the χ field disappers from the theory and we say that it has been "eaten" to give the gauge boson mass. This is called the Higgs mechanism and the χ field is often called a Goldstone boson. In the gauge of Equation 2.11, the particle content of the theory is apparent; a massive gauge boson and a scalar field h, which we also call a Higgs boson. The Higgs mechanism can be summarized by saying that the spontaneous breaking of a gauge theory by a non-zero VEV results in the disappearance of a Goldstone boson and its transformation into the longitudinal component of a massive gauge boson.

The simple Abelian $U(1)$ gauge theory discussed above describes actually electromagnetism, and the gauge boson that becomes massive through spontaneous symmetry breaking is the photon. However, in nature photons are generally massless particles, thus the $U(1)$ symmetry is unbroken.

The Higgs mechanism can also be described by non-Abelian gauge theories, such as the *Weinberg-Salam Model*, which is an $SU(2)_L \times U(1)_Y$ gauge theory and describes the electroweak interaction. In this model, the Higgs mechanism has its most important application and allows W and Z bosons to be massive. The model contains three $SU(2)_L$ gauge bosons, $W^i_\mu, i = 1, 2, 3$, and one $U(1)_Y$ gauge boson, B_μ, with kinetic energy terms,

$$\mathcal{L}_{\text{KE}} = -\frac{1}{4}W^i_{\mu\nu}W^{\mu\nu i} - \frac{1}{4}B_{\mu\nu}B^{\mu\nu}\,, \tag{2.12}$$

where

$$\begin{aligned} W^i_{\mu\nu} &= \partial_\nu W^i_\mu - \partial_\mu W^i_\nu + g\epsilon^{ijk}W^j_\mu W^k_\nu\,, \\ B_{\mu\nu} &= \partial_\nu B_\mu - \partial_\mu B_\nu\,. \end{aligned} \tag{2.13}$$

The gauge fields are coupled to a complex scalar $SU(2)$ doublet, $\Phi = \begin{pmatrix} \phi^+ \\ \phi^0 \end{pmatrix}$, and a scalar potential:

$$V(\Phi) = \mu^2 |\Phi^\dagger \Phi| + \lambda \left(|\Phi^\dagger \Phi| \right)^2 , \tag{2.14}$$

where $\lambda > 0$. As with the Abelian model, the state of minimum energy for $\mu^2 < 0$ is not at $\Phi = 0$ and the scalar field develops a VEV.

We can arbitrarily choose

$$\langle \Phi \rangle = \frac{1}{\sqrt{2}} \begin{pmatrix} 0 \\ \upsilon \end{pmatrix} , \tag{2.15}$$

and with this choice, the scalar doublet has $U(1)_Y$ charge (hypercharge) $Y_\Phi = 1$ and the electromagnetic charge is

$$Q = \frac{\tau_3 + Y}{2} . \tag{2.16}$$

Consequently,

$$Q \langle \Phi \rangle = 0 \tag{2.17}$$

and electromagnetism is unbroken by the scalar VEV.

The contribution of the scalar doublet to the Lagrangian is

$$\mathcal{L}_s = (D^\mu \Phi)^\dagger (D_\mu \Phi) - V(\Phi) , \tag{2.18}$$

where

$$D_\mu = \partial_\mu + i \frac{g}{2} \tau \cdot W_\mu + i \frac{g'}{2} B_\mu Y . \tag{2.19}$$

Since in unitary gauge there are no Goldstone bosons and only the physical Higgs scalar remains in the spectrum after the spontaneous symmetry breaking has occurred, the scalar doublet in unitary gauge can be writen as

$$\Phi = \frac{1}{\sqrt{2}} \begin{pmatrix} 0 \\ \upsilon + h \end{pmatrix} , \tag{2.20}$$

which gives contributions to the gauge boson masses from the scalar kinetic energy term of the Lagrangian,

$$\frac{1}{2} (0, \upsilon) \left(\frac{1}{2} g \tau \cdot W_\mu + \frac{1}{2} g' B_\mu \right)^2 \begin{pmatrix} 0 \\ \upsilon \end{pmatrix} . \tag{2.21}$$

The physical gauge fields are therefore two charged fields, $W^{\pm}$, and two neutral gauge bosons Z and γ.

$$\begin{aligned} W_{\mu}^{\pm} &= \frac{1}{\sqrt{2}}(W_{\mu}^{1} \mp iW_{\mu}^{2}) \\ Z^{\mu} &= \frac{-g'B_{\mu} + gW_{\mu}^{3}}{\sqrt{g^2 + g'^2}} \\ \gamma^{\mu} &= \frac{gB_{\mu} + g'W_{\mu}^{3}}{\sqrt{g^2 + g'^2}} \,. \end{aligned} \tag{2.22}$$

Thus the gauge bosons can obtain masses from the Higgs mechanism:

$$\begin{aligned} M_W &= \frac{g\upsilon}{2} \\ M_Z &= \frac{\sqrt{g^2 + g'^2}\upsilon}{2} \\ M_\gamma &= 0 \,. \end{aligned} \tag{2.23}$$

Since the massless photon must couple with electromagnetic strength, e, the weak mixing angle θ_W is defined by the coupling constants,

$$\begin{aligned} e &= g \sin\theta_W \\ e &= g' \cos\theta_W \,. \end{aligned} \tag{2.24}$$

2.1.4 Proton-proton interaction and parton distribution function

The cross section [33] of the proton-proton interactions can be expressed by:

$$\sigma = \sum_{i,j} \int dx_1 dx_2 f_i(x_1, \mu_F, Q^2) f_j(x_2, \mu_F, Q^2) \hat{\sigma}_{i,j}(x_1, x_2, \mu_R, \mu_F) \,, \tag{2.25}$$

where, f is the parton distribution function (PDF), defined as the probability density for finding a parton with a certain longitudinal momentum fraction x at resolution scale Q^2, $f(x, Q^2)$. The partonic cross section, $\hat{\sigma}_{ij}$, usually depends on the strong coupling constant α_s, which is a function of the renormalisation scale, and its calculation also depends on the factorisation scale:

$$\hat{\sigma}_{i,j} = \sum_{n} \alpha_s^n(\mu_R) \hat{\sigma}^{(n)}(x_1, x_2, \mu_R, \mu_F) \,. \tag{2.26}$$

where n is the order of the perturbation theory, and $\hat{\sigma}^{(n)}$ is the hard coefficient. The factorisation scale, μ_F, is usually thought to be the scale separating long- and

short-distance interactions. Below the scale, perturbation theory is no longer reliable, and the soft and collinear divergences could be absorbed into the PDF. The renormalisation scale, μ_R, is a point chosen to define the renormalised quantities in case of an infinite theoretical calculation (though in principle the prediction of the theory should be independent of the choice of μ_R).

PDF is usually driven by low-scale non-perturbative dynamics, and can not be computed from first principles, at least with current technology, and therefore they are determined using experimental data from a variety of hard-scattering cross sections in lepton-proton and proton-proton collisions.

PDFs and their associated uncertainties play a decisive role in several LHC applications. PDF uncertainties also affect the production of new high-mass resonances, as predicted by many BSM scenarios [34], since they probe PDFs at large values of the momentum fraction x, for which current experimental constraints are scarce.

The most generally used PDF sets in ATLAS are CT10 [35] (or CT14 [36]), NNPDF3.0 [37] and MMHT2014 [38]. Under some well-specified conditions, PDF sets can be statistically combined into an unified set, such as PDF4LHC15 sets [39], which combine the three sets using the Monte Carlo method [40], and are subsequently reduced to small number of Hessian eigenvectors [41, 42] or Monte Carlo replicas [43] to facilitate phenomenological applications.

2.2 Physics beyond the Standard Model

Although the SM perfectly describes all the particles found so far, it is still thought to be an incomplete theory, especially when it comes to a few phenomena that can not be explained by the SM, such as the gravity, dark matter and dark energy, neutrino masses and the asymmetry between matter and antimatter. Therefore BSM physics is believed to exist and a lot of efforts have been made to search for it. There are many theories [44] that have been brought up and developed in recent decades. Supersymmetry (SUSY) is a well-known one, in which each particle from one group would have an associated particle in the other, known as its superpartner. Theorists also predict existences of addtional BSM Higgs boson, such as a SM-like heavy Higgs boson, which is predicted to have very similar properties to the SM Higgs boson but still belongs to an extended scalar sector to the SM.

There are 19 free parameters in the SM that could not be calculated a priori and must be determined from experiments. The naturalness criterion dictates that

the parameters should take values of order 1, and are not fine-tuned. The mass of the Higgs boson has quadratically divergent loop corrections that correspond to the scale of any new physics, Λ_{cutoff}.

$$m_H^2 = m_{H,\text{bare}}^2 + \Delta m_H^2 = m_{H,\text{bare}}^2 + \alpha \Lambda_{\text{cutoff}}^2 \,. \tag{2.27}$$

The SM is accurate up to the Planck Scale, $\Lambda_{\text{Planck}} \sim 10^{19}\,\text{GeV}$. But in such a case, a fine-tuning between the bare mass and the correction term is needed to fix the observed, $m_H^2 \simeq 10^4\,\text{GeV}$. This fine-tuning breaks the principle of naturalness and leads to the hierarchy problem: why the weak scale, Λ_{EW}, so much lower than the Planck scale, Λ_{Planck}?

To resolve the fine-tuning problem, composite Higgs models [45, 46] suggested a new strongly interacting sector with a larger symmetry group, explaining electroweak symmetry breaking without a fundamental scalar. With a careful choice of this expanded symmetry group, spontaneous symmetry breaking, at a scale $\Lambda_{\text{comp}} \ll \Lambda_{\text{Planck}}$ is able to produce a composite Goldstone boson transforming as the SM Higgs doublet, and an unbroken symmetry that corresponds to the electroweak $SU(2) \times U(1)$ symmetry group. In this sense, the global symmetry is also explicitly broken, such as with Yukawa and gauge coupling terms, so that the Goldstone boson that corresponds to the composite Higgs can be massive. The approximate symmetry of the new strongly interacting sector also keeps the Higgs mass low, which addresses the problem of naturalness. Among the predictions of these models are resonances of composite scalars and new heavy gauge bosons near the TeV scale.

Another solution for the hierarchy problem is to postulate warped extra dimensions [47–49], also referred to as the RS models. According to the RS models, the universe is embedded in a five dimensional space (bulk) with constant negative scalar curvature (anti-de Sitter space). The SM particles are localised on a (3 + 1)-dimensional subspace (3-brane), called the weak or TeV brane, whilst there is a separate 3-brane where gravity is relatively strong, called the Planck brane. Only gravity is allowed to propagate in the bulk through the extra dimension. The five dimensional metric can not be factorized. The flat four-dimensional Minkowski metric, $\eta_{\mu\nu} = \text{diag}(-1, 1, 1, 1)$, has an additional warping factor depending explicitly on the extra dimension, ϕ, as described in Equation 2.28 for the space-time interval, ds^2, where, x^μ are the familiar four-dimensional space-time coordinates:

$$ds^2 = e^{-2kr_c|\phi|}\eta_{\mu\nu}dx^\mu dx^\nu + r_c^2 d\phi^2 \,. \tag{2.28}$$

The curvature scale, k, is assumed to be of order the Planck scale. The size of the extra dimension is determined by the compactification radius, r_c. The Planck brane is placed at $\phi = 0$ and the weak brane placed at $\phi = \pi$. In this way, physical mass parameters on the weak brane accumulate a warping factor with regard to their higher dimensional values, $m = e^{-kr_c\pi}m_0$, whilst the Planck mass on a brane depends only weakly on the fifth dimension. Provided that $kr_c \simeq 12$, the observed hierarchy on the weak brane can emerge geometrically from the warped extra dimension, as depicted in Figure 2.7. The RS models predict that Kaluza-Klein (KK) excitations [50], from the massless graviton propagating in the extra dimension, are coupled to SM gauge bosons. The lowest modes are expected near the TeV scale where their masses and couplings are determined.

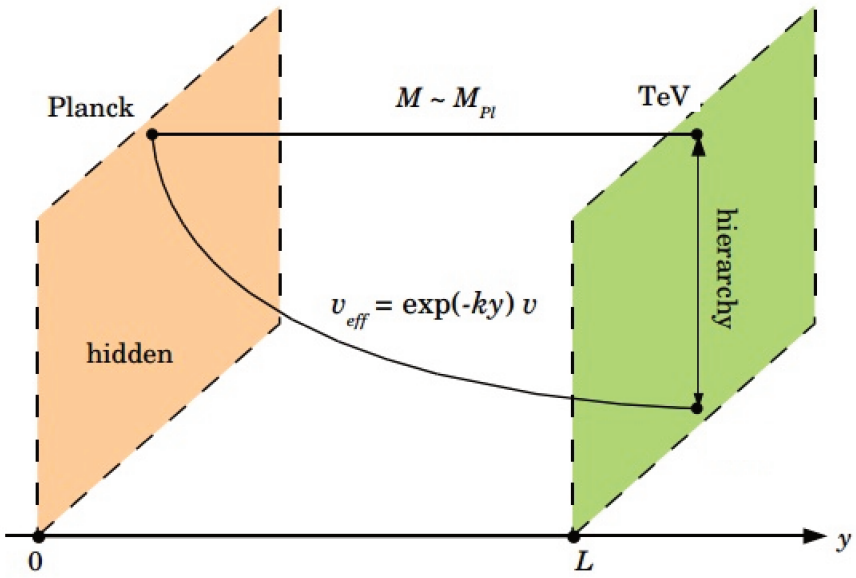

Figure 2.7: In the RS models, the Planck brane and the weak brane are separated by warped extra dimension. The Planck scale on a brane only weakly depends on the extra dimension, whilst the mass scales receive a warping factor [51].

Spontaneous symmetry breaking has been introduced in previous section in this thesis, as a minimal solution to provide mass to gauge bosons, while the Yukawa coupling is placed for fermions to acquire mass. However, theories with an extended Higgs sector [7, 8] preserve all of the SM gauge symmetries but split the functions of the SM doublet between multiple doublets, proposing to have even more exotic extensions with scalars that transform as weak isospin singlets or triplets. The simplest extensions, known as N Higgs doublet models (NHDM), suggest N complex scalar fields that transform as weak isospin doublets with weak hypercharge, $Y = 1$. For instance, with $N = 2$, the two complex scalar

doublets can be described by eight real scalars: three generate mass for the weak bosons, three neutral scalars, and two charged Higgs. Besides the spread of the Yukawa couplings among the additional doublets, theories with extended Higgs sector also offer mechanisms for the CP violation. And the singlet extension can explain dark matter, while a triplet extension explains neutrino masses without introducing a right-handed neutrino. New resonances that are predicted in an extended Higgs sector provide a rich phenomenology through couplings to the massive weak bosons.

Due to the success of the electroweak theory, which unified the electromagnetic and weak forces, so that the two forces could be regarded as two aspects of the same phenomenon, attempts have been made to construct a single theory that is able to unify the four fundamental forces. In the Grand Unified Theories [52–55] (GUT), the SM gauge group is embedded in a single larger group, therefore the strong and electroweak interactions unify at a large scale, Λ_{GUT}, manifesting themselves as separate interactions at lower energies. The ultimate goal of the GUT is to incorporate the gravitational force into the unification by formulating a satisfactory theory of quantum gravitation. This would produce a theory of everything (TOE), and one candidate is string theory.

Several selected benchmark models with different spin values are studied in this thesis and they are briefly described in Section 2.3.

2.3 Signal models

One scenario considered in the analysis for the heavy scalar assumes that the scalar has a width that is much smaller than the detector resolution. This is known as the NWA. A large width assumption (LWA) with widths of 5%, 10% and 15% of the heavy Higgs boson mass, is also considered. The widths of the heavy Higgs boson were chosen actually due to the fact that, for several of the most relevant BSM models, widths above 15% have already been excluded with indirect limits [56].

The two-Higgs-doublet-models (2HDM) are considered in different types [57], defined with assumptions about the couplings of each of the Higgs doublets as well as the discrete symmetries imposed. In the analysis, we consider Type I, in which one Higgs doublet couples to vector bosons and the other couples to fermions, and Type II of the minimal supersymmetric (SUSY)-like model where one Higgs doublet couples to up-type quarks while the other one couples to down-type quarks and charged leptons. In this analysis, a generic charge-conjugation- and parity-

conserving (CP-conserving) 2HDM, with a softly broken Z_2 symmetry [57] was considered. There are several free parameters: (i) five masses, such as m_h and m_H, for the two CP-even neutral states, m_A, for the pseudo-scalar, and $m_{H^\pm}$, for the charged Higgs boson pair, (ii) a mixing angle, α, between the CP-even neutral Higgs fields, and (iii) the ratio of the VEVs of the two Higgs doublets, $\tan\beta = v_2/v_1$. The benchmark is defined by setting the Higgs mass to $m_h = 125\,\text{GeV}$, and by setting the masses of the supersymmetric particles to be heavy enough, so that, the Higgs boson is kinematically forbidden to decay into SUSY particles. The cross sections and the branching fractions are calculated using SusHi and 2HDMC [58, 59].

The neutral member of the fiveplet in the Georgi-Machacek (GM) model [60, 61] also serves as a reference model in the VBF production mode. In the GM model, the Higgs sector is extended with the addition of a real and a complex triplet of $\text{SU}(2)_\text{L}$, and the SM value of $\rho = M_W^2/(M_Z^2\cos^2\theta_W) = 1$ is preserved at tree level, where, m_W and m_Z are the masses of the W and Z bosons, while θ_W is the weak mixing angle. The physical states include a fermiophobic fiveplet, H_5^0, $H_5^\pm$, and $H_5^{\pm\pm}$, of custodial SU(2) symmetry which couples preferentially to vector bosons [62]. For this reason, the GM model is less constrained [63] with production through the VBF process, compared to other standard benchmark models of a triplet Higgs field, e.g. the little Higgs model [64] and the left–right symmetric model [65]. There are many parameters [66, 67] in this model, but, if the other new Higgs bosons are heavier than those of the H_5 multiplet, the production mode is allowed only via the VBF process. The cross section and the decay width into VV are, as a result, proportional to a single parameter, $\sin^2\theta_H$, which characterises the fraction of the gauge boson masses that are generated by the triplet Higgs fields.

The couplings of the new spin-1 heavy bosons to SM particles are parameterised by the HVT Lagrangian [68, 69], in a generic way, and are allowed to mix with SM gauge bosons. The production mechanism of the heavy gauge bosons in the s-channel is primarily via $q\bar{q}$ annihilation (qqA). The HVT bosons are coupled to the Higgs boson and the SM gauge bosons with the coupling strength, $c_h g_V$, and coupled to the fermions with the coupling strength, $g^2 c_F/g_V$. Here g is the SM $\text{SU}(2)_\text{L}$ gauge coupling, c_h and c_F are multiplicative factors that are used to modify the couplings to the Higgs boson and fermions, respectively, and g_V represents the coupling strength to the W and Z bosons. For the case of vector-boson fusion, the coupling to fermions is not assumed, so non-VBF production processes are suppressed.

The spin-2 G_{KK}, as the first Kaluza–Klein (KK) excitation of the graviton in the RS model, is assumed to have a warped extra dimension [11, 50], in which the SM fields are localised in the bulk [12–14].

A tensor resonance signal in the VBF production mode is proposed based on an effective Lagrangian model (ELM) [70], with Λ being a characteristic energy scale of the underlying new physics [70],

$$\mathcal{L} = \frac{1}{\Lambda} T_{\mu\nu} \left(f_1 B^{\alpha\nu} B^{\mu}_{\alpha} + f_2 W_i^{\alpha\nu} W_{\alpha}^{i,\mu} + 2 f_5 (D^{\mu}\Phi)^{\dagger} (D^{\nu}\Phi) \right) ,$$

where, f_i are various coupling parameters, $T_{\mu\nu}$ is the spin-2 singlet field, $B^{\alpha\nu}$ and $W_i^{\alpha\nu}$ are the electroweak field strength tensors, and Φ is the scalar Higgs field. The covariant derivative D^{μ} is defined as $D^{\mu} = \partial^{\mu} - igW_i^{\mu}\sigma^i/2 - ig'YB^{\mu}$, where σ^i are the Pauli matrices, Y is the weak hypercharge, and g and g' are the corresponding gauge coupling constants. The model is different from the RS model with respect to the couplings to fermions or gluons which are not included in the Lagrangian. Besides, the BSM amplitude is multiplied by a form factor that is a function of a cut-off scale, Λ_{ff}, and a suppression power, n_{ff}, used to preserve unitarity at high energies:

$$f(p_1^2, p_2^2, k_{\mathrm{sp2}}^2) = \left(\frac{\Lambda_{ff}^2}{|p_1^2| + \Lambda_{ff}^2} \cdot \frac{\Lambda_{ff}^2}{|p_2^2| + \Lambda_{ff}^2} \cdot \frac{\Lambda_{ff}^2}{|k_{\mathrm{sp2}}^2| + \Lambda_{ff}^2} \right)^{n_{ff}} ,$$

where, p_1^2 and p_2^2 are the squared invariant masses of the incoming electroweak bosons, while k_{sp2}^2 is the squared invariant mass of the sum of the initial boson momenta, which is equivalent to that of an s-channel spin-2 particle. The specific parameter settings for the signal models that used in the analysis are given in Chapter 4.

The different signal models studied are summarised in Table 2.1.

Table 2.1: A summary of different benchmark signal models that are considered in the analysis. The resonance spin and the production mode are also specified. In the table, ggF refers to gluon–gluon fusion, qqA refers to quark–antiquark annihilation and VBF refers to vector-boson fusion.

Model	Resonance spin	Production mode		
		ggF	qqA	VBF
NWA	Spin-0	x		x
2HDM		x		x
LWA		x		x
GM				x
HVT	Spin-1		x	x
Bulk RS	Spin-2	x		
ELM				x

Chapter 3

The Large Hadron Collider and the ATLAS detector

The LHC at CERN, the European Organization for Nuclear Research, is the largest and most powerful collider ever built by human in the world. There are seven detector experiments constructed at the LHC — ATLAS, CMS, ALICE, LHCb, LHCf, TOTEM and MoEDAL. Two of them, ATLAS and CMS, are large, general purpose detectors, aimed mainly at studies of the Higgs boson and searches for new physics. The LHC and the ATLAS detector will be discussed with more details in Sections 3.1 and 3.2, respectively.

3.1 The LHC

The LHC [71] is a two-ring-superconducting-hadron particle accelerator and collider. Being the most famous particle accelerator in the world, the LHC extends the frontiers of particle physics with its unprecedented high energy and luminosity. It was installed in a tunnel of 27 km in circumference and 175 m in depth underground that was constructed between 1984 and 1989 at CERN (located in Geneva, Switzerland, however, the tunnel is actually built beneath the border between France and Switzerland) for the Large Electron-Positron Collider (LEP) machine. The tunnel has eight straight sections and eight arcs, and in addition, there are two transfer tunnels, each approximately 2.5 km in length, linking the LHC to the CERN accelerator complex[2] that acts as injector. The LHC was first started up in 2008 and remains the latest addition to CERN′s accelerator

[2]The CERN accelerator complex is a succession of machines that accelerate particles to higher energies increasingly and sequentially.

complex.

The collision of the beams inside the LHC happens at four locations around the accelerator ring, corresponding to the positions of four particle detectors and experiments — ATLAS, CMS, ALICE and LHCb. Figure 3.1 shows a schematic overview of the LHC, including the four detector sites and the injection accelerator systems. Inside the accelerator, two high-energy particle beams travel at close to the speed of light in opposite directions in separate beam pipes before they are made to collide. They are guided around the accelerator ring by a strong magnetic field maintained by the superconducting dipole magnets. Additional quadrupole magnets are used to keep the beams focused, with stronger quadrupole magnets close to the intersection points to maximize the chances of interaction where the two beams cross. Magnets of higher multipole orders are used to correct smaller imperfections in the field geometry.

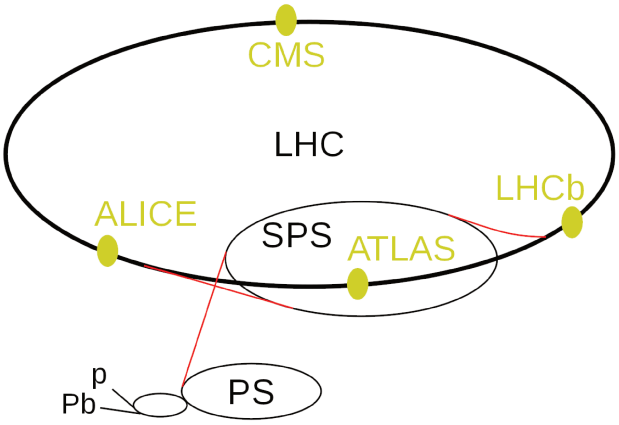

Figure 3.1: The LHC accelerator.

The LHC physics programme is mainly based on proton-proton collisions. However, shorter running periods, typically one month per year, with heavy-ion collisions are included in the programme. While lighter ions are considered as well, the baseline scheme deals with lead ions. The aim of the heavy-ion programme is to investigate quark-gluon plasma, which existed in the early universe. For the proton-proton collision at the LHC, the protons are first accelerated to 1.4 GeV and injected into the Proton Synchrotron (PS), where they are accelerated to 26 GeV. Then the Super Proton Synchrotron (SPS) is used to further increase the energy of the protons to 450 GeV before they are injected (over a period of several minutes) into the main LHC ring. After that, the proton bunches are accumulated, accelerated (over a period of 20 minutes) to their peak energy, and finally

circulated for 5 to 24 hours while collisions occur at the four intersection points.

3.2 The ATLAS detector

ATLAS [72] (A Toroidal LHC ApparatuS) is one of two general-purpose detectors at the LHC, while CMS (Compact Muon Solenoid) being the other one. In this section, the ATLAS detector is discussed. First of all, an overview is presented in Section 3.2.1. The inner detector, calorimetry system, muon spectrometer, forward detectors, trigger and data acquisition system are presented in Sections 3.2.2 - 3.2.6, respectively.

3.2.1 Overview

The ATLAS detector, as the largest particle detector ever constructed, sits in a cavern 100 m underground near the main CERN site, close to the village of Meyrin in Switzerland. More than 3000 scientific authors from about 182 institutions in 38 countries work on the ATLAS experiment.

The ATLAS experiment investigates a wide range of physics, from the search for the Higgs boson to extra dimensions and particles that could make up dark matter. Although it has the same scientific goals as the CMS experiment, it uses different technical solutions and a different magnet-system design. Different detecting subsystems arranged in layers around the collision point record the paths, momentum, and energy of the particles, allowing them to be individually identified. This includes mainly the inner detector, the calorimeters, the muon spectrometer and the magnet systems.

Figure 3.2 shows the overall layout of the ATLAS detector. It is nominally forward-backward symmetric with respect to the interaction point. It uses two large superconducting magnet systems to bend charge particles so that their momenta can be measured. One is the inner soleniod that produces a strong magnetic field surrounding the inner detector. The other is the outer toroidal magnetic field, which is produced by eight very large air-core superconducting barrel loops and two end-caps air toroidal magents. The magnet configuration comprises a thin superconducting solenoid surrounding the inner-detector cavity, and three large superconducting toroids (one barrel and two end-caps) arranged with an eight-fold azimuthal symmetry around the calorimeters. This fundamental choice has driven the design of the rest of the detector.

The interactions in the ATLAS detectors create an enormous flow of data.

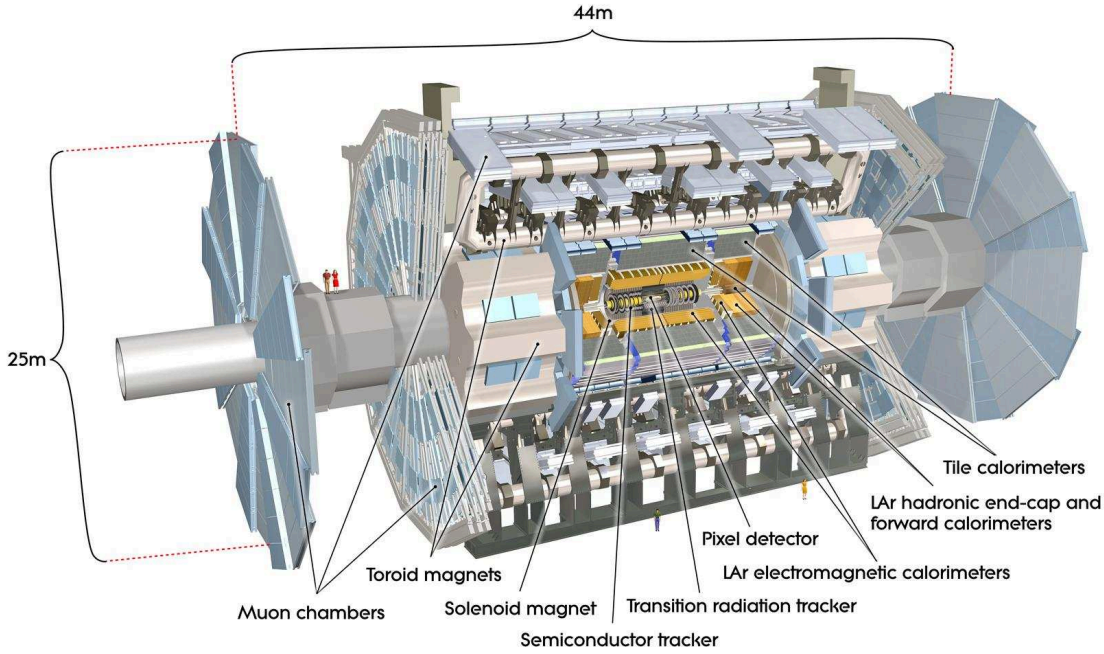

Figure 3.2: Cut-away view of the ATLAS detector. The dimensions of the detector are 25 m in height and 44 m in length. The overall weight of the detector is approximately 7000 tonnes.

To digest the data, ATLAS uses an advanced "trigger" system to tell the detector which events to record and which to ignore. Complex data acquisition and computing systems are then used to analyse the collision events recorded.

As far as the coordinate system is concerned, the nominal interaction point is defined as the origin of the system, while the beam direction defines the z-axis and the $x - y$ plane is transverse to the beam direction. The positive x-axis is defined as pointing from the interaction point to the centre of the LHC ring and the positive y-axis is defined as pointing upwards. The side-A of the detector is defined as that with positive z and side-C is that with negative z. The azimuthal angle ϕ is measured as usual around the beam axis, and the polar angle θ is the angle from the beam axis. The pseudorapidity is defined as $\eta = -\ln\tan\theta/2$ (in the case of massive objects such as jets, the rapidity $y = 1/2\ln[(E+p_z)/(E-p_z)]$ is used). The transverse momentum p_{T}, the transverse energy E_{T}, and the missing transverse energy $E_{\mathrm{T}}^{\mathrm{miss}}$ are defined in the $x - y$ plane unless stated otherwise. The distance ΔR in the pseudorapidity-azimuthal angle space is defined as $\Delta R = \sqrt{\Delta\eta^2 + \Delta\phi^2}$.

3.2.2 Inner detector

The ATLAS inner detector (ID) system, immersed in a 2 T axial magnetic field, is used to provide measurements of trajectory reconstruction for charged particles, with a pseudorapidity coverage of $|\eta| < 2.5$. A cut-away view of it is displayed in Figure 3.3, showing mainly its geometric construction. It consists of three different but complementary subsystems: a silicon pixel detector (pixel), a silicon micro-strip detector (SCT) and a transition-radiation straw-tube tracker (TRT).

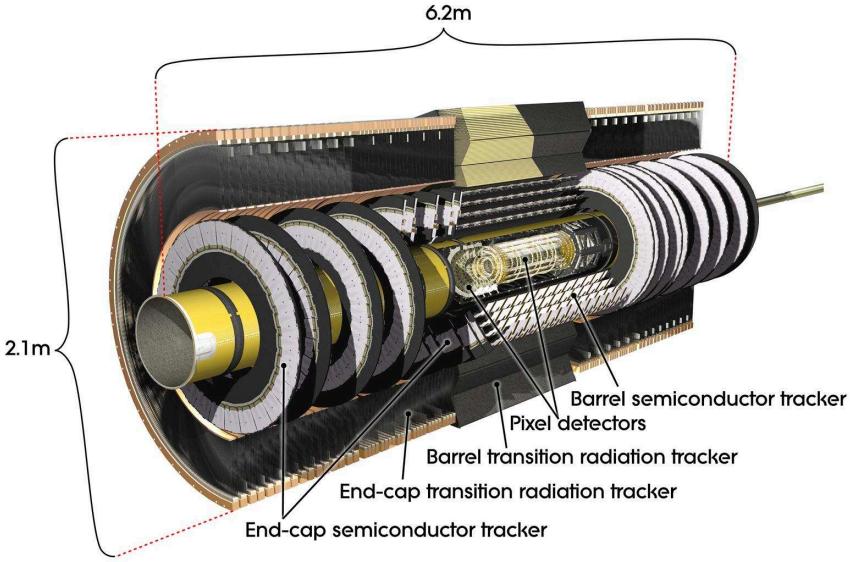

Figure 3.3: Cut-away view of the inner detector.

The reconstruction of interaction vertices helps to identify the locations where particles interact with the material of the ID. The largest source of secondary particles is from nulear interaction of primary particles with the ID material, where primary particles refer to particles that are promptly produced in the pp collision, while secondary particles refer to those produced in the decays of primary particles or their interaction with detector material. The ID is designed such that its material has a minimum effect on the particles traversing its volume. The layout of the ID for Run 2 is shown in Figure 3.4. During the LHC long shutdown in 2013–2014, between Run [3] 1 and Run 2, the ID was upgraded with installing a new pixel-detector layer, referred to as the insertable B-layer (IBL), together with a new, thinner beam pipe which is used to minimise the distance of the IBL from

[3]Run 1 refers to the period of the LHC data-taking in 2008–2012, while Run 2 refers to the period since 2015.

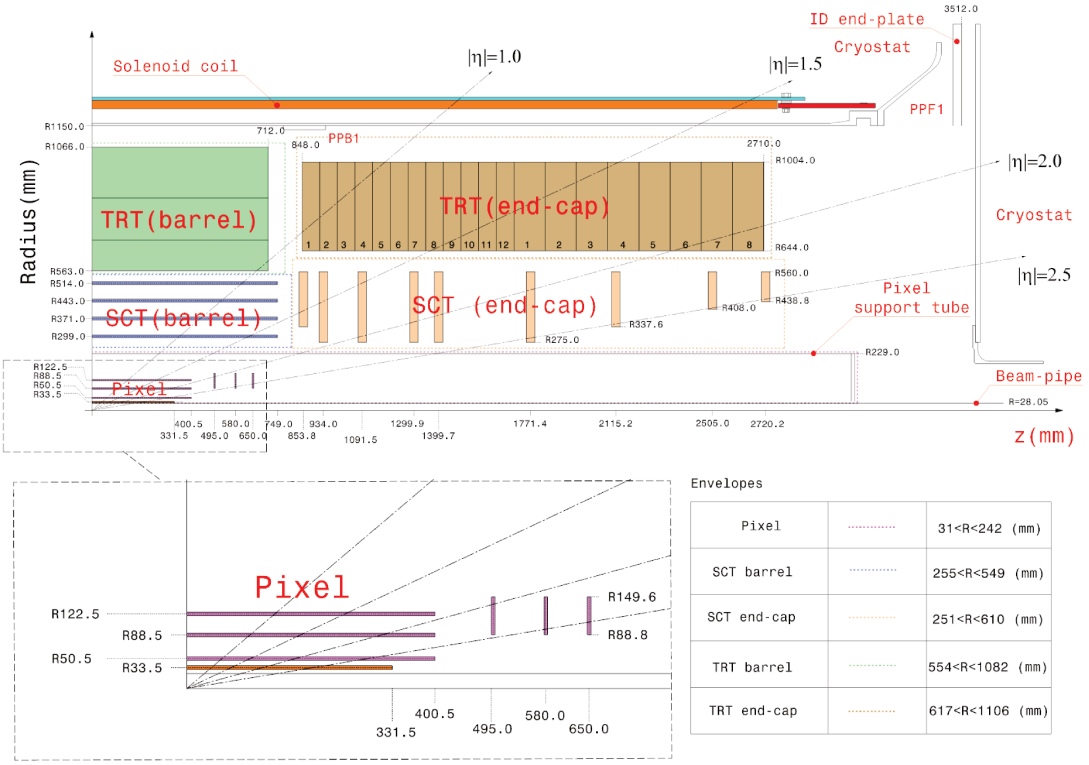

Figure 3.4: Plan view of a quarter-section of the inner detector showing each of the major detector elements with its active dimensions and envelopes. The labels PP1, PPB1 and PPF1 indicate the patch-panels for the inner detector services.

the beam line. In addition, the pixel detector has been extracted and renovated in the meanwhile. The IBL helps to improve the track reconstruction performance, e.g. the resolution of the transverse and longitudinal impact parameters, d_0 and z_0, are improved by more than 40% in the best case of tracks with p_{T} around 0.5 GeV. The transverse impact parameter, d_0, is defined as the shortest distance between a track and the beam axis in the transverse plane. The longitudinal impact parameter, z_0, is defined as the distance in z-aixs between the primary vertex and the point on the track that is used to estimate d_0.

In addition to the IBL, the pixel detector has three other barrel layers (referred to as PIX1, PIX2 and PIX3 inside-out) and two end-caps each made of three disks. It hosts 1744 pixel-sensor modules, each module containing 46080 pixels (there are over 80 million pixels in the ID in total). An octagonal prism structure, referred to as the pixel support frame (PSF) is inserted inside the pixel support tube (PST) to support the barrel and end-cap layers of the pixel detector. In the pixel detectors, the time over threshold (ToT) is used to measure the charge of tracks that is collected by each individual pixel [73]. ToT is defined to be the time when the pulse exceeds a given threshold and it is proportional to the deposited energy. The SCT, shortened from a Semiconductor Tracker, is installed outside of the pixel volume and consists of 4088 silicon micro-strip modules, distributed in four barrel layers (referred to as SCT1, SCT2, SCT3 and SCT4 inside-out) and two end-caps, each having nine wheels. Every module is made of two layers of silicon micro-strip detector sensors that are glued back-to-back. The SCT sensors are not used to collect charge of the tracks. The TRT is the outermost subsystem of the ID and it consists of more than 350,000 gas-filled straw tubes. The reconstruction of tracks is properly extended radially up to a radius of 1082 mm by the TRT. The TRT straw tubes provide the raw timing information, which can be translated into calibrated drift circles that are used to match track candidates that are reconstructed from the SCT. The structures of the SCT and TRT are the same with that used for Run 1.

3.2.3 Calorimetry

Calorimeters measure the energy a particle loses as it passes through the detector. They are usually designed to stop entire or "absorb" most of the particles coming from a collision, forcing them to deposit all of their energy within the detector. Typically calorimeters consist of layers of "passive" or "absorbing" high-density material — for example, lead — interleaved with layers of an "ac-

tive" medium such as solid lead-glass or liquid argon. In this sense, the ATLAS calorimetry system includes two types of calorimeters: the Liquid Argon (LAr) calorimeters and the Tile Hadronic calorimeters.

In terms of functionality and performance, there are two basic calorimeter systems: an inner electromagnetic (EM) calorimeter and an outer hadron calorimeter. Both are sampling calorimeters[4]. The EM calorimeter measures the energy of electrons and photons as they interact with matter electromagnetically. It has high precision in the measurement of energy deposition. The hadron calorimeter absorbs energy from particles that pass through the EM calorimeter but interact via strong force. These particles are primarily hadrons. It is less precise than the EM calorimeter.

The LAr EM calorimeter with high granularity covers the pseudorapidity range $|\eta| < 3.2$. The hadron calorimetry in the range $|\eta| < 1.7$ is provided by a scintillator-tile calorimeter, which is separated into a large central barrel and two smaller extended barrels. In the end-caps ($|\eta| > 1.5$), LAr technology is also used for the hadron calorimeter, matching the outer $|\eta|$ limits of the EM calorimeter end-caps. The LAr forward calorimeters provide both electromagnetic and hadronic energy measurements, and extend the pseudorapidity coverage to $|\eta| = 4.9$. An overall view of the calorimeters is depicted in Figure 3.5.

3.2.3.1 Electromagnetic calorimeter

The EM calorimeter [74] is divided into a barrel section (EMB) with a coverage of $|\eta| < 1.475$ and two end-cap sections (EMEC) covering the pseudorapidity region $1.375 < |\eta| < 3.2$. Each section is housed in its own cryostat. The barrel and end-cap parts are divided into 16 and 8 modules, respectively, in ϕ. The region between the EMB and the EMEC, covering $1.37 < |\eta| < 1.52$, is called the transition region. A high voltage (HV) system is used to generate an electric field of approximately 1 kV/mm, allowing ionisation electrons to drift in the LAr gap. In the EMB, the value of the HV is a constant along η, and in the EMEC, the gap varies continuously with radius, thus it is adjusted in steps along η.

The barrel has accordion-shaped electrodes and energy-absorbing materials are lead and stainless steel, with liquid argon as the sampling materials, and a cryostat is required around the calorimeter to keep it sufficiently cool. The accordion geometry (see Figure 3.6) provides complete ϕ symmetry without azimuthal cracks and fast extraction of the signal at the rear or at the front of the electrodes.

[4]That is, they absorb energy in high-density metal and periodically sample the shape of the resulting particle shower, inferring the energy of the original particle from this measurement.

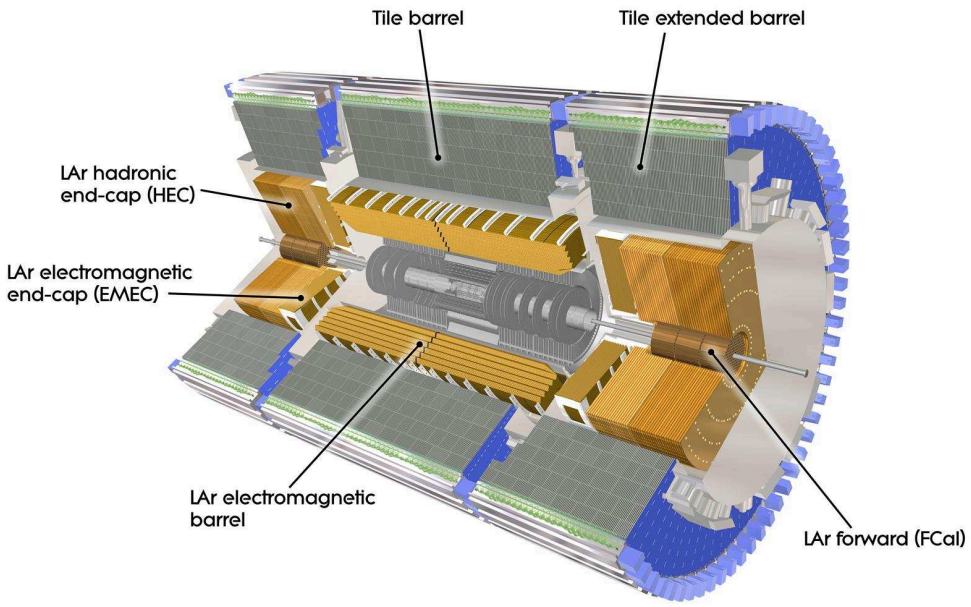

Figure 3.5: Cut-away view of the calorimetry system.

Both the barrel and end-cap calorimeters are segmented longitudinally into three layers in depth of shower within $|\eta| < 2.5$. The first layer (L1), covering $|\eta| < 1.4$ and $1.5 < |\eta| < 2.4$, is composed of high-granularity strips, which have typically, e.g. 0.003×0.1 in $\Delta\eta \times \Delta\phi$ in EMB. Such a design makes it sufficient to provide an event-by-event discrimination between single photon showers and overlapped showers from the decay of neutral hadrons from jets. The second layer (L2), being used to collect most of the deposited energy in the calorimeters from electron and photon showers, has a granularity of 0.025×0.025 in $\Delta\eta \times \Delta\phi$. The third layer (L3), with a granularity of 0.05×0.025 in $\Delta\eta \times \Delta\phi$, is designed mainly to correct the leakage beyond the EM calorimeters for high-energy showers. There is also a thin pre-sampler layer(PS), which has a coverage of $|\eta| < 1.8$ and granularity of 0.025×0.1 in $\Delta\eta \times \Delta\phi$ and is used to correct the energy loss.

Electrons and photons that enter the LAr calorimeters will interact with the lead absorbers and build EM showers which then ionise the LAr in the gaps between the absorbers. The ionisation electrons drift and induce an electrical signal on the electrodes that is proportional to the energy that is deposited in the active volume of the calorimeters. The signal is brought through cables to the read-out Front End Boards, where it is first amplified by a current-sensitive pre-amplifier.

The total energy deposited in an EM calorimeter cell can be reconstructed as

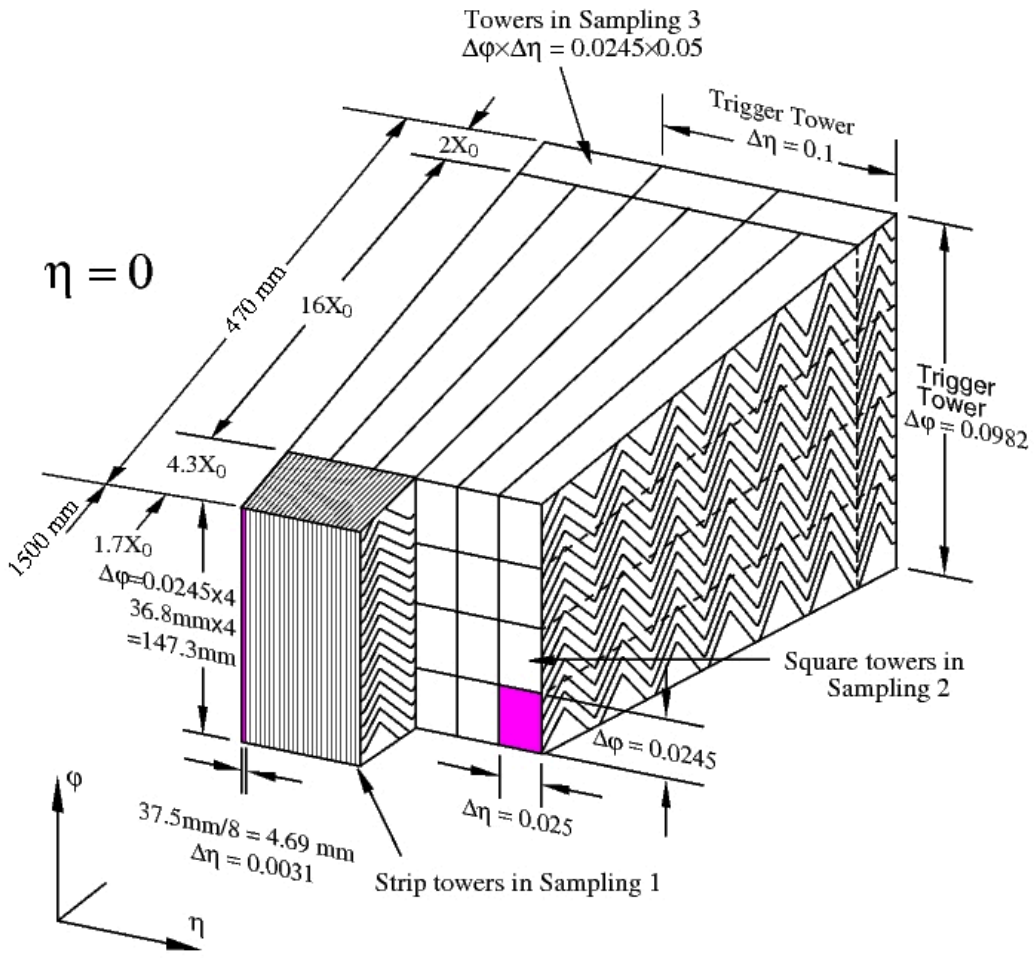

Figure 3.6: Sketch of a barrel module where the different layers are clearly visible with the ganging of electrodes in ϕ. The granularity in η and ϕ of the cells of each of the three layers and of the trigger towers is also shown.

follows:

$$E_{cell} = F_{\mu\mathrm{A}\to\mathrm{MeV}} \times F_{\mathrm{DAC}\to\mu\mathrm{A}} \times \frac{1}{\frac{M_{\mathrm{phys}}}{M_{\mathrm{cali}}}} \times G \times \sum_{j=1}^{\mathrm{N_{samples}}} a_j(s_j - p)\,, \tag{3.1}$$

where s_j are the samples of the shaped ionisation signal digitised in the second electronic gain; p is the read-out electronic pedestal, measured for each gain in dedicated calibration runs; the a_j weights are the optimal filtering coefficients (OFC) derived from the predicted shape of the ionisation pulse and the noise auto-correction, accounting for both the electronic and the pile-up components. The cell gain G is computed by injecting a known calibration signal and reconstructing the corresponding cell response. The factor $\frac{M_{\mathrm{phys}}}{M_{\mathrm{cali}}}$, which quantifies the ratio of the maxima of the physical and calibration pulses corresponding to the same input current, corrects the gain factor G that is obtained with the calibration pulses to adapt it to physics-induced signals; the factor $F_{\mathrm{DAC}\to\mu\mathrm{A}}$ converts digital-to-analog converter (DAC) counts set on the calibration board to a current in μA; the factor $F_{\mu\mathrm{A}\to\mathrm{MeV}}$ converts the ionisation current to the total deposited energy at the EM scale and is determined from test-beam studies.

3.2.3.2 Hadron calorimeter

The energy-absorbing material is steel for the hadron calorimeter, while scintillator tiles are used to sample the deposited energy. The main part of the hadron calorimeter — the tile calorimeter — is placed directly outside the EM calorimeter envelope and is composed of three parts: one central barrel ($|\eta| < 1.0$) and two extended barrels ($0.8 < |\eta| < 1.7$). The hadron calorimeter is extended to larger pseudorapidities ($|\eta| < 4.9$) by the Hadron End-cap Calorimeter (HEC), a copper/liquid-argon detector and the Forward Calorimeter (FCal), a copper-tungsten/liquid-argon detector.

3.2.4 Muon spectrometer

The muon spectrometer (MS) is shown in Figure 3.7. It is the outermost part of the ATLAS detector, being designed to detect muons within $|\eta| < 2.7$. It provides momentum measurements with a relative resolution less than 3% over a wide p_{T} range. The MS is made up of a barrel part ($|\eta| < 1.05$) and two end-cap sections ($1.05 < |\eta| < 2.7$). A system of three large superconducting air-core toroidal magnets, each having eight coils, provides a magnetic field with a bending power

of $\sim 2.5\,\mathrm{Tm}$ in the barrel and up to $6\,\mathrm{Tm}$ in the end-caps.

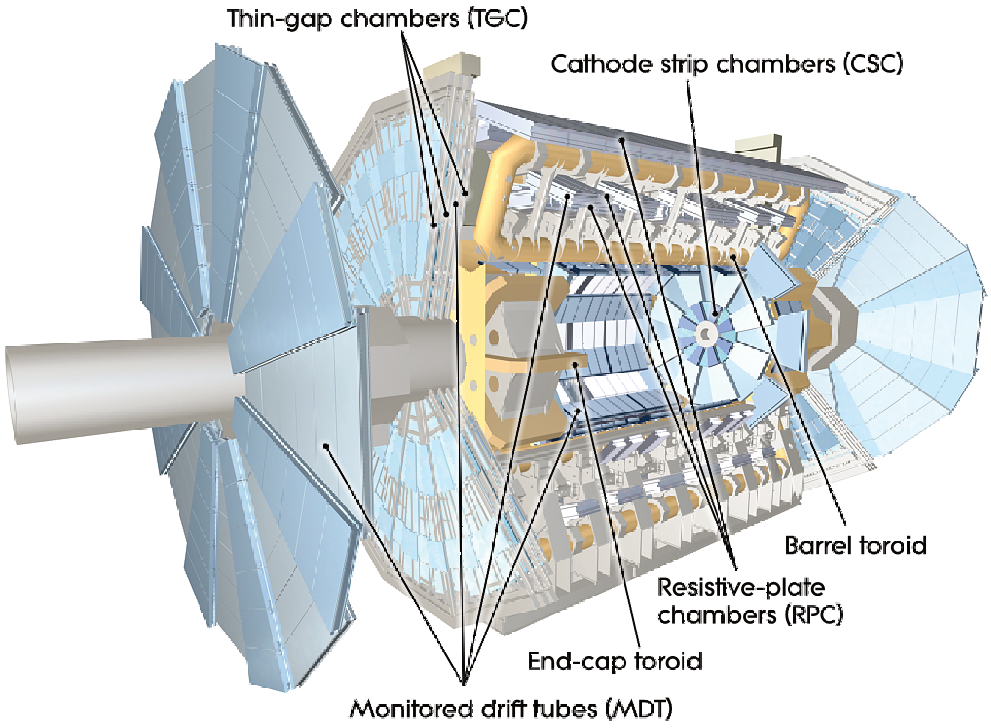

Figure 3.7: Cut-away view of the muon system.

The Resistive Plate Chambers (RPC), which consist of three doublet layers covering $|\eta| < 1.05$, as well as the Thin Gap Chambers (TGC), which have one triplet layer followed by two doublets covering $1.0 < |\eta| < 2.4$, provide triggering capability to the detector and position measurements typically with a spatial resolution of 5–10 mm. The Monitored Drift Tube (MDT), which has three layers and a pseudorapidity coverage up to $|\eta| = 2.7$, provides precise momentum measurements for muons. The Cathode Strip Chambers (CSC) are installed in the innermost tracking layer covering $2 < |\eta| < 2.7$ due to the high rate capability and time resolution.

During the long shutdown in the preparation for the LHC Run 2, the MS has been completed to its initial design by adding the last missing chambers in the transition region between the barrel and the end-caps ($1.0 < |\eta| < 1.4$). The RPC is equipped with four MDT chambers to improve the acceptance. The new MDT chambers use tubes with smaller radius, allowing the detector to cope with higher rates.

3.2.5 Forward detectors

In addition to the main ATLAS detector systems described above, three smaller sets of detectors are built far away from the interaction point, to provide good coverage in the very forward region. This makes it possible to measure elastic scattering at very small angles and provide a good measurement of the absolute luminosity for the ATLAS experiment. Ordered according to the distances of the three detectors from the interaction point: the first system is a Cerenkov detector called LUCID (LUminosity measurement using Cerenkov Integrating Detector), and is the main relative luminosity monitor in ATLAS; the second system is the Zero-Degree Calorimeter (ZDC), located where the LHC beam-pipe is divided into two separate pipes, and mainly used to detect forward neutrons in heavy-ion collisions; the most remote detector is the absolute luminosity detector ALFA (Absolute Luminosity For ATLAS).

3.2.6 Trigger and data acquisition system

The proton-proton interaction rate at the design luminosity of $10^{34}\,\mathrm{cm}^{-2}\mathrm{s}^{-1}$ is approximately 1 GHz, while the event data recording, based on technology and resource limitations, is limited to about 200 Hz. This requires an overall rejection factor of 5×10^6 against minimum-bias processes while maintaining maximum efficiency for the new physics.

The ATLAS trigger system is shown in Figure 3.8. The trigger system has three distinct levels: L1, L2 and the event filter. The Level-1 (L1) trigger system uses a subset of the total detector information to make a decision on whether or not to comtinue processing an event, reducing the data rate to approximately 75 kHz (limited by the bandwidth of the readout system, which is upgradeable to 100 kHz). The subsequent two levels, collectively known as the high-level trigger (HLT), are the Level-2 (L2) trigger and the event filter. They provide the reduction to a final data-taking rate of approximately 200 Hz.

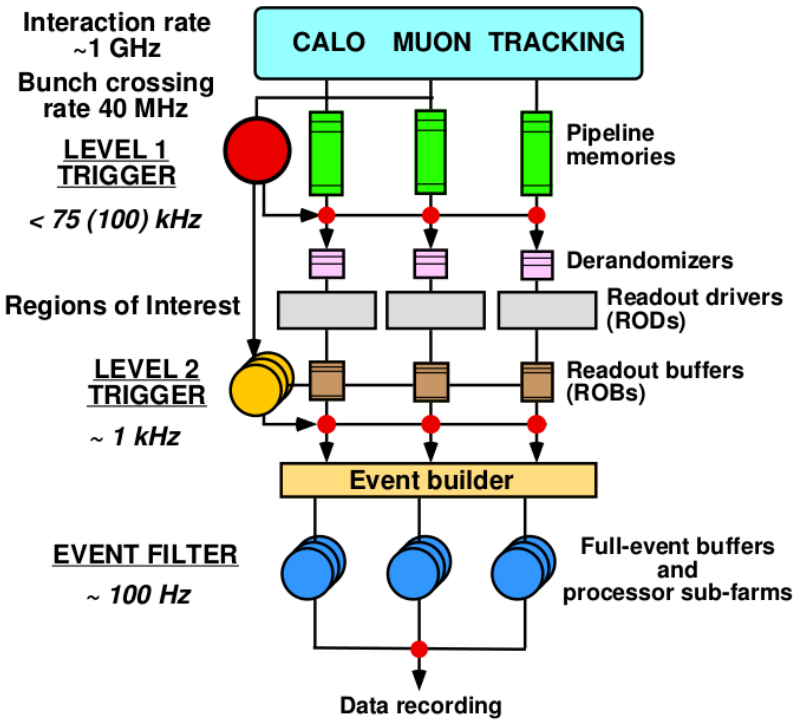

Figure 3.8: Schematic view of the ATLAS trigger system.

Chapter 4

Data and MC samples

The data used in this analysis were collected by the ATLAS detector at the LHC from the pp collisions at the center-of-mass energy $\sqrt{s} = 13\,\text{TeV}$ in 2015 and 2016. The total integrated luminosity of the 2015 and 2016 datasets is $36.1\,\text{fb}^{-1}$. Single-electron and single-muon triggers, as listed in Table 4.1, are used. These triggers have transverse momentum (p_T) thresholds that depend on the data-taking periods for the 2015 and 2016 datasets.

Table 4.1: The minimum p_T requirements used at the different levels of the trigger in different data taking periods. Letters "m","l" and "t" next to the threshold value stand for the medium, loose and tight electron identification requirement, respectively. Letter "i" indicates an isolation requirement, that is less restrictive than the isolation requirement used in the offline selection. The single-lepton trigger with higher-p_T thresholds are more efficient at high lepton p_T than the lower-p_T triggers because of this isolation requirement.

Lepton	Period	Level-1 trigger	High-level trigger
e	2015	20 GeV	24m OR 60m OR 120l GeV
	2016 up to $0.5 \times 10^{34}\,\text{cm}^{-2}s^{-1}$		24m_i OR 60m OR 140l GeV
	2016 up to $1.0 \times 10^{34}\,\text{cm}^{-2}s^{-1}$		24t_i OR 60m OR 140l GeV
	2016 up to $1.2 \times 10^{34}\,\text{cm}^{-2}s^{-1}$		26t_i OR 26m_i OR 60m OR 140l GeV
μ	2015	15 GeV	20i OR 50 GeV
	2016 up to $0.5 \times 10^{34}\,\text{cm}^{-2}s^{-1}$	20 GeV	24i OR 40 OR 50 GeV
	2016 up to $1.0 \times 10^{34}\,\text{cm}^{-2}s^{-1}$		24i OR 50 GeV
	2016 up to $1.2 \times 10^{34}\,\text{cm}^{-2}s^{-1}$		26i OR 50 GeV

For the 2016 datasets, the un-prescaled triggers with the lowest p_T thresholds depend on the maximum instantaneous luminosity: up to $0.5 \times 10^{34}\,\text{cm}^{-2}s^{-1}$, they are `e24_lhmedium_ivarloose (nod0)` and `mu24_ivarloose/iloose` for single electrons and muons, respectively; up to $1.0 \times 10^{34}\,\text{cm}^{-2}s^{-1}$, `e24_lhtight_ivarloose (nod0)` and `mu24_ivarmedium/imedium`; and up to $1.2 \times 10^{34}\,\text{cm}^{-2}s^{-1}$, `e26_lhtight_ivarloose (nod0)`,

e26_lhtight_smooth_ivarloose and mu26_ivarmedium/imedium. Each event is required to pass at least one of the single-lepton triggers. A so-called "trigger matching" cut is also applied just after the trigger application, in order to verify that the two selected leptons have an electron that fired a single-electron trigger, or a muon that fired a single-muon trigger.

The menus postfixed with _ivarloose, _ivarloose, _ivarmedium or _imedium contain online isolation cuts which are usually looser than those used in the offline selection. There is no isolation cut applied for the trigger menus used for 2015 data analysis.

The single-lepton trigger efficiencies were measured using Z boson candidates as a function of lepton p_{T} and η [75]. A tag-and-probe method was used to determine the L1 and HLT lepton efficiencies. The efficiency is calculated as the ratio of the number of probe leptons (e or μ) passing the trigger selection to the number of probe leptons. The trigger efficiencies for electrons are approximately 100% and 90% for L1 and HLT, respectively, in the range of $|\eta| < 2.40$. The L1 muon trigger efficiencies are approximately 70% and 90% in the barrel ($|\eta| < 1.05$) and the end-caps ($1.05 < |\eta| < 2.40$), respectively. The difference is due to the different geometrical acceptance of the barrel and end-cap trigger systems and inefficiencies of the local detectors. The relative efficiency of HLT with regard to L1 is close to 100% in both the barrel and the end-caps. The trigger efficiency for WW events passing the event selection (described in Chapter 6) has also been studied and described in detail in Appendix A. This includes two sets of efficiencies: the trigger efficiency and the trigger and trigger matching efficiency. Both are found to be greater than 99%. Data quality criteria were applied to ensure that events are recorded with stable beam conditions and with all relevant subdetector systems operational.

Samples of simulated signal and background events are used to optimise the event selection and to estimate the signal acceptance and the background yields from various SM processes.

The sample for the NWA heavy Higgs boson signal was generated with Powheg-Box 2.0 [76–78] which calculates separately the ggF [79] and VBF [80] production mechanisms with matrix elements up to next-to-leading order (NLO) in QCD. It uses the CT10 NLO PDF set [35] and is interfaced with Pythia 8.186 [81] for the $H \to WW$ decays, for parton showering and for hadronisation. The AZNLO tune [82] is used for the underlying event description. The NWA Higgs boson was generated with a width of 4 MeV. This same event sample is used to derive the exclusion regions for 2HDM.

The POWHEG-BOX samples only describe the production of a ggF induced Higgs-like resonance in association with one jet at leading-order (LO) precision, while further jets were emulated by the parton shower generator, PYTHIA. A more precise calculation of higher jet multiplicities is provided by using the MADGRAPH5_aMC@NLO generator [83] to simulate $gg \to H$ events in association with up to two jets at NLO precision. Here, the overlap between identical final states generated at the matrix element (ME) and the parton shower (PS) stage is removed using FxFx merging [84]. The fraction of ggF events passing the event selection requirements of the $N_{\text{jet}} = 1$ and ≥ 2 VBF categories (defined in Section 6.2) predicted by the POWHEG-BOX generator is reweighted to match that of the MADGRAPH5_aMC@NLO FxFx samples, with a detailed study described in Appendix B. The corresponding scale factors are calculated for several hypothetical heavy Higgs masses. They are the largest, 1.14 (0.91), for the 200 GeV mass point, and decrease with increasing resonance mass to a value of 0.85 (0.73) for the 4 TeV mass point, for the $N_{\text{jet}} = 1$ ($N_{\text{jet}} \geq 2$) VBF category.

The LWA heavy Higgs boson signal is simulated at NLO using MADGRAPH5_aMC@NLO with the NNPDF23LO PDF set [85]. The generated particles at matrix element level were showered by PYTHIA 8.186 with the A14 setting [86] for the tunable parameters of the underlying event. The mass of the heavy Higgs boson signals considered in this analysis spans the range between 200 GeV and 4 TeV. Both NWA and LWA samples have been generated in steps of 100 GeV up to 1 TeV, and in steps of 200 GeV thereafter.

Samples for the GM, HVT and bulk RS graviton benchmark signal models were generated at LO using MADGRAPH5_aMC@NLO, which is interfaced to PYTHIA 8.186 with the NNPDF23LO PDF set. For the GM benchmark model, a value of $\sin\theta_H = 0.4$ was chosen. Samples for the HVT interpretation in the qqA production mode were generated according to the extended gauge symmetry model A [69] with $g_V = 1$, while for the VBF production mode, samples were generated using the same g_V value but the couplings to the fermions are set to zero, such that the new vector boson couples only to the SM vector and Higgs bosons. For the RS graviton signal model, a curvature scale parameter $k/\bar{M}_{\text{Pl}}$ being either 0.5 or 1 is considered. The branching ratio for the decays $G_{\text{KK}} \to WW$ is larger than 30%. The VBF spin-2 signals were produced at LO with VBFNLO v3.0.0 beta 2 [87] with the NNPDF30LO PDF set [37] and the following parameter setting [70] was used: $\Lambda_{ff} = 3$ TeV, $n_{ff} = 4$, $\Lambda = 1.5$ TeV and $f_1 = f_2 = f_5 = 1$. The mass range considered in the analysis is between 200 GeV and 5 TeV for the KK graviton signal, and between 250 GeV and 5 TeV for the HVT qqA signal. For the GM and

ELM VBF signals, the mass range is between 200 GeV and 1 TeV, while for the HVT VBF signal, the range is between 300 GeV and 1 TeV.

Events from the production of single-top quark, $t\bar{t}$, dibosons (WW, WZ and ZZ), Z/γ^*+jets and W+jets are the main sources of SM backgrounds. Samples for single-top quark were generated with POWHEG-BOX 2.0 [88, 89] using the CT10 NLO PDF set, which is interfaced to PYTHIA 6.428 [90] for the parton showering, and PERUGIA2012 [91] tune and CTEQ6L1 PDF [92] were used for the underlying event description. The simulated $t\bar{t}$ events were generated with POWHEG-BOX 2.0 [93] using the NNPDF30NLO PDF set [37], that is interfaced to PYTHIA 8.186 for the parton showering, with the A14 tune and CTEQ6L1 PDF used for the description of the underlying events. The resummation damping parameter, h_{damp}, was set to be one and a half times of the top-quark mass, m_{top}, which was set at 172.5 GeV. The h_{damp} parameter is used to control the ME/PS matching and effectively regulate the high-p_{T} radiation. The properties of the bottom and charm hadron decays were modelled by the EVTGEN 1.2.0 [94] package. For the diboson backgrounds, simulated events were generated using SHERPA 2.1.1 [95–99], for the gg production processes, and SHERPA 2.2.1, for the $q\bar{q}$ production processes. CT10 NLO and NNPDF30NNLO PDF sets were used for the two different processes, respectively. The SHERPA generator for the $q\bar{q}$ production processes produced up to one additional parton at NLO and up to three additional partons at LO. The W and Z bosons in association with jets were also generated with SHERPA 2.1.1, with the CT10 NLO PDF set, where b- and c-quarks are treated to be massive particles. In the $gg \to WW$ production, the contribution of the SM Higgs boson at 125 GeV and the interference effects between the two were also included. The VBF part of the SM Higgs boson was generated with POWHEG-BOX [80], that is interfaced to PYTHIA 8.186 for the parton showering.

The impact of multiple pp interactions occured in the same and neighbouring bunch crossings (pile-up) is also included by overlaying minimum-bias collisions, that are generated with PYTHIA 8.186, and considered for each generated signal and background event. The number of overlaid collisions is configured such that the distribution of the average number of interactions per pp bunch crossing, $\langle\mu\rangle$, in the simulation is matched to the pile-up conditions observed in the data, which is approximately 25 interactions per bunch crossing on average. Figure 4.1 shows the mean number of interactions per crossing for the 2015 and 2016 pp collision data at 13 TeV centre-of-mass energy. The generated samples were processed through a GEANT4-based detector simulation [100, 101], followed by the standard ATLAS

reconstruction software used for collision data.

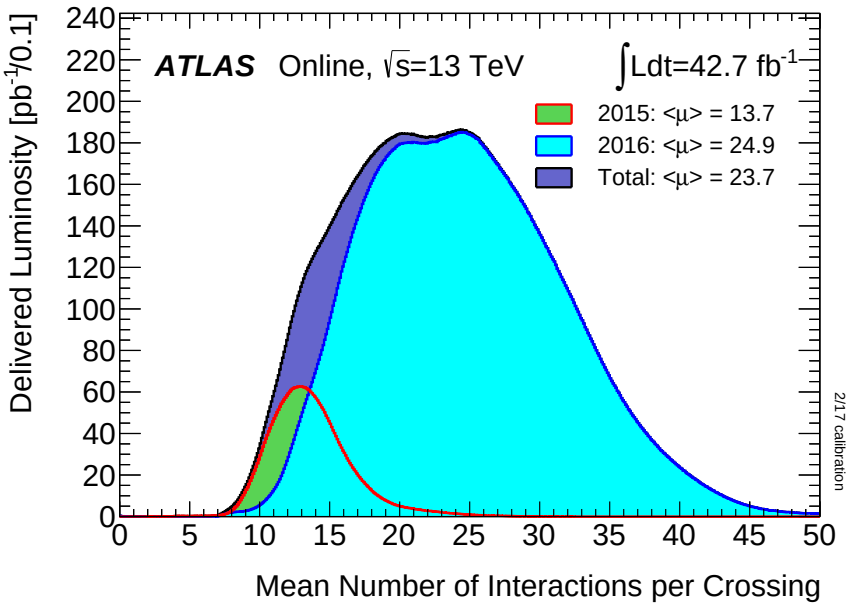

Figure 4.1: Mean number of interactions per crossing for the 2015 and 2016 pp collision data at 13 TeV. All data delivered to ATLAS during stable beams is shown. The integrated luminosity and $\langle\mu\rangle$ are given in the figure.

Chapter 5

Event reconstruction

The reconstruction of particles and physics quantities is very important for the analysis and is described in this chapter. The following sections will give more details about the reconstruction of tracks and vertices, electrons and photons, muons and jets in the ATLAS detector, the definition of missing transverse energy and the isolation requirements that are used in the analysis.

5.1 Tracks and vertices

Charged particle tracks ($p_{\mathrm{T}} > 0.5\,\mathrm{GeV}$ and $|\eta| < 2.5$) are reconstructed and measured in the inner detector with the help of the solenoid field. The efficiency of the reconstruction at low p_{T} is, however, limited because of the large amount of material in the inner detector. The track reconstruction software follows a modular and flexible software design, that includes features covering the requirements of both the inner detector and muon spectrometer reconstruction. These features comprise a common event data model and detector description, which allow for standardised interfaces to all reconstruction tools, such as track extrapolation, track fitting including material corrections, and vertex fitting. The extrapolation package combines propagation tools with an accurate and optimised description of the active and passive material of the full detector to allow for material corrections in the reconstruction process.

Track reconstruction in the inner detector is logically divided into three stages [72]:

1. The first stage is the pre-processing. In this stage, the raw data from the pixel and SCT detectors are converted into clusters while the TRT raw timing information is turned into calibrated drift circles. The SCT clusters are

transformed into space-points, using a combination of the cluster information from opposite sides of a SCT module.

2. The second stage is the track-finding, in which different tracking strategies are optimised to cover different applications and implemented. The default tracking exploits the high granularity of the pixel and SCT detectors to find out prompt tracks that originate from the vicinity of the interaction region. A complementary track-finding strategy, called back-tracking, is used to search for unused track segments in the TRT. Such segments are extended into the SCT and pixel detectors, and therefore to improve the tracking efficiency for secondary tracks from conversions or decays of long-lived particles.

3. The final one is the post-processing stage, in which a dedicated vertex finder is used to reconstruct primary vertices. This is followed by algorithms dedicated to the reconstruction of photon conversions and secondary vertices.

In this analysis, events are reconstructed by requiring that there are at least one primary vertex with a minimum of two associated tracks, with each of the tracks satisfying $p_{\mathrm{T}} > 400\,\mathrm{MeV}$. In case that there is more than one vertex that are reconstructed in an event and also meet these conditions, the one with the highest sum of track p_{T}^2 is chosen as the primary vertex and is subsequently used for the calculation of properties of the physics objects in this analysis.

Besides, to ensure that leptons originate from the interaction point, a requirement of $|d_0|/\sigma_{d_0} < 5\,(3)$ is imposed on the electrons (muons) and $|z_0 \sin\theta| < 0.5\,\mathrm{mm}$ is applied on both lepton types. Here, σ_{d_0} is the uncertainty on the measured value of d_0.

5.2 Electrons and photons

The reconstruction of electrons and photons [74] in the pseudorapidity region $|\eta| < 2.47$ is started from clusters with deposited energy in the EM calorimeters. First the calorimeters are divided into a grid of towers ($N_\eta \times N_\phi$) with a constant size of $\Delta\eta \times \Delta\phi = 0.025 \times 0.025$. The energy deposition in the towers is calculated by an integration over all the cells in all longitudinal layers. A sliding-window algorithm [102] with a window size of 3×5 towers is then applied to search for clusters that have a total transverse energy above 25 GeV. Such a cluster will be chosen as a seed, and the reconstruction is continued around this seed. The

energy of these clusters is calibrated to the original energy using multivariate techniques [74] based on simulated MC samples. A match is performed from the seed clusters to the tracks that are well-reconstructed and originate from the primary vertex in the inner detector. Matched clusters are considered as electron candidates or converted photons if the track is consistent with originating from a photon conversion. Clusters without matching any tracks are considered as unconverted photons. The clusters are then rebuilt using a set of calorimeter cells[5]. This choice gives an optimised balance between the conflicting requirements of collecting all the energies even in the case of hard bremsstrahlung and of preserving the energy resolution by minimizing the contributions from the noise and pile-up. Electrons and photons reconstructed near regions of the calorimeter affected by read-out or HV failures are rejected.

The relative energy resolution can be parameterised as follows:

$$\frac{\sigma}{E} = \frac{a}{\sqrt{E}} \oplus \frac{b}{E} \oplus c\,, \tag{5.1}$$

where a, b and c are η-dependent parameters: a is the sampling term, which contributes mostly at low energy; b is the noise term, which is dominated by the pile-up noise at high η; c is the constant term. At high energy, the resolution tends asymptotically to the constant term, c, which has a design value of 0.7%.

However, what we are interested in in our analysis are prompt electrons decayed from the W boson, instead of other background objects that can also be built as electron candidates by reconstruction algorithms, including hadronic jets and electrons from photon conversions, Dalitz decays and semi-leptonic heavy-flavour hadron decays. Therefore, the identification algorithms are also necessary in the reconstruction of electrons. This is usually done in two different ways. One is called the cut-based method and the other is the likelihood (LH) method [103]. Both make use of variables that can describe the longitudinal and lateral shapes of the EM showers in the calorimeters, the properties of the tracks in the ID and the matching between tracks and energy clusters. Electrons used in this analysis are identified using the LH identification method. In the LH identification, multivariate analysis (MVA) techniques [104] are used and the final discriminant

[5]For electrons, this correspondes to 3×7 cells in the EMB and 5×5 cells in the EMEC in the second layer.

variable can be expressed as:

$$d_{\mathcal{L}} = \frac{\mathcal{L}_{\mathrm{S}}}{\mathcal{L}_{\mathrm{S}} + \mathcal{L}_{\mathrm{B}}},\ \mathcal{L}_{\mathrm{S(B)}}(\vec{x}) = \prod_{i=1}^{n} P_{\mathrm{S(B)},i}(x_i) \tag{5.2}$$

where $\vec{x}$ is the vector of variable values, while $P_{\mathrm{S},i}(x_i)$ and $P_{\mathrm{B},i}(x_i)$ are the values of the probability density functions of the i-th variable evaluated from data at x_i for the prompt electrons and other background objects, respectively.

Three sets of requirement on the discriminant variable have been developed so far in order to reject light-flavour jets and conversions:

LooseLH selection: features the most powerful variables for discrimination against ligh-flavour jets. In addition, a requirement on the number of hits on the track in the B-layer is applied to better reject photon conversions.

MediumLH selection: uses tighter requirements on the discriminant variable than the "LooseLH" selection. Besides, the transverse impact parameter d_0 and its significance σ_{d_0} defined as the ratio of the magnitude of d_0 to its uncertainty are also used to construct the MVA discriminant variable.

TightLH selection: has the tightest requirements and the smallest selection efficiency. In addition to the variables used for the "MediumLH" selection, electron candidates that are matched to reconstructed photon conversions are vetoed.

The "LooseLH", "MediumLH" and "TightLH" regimes are defined such that the samples selected by them are subsets of one another, i.e. electrons selected by "MediumLH" are all selected by "LooseLH", and "TightLH" electrons are all selected by "MediumLH".

The electron identification performance may be affected by the parasitic collisions in the same beam crossing (called in-time pile-up) or a consecutive bunch crossing (called out-of-time pile-up) as the hard *pp* collision producing the electron candidates [105]. Some shower shape distributions depend on the number of pile-up collisions per bunch crossing, therefore, the requirements on the discriminant variable are loosened as a function of the number of primary vertices, which makes the LH identification still efficient at high pile-up without background increased dramatically.

In addition to the reconstruction and identification criteria described above, electrons are usually required to fulfil isolation requirements [105] to further disen-

tangle prompt electrons from the background objects. Two discriminant variables are designed for this purpose:

- calorimeter isolation variable, $E_{\mathrm{T}}^{\mathrm{cone0.2}}$, defined as the sum of transverse energies of the EM topological clusters within a cone of $\Delta R = 0.2$ around the candidate electron cluster.

- track isolation variable, $p_{\mathrm{T}}^{\mathrm{varcone0.2}}$, defined as the sum of transverse momenta of all tracks that satisfies quality requirements [105] within a cone of $\Delta R = \min(0.2, 10\,\mathrm{GeV}/E_{\mathrm{T}})$ around the candidate electron track.

Depending on the requirements on the two variables mentioned above, two different kinds of working points are developed: fixed requirement working points where the upper thresholds on the isolation variables are constant, and efficiency targeted working points where requirements are varied to obtain a given isolation efficiency, which is estimated typically from simulated $Z \to ee$ events. Table 5.1 shows the definition of the various efficiency targeted working points for electron isolation.

Table 5.1: Efficiency targeted isolation working points for electrons. For the Gradient and GradientLoose working points, E_{T} is in GeV. The calorimeter and track isolations refer to the selection based on $E_{\mathrm{T}}^{\mathrm{cone0.2}}/E_{\mathrm{T}}$ and $p_{\mathrm{T}}^{\mathrm{varcone0.2}}/E_{\mathrm{T}}$, respectively.

	Efficiency		
Working points	calorimeter isolation	track isolation	total efficiency
LooseTrackOnly	-	99%	99%
Loose	99%	99%	$\sim 98\%$
Tight	96%	99%	$\sim 95\%$
Gradient	$0.1143\% \times E_{\mathrm{T}} + 92.14\%$	$0.1143\% \times E_{\mathrm{T}} + 92.14\%$	90/99% at 25/60 GeV
GradientLoose	$0.057\% \times E_{\mathrm{T}} + 95.57\%$	$0.057\% \times E_{\mathrm{T}} + 95.57\%$	95/99% at 25/60 GeV

In this analysis, for the electron identification, "MediumLH" and "TightLH" selections are used for the leading two leptons ($p_{\mathrm{T}} > 25\,\mathrm{GeV}$) and vetoing additional leptons ($15\,\mathrm{GeV} < p_{\mathrm{T}} < 25\,\mathrm{GeV}$), respectively, corresponding to efficiencies of $\sim 84\%$ and $\sim 74\%$ at $p_{\mathrm{T}} = 25\,\mathrm{GeV}$. The corresponding probabilities of misidentification of electrons from hadrons are $\sim 0.5\%$ and $\sim 0.3\%$, respectively. While for the electron isolation, the "Gradient" and "GradientLoose" working points are used for the leading two leptons and vetoing additional leptons, respectively, corresponding to efficiencies of 90% and 95% at $p_{\mathrm{T}} = 25\,\mathrm{GeV}$ (99% at $p_{\mathrm{T}} = 60\,\mathrm{GeV}$ for both).

5.3 Muons

Muon reconstruction is usually first performed in the ID and MS independently. Then, the information from each of them is combined to reconstruct tracks that are finally used in physics analyses. The reconstruction of muons in the ID is same as any other charged particles, as described in Section 5.1.

There are four types of muons depending on the subdetectors used in the reconstruction [106]:

Combined (CB) muon: the combined track is formed with a global fit using the hits from the ID and the MS. During the fit, MS hits can be added or removed from the track to improve the fit quality. Most muons are reconstructed following an outside-in pattern recognition, where muons are first reconstructed in the MS and then extrapolated inward to be matched to an ID track. As a complementary approach, an inside-out reconstruction is used, in which ID tracks are extrapolated outwards and matched to MS tracks.

Segment-tagged (ST) muons: if a track in the ID can be extrapolated to the MS and is associated with at least one local track segment in the MDT or CSC chambers, it will be classified as a muon. Such kind of muons is usually used when muons cross only one layer of MS chambers (either because of their low p_{T} or because they fall in regions with reduced MS acceptance).

Calorimeter-tagged (CT) muons: if a track in the ID can be matched to an energy deposit in the calorimeters compatible with a minimum-ionizing particle, it will also be identified as a muon. "CT muons" have the lowest purity of all the types of muons, but they recover acceptance in the region where the MS is only partially instrumented (to allow for cabling and services for the ID and calorimeters).

Extrapolated (ME) muons: the muon trajectory is reconstructed based only on the MS track and a loose requirement on compatibility with originating from the interaction point. Energy loss of the muons in the calorimeters is also estimated and taken into account. Generally, muons are required to traverse at least two layers of the MS chambers (three layers in the forward region) to provide a track measurement. This type of muons is mainly used to extend the acceptance in the region $2.5 < |\eta| < 2.7$, which can not be covered by the ID.

Overlaps between different muon types are also considered and resolved for physics analyses. When two different types share the same ID track, the priority is in order of: "CB muons", "ST muons" and "CT muons". The overlap with "ME muons" is resolved by analysing the hits of the track and selecting the track with better fit quality and larger number of hits.

Muon momentum calibration is also performed to identify the corrections to the simulated muon transverse momentum reconstructed in the ID and MS subdetectors, in order to precisely describe the measurement of the same quantities in data. Only "CB muons" are used to extract the calibration parameters. The ID (MS) track reconstruction uses hits from the corresponding detector and is extrapolated to the interaction point. Corrections are also applied to the momentum resolution according to the following formula:

$$\frac{\sigma(p_{\mathrm{T}})}{p_{\mathrm{T}}} = r_0/p_{\mathrm{T}} \oplus r_1 \oplus r_2 p_{\mathrm{T}} \,, \tag{5.3}$$

where, $\oplus$ denotes a sum in quadrature, and the first term accounts mainly for fluctuations of the energy loss in the transverse material, the second term for multiple scattering, local magnetic field inhomogeneities and local radial displacements of the hits, and the third term describes intrinsic resolution effects that are caused by spatial resolution of the hit measurements and residual misalignment of the muon spectrometer.

Muon identification is generally performed by applying quality requirements that suppress backgrounds, mainly from pion and kaon decays. This should be aimed at selecting prompt muons with high efficiency (usually simulated $t\bar{t}$ events are used with muons from W decays categorised as signal muons and muon candidates from light-hadron decays categorised as background muons) with a robust momentum measurement. Variables providing good discrimination between prompt muons and background muons are used. To ensure a robust momentum measuremtn, specific requirements on the number of hits in the ID and MS are used.

Four muon identification four selections [106] have been developed for physics analyses in ATLAS:

Loose muons: developed to maximise the reconstruction efficiency but also providing good-quality muon tracks. They are specifically optimised for Higgs boson reconstruction with a four-lepton final state. All types of muon reconstruction are used.

Medium muons: designed to be used as a default selection for muons in ATLAS, while minimising the systematic uncertainties that are associated with the reconstruction and calibration of muons. Only "CB muons" and "ME muons" are used. Besides, a loose selection on the compatibility between the momentum measurement in the ID and that in the MS is applied to suppress the misidentification of hadrons as muons.

Tight muons: selected to maximise the purity of muons at the cost of losing some efficiency. Only "CB muons" with hits in at least two stations of the MS but satisfying the "Medium" selection criteria are considered.

High-p_{T} muons: aimed to maximise the momentum resolution for tracks with $p_{\mathrm{T}} > 100\,\mathrm{GeV}$. And this type is mainly developed and optimised for searches for high-mass Z' and W' resonances. "CB muons" passing the "Medium" selection are selected but additionally they are required to have at least three hits in three stations of the MS.

As with the electron identification, these selections are inclusive categories such that muons identified with tighter selections are also included in the looser categories. The misidentification is usually estimated using MC simulation and validated using data by measuring the probability that pions are reconstructed as muons.

In this analysis, "CB muons" are used and the muon candidates are required to have $|\eta| < 2.5$ and pass the "Medium" (when $p_{\mathrm{T}} > 25\,\mathrm{GeV}$) or the "Tight" (when $p_{\mathrm{T}} < 25\,\mathrm{GeV}$) selection. These selections have a reconstruction efficiency of approximately 96% and 92%, respectively, for muons originating from the decay of W bosons [106]. The corresponding probabilities to identify hadrons as muons are approximately 0.2% and 0.1%, respectively.

Although the "High-p_{T} muons" regime is not directly used in this analysis, it is thought to be mostly included by the "Medium" working point. Anyway, study was performed to check this, as described in Appendix C, and there is no indication that this would have a significant impact on the results, taking also the limited statistics of data into account. The isolation and isolation efficiency for muons are the same as that for electrons, except that the variable cone size starting at $\Delta R = 0.3$ for the track isolation.

5.4 Jets

Jets are reconstructed from the three-dimensional clusters of energy deposits in the calorimeters. The anti-k_t algorithm [107], with a radius parameter of $R = 0.4$, is used. The four-momenta are calculated as the sum of that of their constituents, that are assumed to be massless. Jets are corrected for energy from pile-up by using the pile-up subtraction method based on jet areas [108]. The estimation for jet energy scale is described in Ref. [109]. Jets are required to satisfy the two requirements: $p_{\mathrm{T}} > 30\,\mathrm{GeV}$ and $|\eta| < 4.5$.

The multivariate "jet vertex tagger" algorithm [110] is used to suppress jets from pile-up events, for jets with $p_{\mathrm{T}} < 60\,\mathrm{GeV}$ and $|\eta| < 2.5$. To avoid double counting, jets of any transverse momentum are discarded if they are within a cone of size $\Delta R < 0.2$ of an electron candidate or if they have fewer than three associated tracks and are within a cone of size $\Delta R < 0.2$ of a muon candidate. If a lepton and a jet overlap in a cone within $\Delta R < 0.4$, but with $\Delta R > 0.2$, the lepton is rejected.

The identification of b-quark jets is based on distinct strategy encoded in three basic b-tagging algorithms: impact parameter-based algorithm, an inclusive secondary vertex reconstruction algorithm and a decay chain multi-vertex reconstruction algorithm. The output of the three algorithms is finally combined in a multivariate discriminant (MV2), providing the best separation between different jet flavours. Jets with $p_{\mathrm{T}} > 20\,\mathrm{GeV}$ and within $|\eta| < 2.5$ are considered to contain a b-hadron if they yield a b-tagging algorithm discriminant value exceeding a reference value. The MV2c10 [111, 112] is chosen at the 85% b-tagging efficiency benchmark point, estimated from b-jets in simulated $t\bar{t}$ events. MV2c10 is a variant of MV2, where the names of the taggers indicate the c-jet fraction in the training, i.e. the background sample if composed of 10% (90%) c- (light-flavour) jets. The misidentification rate for jets that is originated from a light quark or gluon is less than 1%, while the rate for c-jets is approximately 17%.

The reconstruction of the jet kinematics is also affected by pile-up interactions. To mitigate these effects, the contribution from pile-up is estimated on an event-by-event and jet-by-jet basis as the product of the pile-up p_{T}-density ρ and the jet area A^{jet} which is determined with the FastJet program [113]. The jet energy scale (JES) calibration [109] is derived first as a correction of the reconstructed jet energy to the truth jet energy. Reconstructed jets are geometrically matched to truth jets within $\Delta R = 0.3$. Only isolated jets are used, to avoid any ambiguities in the matching of calorimeter jets to truth jets. An isolated calorimeter jet is

required to have no other calorimeter jet of $p_{\mathrm{T}} > 7\,\mathrm{TeV}$ within $\Delta R = 0.6$, and only one truth jet of $p_{\mathrm{T}} > 7\,\mathrm{TeV}$ within $\Delta R = 1.0$.

5.5 Missing transverse energy

The missing transverse momentum, with a magnitude $E_{\mathrm{T}}^{\mathrm{miss}}$, is calculated as the negative vectorial sum of the transverse momenta of calibrated objects, such as electrons, muons, jets, and tracks with $p_{\mathrm{T}} > 500\,\mathrm{MeV}$ that are compatible with the primary vertex and not associated to any of the other objects [114].

A very good measurement of the missing transverse momentum, $E_{\mathrm{T}}^{\mathrm{miss}}$, is a critical requirement for the study of many physics channels with neutrinos in the final state in ATLAS, in particular in the searches for new physics. In this analysis, it is mainly used to reconstruct the transverse mass observable.

The $E_{\mathrm{T}}^{\mathrm{miss}}$ is reconstructed by measuring the missing transverse momentum in an event using selected calibrated hard objects. The $E_{x(y)}^{\mathrm{miss}}$ components that are projections of $E_{\mathrm{T}}^{\mathrm{miss}}$ onto the x and y directions, are calculated as:

$$E_{x(y)}^{\mathrm{miss}} = E_{x(y)}^{\mathrm{miss},e} + E_{x(y)}^{\mathrm{miss},\gamma} + E_{x(y)}^{\mathrm{miss},\tau} + E_{x(y)}^{\mathrm{miss,jets}} + E_{x(y)}^{\mathrm{miss},\mu} + E_{x(y)}^{\mathrm{miss,soft}}\,, \tag{5.4}$$

where each object term is defined to be the negative vectorial sum of the momenta of the respective calibrated objects described in Ref. [114]. Calorimeter signals are associated with the reconstructed objects in the following order: electrons (e), photons (γ), hadronically decaying τ-leptons, jets and muons (μ). The soft term is reconstructed using objects that are not associated with any object mentioned above. It can be a track-based soft term (TST) or a calorimeter-based soft term (CST).

The azimuthal angle ϕ^{miss} and the magnitude of $E_{\mathrm{T}}^{\mathrm{miss}}$ are calculated as:

$$\begin{aligned} \phi^{\mathrm{miss}} &= \arctan(E_y^{\mathrm{miss}}/E_x^{\mathrm{miss}})\,, \\ E_{\mathrm{T}}^{\mathrm{miss}} &= \sqrt{(E_x^{\mathrm{miss}})^2 + (E_y^{\mathrm{miss}})^2}\,. \end{aligned} \tag{5.5}$$

Chapter 6

Event selections

6.1 Optimisation Strategy

A simple strategy was developed to optimise event selections to improve the sensitivity for signals for this analysis. However, the strategy is general and can be easily applied to all other analyses both for new physics searches and precision measurements. In this section, the strategy will be discussed in detail, followed by two examples showing how it can be applied successfully to analysis.

6.1.1 Introduction

Optimisation of event selection is an important step in all data analyses aiming for precision measurements or searching for new physics. One uses often different strategies in performing the optimisation. Two main categories are cut-based selections and MVA. Both have their own advantages but one usually lacks a means to tell if one uses more variables than one needs or if the cuts are really optimal or not. More variables one uses, larger systematic uncertainties one may introduce.

In this section, a combined strategy of MVA-based variable selections and cut-based scans is proposed. It has two main steps:

1. In the first step, a few discriminant variables from both a signal sample and a background sample containing all background processes are selected as inputs to a multivariate algorithm. Two output informations are used: the ranking of the variables and correlation matrices of the signal and background samples. Variables having high ranking values are selected. In the examples that are shown in this section, variables having a relative ranking

value below 40% of the highest one are removed. Among the selected high ranking variables, the correlation is then checked. If two variables are highly correlated (e.g. greater than 80%) for both the signal and the background, the lower ranking variable is further removed. The remaining selected variables are kept for the next step.

2. In the second step, a signal significance is defined. Depending on the analysis, e.g. for an event counting experiment, one could define a global significance based on [115]

$$s = \sqrt{2\left[(n_{\mathrm{S}} + n_{\mathrm{B}})\ln\left(1 + \frac{n_{\mathrm{S}}}{n_{\mathrm{B}}}\right) - n_{\mathrm{S}}\right]} \tag{6.1}$$

where n_{S} and n_{B} are the number of signal and background events, respectively. If the background sample is large or if the signal is widely distributed, one could extend the significance definition more differentially over a distribution which has different shapes between the signal and the background as

$$s_{\text{1-d}} = \sqrt{\sum_i s_i^2} \tag{6.2}$$

where subscript 1-d refers to the one-dimensional distribution and s_i stands for the significance value of the i-th bin calculated with the same formula (6.1). Extension in n dimensions with n different distributions is simply:

$$s_{\text{n-d}} = \sqrt{\sum_{j=1}^{n}\sum_i \left(s_i^j\right)^2}. \tag{6.3}$$

Then a significance scan with different cuts for each of the selected variables is performed. The cut value corresponding to the maximum significance is chosen as an initial cut value of the variable. If the significance has a flat plateau, the cut value which gives a larger signal efficiency (or a smaller background efficiency) is favourably selected. These initial cut values are then checked in a new scan by applying all the other cut values except for the one on the variable under consideration. If the new cut values are different from those of the initial scans, the iteration continues. However given the fact that the highly correlated variables are removed in the first step, only one iteration is usually sufficient to define the optimal cuts. For a given variable, if the significance maximum corresponds to the location

where no cut is applied, then this variable is further removed from the list.

In Sections 6.1.2 and 6.1.3, two example applications are shown, followed by a summary in Section 6.1.4.

6.1.2 Application to heavy Higgs boson search in the $H \to WW \to \ell\nu\ell\nu$ channel

Following [15], the following nine variables are used as inputs to an MVA training: $p_{\mathrm{T}}^{\mathrm{lead}}$, $p_{\mathrm{T}}^{\mathrm{sublead}}$, $p_{\mathrm{T}}^{\ell\ell}$, $m_{\ell\ell}$, $\Delta\eta_{\ell\ell}$, $p_{\mathrm{T}}^{\mathrm{miss}}$, $p_{\mathrm{T,rel}}^{\mathrm{miss}}$, $E_{\mathrm{T}}^{\mathrm{miss}}$, and $E_{\mathrm{T,rel}}^{\mathrm{miss}}$ corresponding to the transverse momenta of the leading and subleading leptons and of the dilepton system, its invariant mass, the pseudorapidity difference between the two leptons, as well as various track or calorimeter based missing transverse momenta or energies. The same MC samples as the Run-1 publication [15] are used. We take the $e\nu\mu\nu$ channel and the zero-jet category as an example.

The ranking of the variables based on a Boosted Decision Tree (BDT) training is shown in Figure 6.1 as a function of heavy Higgs boson mass. Some variation from one mass point to another is observed due to small difference between some of the variables. To avoid such a variation, an average is performed over all the mass points and the resulting absolute and relative ranking values are shown in Table 6.1. Among the nine variables, three of them in the last three columns have a relative ranking value below 40% and are therefore removed.

Table 6.1: Absolute and relative ranking order averaged over heavy Higgs boson mass points between 600 and 1 000 GeV in the $H \to WW \to \ell\nu\ell\nu$ channel.

Variable	$m_{\ell\ell}$	$\Delta\eta_{\ell\ell}$	$p_{\mathrm{T}}^{\mathrm{lead}}$	$p_{\mathrm{T}}^{\mathrm{sublead}}$	$p_{\mathrm{T,rel}}^{\mathrm{miss}}$	$p_{\mathrm{T}}^{\mathrm{miss}}$	$E_{\mathrm{T}}^{\mathrm{miss}}$	$p_{\mathrm{T}}^{\ell\ell}$	$E_{\mathrm{T,rel}}^{\mathrm{miss}}$
Absolute	0.225	0.118	0.110	0.107	0.107	0.096	0.084	0.079	0.074
Relative (%)	100	53	49	48	47	43	37	35	33

Checking now the correlation between the variables shown in Figure 6.2 which have also been averaged over the mass points, among the six remaining variables, variable $p_{\mathrm{T}}^{\mathrm{sublead}}$ has a correlation coefficient of 83% for the signal and 80% for the background with $m_{\ell\ell}$ which meets the 80% rejection requirement, the lower ranking variable $p_{\mathrm{T}}^{\mathrm{sublead}}$ is thus removed. The other correlated variables have already been removed with the lower ranking requirement (40%). This concludes the first step of the strategy with five selected variables: $m_{\ell\ell}$, $\Delta\eta_{\ell\ell}$, $p_{\mathrm{T}}^{\mathrm{lead}}$, $p_{\mathrm{T,rel}}^{\mathrm{miss}}$ and $p_{\mathrm{T}}^{\mathrm{miss}}$.

A significance scan is then performed. The results for a heavy Higgs boson at 600 GeV are shown in Figure 6.3, where the four curves in each panel correspond

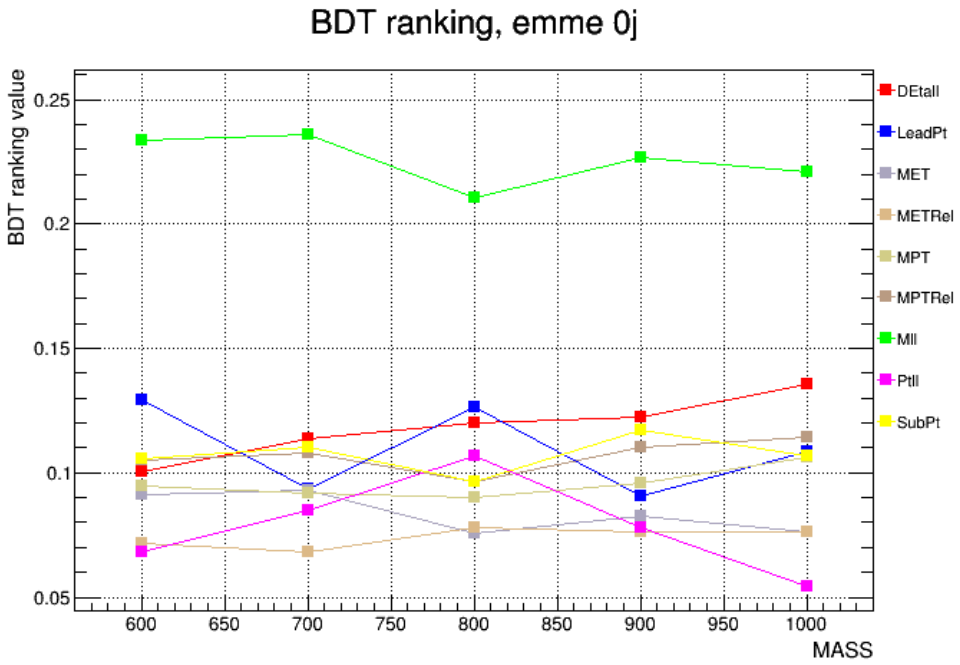

Figure 6.1: Ranking of selected discriminant variables as function of heavy Higgs boson mass in the $H \to WW \to \ell\nu\ell\nu$ search channel.

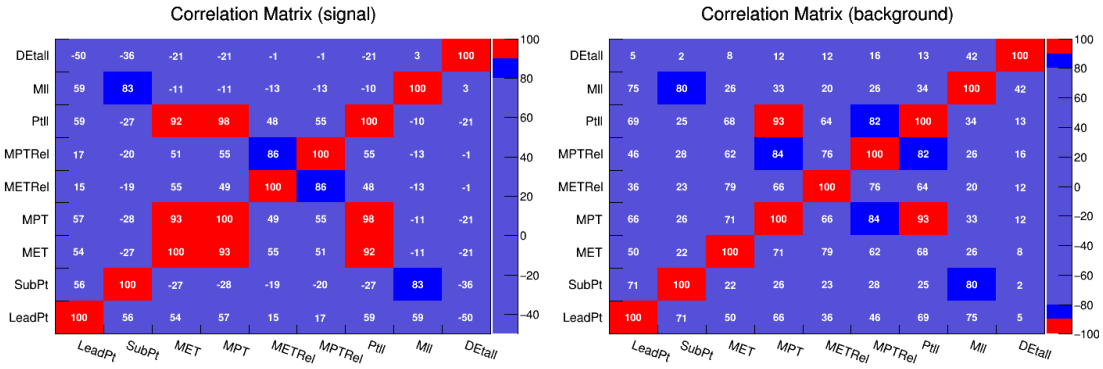

Figure 6.2: Correlation matrices between variables for signal (left) and background (right). For the signal, averaged over the mass values between 600 GeV and 1 000 GeV.

to the signal efficiency (blue), the background efficiency (black), the global significance s (magenta) and the m_{T}-based 1-d significance $s_{\text{1-d}}[m_{\mathrm{T}}]$ (red). For an easy display, the significance curves have been scaled with a scale factor indicated on the panel. It is interesting to note that the 1-d curve $s_{\text{1-d}}[m_{\mathrm{T}}]$ is significantly higher than the global one s. The gain using more differential bins is expected. Based on $s_{\text{1-d}}[m_{\mathrm{T}}]$, the following cuts are chosen as an initial set of the cuts: $m_{\ell\ell} > 100\,\mathrm{GeV}$[6], $\Delta\eta_{\ell\ell} < 1.8$, $p_{\mathrm{T}}^{\mathrm{lead}} > 120\,\mathrm{GeV}$ and $p_{\mathrm{T}}^{\mathrm{miss}} > 40\,\mathrm{GeV}$. These cuts correspond to $s_{\text{1-d}}[m_{\mathrm{T}}]$ being on the plateau. Within a same plateau, the cut value corresponding to higher signal efficiency is preferably selected. The background rejection is of course another consideration. No cut is selected for $p_{\mathrm{T,rel}}^{\mathrm{miss}}$ as any cut would decrease the significance value of $s_{\text{1-d}}[m_{\mathrm{T}}]$.

A new scan is repeated by applying all these initial cuts except for the one on the variable under scan (see Figure 6.4). It is found that no change is needed for any of these initial cut values. This implies that a simultaneous scan in multi-dimensions is not needed. In fact the latter scan is not preferable as it either can be time consuming or may not lead to a unique set of cuts given that the variation of the significance on some of the variable is fairly weak as one can see from Figure 6.3. The individual scan on the other hand allows one to better appreciate the dependence of the significance which differs from one variable to another.

When selecting these cuts, it has been checked (by comparing Figures 6.5 and 6.6 with Figure 6.3) that they apply also to a high mass signal up to 1 000 GeV as well as to the 1-jet channel.

These new cuts are finally compared with those used in the Run-1 publication [15] in Table 6.2. Both the signal significance value ($s_{\text{1-d}}[m_{\mathrm{T}}]$) and the expected limit at 95% CL on the signal strength are improved with the newly optimised cuts for a heavy Higgs boson at 600 GeV. One also observes that the $p_{\mathrm{T}}^{\ell\ell}$ cut and a strict cut on $p_{\mathrm{T}}^{\mathrm{sublead}}$ are not needed with this optimisation strategy.

A similar comparison as a function of heavy Higgs boson mass m_H is shown in Figure 6.7. The improvement is observed over all the mass points considered.

[6]For a heavy Higgs boson of 600 GeV and up to 1 000 GeV, a more stringent cut could be selected. On the other hand, Higgs bosons at lower masses need a lower cut on $m_{\ell\ell}$. So this cut is a kind of compromise.

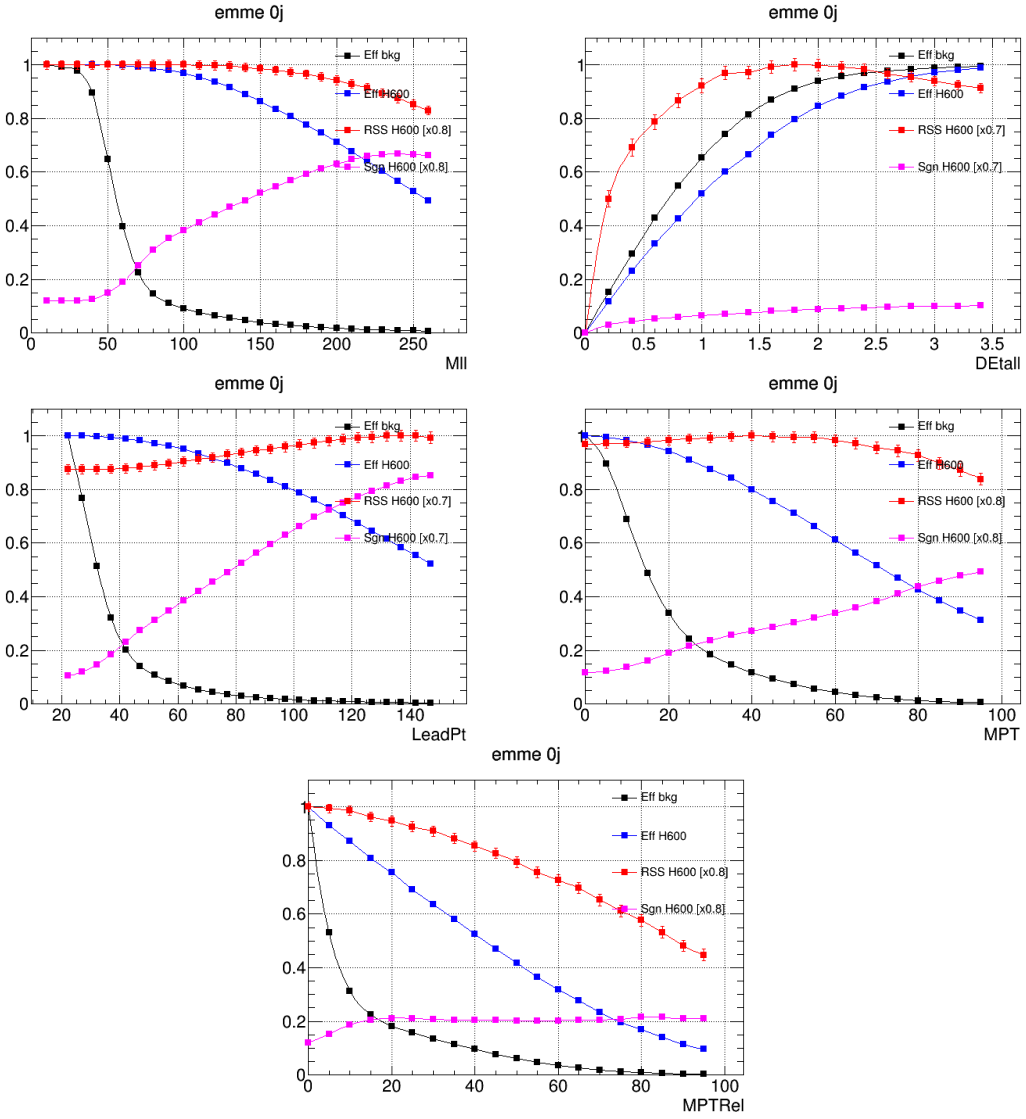

Figure 6.3: Significance scan for five variables, $m_{\ell\ell}$ (Mll), $\Delta\eta_{\ell\ell}$ (DEtall), $p_{\mathrm{T}}^{\mathrm{lead}}$ (LeadPt), $p_{\mathrm{T}}^{\mathrm{miss}}$ (MPT) and $p_{\mathrm{T,rel}}^{\mathrm{miss}}$ (MPTRel), selected from the first step for a heavy Higgs boson at 600 GeV in the $H \to WW \to e\mu + \mu e$ channel in the zero-jet category. The four curves correspond to the efficiency of the signal (Eff H600), the efficiency of the background (Eff bkg), the m_{T}-based significance (RSS H600) and the global significance (Sgn H600). The number in the brackets corresponds to the scale factor applied to the significance curves for an easy display.

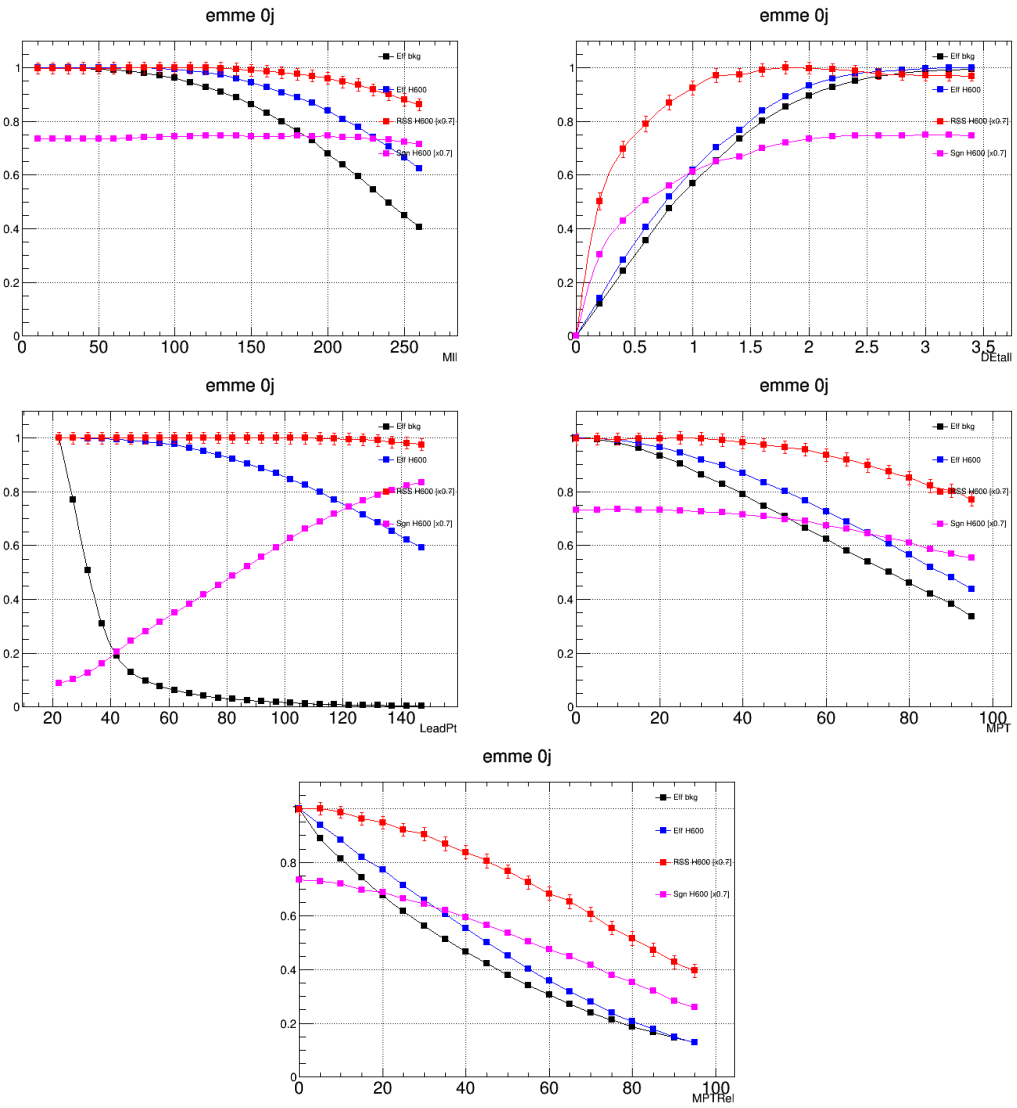

Figure 6.4: Same as Figure 6.3 except that here all initial cuts have been applied except for that one on the variable under consideration.

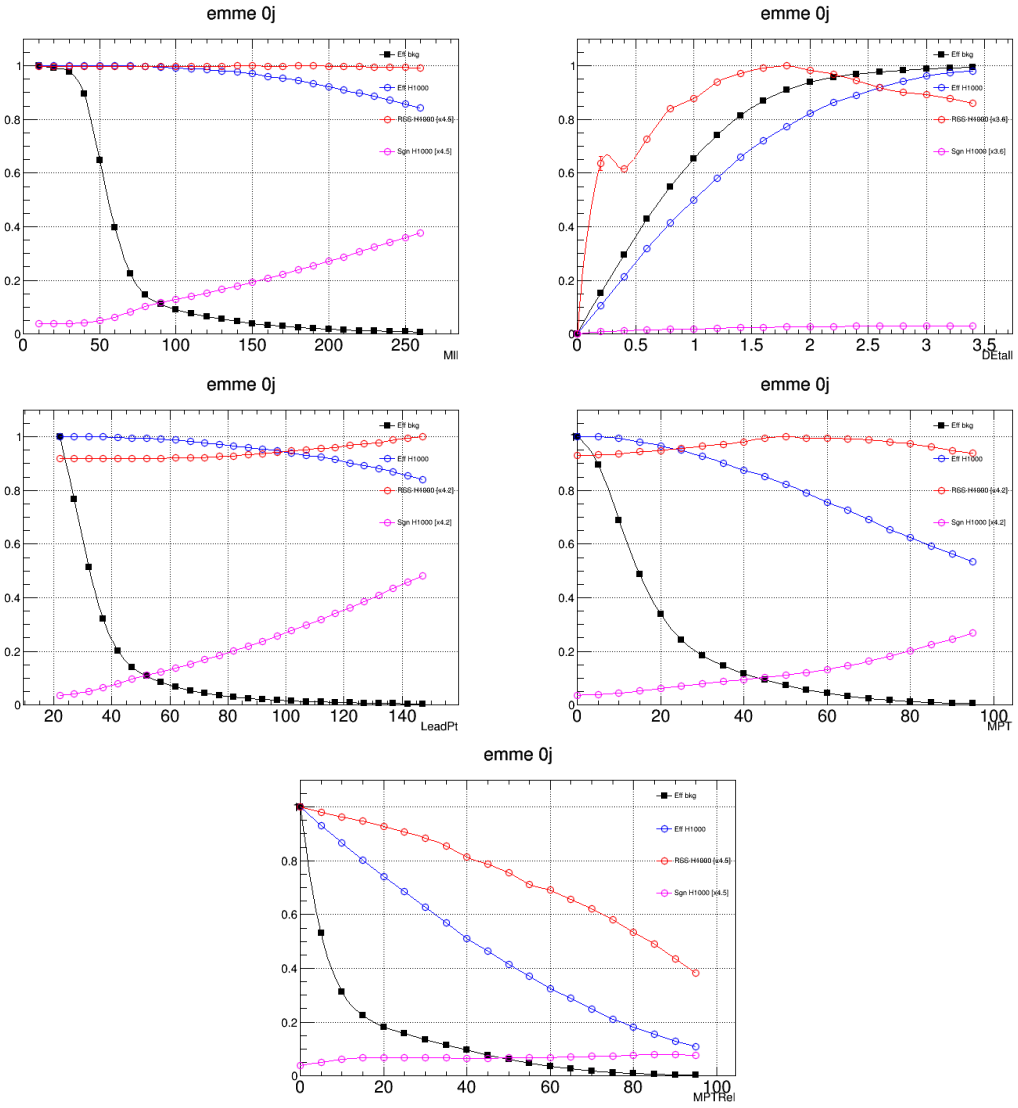

Figure 6.5: Same as Figure 6.3 except that here the signal is at 1 TeV instead of 600 GeV.

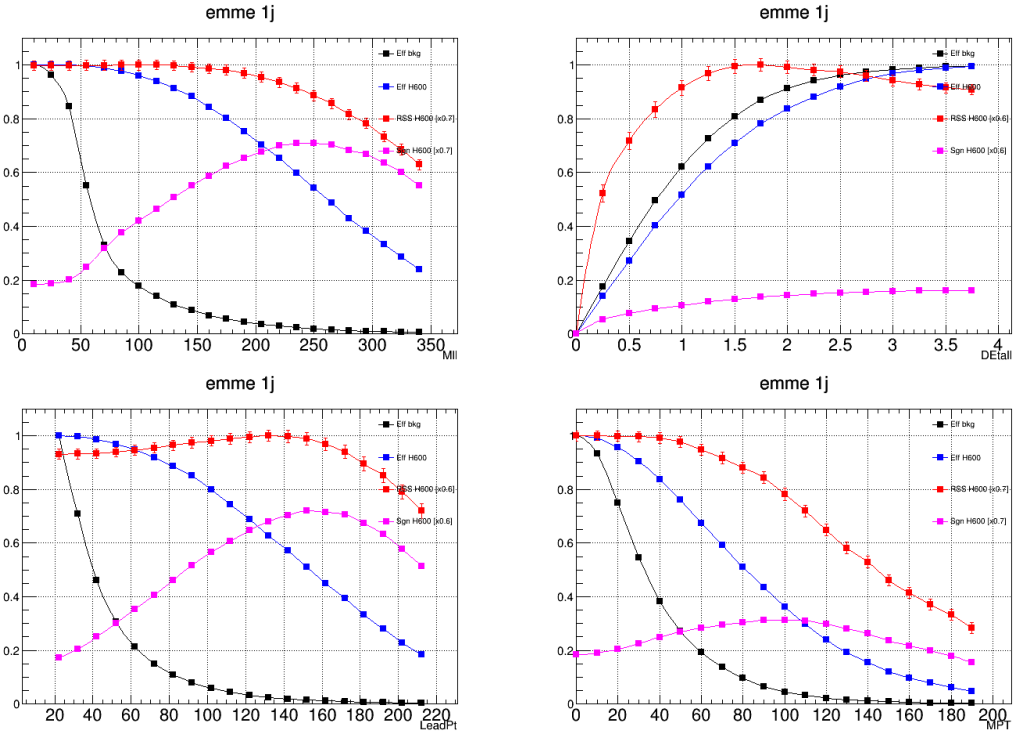

Figure 6.6: Same as Figure 6.3 except that this is for 1-jet channel instead of zero-jet channel.

Table 6.2: Comparison of the new optimal cuts with those used in the Run-1 publication [15]. The comparison for the significance values and expected 95% CL limits on the signal strength μ is given for $m_H = 600\,\text{GeV}$.

Comparison	New	Publication
Common pre-selection	$p_{\text{T}}^{\text{lead}} > 22\,\text{GeV}$ $p_{\text{T}}^{\text{sublead}} > 15\,\text{GeV}$	
Additional cuts	$p_{\text{T}}^{\text{lead}} > 120\,\text{GeV}$ $p_{\text{T}}^{\text{miss}} > 40\,\text{GeV}$ $m_{\ell\ell} > 100\,\text{GeV}$ $\Delta\eta_{\ell\ell} < 1.8$	$p_{\text{T}}^{\text{lead}} > 60\,\text{GeV}$ $p_{\text{T}}^{\text{sublead}} > 30\,\text{GeV}$ $p_{\text{T}}^{\text{miss}} > 45\,\text{GeV}$ $p_{\text{T}}^{\ell\ell} > 60\,\text{GeV}$ $m_{\ell\ell} > 60\,\text{GeV}$ $\Delta\eta_{\ell\ell} < 1.35$
Significance ($s_{\text{1-d}}[m_{\text{T}}]$)	1.37 ± 0.02	1.24 ± 0.03
Limit on μ (95% CL)	1.54	1.70

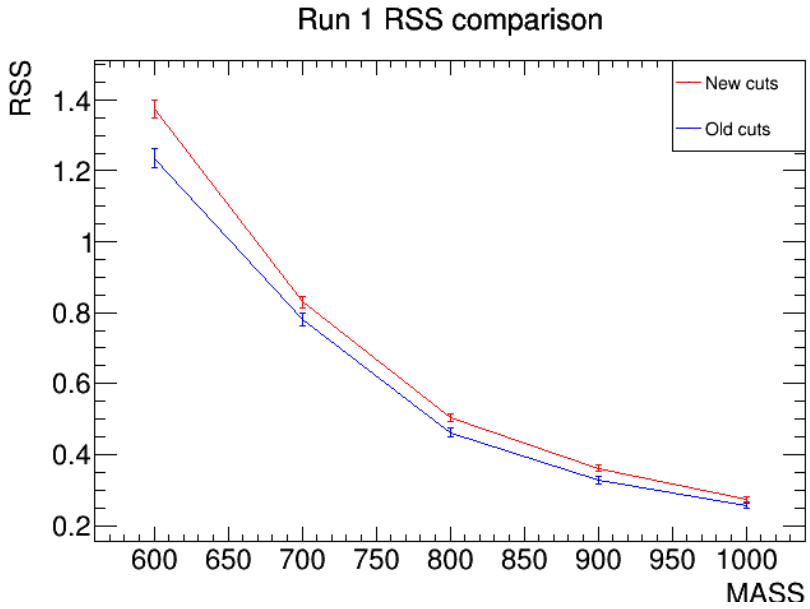

Figure 6.7: Comparison of the signal significance $s_{\text{1-d}}[m_{\text{T}}]$ (RSS) between the new and published selection is shown as a function of heavy Higgs boson mass m_H.

6.1.3 Application to SM Higgs boson discovery analysis in the $H \to WW^* \to \ell\nu\ell\nu$ channel

The same strategy is also applied to and compared with the low-mass analysis which has previously allowed us to observe the Higgs boson in the $h \to WW^*$ channel alone [116]. For the 0 and 1-jet channels of this analysis, the following variables have been used in the event selection: $p_{\text{T}}^{\text{lead}}$, $p_{\text{T}}^{\text{sublead}}$, $m_{\ell\ell}$, $\Delta\phi_{\ell\ell}$, $p_{\text{T}}^{\text{miss}}$, $p_{\text{T}}^{\ell\ell}$ and $\Delta\phi_{\ell\ell,\text{MET}}$.

In the first step, the ranking order obtained from a BDT training is shown in Table 6.3. Among the seven variables, $\Delta\phi_{\ell\ell,\text{MET}}$ has a low ranking value below 40% and is removed from the list. In addition, $p_{\text{T}}^{\ell\ell}$ is also removed as it has a strong correlation with $p_{\text{T}}^{\text{miss}}$ (Figure 6.8) but a lower ranking value (Table 6.3). Therefore after the first step, only five variables are selected: $m_{\ell\ell}$, $\Delta\phi_{\ell\ell}$, $p_{\text{T}}^{\text{sublead}}$, $p_{\text{T}}^{\text{lead}}$ and $p_{\text{T}}^{\text{miss}}$.

Table 6.3: Absolute and relative ranking order for the SM Higgs boson at 125 GeV in the $H \to WW^* \to \ell\nu\ell\nu$ channel.

Variable	$m_{\ell\ell}$	$\Delta\phi_{\ell\ell}$	$p_{\text{T}}^{\text{sublead}}$	$p_{\text{T}}^{\text{lead}}$	$p_{\text{T}}^{\text{miss}}$	$p_{\text{T}}^{\ell\ell}$	$\Delta\phi_{\ell\ell,\text{MET}}$
Absolute	0.217	0.197	0.153	0.146	0.128	0.102	0.0058
Relative (%)	100	91	70	67	59	47	27

In the second step, a significance scan is performed. Three significance quan-

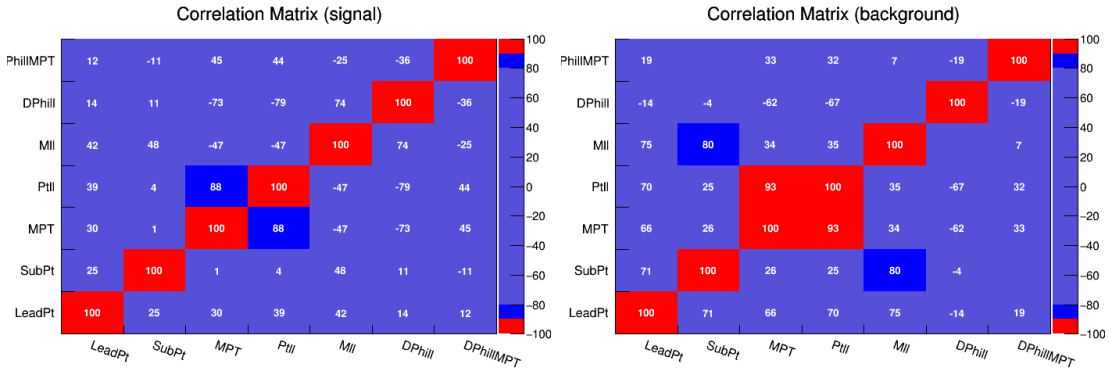

Figure 6.8: Correlation matrices between variables for signal (left) and background (right) in the SM Higgs boson analysis.

tities are defined, the global one s, the m_{T}-based one $s_{\text{1-d}}[m_{\mathrm{T}}]$ and the two-dimensional one in $p_{\mathrm{T}}^{\mathrm{sublead}}$ and m_{T} $s_{\text{2-d}}[p_{\mathrm{T}}^{\mathrm{sublead}}, m_{\mathrm{T}}]$. The significance results together with the signal and background efficiencies are shown in Figure 6.9. As expected, the 2-d significance curve $s_{\text{2-d}}[p_{\mathrm{T}}^{\mathrm{sublead}}, m_{\mathrm{T}}]$ is systematically higher than the 1-d curve $s_{\text{1-d}}[m_{\mathrm{T}}]$ but the gain is smaller from 1-d to 2-d than from the global one to 1-d. Based on $s_{\text{2-d}}[p_{\mathrm{T}}^{\mathrm{sublead}}, m_{\mathrm{T}}]$, the initial cuts are defined as: $m_{\ell\ell} < 45\,\mathrm{GeV}$, $\Delta\phi_{\ell\ell} < 2$ and $p_{\mathrm{T}}^{\mathrm{miss}} > 35\,\mathrm{GeV}$. No strict cuts on $p_{\mathrm{T}}^{\mathrm{lead}}$ and $p_{\mathrm{T}}^{\mathrm{sublead}}$ are needed, so the cuts at the pre-selection level corresponding to the starting point of the scan are kept.

A new scan is then performed by applying all the other cuts except for the one on the variable under the new scan (the results are shown in Figure 6.10). It turns out that a minor adjustment is needed for $m_{\ell\ell}$ from 45 GeV to 50 or 55 GeV and for $p_{\mathrm{T}}^{\mathrm{miss}}$ from 35 GeV to 30 GeV. Further iteration shows that these cuts are stable. The final cuts are compared [7] with those used in the Run-1 publication [116] in Table 6.4.

6.1.4 Summary

A simple strategy combining a selection of variables from the ranking order and the correlation matrices provided by a BDT training and a significance scan of the BDT selected variables is proposed to define optimal event selection for a data analysis. Two examples have been shown by applying the strategy. In both

[7] It should be noted that in the Run-1 publication [116] a 3-d based likelihood analysis was used, it is expected that the corresponding signal significance is slightly better than the 2-d significance shown here. But the cuts that are proposed here should be fairly independent of the 3-d and 2-d significance scan since the difference between the 1-d and 2-d curves is small, which can be found in Figure 6.9.

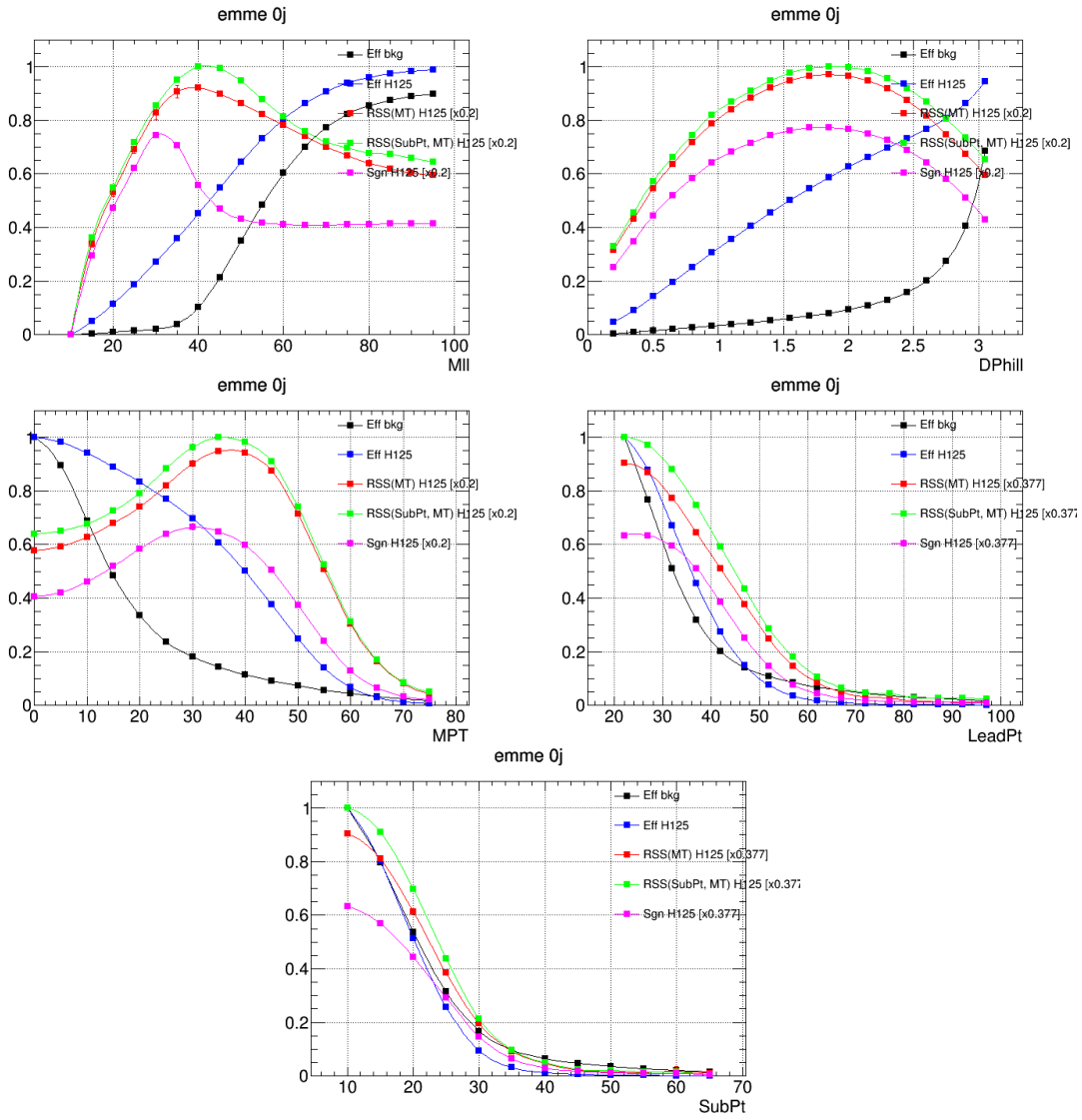

Figure 6.9: Significance scan for five variables, $m_{\ell\ell}$ (Mll), $\Delta\phi_{\ell\ell}$ (DPhill), $p_{\mathrm{T}}^{\mathrm{miss}}$ (MPT), $p_{\mathrm{T}}^{\mathrm{lead}}$ (LeadPt) and $p_{\mathrm{T}}^{\mathrm{sublead}}$ (SubPt), selected from the first step for the SM Higgs boson at 125 GeV in the $h \to WW^* \to e\mu{+}\mu e$ channel in the zero-jet category. The four curves correspond to the efficiency of the signal (Eff H125), the efficiency of the background (Eff bkg), the $p_{\mathrm{T}}^{\mathrm{sublead}}$ and m_{T}-based significance (RSS(SubPt, MT) H125), the m_{T}-based significance (RSS(MT) H125) and the global significance (Sgn H125). The number in the brackets corresponds to the scale factor applied to the significance curves for an easy display.

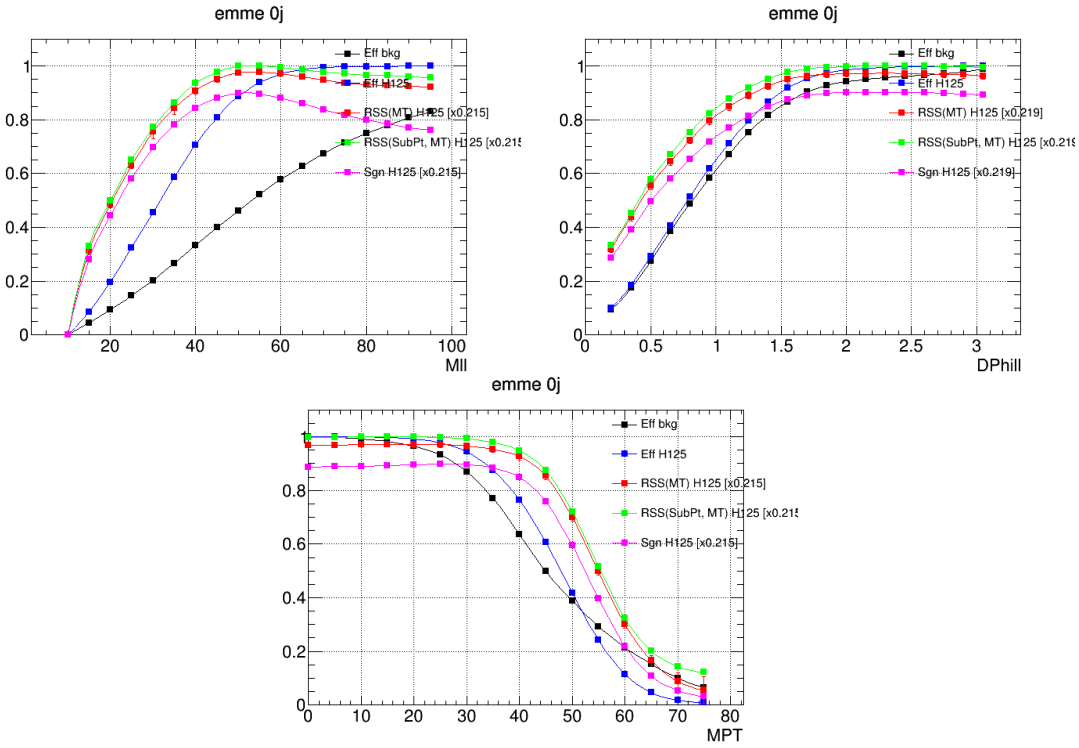

Figure 6.10: Same as Figure 6.9 except that here all initial cuts have been applied except for that one on the variable under consideration.

Table 6.4: Comparison of the new optimal cuts with those used in the Run-1 publication [116]. The comparison for the significance values is given for $m_h = 125\,\text{GeV}$.

Comparison	New	Publication
Common pre-selection	$p_{\text{T}}^{\text{lead}} > 22\,\text{GeV}$ $p_{\text{T}}^{\text{sublead}} > 10\,\text{GeV}$	
Additional cuts	$m_{\ell\ell} < 55\,\text{GeV}$ $\Delta\phi_{\ell\ell} < 2$ $p_{\text{T}}^{\text{miss}} > 30\,\text{GeV}$	$m_{\ell\ell} < 55\,\text{GeV}$ $\Delta\phi_{\ell\ell} < 1.8$ $p_{\text{T}}^{\text{miss}} > 20\,\text{GeV}$ $p_{\text{T}}^{\ell\ell} > 30\,\text{GeV}$ $\Delta\phi_{\ell\ell,\text{MET}} > 1.55$
Significance ($s_{\text{2-d}}[p_{\text{T}}^{\text{sublead}}, m_{\text{T}}]$)	4.682 ± 0.011	4.662 ± 0.012

cases, improvement in signal significance is achieved with fewer variables than previously used.

In comparison with a pure MVA analysis, the strategy allows one to use fewer discriminant variables to performed cut-based like analysis so that the data and MC agreement of the selected variables can be checked in detailed in particular around the cut value.

In comparison with a pure cut-based analysis, the use of the MVA training allows one to select only the most discriminant and less correlated variables.

This strategy can be easily extended to other analyses both for hunting for new physics and for performing precision measurements.

6.2 Definition of signal regions

The event selections in the SRs include basically two parts: the pre-selection aimed at selecting WW candidate events with very general and initial cuts, and the additional cuts aimed at defining specific SRs.

The event pre-selection includes requirements on the leading and subleading lepton (e or μ) transverse momentum p_{T}^{ℓ}: $p_{\mathrm{T}}^{\ell,\mathrm{lead}} > 25\,\mathrm{GeV}$ and $p_{\mathrm{T}}^{\ell,\mathrm{sublead}} > 25\,\mathrm{GeV}$. Each event is required to have two oppositely charged leptons with different flavours and no additional lepton with $p_{\mathrm{T}}^{\ell,\mathrm{other}} > 15\,\mathrm{GeV}$ in order to suppress diboson backgrounds. The identification requirement for the addtional leptons are same with the two leading leptons when $p_{\mathrm{T}} > 25\,\mathrm{GeV}$, satisfying the minimal quality criteria ("MediumLH" for electrons and "Medium" for muons) as discussed in Chapter 5, but more strict ("TightLH" for electrons and "Tight" for muons) when $15\,\mathrm{GeV} < p_{\mathrm{T}} < 25\,\mathrm{GeV}$. The isolation requirement for the additional leptons is looser ("GradientLoose" in stead of "Gradient" for the two leading leptons). Backgrounds from low-mass resonances decaying to different flavour final states via $\tau^{+}\tau^{-}$ are rejected by requiring $m_{\ell\ell} > 10\,\mathrm{GeV}$, with $m_{\ell\ell}$ being the invariant mass of the leading and subleading leptons.

Additional cuts, that are used in the SRs, are optimised according to the optimisation strategy described in Section 6.1. For this optimisation, the NWA signal samples are used. Nevertheless, the same event selections are applied to all signal models and mass points.

Since the background rate and composition, as well as the signal topology are significantly dependent on the jet multiplicity, three orthogonal event categories are defined, two of them with one and at least two jets optimised for the VBF production and one quasi-inclusive category (excluding the VBF phase space) optimised for the ggF production. This is due to the fact that the VBF process is mostly associated with two or more jets, while in contrast, signal without accompanying forward jets is dominated by the ggF process. The resulting selections that define the three event categories or SRs, namely the quasi-inclusive ggF ($\mathrm{SR}_{\mathrm{ggF}}$), the $N_{\mathrm{jet}} = 1$ VBF ($\mathrm{SR}_{\mathrm{VBF1J}}$) and the $N_{\mathrm{jet}} \geq 2$ VBF ($\mathrm{SR}_{\mathrm{VBF2J}}$) are summarised in Table 6.5. For the VBF $N_{\mathrm{jet}} = 1$ category, two discriminating variables are used to minimise the contribution of the ggF signal: the (absolute) pseudorapidity of the jet, $|\eta_j|$, and the minimum value of the pseudorapidity distance between the jet and either of the leptons, $\min(|\Delta\eta_{j\ell}|)$. For the VBF $N_{\mathrm{jet}} \geq 2$ category, the invariant mass, m_{jj}, and the rapidity difference, $|\Delta y_{jj}|$, of the two leading jets are used to select the VBF signal.

Table 6.5: Selection conditions and phase space definitions used in the ggF and VBF signal regions.

SR_{ggF}	SR_{VBF1J}	SR_{VBF2J}
Common selections		
$N_{b\text{-tag}} = 0$ $\lvert\Delta\eta_{\ell\ell}\rvert < 1.8$ $m_{\ell\ell} > 55\,\text{GeV}$ $p_{\text{T}}^{\ell,\text{lead}} > 45\,\text{GeV}$ $p_{\text{T}}^{\ell,\text{sublead}} > 30\,\text{GeV}$ veto if $p_{\text{T}}^{\ell,\text{other}} > 15\,\text{GeV}$ $\max(m_{\text{T}}^{W}) > 50\,\text{GeV}$		
ggF phase space	VBF1J phase space	VBF2J phase space
Inclusive in N_{jet} but excluding VBF1J and VBF2J phase space	$N_{\text{jet}} = 1$ and $\lvert\eta_j\rvert > 2.4$, $\min(\lvert\Delta\eta_{j\ell}\rvert) > 1.75$	$N_{\text{jet}} \geq 2$ and $m_{jj} > 500\,\text{GeV}$, $\lvert\Delta y_{jj}\rvert > 4$

The selected variables for discriminating signals from the large SM backgrounds are $p_{\text{T}}^{\ell,\text{lead}}$, $m_{\ell\ell}$ and $|\Delta\eta_{\ell\ell}|$, the latter being the pseudorapidity difference between the leading and subleading leptons. The signals tend to be at high $m_{\ell\ell}$ for high m_{H}. The cut applied on $|\Delta\eta_{\ell\ell}|$ is actually due to the special kinematics of the Higgs boson (or other scalars) decaying in the WW channel. The W pairs originating from the decay of a scalar have to have opposite spin orientation, and due to the V-A structure in the W decay, the left-handed e^- (right-handed μ^+) is emitted along the W^- (W^+) spin, assuming the final state is $e^-\bar{\nu}_e\mu^+\nu_\mu$. Consequently, one of the two charged leptons is emitted along the momentum direction of the two W's while the other one is emitted in the opposite direction. In addition, to suppress the top quark background, events with number of b-jets ($N_{b\text{-jet}}$) greater than 0 are rejected from the signal regions. To reduce the Z+jets and W+jets contributions, two other variables are used: the transverse momentum of the subleading lepton ($p_{\text{T}}^{\ell,\text{sublead}}$) and the maximum value of the transverse mass calculated with either of the two leptons and the missing transverse momentum:

$$m_{\text{T}}^{W} = \sqrt{2p_{\text{T}}^{\ell}E_{\text{T}}^{\text{miss}}(1-\cos(\phi^{\ell}-\phi^{E_{\text{T}}^{\text{miss}}}))}\,, \tag{6.4}$$

where p_{T}^{ℓ} and ϕ^{ℓ} are the transverse momentum and azimuthal angle of a given lepton and $\phi^{E_{\text{T}}^{\text{miss}}}$ is the azimuthal angle of the missing transverse momentum vector.

The discriminating variable used in this search is the transverse mass, m_{T}, defined as

$$m_{\text{T}} = \sqrt{(E_{\text{T}}^{\ell\ell}+E_{\text{T}}^{\text{miss}})^2 - |\mathbf{p}_{\text{T}}^{\ell\ell}+\boldsymbol{E}_{\text{T}}^{\text{miss}}|^2}\,, \tag{6.5}$$

where

$$E_{\mathrm{T}}^{\ell\ell} = \sqrt{|\mathbf{p}_{\mathrm{T}}^{\ell\ell}|^2 + m_{\ell\ell}^2}\,, \tag{6.6}$$

and $\mathbf{p}_{\mathrm{T}}^{\ell\ell}$ is the transverse momentum vector of the leading and subleading leptons.

The relative efficiencies of the additional cuts used to define the signal regions except for the pre-selection for the Higgs bosons with the NWA lineshape with mass values between 200 GeV and 4 TeV (3 TeV for VBF signal) are displayed in Figure 6.11. The corresponding plots for the other signal models are shown in Figures 6.12 and 6.13.

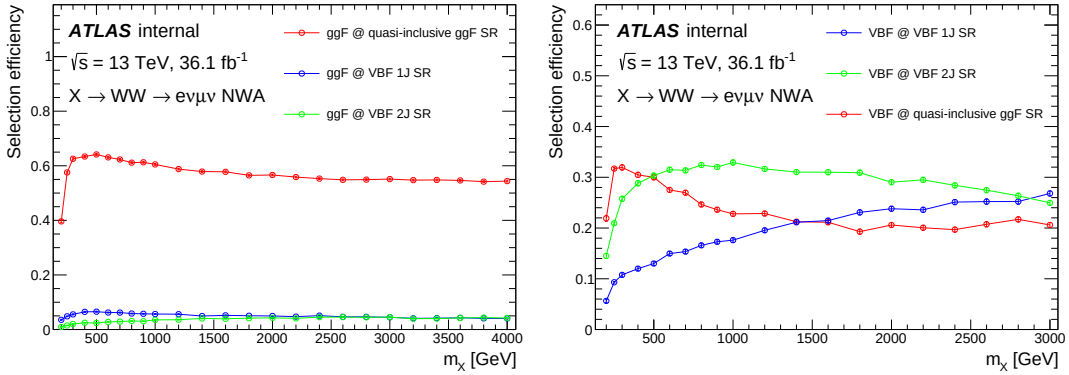

Figure 6.11: Efficiencies relative to the pre-selection efficiencies of those signal region additional cuts, defined on top of the pre-selection, as a function of heavy Higgs boson mass for ggF (left) and VBF (right) signals with the NWA lineshape. The legend e.g. "ggF @ VBF 1J SR" means the efficiency of the ggF signals in the VBF $N_{\mathrm{jet}} = 1$ category.

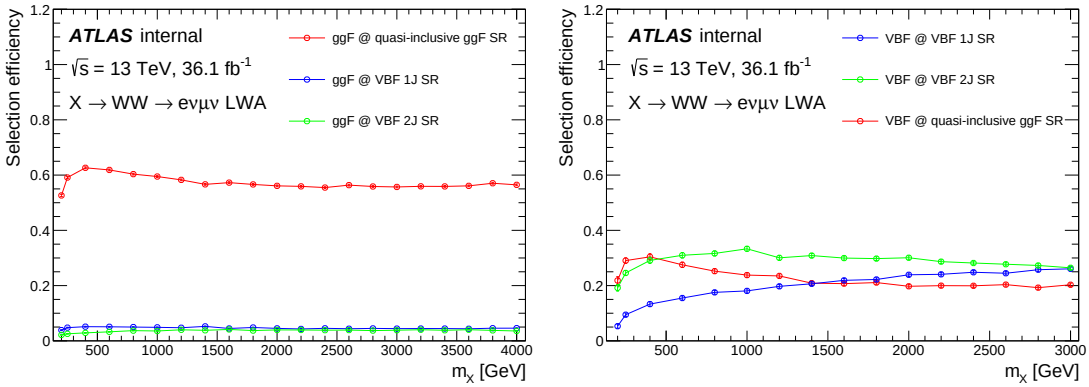

Figure 6.12: Efficiencies relative to the pre-selection efficiencies of those signal region additional cuts, defined on top of the pre-selection, as a function of heavy Higgs boson mass for the LWA signal model (width: 15% of m_H) with both ggF (left) and VBF (right) production modes. The legend e.g. "ggF @ VBF 1J SR" means the efficiency of the ggF signals in the VBF $N_{\mathrm{jet}} = 1$ category.

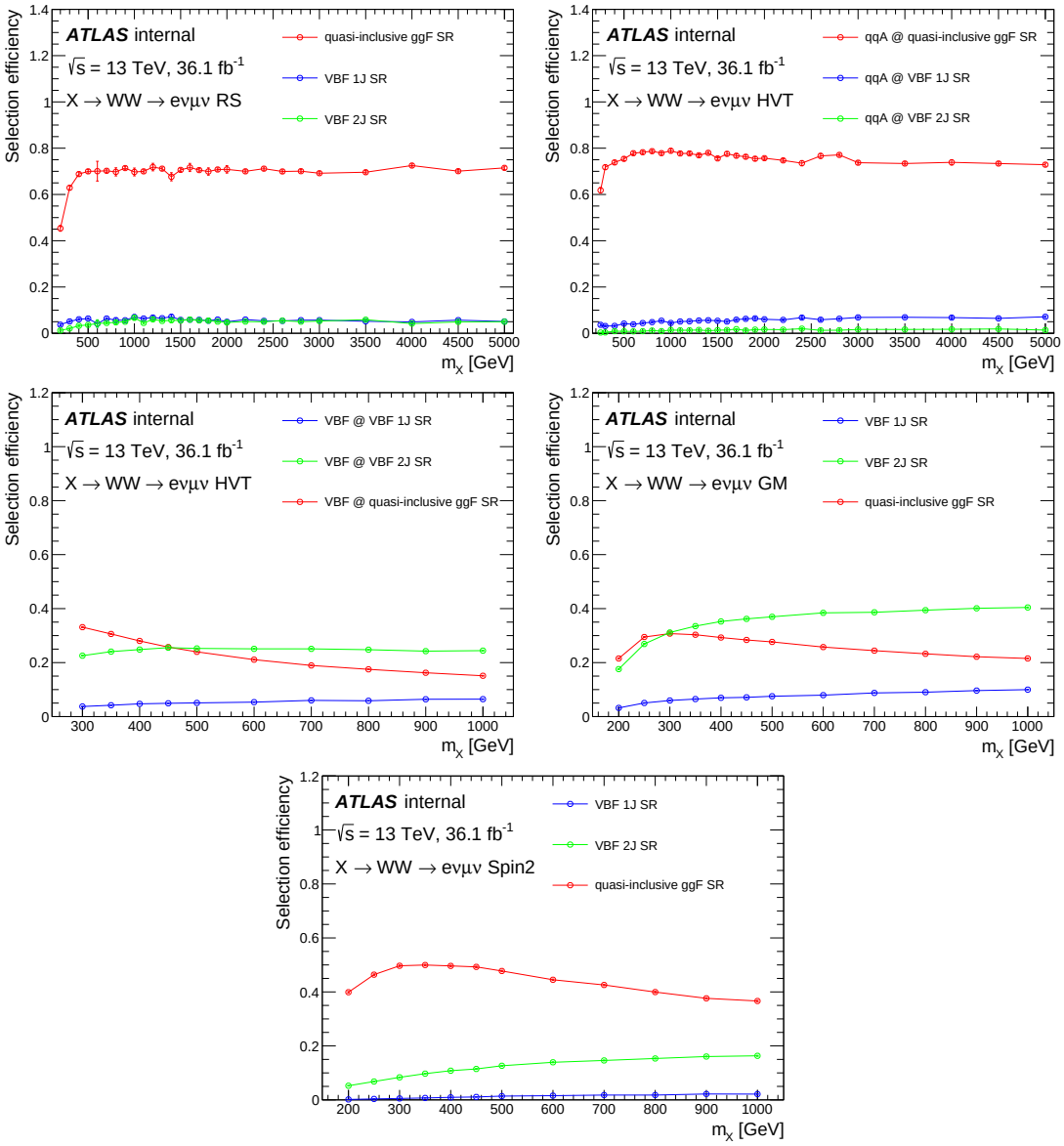

Figure 6.13: Efficiencies relative to the pre-selection efficiencies of those signal region additional cuts, defined on top of the pre-selection, as a function of heavy resonance mass for the exotic signal models: RS with $k/\bar{M}_{\mathrm{Pl}} = 1$ (top left), HVT qqA (top right) and VBF (middle left), GM VBF (middle right) and Spin-2 VBF (bottom). The legend e.g. "qqA @ VBF 1J SR" means the efficiency of the qqA signals in the VBF $N_{\mathrm{jet}} = 1$ category.

The geometrical acceptance times event selection efficiency, namely the overall selection efficiency including the pre-selection and additional cuts in the SRs for the NWA signal model is displayed in Figure 6.14. The corresponding plots for the other signal models are shown in Figures 6.15 and 6.16. For samples with lower resonance masses, the acceptance times efficiency is lower because the leptons are softer (smaller p_{T} and $m_{\ell\ell}$). This is due to the fact that the same selection is applied to all signal models and mass points in this analysis. This is also the reason why the search is limited to signal mass values greater than about 200GeV. Therefore, the different selection efficiencies between the models are as expected which is mainly due to different $|\Delta\eta_{\ell\ell}|$ distributions for the different spin states.

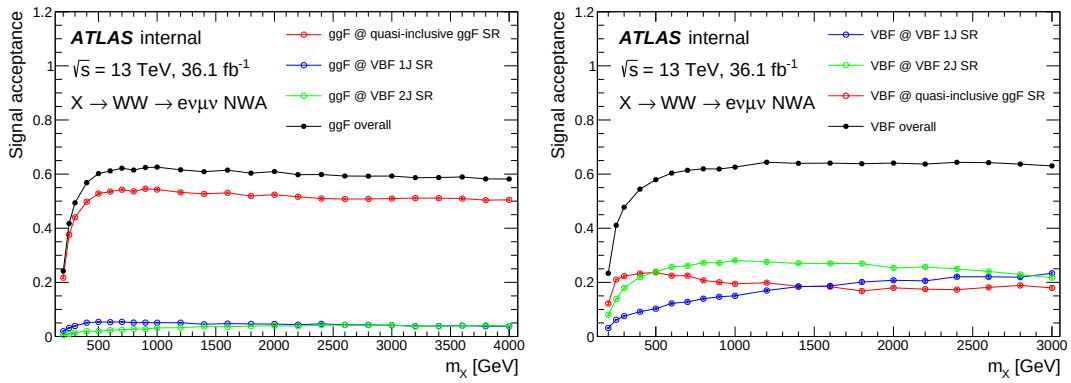

Figure 6.14: Geometrical acceptance times selection efficiency (shortened as "Signal acceptance" in the plots) as a function of heavy Higgs boson mass for ggF (left) and VBF (right) signals with the NWA lineshape. The legend e.g. "ggF @ VBF 1J SR" means the efficiency of the ggF signals in the VBF $N_{\mathrm{jet}} = 1$ category, and "overall" means that the efficiencies of a signal sample to all the three signal event categories are combined.

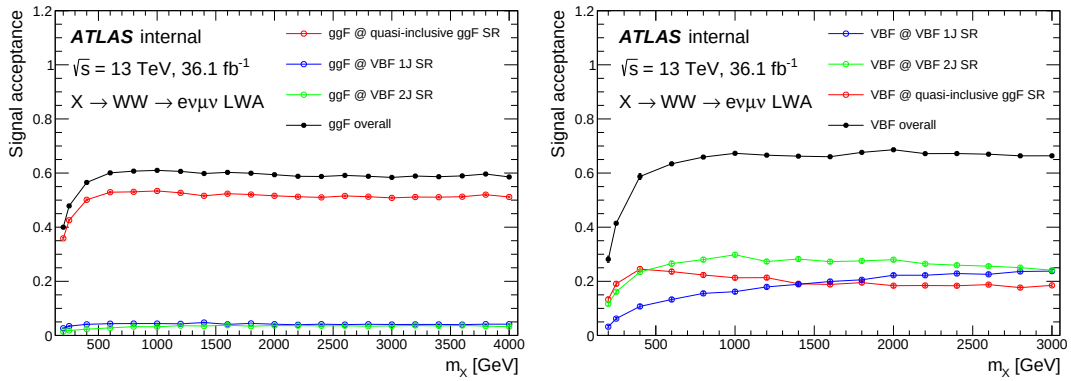

Figure 6.15: Geometrical acceptance times selection efficiency (shortened as "Signal acceptance" in the plots) as a function of heavy Higgs boson mass for the LWA signal model (width: 15% of m_H) with both ggF (left) and VBF (right) production modes. The legend e.g. "ggF @ VBF 1J SR" means the efficiency of the ggF signals in the VBF $N_{\text{jet}} = 1$ category, and "overall" means that the efficiencies of a signal sample to all the three signal event categories are combined.

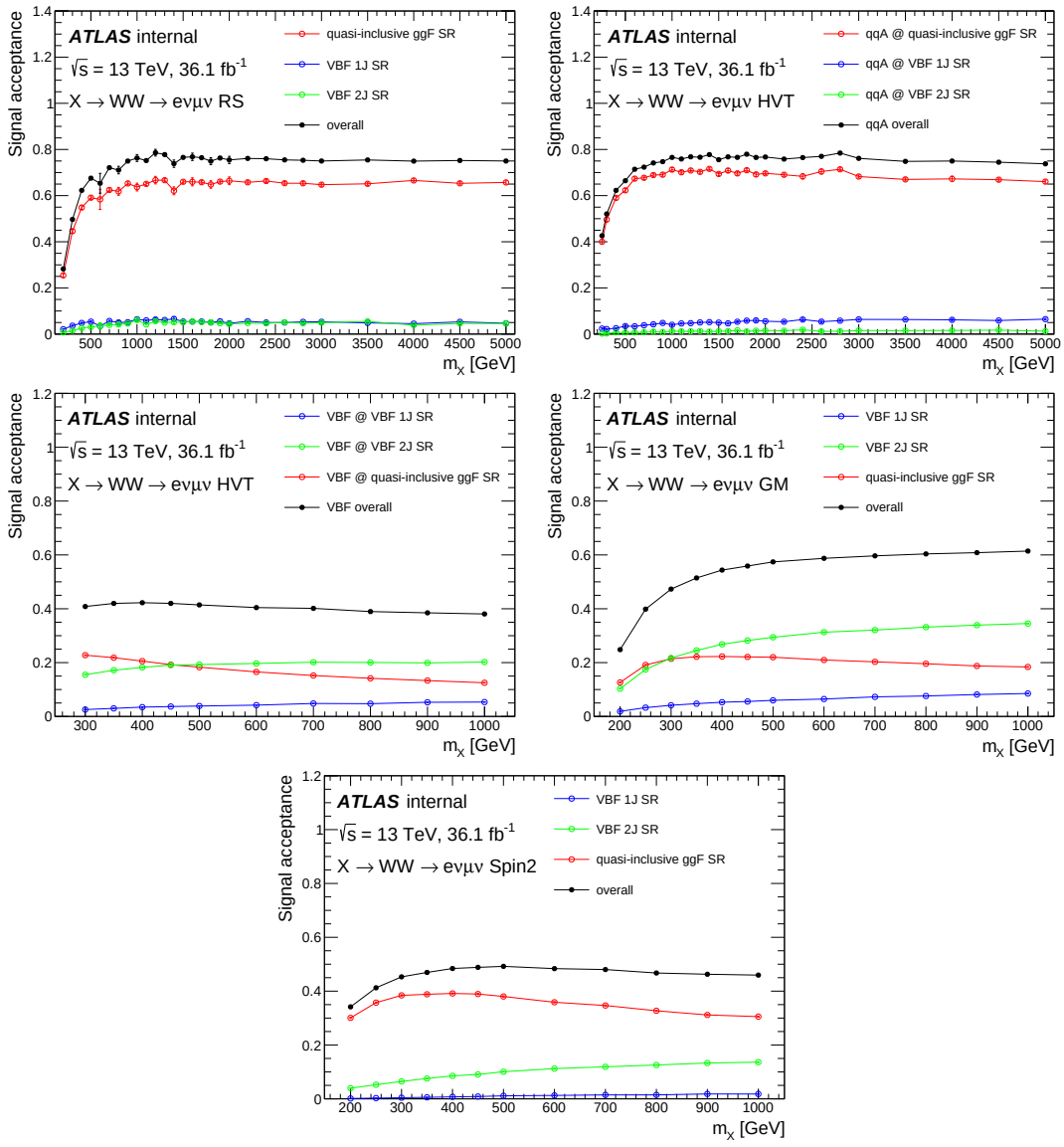

Figure 6.16: Geometrical acceptance times selection efficiency (shortened as "Signal acceptance" in the plots) as a function of heavy resonance mass for the exotic signal models: RS with $k/\bar{M}_{\mathrm{Pl}} = 1$ (top left), HVT qqA (top right) and VBF (middle left), GM VBF (middle right) and Spin-2 VBF (bottom). The legend e.g. "qqA @ VBF 1J SR" means the efficiency of the qqA signals in the VBF $N_{\mathrm{jet}} = 1$ category, and "overall" means that the efficiencies of a signal sample to all the three signal event categories are combined.

Chapter 7

Background estimation

The major backgrounds for the $e\nu\mu\nu$ final state arise from top quark and WW production processes, with additional contributions from V+jets and the diboson processes VZ, $V\gamma$ and $V\gamma^*$, with V standing for both Z and W bosons. Since the discriminating variable used for this search is the transverse mass, m_{T}, both the background normalisations and the shapes of the background m_{T} distributions must be estimated. The m_{T} shapes of the backgrounds are modelled using simulated events while the top quark and WW background normalisations are determined from a simultaneous fit (Chapter 9) to the data in m_{T}-binned distributions in the signal regions and the total event yields in the control regions (the m_{T} binning is optimised in all SRs to achieve maximum signal sensitivities, as described in Appendix D). The normalisation factors of the fit (named "post-fit" normalisation factors hereafter) provide the best overall matching between the number of the observed data events and the corresponding SM background expectations in all the signal and control regions.

The control regions (CRs) are defined by criteria similar to those used for the SRs, but with some requirements loosened or reversed to obtain signal-depleted samples, enriched in the relevant backgrounds. These criteria are summarised in Table 7.1.

A comparison of the common variables that are used in the additional cuts of the SRs and CRs after the pre-selection between data and MC is made at the pre-selection level and shown in Figure 7.1.

The following subsections describe in more details the methods used to estimate the most important backgrounds, namely top quark, WW, and W+jets. The Drell-Yan and non-WW diboson backgrounds are small, and the former samples are normalised to next-to-next leading order (NNLO) cross sections [117] and the latter ones to NLO cross sections from the Sherpa generator. The small back-

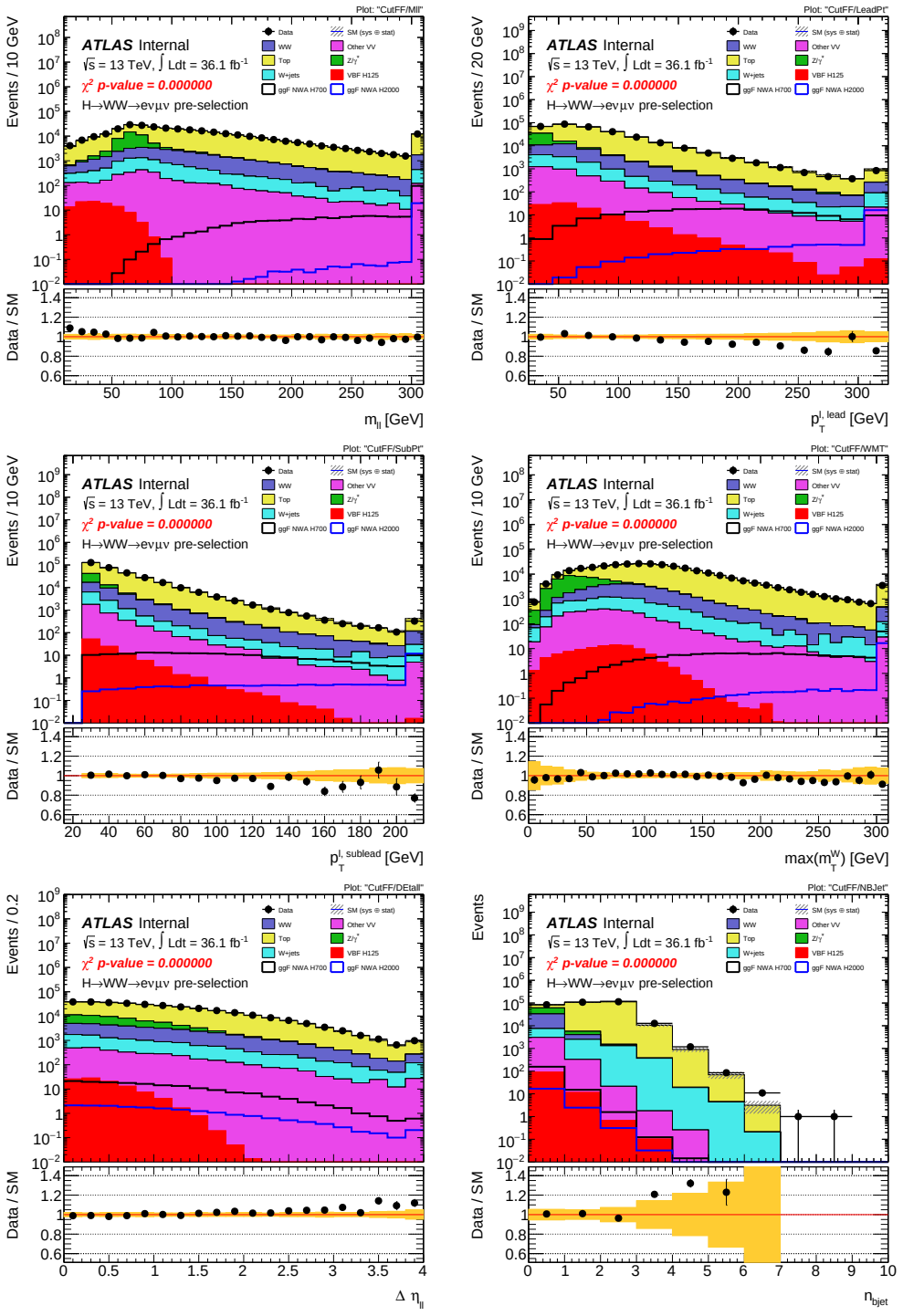

Figure 7.1: Comparison of data and MC at the event pre-selection level for the variables: $m_{\ell\ell}$ (top left), $p_{\mathrm{T}}^{\ell,\mathrm{lead}}$ (top right), $p_{\mathrm{T}}^{\ell,\mathrm{sublead}}$ (middle left), $\max(m_{\mathrm{T}}^{W})$ (middle right), $\Delta\eta_{\ell\ell}$ (bottom left), and $N_{b\text{-jet}}$ (bottom right). The hatched band in the upper panel and the shaded band in the lower panel show the combined statistical and experimental uncertainties on the predictions. The last bin contains the overflow.

Table 7.1: Summary of all the selections used in the ggF and VBF WW and top-quark control regions. The common selection "veto if $p_{\mathrm{T}}^{\ell,\mathrm{other}} > 15\,\mathrm{GeV}$" applied to all the regions is not explicitly shown.

WW $\mathrm{CR}_{\mathrm{ggF}}$	Top $\mathrm{CR}_{\mathrm{ggF}}$	WW $\mathrm{CR}_{\mathrm{VBF1J}}$	Top $\mathrm{CR}_{\mathrm{VBF}}$
$N_{b\text{-tag}} = 0$	$N_{b\text{-tag}} = 1$	$N_{b\text{-tag}} = 0$	$N_{b\text{-tag}} \geq 1$
$\lvert\Delta\eta_{\ell\ell}\rvert > 1.8$	$\lvert\Delta\eta_{\ell\ell}\rvert < 1.8$	($\lvert\Delta\eta_{\ell\ell}\rvert > 1.8$ or	–
$m_{\ell\ell} > 55\,\mathrm{GeV}$		$10\,\mathrm{GeV} < m_{\ell\ell} < 55\,\mathrm{GeV}$)	$m_{\ell\ell} > 10\,\mathrm{GeV}$
$p_{\mathrm{T}}^{\ell,\mathrm{lead}} > 45\,\mathrm{GeV}$		$p_{\mathrm{T}}^{\ell,\mathrm{lead}} > 25\,\mathrm{GeV}$	
$p_{\mathrm{T}}^{\ell,\mathrm{sublead}} > 30\,\mathrm{GeV}$		$p_{\mathrm{T}}^{\ell,\mathrm{sublead}} > 25\,\mathrm{GeV}$	
$\max(m_{\mathrm{T}}^{W}) > 50\,\mathrm{GeV}$		–	
Excluding VBF1J and VBF2J phase space		VBF1J phase space	VBF1J and VBF2J phase space

ground from the $m_h \simeq 125\,\mathrm{GeV}$ Higgs boson resonance and its off-shell component is included and its interference with the continuum WW background is taken into account.

7.1 Top quark background

Top quark events can be produced as a $t\bar{t}$ pair or as a single-top quark in association with a W boson or a quark of another flavour. In this analysis, contributions from $t\bar{t}$ and single-top quark events are estimated together, with their relative contributions determined by their predicted cross sections and by their relative acceptances obtained from MC simulation. The single-top-quark contribution varies from about 10% to 30% depending on the signal event category.

The top quark background for the quasi-inclusive ggF category is determined in a control region (Top $\mathrm{CR}_{\mathrm{ggF}}$) where one tagged b-jet is required in addition to all other selection conditions used in the signal region. A comparison of the common variables (with the cut on the variable removed once at a time) in the CR between data and MC is shown in Figure 7.2. The purity of the top quark background in this CR is high (97%) and thus allows to check any mis-modelling of MC simulation.

As can be seen in the top right plot of Figure 7.2, the distribution of the simulated leading lepton p_{T} in the Top $\mathrm{CR}_{\mathrm{ggF}}$ has been found to disagree with the data, with the data-over-MC ratio decreased as $p_{\mathrm{T}}^{\ell,\mathrm{lead}}$ increased. The reason of this mismodelling is thought to be due to the missing high order corrections. In order to fix this mis-modelling, an in-situ correction [8] (see Figure 7.3) was derived

[8] A correction from NLO to NNLO QCD has also been tried but is found to be not sufficient

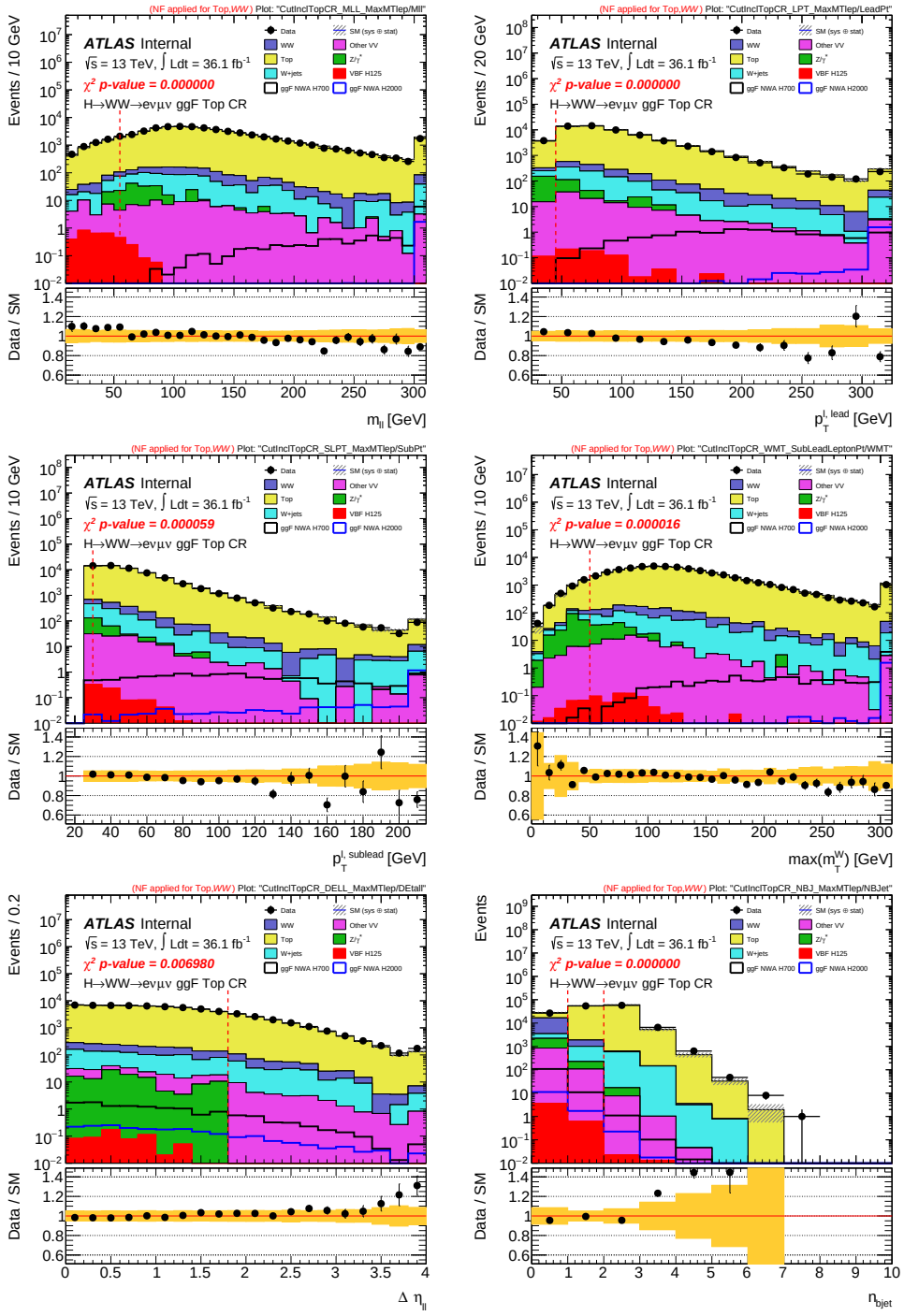

Figure 7.2: Comparison of data and MC in the ggF top-quark control region when one of these cuts is removed from the selection: $m_{\ell\ell}$ (top left), $p_{\mathrm{T}}^{\ell,\mathrm{lead}}$ (top right), $p_{\mathrm{T}}^{\ell,\mathrm{sublead}}$ (middle left), $\max(m_{\mathrm{T}}^{W})$ (middle right), $\Delta\eta_{\ell\ell}$ (bottom left), and $N_{b\text{-jet}}$ (bottom right). The hatched band in the upper panel and the shaded band in the lower panel show the combined statistical and experimental uncertainties on the predictions. The last bin contains the overflow. Normalisation factors obtained from a comparison of data and predictions have been applied in these figures. The red dashed vertical line indicates the cut value.

from a MC sample in a larger phase space (with the $p_{\mathrm{T}}^{\ell,\mathrm{lead}}$ cut relaxed from 45 GeV to 25 GeV and the $\Delta\eta_{\ell\ell}$ cut removed) instead of the ggF Top CR, by fitting the data-over-MC (only the shapes of data with non-top backgrounds subtracted and top quark background are compared) ratio with a linear function. The resulting correction function is then applied to the simulated top quark background events in the $\mathrm{SR}_{\mathrm{ggF}}$ and the corresponding CRs. The correction varies in the form of linear function between +4% and −10% as $p_{\mathrm{T}}^{\ell,\mathrm{lead}}$ increases from 50 GeV to 200 GeV. No such a mismodelling is observed in the VBF top CR (see Figure 7.6), maybe due to the limited statistics or the very different phase spaces.

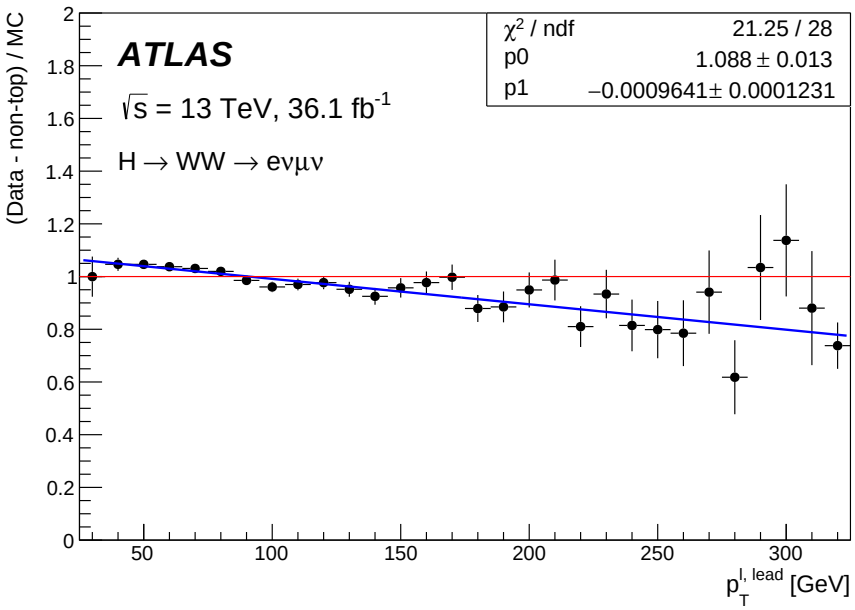

Figure 7.3: Fitted p_{T} correction for the leading lepton for top quark background events in a sample similar to the ggF top CR with the $p_{\mathrm{T}}^{\ell,\mathrm{lead}}$ cut relaxed from 45 GeV to 25 GeV and the $|\Delta\eta_{\ell\ell}|$ cut removed.

It has been checked that this correction is independent of the $e\mu$ and μe channels and whether the $\Delta\eta_{\ell\ell}$ cut is applied or not (see Table 7.2). That is also the reason why the correction can be applied in all the regions (the top CR, WW CR and SR) of the ggF category.

Figure 7.4 shows the same distributions as Figure 7.2 but after the correction. Better agreement between data and MC is observed in all the distributions.

The p_{T} correction has also been checked by comparing the m_{T} distributions before and after the correction. This is shown in Figure 7.5, where the normalization factors are determined from the CRs only and applied to the top and WW

to fix such a mis-modelling.

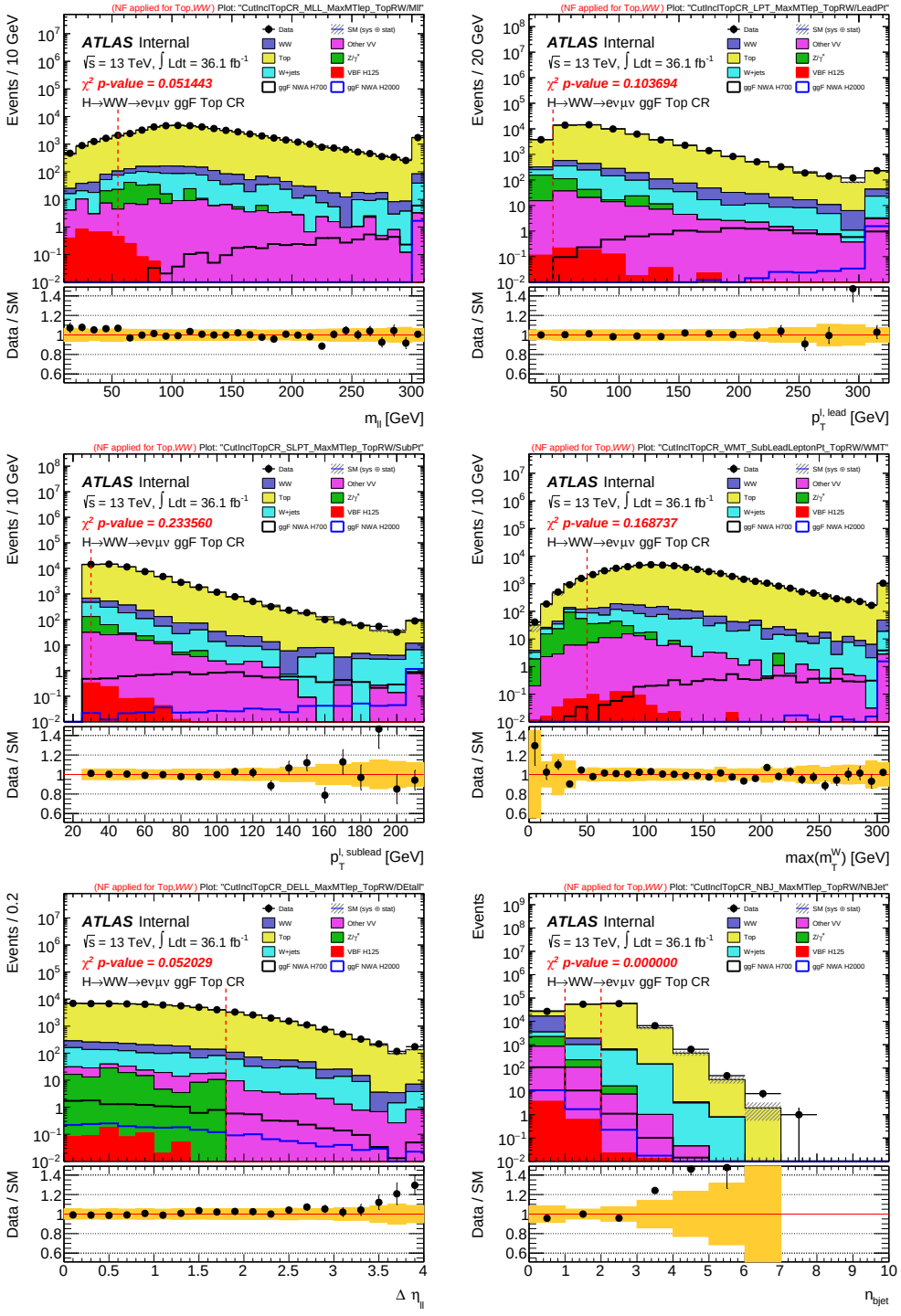

Figure 7.4: Same distributions as Figure 7.2 except that the p_{T} correction has been applied.

Table 7.2: Comparison of fitted parameters of the data and MC ratio as a function of the leading lepton p_{T} in a sample similar to the ggF top CR for different channels and with or without the $|\Delta\eta_{\ell\ell}|$ cut. The numbers in bold are used in the analysis.

Channel	p0	p1	χ^2/ndf
$\|\Delta\eta_{\ell\ell}\| > 1.8$			
$e\mu$	1.084 ± 0.020	$(-0.903 \pm 0.189) \times 10^{-3}$	15.09/28
μe	1.103 ± 0.020	$(-1.123 \pm 0.194) \times 10^{-3}$	28.61/28
$e\mu + \mu e$	1.091 ± 0.014	$(-0.981 \pm 0.136) \times 10^{-3}$	22.25/28
No $\|\Delta\eta_{\ell\ell}\|$ cut			
$e\mu$	1.082 ± 0.018	$(-0.892 \pm 0.173) \times 10^{-3}$	14.07/28
μe	1.098 ± 0.018	$(-1.091 \pm 0.176) \times 10^{-3}$	27.66/28
$\boldsymbol{e\mu + \mu e}$	$\mathbf{1.088 \pm 0.013}$	$\mathbf{(-0.964 \pm 0.123) \times 10^{-3}}$	**21.25/28**

backgrounds. An obvious improvement can be seen in the agreement between the data and MC after the correction.

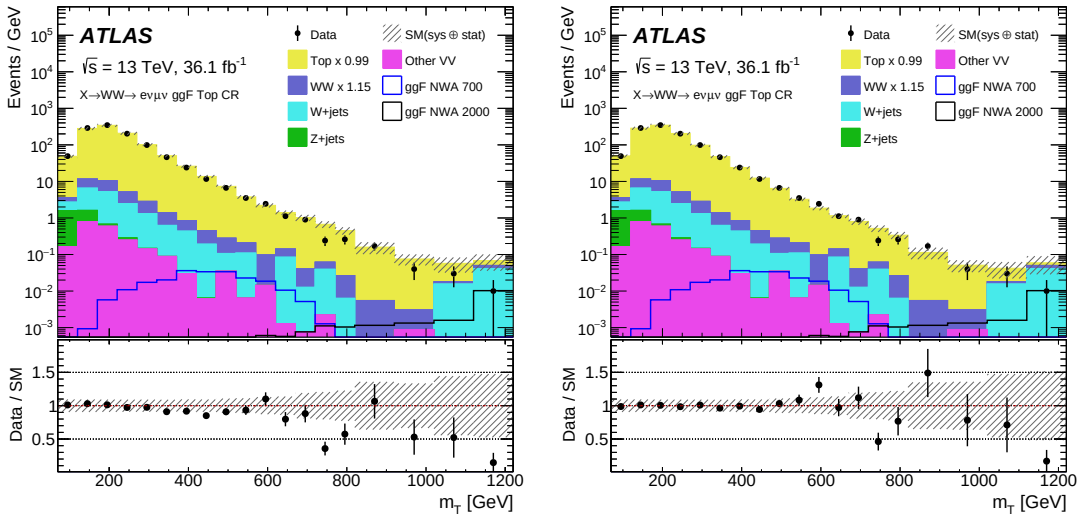

Figure 7.5: m_{T} distribution in the ggF top-quark control region before (left) and after (right) the leading lepton p_{T} correction. In each plot, the last bin contains the overflow. The hatched band in the upper and lower panels shows the combined statistical, experimental and theoretical uncertainties in the predictions. The top and WW backgrounds are scaled by the indicated normalisation factors that are determined from the corresponding CRs. The yields of signal events, which are normalised to the expected limits on $\sigma_H \times B(H \to WW)$, are shown for masses of 700 GeV and 2000 GeV in the NWA scenario.

The top quark background control regions for the VBF categories (Top $\mathrm{CR_{VBF}}$) have limited data statistics, so they are merged together by requiring at least one tagged b-jet. In addition, the selections on $p_{\mathrm{T}}^{\ell,\mathrm{lead}}$ and $p_{\mathrm{T}}^{\ell,\mathrm{sublead}}$ are both relaxed to 25 GeV, and the selection on $|\Delta\eta_{\ell\ell}|$, $m_{\ell\ell}$ and $\max(m_{\mathrm{T}}^{W})$ is also removed.

The comparison of data and MC for the common variables is shown in Figure 7.6. Similar comparisons for m_{jj} and Δy_{jj} are shown in Figure 7.7.

In this control region, the purity of the top quark background is 96%, without any mis-modelling of the $p_{\mathrm{T}}^{\ell,\mathrm{lead}}$ distribution observed.

The cutflow of the event yields in the CRs is shown in Table 7.3. Pre-fit normalisation factors (estimated by fitting MC to data in CRs only) are applied to the dominant top and WW backgrounds, while the other backgrounds that have small contributions use predictions from MC simulation.

The post-fit normalisation factors obtained from the simultaneous fit are 0.96 ± 0.05 and $1.12^{+0.13}_{-0.12}$ in the ggF and the VBF control regions, respectively, where the uncertainties quoted include both statistical and systematic errors.

Figure 7.8 shows the post-fit m_{T} distributions in the ggF and VBF top quark CRs. The different background components have been scaled according to the event yields obtained from the simultaneous fit. In the control regions, the fit uses only the integrated event yields. The m_{T} distributions for 700 GeV and 2 TeV NWA Higgs signals are also shown, normalised to the expected limits from this analysis on $\sigma_H \times \mathrm{BR}(H \to WW)$. The ggF contribution of the SM Higgs boson is included in the WW component, while the VBF contribution is negligibly small and is not shown in this and following figures.

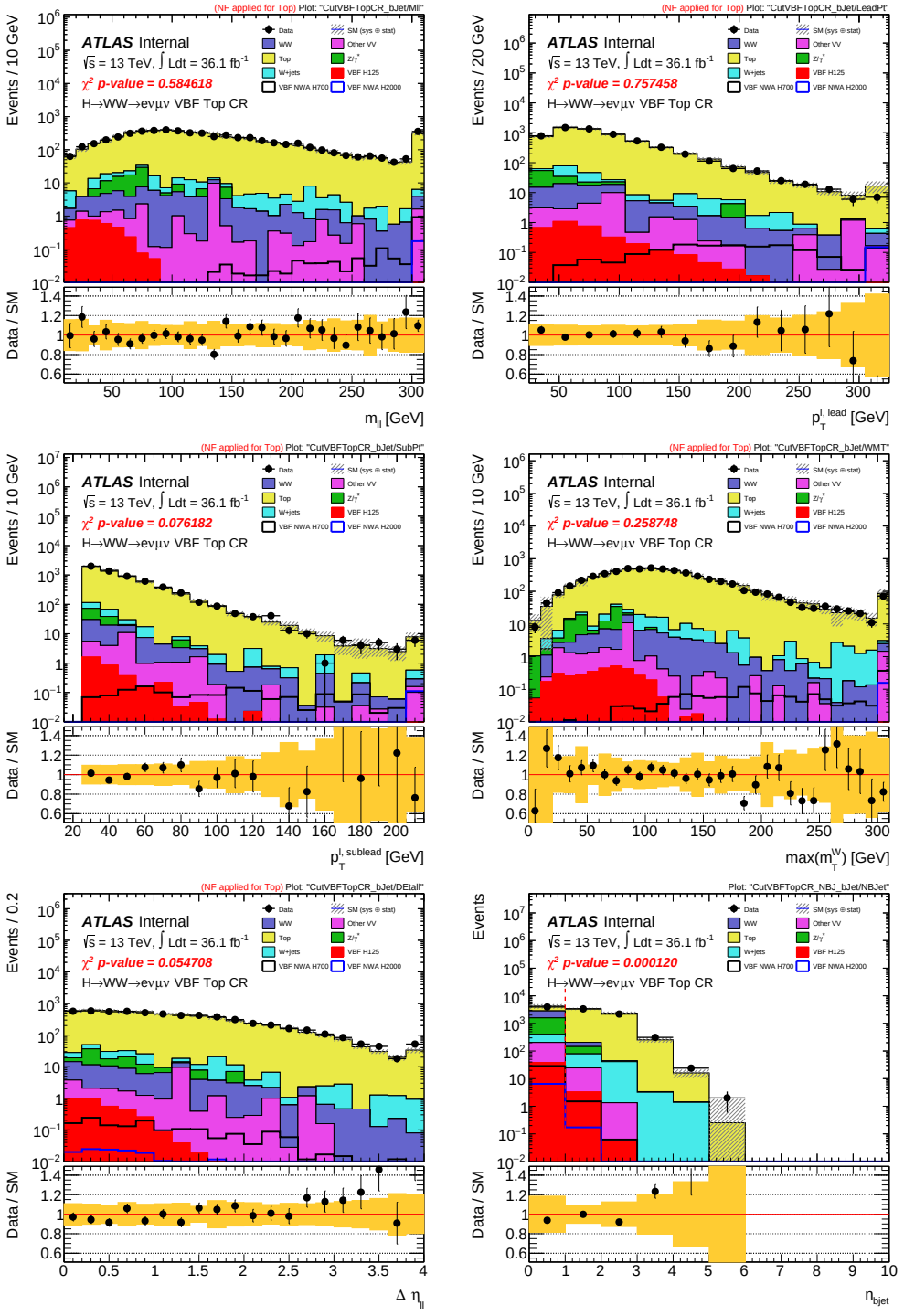

Figure 7.6: Comparison between data and MC in the VBF top-quark control region: $m_{\ell\ell}$ (top left), $p_{\mathrm{T}}^{\ell,\mathrm{lead}}$ (top right), $p_{\mathrm{T}}^{\ell,\mathrm{sublead}}$ (middle left), $\max(m_{\mathrm{T}}^{W})$ (middle right), $\Delta\eta_{\ell\ell}$ (bottom left), and $N_{b\text{-jet}}$ (bottom right). The hatched band in the upper panel as well as the shaded band in the lower panel shows the combined statistical and experimental uncertainties on MC. The last bin contains the overflow. Normalisation factors obtained from a comparison between data and predictions are also applied. The red dashed vertical line indicates the cut value.

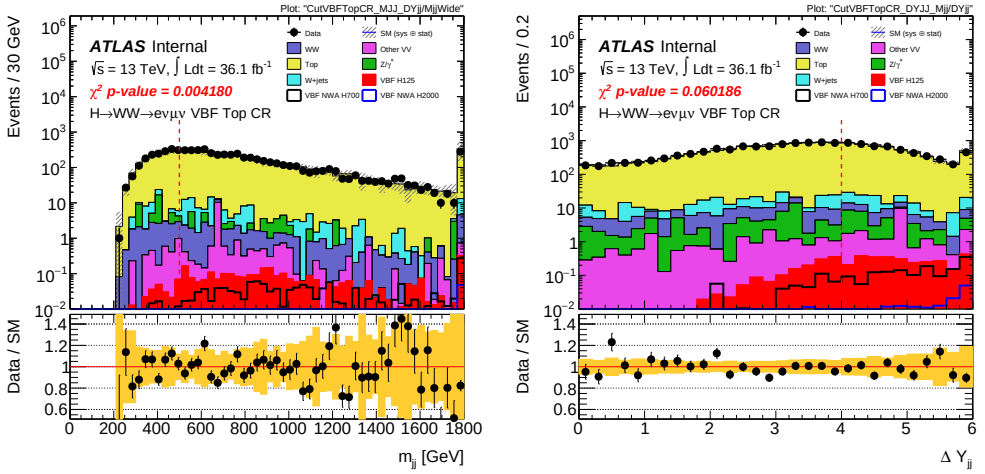

Figure 7.7: Comparison between data and MC in the VBF top-quark control region when one of the cuts is removed from the selection: m_{jj} (left) and Δy_{jj}. The hatched band in the upper panel as well as the shaded band in the lower panel shows the combined statistical and experimental uncertainties on MC. The last bin contains the overflow. Normalisation factors obtained from a comparison between data and predictions are also applied. The red dashed vertical line indicates the cut value.

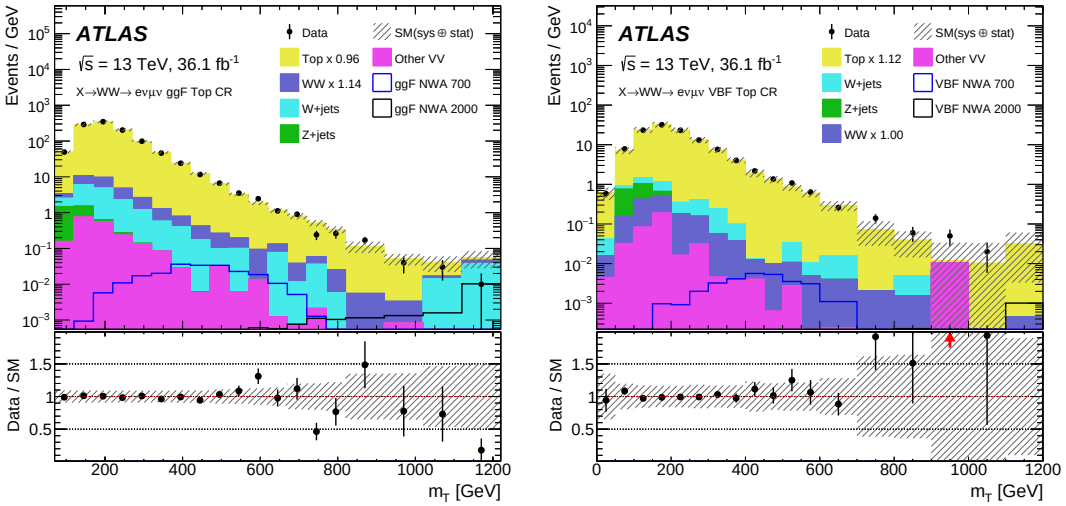

Figure 7.8: Post-fit m_{T} distributions in the quasi-inclusive ggF and VBF top quark control regions. The last bin contains the overflow. The hatched band in the upper panel as well as the shaded band in the lower panel shows the combined statistical and experimental uncertainties on MC. The top quark and WW backgrounds are scaled by the indicated normalisation factors that are obtained from the simultaneous fit to all SRs and CRs. The event yield of the heavy Higgs boson signal is normalised to the expected limits on $\sigma_H \times \mathrm{BR}(H \to WW)$, and is shown for masses of 700 GeV and 2 TeV, with an NWA lineshape.

Table 7.3: Cutflow table for different WW and top-quark CRs in various categories. The ggF and VBF heavy Higgs boson signal at 700 GeV is based on NWA samples. The quoted errors are statistical only. The pre-fit Normalisation Factor (NF) shown is applied to the entries of the following rows in the same column. The 1st, 2nd, 4th, 5th, 7th and 8th blocks correspond to the pre-selection level, W+jets CR, inclusive ggF WW CR, inclusive ggF top CR, VBF $N_{\text{jet}} = 1$ WW CR and VBF top CR, respectively. The event yields of the ggF and VBF signals at 700 GeV are normalised to the expected limits.

$\sqrt{s} = 13TeV$, $\mathcal{L} = 36.1fb^{-1}$,	H GGF [NWA, 700]	H VBF [NWA, 700]	VBF [125]	WW	Other VV	$t\bar{t}$	Single Top	Z/γ^*	W+jet (DD)	Total Bkg.	Data	Data/Bkg
Channel Selection	199.42 ± 1.31	58.38 ± 0.56	285.72 ± 1.45	48387.68 ± 84.54	42788.27 ± 192.89	401839.07 ± 396.52	39675.82 ± 84.28	211415.91 ± 1511.11	785026.10 ± 2617.52	1529418.56 ± 3056.73	1088505	0.71 ± 0.00
W+jets flavour split muon	199.42 ± 1.31	58.38 ± 0.56	285.72 ± 1.45	48387.68 ± 84.54	42788.27 ± 192.89	401839.07 ± 396.52	39675.82 ± 84.28	211415.91 ± 1511.11	785026.10 ± 2617.52	1529418.56 ± 3056.73	1088505	0.71 ± 0.00
W+jets flavour split electron	199.42 ± 1.31	58.38 ± 0.56	285.72 ± 1.45	48387.68 ± 84.54	42788.27 ± 192.89	401839.07 ± 396.52	39675.82 ± 84.28	211415.91 ± 1511.11	785026.10 ± 2617.52	1529418.56 ± 3056.73	1088505	0.71 ± 0.00
LWA width reweight	199.42 ± 1.31	58.38 ± 0.56	285.72 ± 1.45	48387.68 ± 84.54	42788.27 ± 192.89	401839.07 ± 396.52	39675.82 ± 84.28	211415.91 ± 1511.11	785026.10 ± 2617.52	1529418.56 ± 3056.73	1088505	0.71 ± 0.00
GRL Selection	199.42 ± 1.31	58.38 ± 0.56	285.72 ± 1.45	48387.68 ± 84.54	42788.27 ± 192.89	401839.07 ± 396.52	39675.82 ± 84.28	211415.91 ± 1511.11	718498.10 ± 2604.79	1462890.56 ± 3045.82	1048583	0.72 ± 0.00
Jet Cleaning	196.77 ± 1.30	54.88 ± 0.54	283.45 ± 1.44	48290.46 ± 84.45	42650.20 ± 192.63	400634.92 ± 395.79	39563.01 ± 84.13	210942.02 ± 1509.76	712868.94 ± 2601.39	1455233.00 ± 3042.14	1043528	0.72 ± 0.00
Trigger Selection	193.59 ± 1.29	53.96 ± 0.54	241.85 ± 1.33	43729.27 ± 80.64	31958.57 ± 151.18	367952.99 ± 379.65	36185.36 ± 79.87	141122.92 ± 1201.48	407049.03 ± 1900.74	1028239.98 ± 2288.28	817002	0.79 ± 0.00
Trigger Matching	193.34 ± 1.29	53.93 ± 0.54	236.09 ± 1.32	43004.35 ± 80.05	29352.51 ± 144.53	363150.32 ± 377.33	35754.50 ± 79.34	128716.72 ± 1143.61	380541.96 ± 1810.05	980756.44 ± 2181.77	785246	0.80 ± 0.00
Only two Leptons	192.91 ± 1.29	53.90 ± 0.54	235.86 ± 1.31	42985.95 ± 80.03	19839.36 ± 132.47	360563.79 ± 375.99	35594.88 ± 79.18	119262.41 ± 1090.70	382403.89 ± 1722.81	960886.14 ± 2080.70	763184	0.79 ± 0.00
$p_t^{lead} > 25$ GeV	192.91 ± 1.29	53.90 ± 0.54	235.40 ± 1.31	42935.05 ± 79.99	19738.74 ± 131.87	360328.44 ± 375.87	35571.78 ± 79.15	118306.69 ± 1086.41	378132.67 ± 1716.05	955248.76 ± 2072.79	760135	0.80 ± 0.00
$p_t^{sublead} > 25$	182.73 ± 1.26	50.89 ± 0.52	123.34 ± 0.96	30631.32 ± 67.61	8730.99 ± 78.07	258912.17 ± 320.60	24968.63 ± 65.19	36372.94 ± 610.20	84618.26 ± 1093.80	444357.64 ± 1298.63	392573	0.88 ± 0.00
OS Leptons	180.32 ± 1.25	50.31 ± 0.52	122.52 ± 0.96	30201.11 ± 67.25	4476.03 ± 54.36	256343.61 ± 319.06	24622.68 ± 64.60	34871.49 ± 589.51	58364.09 ± 1034.35	409001.53 ± 1237.28	373427	0.91 ± 0.00
$M_{\ell\ell} > 10$ GeV	180.31 ± 1.25	50.31 ± 0.52	116.93 ± 0.93	30092.49 ± 67.17	4300.75 ± 52.85	255439.64 ± 318.51	24529.93 ± 64.46	34692.01 ± 586.43	50614.23 ± 1027.02	399785.98 ± 1229.47	368496	0.92 ± 0.00
Leptons ID, W+jets 1 anti-ID,1 ID	173.62 ± 1.23	48.66 ± 0.51	101.38 ± 0.86	27434.53 ± 64.02	3308.03 ± 47.54	228933.97 ± 300.75	21992.93 ± 60.47	29779.70 ± 529.26	31476.19 ± 553.59	343026.74 ± 828.88	320763	0.94 ± 0.00
Apply fake factor	173.62 ± 1.23	48.66 ± 0.51	101.38 ± 0.86	27434.53 ± 64.02	3308.03 ± 47.54	228933.97 ± 300.75	21992.93 ± 60.47	29779.70 ± 529.26	8333.05 ± 207.81	319883.60 ± 650.98	320763	1.00 ± 0.00
Scale factors				NF $= 1.15 \pm 0.03$		NF $= 0.99 \pm 0.01$	NF $= 0.99 \pm 0.01$					
VBFVeto	153.62 ± 1.15	18.35 ± 0.31	59.70 ± 0.66	29935.97 ± 71.58	3123.23 ± 45.83	220580.16 ± 293.88	21119.92 ± 59.03	28521.37 ± 520.28	8043.56 ± 205.06	311383.91 ± 640.17	310937	1.00 ± 0.00
VBFVeto: b-veto	137.81 ± 1.08	16.57 ± 0.30	50.80 ± 0.61	28065.56 ± 69.76	2806.99 ± 43.56	16342.90 ± 76.49	4197.91 ± 25.41	26804.10 ± 509.08	4248.78 ± 177.06	82517.03 ± 551.16	79955	0.97 ± 0.01
Incl. WW CR: $\Delta\eta_{ll} > 1.8$	26.44 ± 0.48	3.13 ± 0.13	0.01 ± 0.01	5527.91 ± 33.68	480.16 ± 17.81	2977.16 ± 32.71	682.86 ± 10.37	276.57 ± 50.92	794.21 ± 27.82	10738.89 ± 77.43	10869	1.01 ± 0.01
Incl. WW CR: $M_{ll} > 55$ GeV	26.44 ± 0.48	3.13 ± 0.13	0.01 ± 0.01	5527.78 ± 33.68	480.16 ± 17.81	2977.16 ± 32.71	682.86 ± 10.37	276.57 ± 50.92	794.21 ± 27.82	10738.76 ± 77.43	10869	1.01 ± 0.01
Incl. WW CR: $p_T^{lead} > 45$ GeV	26.00 ± 0.48	3.10 ± 0.13	0.00 ± 0.00	4181.49 ± 29.84	337.99 ± 14.27	2563.53 ± 30.63	567.04 ± 9.35	47.06 ± 15.36	482.39 ± 21.46	8179.51 ± 53.07	8210	1.00 ± 0.01
Incl. WW CR: $p_T^{sub-lead} > 30$ GeV	24.69 ± 0.47	2.97 ± 0.13	0.00 ± 0.00	3615.35 ± 28.13	279.02 ± 12.04	2205.00 ± 28.51	481.72 ± 8.66	27.91 ± 12.23	347.25 ± 18.96	6956.26 ± 48.30	7034	1.01 ± 0.01
Incl. WW CR: $max(M_{\text{T}}^{\ell}) > 50$ GeV	24.28 ± 0.47	2.92 ± 0.13	0.00 ± 0.00	3403.41 ± 27.97	245.71 ± 11.26	2087.26 ± 27.84	453.06 ± 8.30	20.91 ± 10.02	304.67 ± 17.91	6515.01 ± 46.63	6515	1.00 ± 0.01
VBFVeto: $n_{b-jets} = 1$	13.90 ± 0.38	1.68 ± 0.11	8.07 ± 0.25	1698.39 ± 15.72	296.21 ± 13.72	85401.99 ± 180.08	12510.77 ± 45.81	1556.35 ± 113.58	2128.20 ± 71.97	103599.99 ± 230.31	105356	1.02 ± 0.00
Incl. Top CR: $\Delta\eta_{ll} < 1.8$	11.22 ± 0.35	1.38 ± 0.10	8.07 ± 0.25	1401.19 ± 14.07	252.38 ± 12.97	69710.53 ± 162.39	10472.18 ± 41.81	1543.98 ± 113.47	1749.68 ± 66.14	85138.02 ± 213.85	86102	1.01 ± 0.00
Incl. Top CR: $M_{ll} > 55$ GeV	11.22 ± 0.35	1.38 ± 0.10	1.30 ± 0.10	1164.82 ± 13.15	183.06 ± 10.30	59348.08 ± 150.35	8932.43 ± 38.73	1127.14 ± 105.61	1303.60 ± 58.46	72060.43 ± 197.37	72237	1.00 ± 0.00
Incl. Top CR: $p_T^{lead} > 45$ GeV	11.19 ± 0.35	1.38 ± 0.10	1.02 ± 0.09	1025.32 ± 11.91	148.29 ± 9.18	54244.08 ± 144.07	8260.05 ± 37.28	428.68 ± 64.33	1075.24 ± 50.10	65182.68 ± 170.35	65094	1.00 ± 0.00
Incl. Top CR: $p_T^{sub-lead} > 30$ GeV	10.94 ± 0.34	1.34 ± 0.10	0.81 ± 0.08	911.75 ± 11.29	123.50 ± 7.59	48239.33 ± 135.94	7311.88 ± 35.05	287.42 ± 56.23	859.16 ± 44.81	57733.86 ± 158.32	57506	1.00 ± 0.00
Incl. Top CR: $max(M_{\text{T}}^{\ell}) > 50$ GeV	10.88 ± 0.34	1.32 ± 0.10	0.62 ± 0.07	850.19 ± 10.92	106.45 ± 7.13	45593.36 ± 131.96	6848.71 ± 33.71	118.01 ± 20.77	777.67 ± 43.22	54295.01 ± 144.98	54295	1.00 ± 0.01
Scale factors						NF $= 0.98 \pm 0.02$	NF $= 0.98 \pm 0.02$					
VBFLike	20.00 ± 0.43	30.31 ± 0.40	41.68 ± 0.55	1312.40 ± 14.06	184.80 ± 12.66	6260.59 ± 49.39	671.00 ± 10.23	1258.34 ± 97.08	289.49 ± 33.70	10018.28 ± 116.03	9826	0.98 ± 0.02
VBFLike: b-veto	18.70 ± 0.41	28.72 ± 0.39	38.29 ± 0.52	1243.51 ± 13.77	165.65 ± 11.10	1066.57 ± 19.41	273.18 ± 6.42	1191.30 ± 94.60	191.41 ± 29.29	4169.92 ± 102.66	3937	0.94 ± 0.03
Scale factors				NF $= 0.92 \pm 0.13$		NF $= 0.98 \pm 0.02$	NF $= 0.98 \pm 0.02$					
VBFLike: $n_{jets} = 1$	12.54 ± 0.35	9.04 ± 0.23	9.44 ± 0.26	894.61 ± 11.94	117.11 ± 9.68	428.67 ± 12.43	191.88 ± 5.48	984.39 ± 90.59	143.77 ± 26.06	2769.88 ± 96.47	2649	0.96 ± 0.04
VBF WW CR 1J: $\Delta\eta_{ll} > 1.8$ OR $M_{ll} < 55$ GeV	1.51 ± 0.11	1.33 ± 0.08	7.68 ± 0.23	273.59 ± 5.97	40.70 ± 7.06	103.44 ± 6.12	45.64 ± 2.74	76.23 ± 25.45	46.73 ± 10.04	594.00 ± 29.65	594	1.00 ± 0.06
VBF Top CR: $n_{b-jets} \geq 1$	1.33 ± 0.12	1.56 ± 0.10	3.35 ± 0.18	65.39 ± 2.93	22.43 ± 9.42	5233.00 ± 46.46	400.54 ± 8.09	65.92 ± 24.29	98.38 ± 16.48	5889.00 ± 56.42	5889	1.00 ± 0.02

7.2 WW background

The same selection are used in the WW CR for the quasi-inclusive ggF category (WW $\mathrm{CR_{ggF}}$) as for the SR, except for the cut on $|\Delta\eta_{\ell\ell}|$ which is reversed so that the CR and SR are orthogonal. The selection conditions are shown in Table 7.1.

The m_{T} distributions of the $q\bar{q} \to WW$ Sherpa MC sample in the $\mathrm{SR_{ggF}}$ and WW $\mathrm{CR_{ggF}}$ are compared with the corresponding predictions at generator level, by combining the NNLO QCD calculations using the Matrix package [118] with the NLO electroweak (EW) corrections [119]. Whilst the integrated yields of the distributions agree within up to 3% in both the $\mathrm{SR_{ggF}}$ and the WW $\mathrm{CR_{ggF}}$, a small m_{T} shape difference is still observed in particular in the SR. The m_{T} distributions are thus corrected through a reweighting to the combined NNLO QCD and NLO EW predictions for the Sherpa MC samples. More details could be found in Appendix E.

For the $gg \to (h^*) \to WW$ process, in which the SM 125 GeV Higgs boson is off-shell, it is modelled at LO using the Sherpa generator with a k-factor of 1.7. The k-factor is used to account for higher-order cross-section corrections. An uncertainty of 60% has been assigned, following the studies in Refs. [120–123]. This k-factor of 1.7 is actually applied on top of another recommended k-factor of 0.91 for Sherpa diboson samples to account for a different EW scheme with regard to that in the Powheg diboson samples[124].

A comparison of the distributions for the common variables, but with the cut on the variable removed once at a time, between data and MC in the CR is presented in Figure 7.9.

The post-fit normalisation factor that is obtained from the simultaneous fit to data for the WW contributions in the quasi-inclusive ggF categories is 1.14 ± 0.09. The uncertainty quoted here includes both statistical and systematic uncertainties. The purity of the WW background in the control region after the simultaneous fit is 51%.

In order to increase the data statistics, the WW CR for the $N_{\mathrm{jet}} = 1$ VBF category (WW $\mathrm{CR_{VBF1J}}$) uses a slightly different selection (shown in Table 7.1) from the one in the SR, but still orthogonal to the SR. The normalisation factor obtained from the same simultaneous fit for the WW contribution in the WW $\mathrm{CR_{VBF1J}}$ is 1.0 ± 0.2, where the uncertainty quoted includes the full statistical and systematic error. The post-fit purity of the WW background in the control region is 44%.

The comparison of the distributions between data and MC for the common

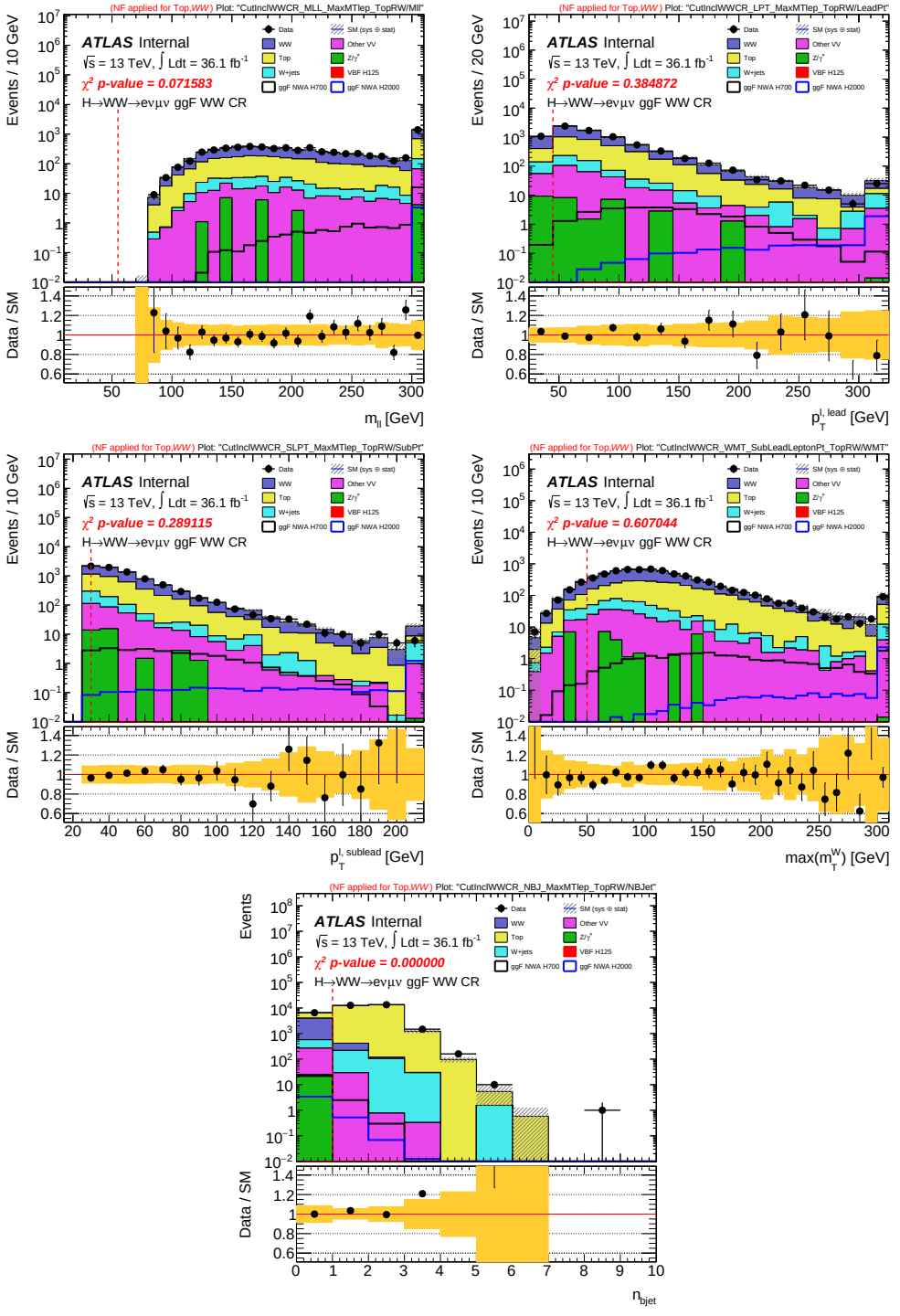

Figure 7.9: Comparison of distributions between data and MC in the ggF WW CR where one of these cuts is removed from the selection: $m_{\ell\ell}$ (top left), $p_{\mathrm{T}}^{\ell,\mathrm{lead}}$ (top right), $p_{\mathrm{T}}^{\ell,\mathrm{sublead}}$ (middle left), $\max(m_{\mathrm{T}}^{W})$ (middle right) and $N_{b\text{-jet}}$ (bottom). The hatched band in the upper panel as well as the shaded band in the lower panel shows the combined statistical and experimental uncertainties on MC. The last bin contains the overflow. Normalisation factors obtained from a comparison between data and predictions are also applied. The red dashed vertical line indicates the cut value.

variables in this CR is shown in Figure 7.10.

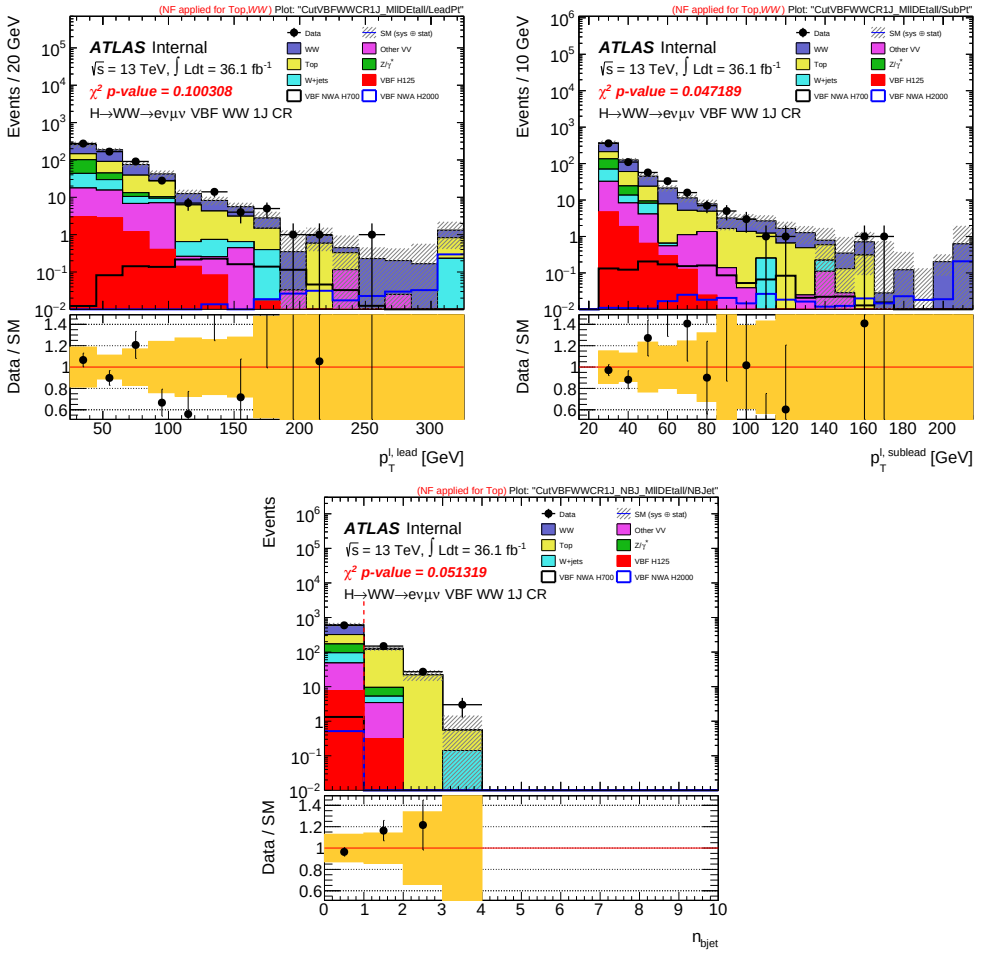

Figure 7.10: Comparison of distributions between data and MC in the VBF 1-jet WW CR: $p_{\mathrm{T}}^{\ell,\mathrm{lead}}$ (top left), $p_{\mathrm{T}}^{\ell,\mathrm{sublead}}$ (top right) and $N_{b\text{-jet}}$ (bottom), where the cut is removed for $N_{b\text{-jet}}$. The hatched band in the upper panel as well as the shaded band in the lower panel shows the combined statistical and experimental uncertainties on MC. The last bin contains the overflow. Normalisation factors obtained from a comparison between data and predictions are also applied. The red dashed vertical line indicates the cut value.

The contribution of the WW background in the $N_{\mathrm{jet}} \geq 2$ VBF category is small (approximately 20%). Its prediction is taken from simulation, since it is difficult to isolate a kinematic region with a sufficient number of WW events without a large contamination from the top quark background.

As with the top quark backgrounds, the cutflow of the pre-fit event yields for this CR is also shown in Table 7.3.

Figure 7.11 shows the post-fit m_{T} distributions in the WW $\mathrm{CR}_{\mathrm{ggF}}$ and $\mathrm{CR}_{\mathrm{VBF1J}}$. The different backgrounds are scaled to the event yields that are obtained from the simultaneous fit. As with the top quark control regions, only the

integrated event yields of the WW control regions are used in the fit.

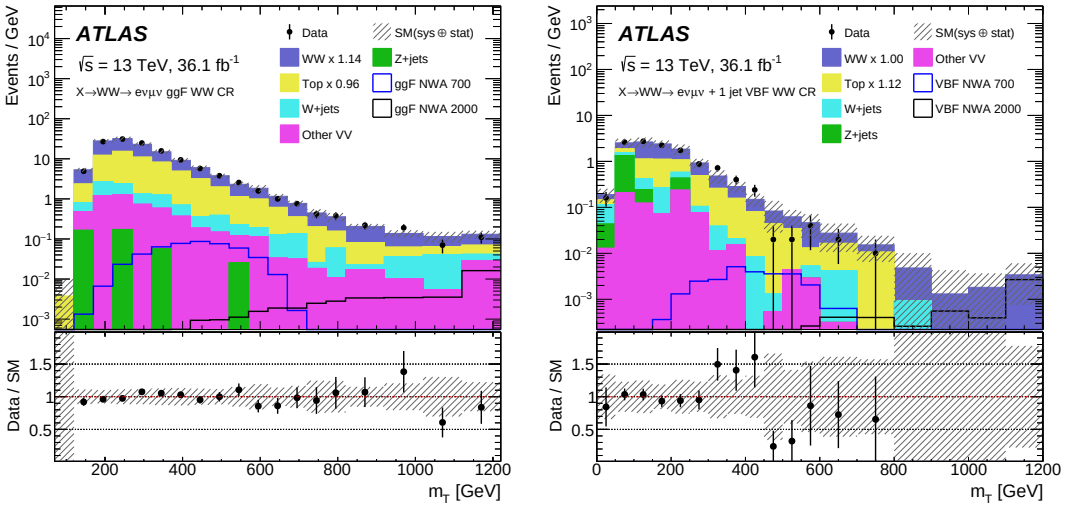

Figure 7.11: Post-fit m_{T} distributions in the quasi-inclusive ggF and $N_{\mathrm{jet}} = 1$ VBF WW control regions. The last bin contains the overflow. The hatched band in the upper panel as well as the shaded band in the lower panel shows the combined statistical and experimental uncertainties on MC. The top quark and WW backgrounds are scaled by the indicated normalisation factors that are obtained from the simultaneous fit to all SRs and CRs. The event yield of the heavy Higgs boson signal is normalised to the expected limits on $\sigma_H \times \mathrm{BR}(H \to WW)$, and is shown for masses of 700 GeV and 2 TeV, with an NWA lineshape.

7.3 W+jets background

Production of W bosons in association with jets may enter the SR when a jet is misidentified as a lepton. Due to the difficulties in accurately modelling the misidentification process in simulation, the W+jets background contribution is estimated using the fake-factor (FF) based data-driven method developed for the SM $H \to WW$ analysis [116]. The estimation uses a sample of events satisfying all event selection criteria, except one of the two lepton candidates fails to meet the quality criteria for "fully identified" leptons but satisfies a less restrictive selection (denoted as "anti-identified"). These selection criteria are listed in Table 7.4.

The anti-identified sample is orthogonal to the identified sample and has loosened isolation and impact parameter (likelihood identification) criteria for muons (electrons). From this data sample the non-W+jets contribution, dominated by top quark and WW backgrounds, is subtracted based on MC predictions. The W+jet purity of the samples is 46%, 59% and 22% for the quasi-inclusive ggF, $N_{\mathrm{jet}} = 1$ and $N_{\mathrm{jet}} \geq 2$ VBF categories, respectively.

Table 7.4: The requirements for fully identified and anti-identified leptons.

Id electron	Anti-id electron	Id muon	Anti-id muon
$p_{\mathrm{T}} > 15$ GeV		$p_{\mathrm{T}} > 15$ GeV	
$\lvert\eta\rvert < 2.47$,excluding $1.37 < \lvert\eta\rvert < 1.52$		$\lvert\eta\rvert < 2.45$	
$\lvert z_0 \sin\theta\rvert < 0.5$ mm		$\lvert z_0 \sin\theta\rvert < 0.5$ mm	
Pass LHTight if $p_{\mathrm{T}} < 25$ GeV Pass LHMedium if $p_{\mathrm{T}} > 25$ GeV	Pass LHLoose	Pass Quality Tight if $p_{\mathrm{T}} < 25$ GeV Pass Quality Medium if $p_{\mathrm{T}} > 25$ GeV	
$\lvert d_0\rvert/\sigma(d_0) < 5$		$\lvert d_0\rvert/\sigma(d_0) < 3$	$\lvert d_0\rvert/\sigma(d_0) < 6$
Pass Gradient isolation	Veto against identified electron	Pass Gradient Isolation	Veto against identified muon

The W+jets contamination in the signal region is determined by scaling the number of events in the selected data sample by the fake-factor, an extrapolation factor, which is measured in a data sample of di-jet events. The di-jet sample is collected with prescaled low-p_{T} single lepton triggers. Events are selected with exactly one fake candidate object, back-to-back with the leading jet. The electroweak processes in the di-jet event sample, dominated by W+jets and Z/γ^* background contributions, are subtracted. The fake-factor is the ratio of the number of fully identified leptons to the number of anti-identified leptons, measured in bins of lepton p_{T} and η. The estimation of W+jets background can be expressed by the following equation:

$$\begin{aligned} N_{\text{id+id}}^{W+\text{jets}} &= N_{\text{id+anti-id}}^{W+\text{jets}} \times \text{FF} \\ &= (N_{\text{id+anti-id}} - N_{\text{id+anti-id}}^{\text{EW}}) \times \frac{N_{\text{id}}}{N_{\text{anti-id}}}\,, \end{aligned} \tag{7.1}$$

where $N_{\text{id+anti-id}}^{W+\text{jets}}$ is the number of events in the selected data sample, $N_{\text{id+anti-id}}$ and $N_{\text{id+anti-id}}^{\text{EW}}$ correspond to the number of data events and the EW background contribution that is subtracted from the data, and $\frac{N_{\text{id}}}{N_{\text{anti-id}}}$ is the definition of the FF, a ratio of the number of fully identified leptons to the number of anti-identified leptons.

The measured fake-factors are applied to the anti-id lepton in the W+jets control sample. Most of the time the anti-id lepton is softer, not triggered lepton in the event. To measure a suitable fake-factor for these anti-id leptons a data sample collected using the low-p_{T} single-lepton prescaled trigger (`HLT_e12_lhvloose_nod0_L1EM10VH` for electrons and `HLT_mu14_L1_MU10` for muons) is used. The corresponding fake-factors are called "nominal" fake-factors and are shown in Figure 7.12. The original p_{T} distributions of the fully identified and anti-identified leptons before the EW background subtraction are shown in Figure 7.13. When the p_{T} of the anti-id lepton is sufficiently high, it can be that the anti-id lepton in the W+jets control sample is the only lepton which fires one of the un-prescaled single-lepton triggers used by the analysis, listed in Table 4.1.

The relative fraction of the two samples in the W+jets control sample is 92% and 8%. If the nominal fake-factor is applied to this latter event sample, a small trigger bias is introduced in the W+jets background estimation. To avoid this trigger bias, separate fake-factors are extracted using a data set from the di-jet events triggered by the un-prescaled triggers mentioned above. These fake-factors are called "triggered" fake-factors and are shown in Figure 7.14. The difference between these two sets of fake-factors are expected given the different isolation requirements used in the prescaled and un-prescaled triggers. Also the triggered fake-factors are period dependent as the triggers have changed from one period to another (see Table 4.1).

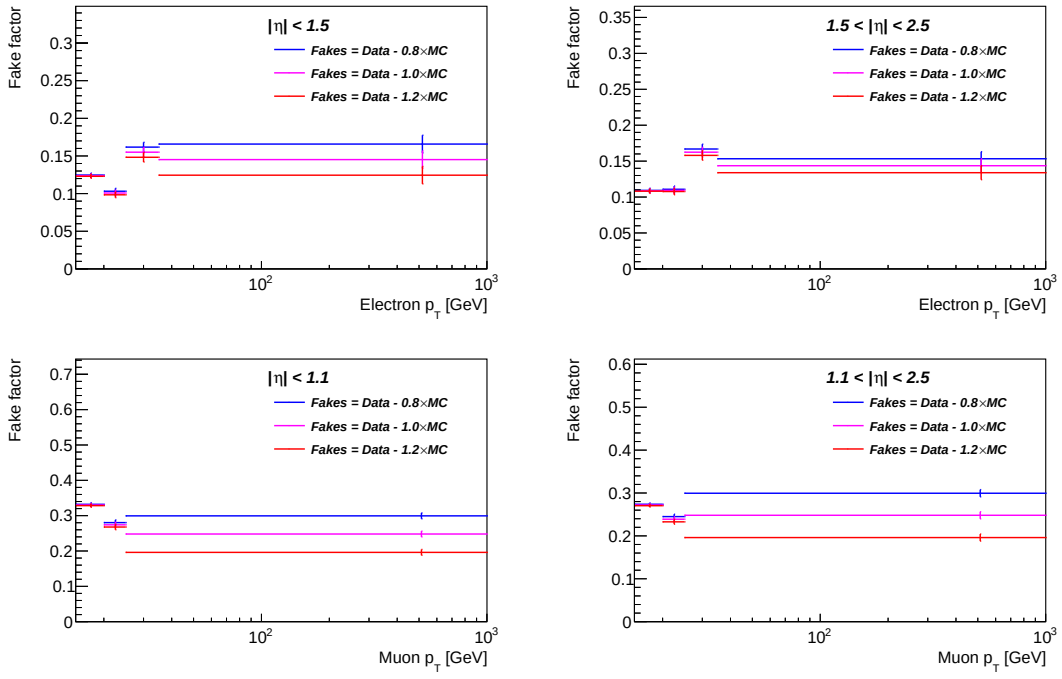

Figure 7.12: Nominal fake-factors (data points in magenta) determined from fake-enriched di-jet samples in data for electrons (top) and muons (bottom) and in central (left) and forward (right) regions. The blue and red lines correspond to variations of the fake-factors by scaling the electroweak subtraction by ±20%. The error bars show the statistical uncertainty of the corresponding data samples.

A closure test has also been performed by comparing the W+jets MC prediction with the corresponding estimation using the fake-factor method. The MC prediction is based on the selection with two fully identified leptons and the fake-factor estimation is obtained by applying the fake-factors determined with the same MC sample to an event sample selected with one fully identified lepton and one anti-identified lepton. The comparison results are shown in Table 7.5 and

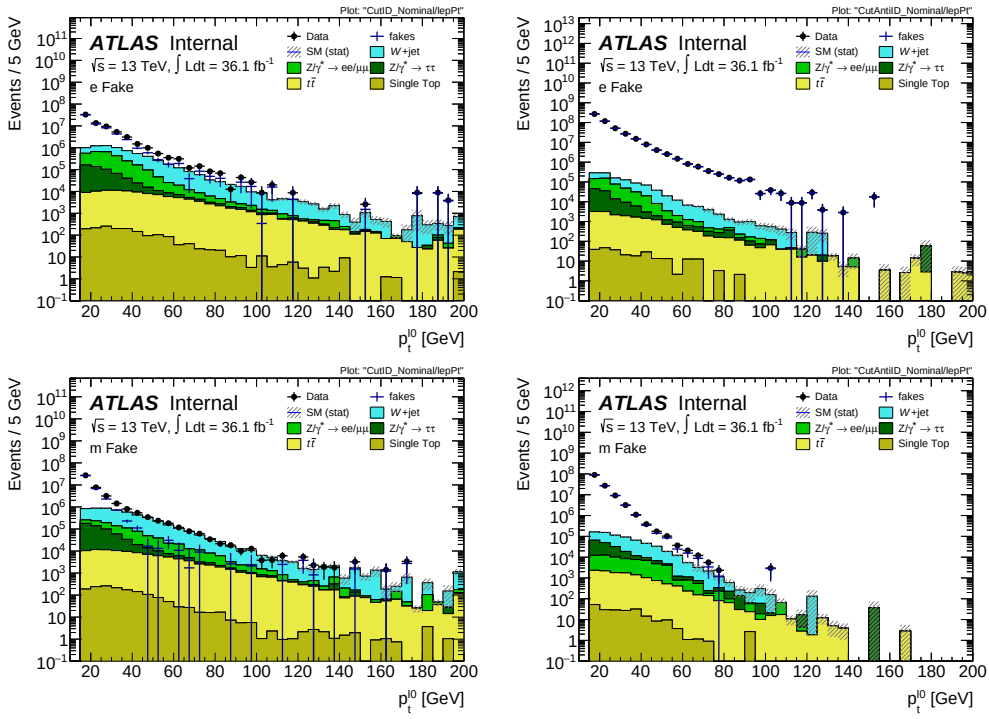

Figure 7.13: Distributions of p_{T} of fully identified (left) and anti-identified (right) electrons (top) and muons (bottom) selected from di-jet events in data for determining the nominal fake-factors.

Figure 7.15. The statistics of the W+jets is very limited in particular in the VBF phase space. However, agreement is observed within the limited statistical precision.

Table 7.5: Comparison of the W+jets estimation based on the fake-factor method with the corresponding MC prediction at the pre-selection level and in different SRs. The uncertainties of the event yields are statistical only.

Category	FF estimation	MC prediction
Pre-selection	4857 ± 285	4756 ± 130
ggF SR	742 ± 104	656 ± 47
VBF $N_{\mathrm{jet}} = 1$ SR	73 ± 53	29 ± 20
VBF $N_{\mathrm{jet}} \geq 2$ SR	0	1.8 ± 1.3

The fake-factor method has also been applied to a different event sample in which all the cuts are identical to the nominal analysis except that the charge of the two leading leptons is the same (so-called the Same-Sign (SS) sample). In this sample, the W+jets background is one of the leading background contributions as it is shown in Figure 7.16 at the pre-selection level (left) and a region similar to the quasi-inclusive ggF signal region (right). Agreement between data and background

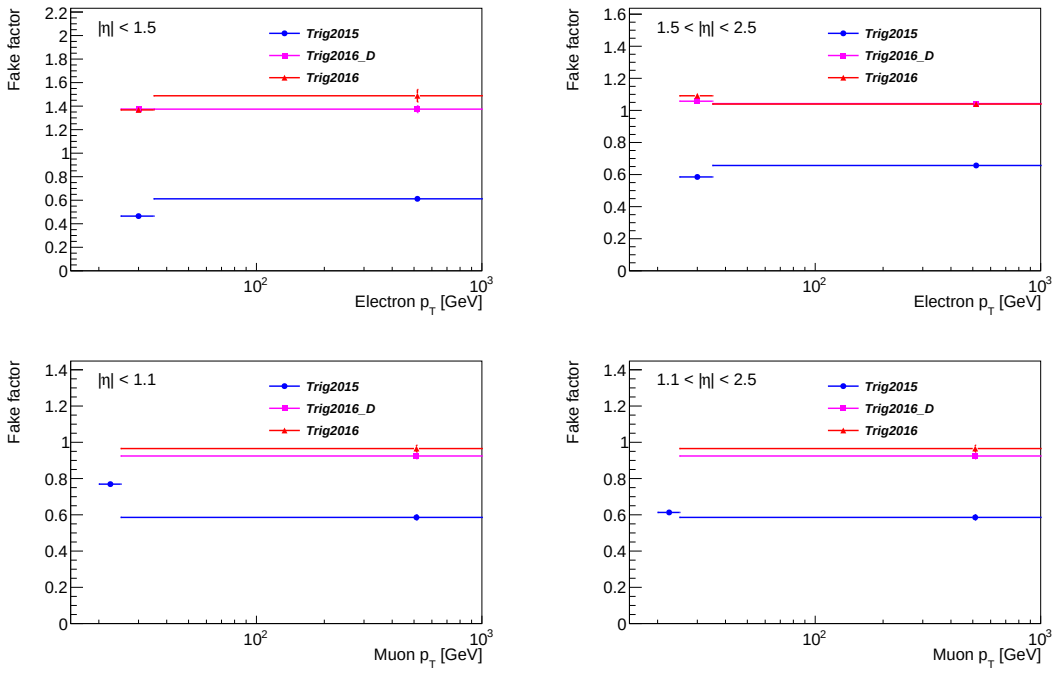

Figure 7.14: Triggered fake-factors determined from fake-enriched di-jet samples in data for electrons (top) and muons (bottom) and in central (left) and forward (right) regions. The blue, magenta and red points correspond to different periods of data taking. The error bars show the statistical uncertainty of the corresponding data samples.

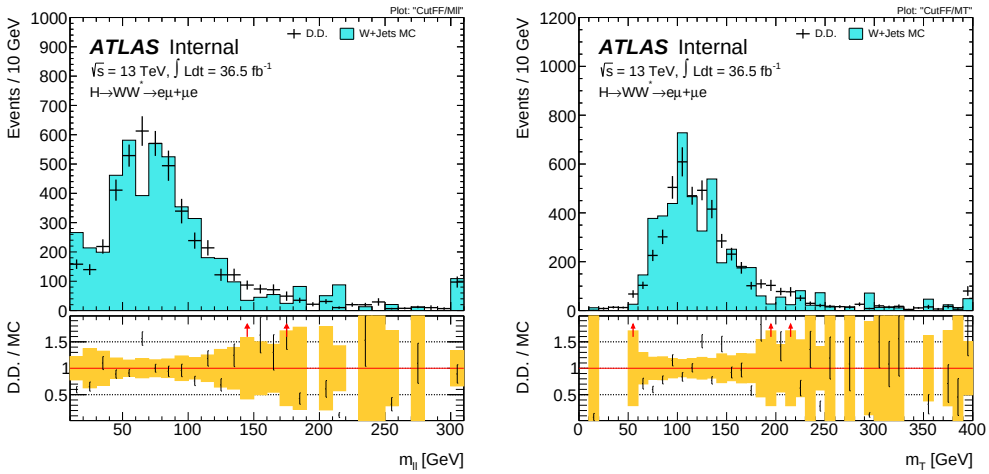

Figure 7.15: Distributions of $m_{\ell\ell}$ (left) and m_{T} (right) for the estimation obtained with the fake-factor method (data points) and the corresponding MC prediction (histogram) at the pre-selection level. The error bands in the lower plots correspond to the statistical uncertainty of the W+jets MC sample.

contributions provides a nontrivial validation of the fake-factor method.

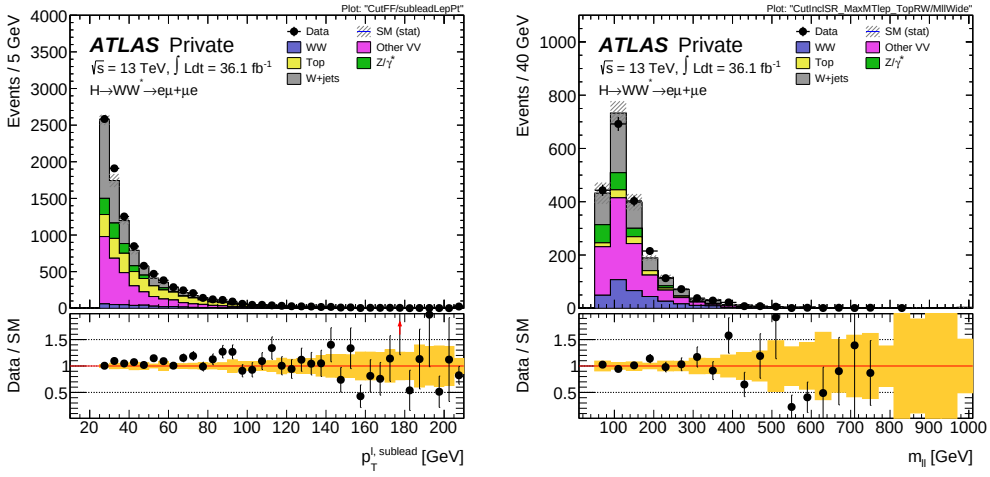

Figure 7.16: Comparison of the same-sign data sample with the corresponding background contributions at the pre-selection level for $p_{\mathrm{T}}^{\ell,\mathrm{sublead}}$ (left) and in a region similar to the quasi-inclusive ggF signal region for $m_{\ell\ell}$ (right). The hatched band in the upper panel and the shaded band in the lower panel show the statistical uncertainty only on the background predictions.

The dominating systematic uncertainty on the W+jets estimation originates from sample composition differences between the di-jets and W+jets samples. All systematic uncertainties associated to this background estimate are discussed in Section 8.8.

Chapter 8

Systematic uncertainties

In this section, experimental and theoretical uncertainties of the backgrounds and the signals are described. An overview of these uncertainties is presented in Section 8.1. More detailed studies about the experimental and theoretical uncertainties on the top quark and WW backgrounds and signals, as well as the uncertainties on the data-driven W+jets backgrounds are discussed in the Sections 8.2-8.8.

8.1 Overview

Both the experimental and theoretical uncertainties include two kinds of uncertainties that are studied and applied in the analysis: the normalisation uncertainty and the shape uncertainty of the m_{T} distribution. As for the shape uncertainty, unless explicitly discussed in this section, most of the shape uncertainties are very small and therefore neglected in the analysis. The normalisation uncertainty is considered as the relative difference in the integrated event yields between the nominal and alternative MC samples. The experimental uncertainty is treated by varying the parameters of one source of uncertainty at a time, and then re-running the full analysis. The theoretical uncertainty includes generally uncertainties due to the choice of generator and parton shower modelling, QCD renormalisation and factorisation scales, PDF model used to evaluate the cross section and acceptance, etc.

In the analysis, the variation of μ_R and μ_F is used to estimate the uncertainties due to missing higher order corrections. The mostly used method is called 7-point scale variations, i.e. pairwise variations of

$$\{\mu_R, \mu_F\} \times \{0.5, 0.5\}, \{1, 0.5\}, \{0.5, 1\}, \{1, 1\}, \{2, 1\}, \{1, 2\}, \{2, 2\}. \tag{8.1}$$

If a 7-point variation is not available, a 3-point variation with the scales varied simultaneously can be used:

$$\{\mu_R, \mu_F\} \times \{0.5, 0.5\}, \{1, 1\}, \{2, 2\}\,, \tag{8.2}$$

which should in general lead to larger variations than the independent variation of μ_R and μ_F.

The estimation of PDF uncertainty can usually be done in three different ways depending on what PDF set is used in the nominal samples:

Symmetric Hessian: e.g. CTEQ66. The idea is that each PDF has n (uncorrelated) eigenvalues and hence each eigenvalue can be varied independently by $+/-1\sigma$ to create a new PDF. The uncertainty is given by

$$\Delta X = \frac{1}{2}\sqrt{\sum_i (X_{i+} - X_{i-})^2} \tag{8.3}$$

if variations are provided as pairs, or

$$\Delta X = \sqrt{\sum_i (X_i - X_0)^2} \tag{8.4}$$

if provided as single values, where X_0 is the central value and X_i corresponds to the variation of the i-th eigenvalue, with X_{i+} and X_{i-} corresponding to the $+/-1\sigma$ variation.

Asymmetric Hessian: e.g. CT10 and MSTW. The idea is similar to the Symmetric Hessian method, but if the $+/-1\sigma$ variations are in the same direction, the largest is used:

$$\Delta X_+ = \sqrt{\sum_i \max(0, X_{i+} - X_0, X_{i-} - X_0)^2} \tag{8.5}$$

and

$$\Delta X_- = \sqrt{\sum_i \max(0, X_0 - X_{i+}, X_0 - X_{i-})^2} \tag{8.6}$$

Standard deviation: e.g. NNPDF. The NNPDF set does not provide a set of error PDFs. Instead of a central value and some error PDFs with eigenvalues varied they provide an ensemble of PDFs, which is made from fits to the ensemble test on the input data. In that way, the best value would be

the mean value of all the ensembles and the uncertainty is the standard deviation:

$$\Delta X = \sqrt{\frac{1}{N}\sum_i (X_i - X_0)^2} \tag{8.7}$$

where X_0 is the central value or the mean value, and N, the number of ensembles, is usually 100 for NNPDF.

The uncertainty on the integrated luminosity is 2.1% for the 2015 dataset, 2.2% for the 2016 dataset, and 2.1% for the 2015 + 2016 combined dataset. The estimation of the luminosity uncertainties follows a methodology similar to that described in Ref. [125], from a calibration of the luminosity scale using $x - y$ beam-separation scans performed in August 2016 and May 2016.

For both signals and backgrounds, the dominant experimental uncertainties are found to arise from the jet energy scale and resolution (Jet) [109], the b-tagging efficiency (b-tag) [111], and the pile-up modelling [110]. Sources of experimental uncertainties, such as trigger efficiency, lepton reconstruction and identification efficiencies, lepton momentum scale and resolution [106, 126], missing transverse momentum reconstruction [114] and jet vertex tagger [110], are also considered in the analysis (see Sections 8.2, 8.3, 8.4 and 8.8 for the experimental uncertainties for top, WW, signal and W+jets, respectively). The uncertainty that is associated with pile-up modelling is estimated by performing a variation of ±9% in the number of simulated pile-up interactions which covers the uncertainty in the ratio of the predicted and measured cross sections of non-diffractive inelastic events that produce a hadronic system of mass $m_{X,\text{had}} > 13\,\text{GeV}$ [127].

The dominant uncertainties, including both experimental and theoretical uncertainties, for the top and WW backgrounds are summarised in Tables 8.2 and 8.2. Systematic uncertainties from lepton identification efficiencies, momentum and scale resolutions, are found to be approximately 1%, and thus not shown in the tables. But they, as well as the other sources with very small uncertainties, are all included in the total uncertainty as shown in the last column in the tables. The correlation between the SRs and CRs is also taken into account in the simultaneous fit.

For the top-quark background, the uncertainties arised from the event generator and parton shower modelling (ME+PS) are estimated by comparing the nominal Powheg-Box+Pyhtia8 generated samples with the samples generated by an alternative event generator, Sherpa 2.2.1. The uncertainty which is named "Scale" in Table 8.2, corresponds to the variations of the renormalisation

Table 8.1: Relative impact (in %) of the dominant experimental and theoretical uncertainties in the event yields for the top-quark background in the three SRs (SR_{ggF}, SR_{VBF1J} and SR_{VBF2J}) and the top-quark and WW CRs (Top $CR_{ggF/VBF}$ and the WW $CR_{ggF/VBF1J}$). Jet and b-tag are the dominant sources of the experimental uncertainty, while ME+PS, Scale, Single top and PDF are the dominant theoretical uncertainties. The last column corresponds to the total uncertainty including those not listed here.

Source	Jet	b-tag	ME+PS	Scale	Single top	PDF	Total
SR_{ggF}	5.2	17	1.3	3.0	4.2	2.5	19
SR_{VBF1J}	9.6	7.8	1.0	1.6	5.9	2.6	15
SR_{VBF2J}	9.7	14	9.5	5.0	2.1	3.4	21
Top CR_{ggF}	2.2	4.8	0.34	0.21	2.6	3.0	6.6
WW CR_{ggF}	5.3	18	1.1	6.3	4.0	3.2	20
Top CR_{VBF}	8.2	3.5	10	1.5	1.3	3.7	14
WW CR_{VBF1J}	9.9	8.3	9.4	3.9	5.3	2.7	18

Table 8.2: Relative impact (in %) of the dominant experimental and theoretical uncertainties in the event yields for the WW background in the three SRs (SR_{ggF}, SR_{VBF1J} and SR_{VBF2J}) and the top-quark and WW CRs (Top $CR_{ggF/VBF}$ and the WW $CR_{ggF/VBF1J}$). Jet and Pile-up are the dominant sources of the experimental uncertainty, while ME+PS, μ_R, Resummation and PDF are the dominant theoretical uncertainties. The last column corresponds to the total uncertainty including those not listed here.

Source	Jet	Pile-up	ME+PS	μ_R	Resummation	PDF	Total
SR_{ggF}	1.2	1.8	2.4	1.7	3.1	2.7	5.5
SR_{VBF1J}	17	2.8	11	7.3	5.0	2.3	23
SR_{VBF2J}	18	3.1	38	18	1.4	2.1	47
WW CR_{ggF}	1.1	1.8	2.6	0.95	2.9	3.6	5.9
WW CR_{VBF1J}	16	4.5	12	11	2.3	2.8	23

μ_{R} and factorisation μ_{F} scales, as well as the variations of h_{damp}. The variations for μ_{R} and μ_{F} are from 0.5 to 2 with regard to the nominal scale of $\sqrt{m_{\mathrm{top}}^2 + p_{\mathrm{T}}^2}$, where p_{T} is the transverse momentum of the top quark. The parameter h_{damp} is varied between m_{top} and $2 \cdot m_{\mathrm{top}}$ from the nominal scale $h_{\mathrm{damp}} = 1.5 \cdot m_{\mathrm{top}}$. Since the single-top-quark and $t\bar{t}$ processes are studied together in the analysis, an uncertainty of 20% [128, 129] is assigned to the relative contribution of the single-top-quark processes, which corresponds to the source "Single top" in the table. The PDF uncertainty for the top-quark background is estimated by taking the envelope of the uncertainty of the NNPDF30NLO PDF set and the differences of its central value with the CT14 [36] and MMHT 2014 [38] PDF sets, following the recommendations of Ref. [35]. The PDF uncertainties are m_{T} dependent, increased from 2% to 10% as a function of m_{T} (see Figure 8.1 in Section 8.5). This m_{T} dependence is taken into account in the signal regions. In the ggF quasi-inclusive category, two additional shape systematic uncertainties (see Section 8.5) that are associated with the scale variations and the leading lepton p_{T} reweighting for the top-quark background are applied, the latter corresponding to $\pm 50\%$ of the reweighting correction. These two uncertainties are comparable, varying from a few percent at low m_{T} to about 10% at $m_{\mathrm{T}} \simeq 1\,\mathrm{TeV}$, without affecting the integrated event yield of the top-quark background in the category.

For the WW background, the ME+PS modelling uncertainty is obtained by comparing the nominal sample generated by Sherpa 2.2.1 with the alternative sample generated by Powheg-Box+Pythia8. The renormalisation, factorisation and resummation scales are varied separately by factors of 0.5 and 2.0. The factorisation scale uncertainty is very small, compared to the other uncertainties and thus not shown in the table. The PDF uncertainty is obtained and treated in the same way as for the top-quark background (see Figure 8.3 in Section 8.6). An additional shape uncertainty in the m_{T} distribution from ME+PS is applied in the ggF quasi-inclusive category, varied from a few percent at low m_{T} to about 20% at $m_{\mathrm{T}} \simeq 1\,\mathrm{TeV}$. There is no significant shape uncertainty observed in the VBF categories. In addition to the scale uncertainties described above, a relative uncertainty of $\pm 50\%$ is assigned to the correction of the $q\bar{q} \to WW$ Sherpa sample to the combined NNLO QCD and NLO EW predictions in the ggF SR and WW CR. Both the scale and the $q\bar{q} \to WW$ reweighting uncertainties are further discussed in Section 8.6. Besides, as discussed in Section 7.2, an uncertainty of 60% [120–123] is assigned to the high order cross section k-factor (1.7) for the $gg \to (h^*) \to WW$ process.

For the other background processes that have small contributions to the yields,

such as WZ, ZZ, Z/γ^*+jets and WW in the $N_{\text{jet}} \geq 2$ VBF category, the uncertainties in their yields due to the uncertainties in the predictions are evaluated with the same prescription as described above. The impact of these uncertainties is small (see Tables 9.2 and 9.3 in Chapter 9).

For the theoretical uncertainties in the signal acceptance, effects due to the choice of QCD renormalisation and factorisation scales and the PDF set, as well as the underlying-event modelling, parton shower model and parton shower tune are all considered. These uncertainties are estimated separately in three event categories, as a function of the resonance mass, independently for ggF- and VBF-induced resonances. To estimate the uncertainty associated to the missing high-order corrections in QCD, the renormalisation and factorisation scales are varied independently by factors of 0.5 and 2.0 from the nominal scale, $\sqrt{m_H^2 + p_{\text{T},H}^2}$, where m_H is the mass and $p_{\text{T},H}$ is the transverse momentum of the heavy Higgs boson. The signal acceptance obtained using the modified MC samples are then compared to the nominal sample. The uncertainties for resonances produced via ggF are found to be negligible in the quasi-inclusive ggF and $N_{\text{jet}} = 1$ VBF categories, whilst in the $N_{\text{jet}} \geq 2$ VBF category the uncertainties range between 2.5% and 0.2% with the resonance mass varied from 200 GeV to 4 TeV (unless stated otherwise, the uncertainties shown in the following are quoted for the same mass range). The uncertainties for resonances produced via vector-boson fusion are found to be ranged from 0.9% to 2.8% in the quasi-inclusive ggF category, from 1.9% to 3.6% in the $N_{\text{jet}} = 1$ VBF category, and from 1.0% to 7.3% in the $N_{\text{jet}} \geq 2$ VBF category. The PDF-induced uncertainties in the signal acceptance are estimated in the same way as that for the top-quark and WW background. The corresponding uncertainties for the ggF-induced (VBF-induced) signal, are found to be up to 0.4% (1.7%), 1.5% (1.2%) and 1.6% (1.5%) for the quasi-inclusive ggF, $N_{\text{jet}} = 1$ and $N_{\text{jet}} \geq 2$ VBF event categories, respectively. To estimate the uncertainties associated to the parton shower tune and underlying event, the internal parameters that are associated with final-state radiation or the multiple parton interactions in the Pythia generator are varied independently, up or down, such that their influence on the signal acceptance of the various signal mass points can be studied separately. In each event category, and for every mass point, the uncertainties are compared with that due to the choice of the parton shower model, which are estimated by comparing the results obtained for the nominal parton shower generator with those obtained using the alternative one with Herwig++ [130, 131]. The tune uncertainties are not considered in the final results, due to the fact that they are found to be very small compared with the shower

uncertainties for all mass points. The shower uncertainties for ggF-induced signals are found to increase from 1.3% to 3.1% for increasing resonance masses in the quasi-inclusive ggF category, from 13% to 28% in the $N_{\text{jet}} = 1$ category, and from 2.3% to 15% in the $N_{\text{jet}} \geq 2$ VBF category. The uncertainties for VBF-induced signals increase from 4.3% to 19%, from 5.1% to 9.0%, and from 3.3% to 8.0% in the three categories, respectively. The uncertainties due to missing high-order corrections in QCD are also evaluated for ggF-induced processes in each event category, with the event migration effects between different event categories considered. The method that is used for the estimation of the corresponding uncertainties is proposed by Stewart and Tackmann [132]. The resulting uncertainties associated to this are found to be ranged from 3% to 10% for the quasi-inclusive ggF category and from 4% to 30% (30%−60%) for the $N_{\text{jet}} = 1$ ($N_{\text{jet}} \geq 2$) VBF event categories. More details about the signal theoretical uncertainty are presented in Section 8.7.

For the estimation of the data-driven W+jets background, there are several sources of systematic uncertainty. The subtraction of the subdominant electroweak processes (Section 7.3) is found to have a significant impact on the calculation of the extrapolation factor at high lepton p_{T}. As described in Ref. [116], the subtraction is varied. The variation of the event yields in the SR is taken as the uncertainty, assuming that the extrapolation factors of the dijet and W+jets samples are the same. An additional systematic uncertainty source is introduced due to the differences in the jet flavour composition between dijet and W+jets events. This uncertainty is taken to be the sum of two contributions in quadrature: one corresponds to the differences between the extrapolation factors that are calculated with dijet samples and Z+jets samples in data, while the other corresponds to the differences between the extrapolation factors estimated with W+jets and Z+jets MC samples. The statistical uncertainties of the different data and MC samples that are used to estimate the extrapolation factors are taken as another source of systematic uncertainty. The overall relative systematic uncertainty of the W+jets background is finally found to be approximately 35% in each categorie. The dominant uncertainty is found to be associated to the jet flavour composition.

8.2 Experimental uncertainties on top quark background

In this section (and the following sections) the experimental uncertainty is studied and presented in terms of the uncertainty sources in two parts: one af-

fecting the scale and resolution of the reconstructed objects ("four-momentum" uncertainty), one affecting the efficiency corrections ("scale-factor" uncertainty).

The four-momentum experimental uncertainties for the top quark background in the quasi-inclusive ggF category and VBF categories are presented in Tables 8.3 and 8.4, respectively. Similarly, the scale-factor experimental uncertainties are presented in Tables 8.5 and 8.6. The quantity α corresponds to the extrapolation uncertainties from the top or WW CR to the SR, while β corresponds to the extrapolation from the top CR to the WW CR. The various sources that are presented in the tables, as well as the following tables in this thesis, are discussed in Appendix F. The uncertainty originating from the limited MC statistics in the various regions is also added in the tables for comparison.

Table 8.3: Relative experimental uncertainties in % related to the lepton, jets and missing transverse energy scale and resolution on the top quark background in the ggF quasi-inclusive SR (2nd column), the corresponding WW CR (3rd column) and top-quark CR (4th column) and on the transfer factors from the top-quark CR to the SR (5th column) and from the top-quark CR to the WW CR (last column). The two uncertainty values in each column represent the up and down variations. The row labeled "Total" is the squared sum of all sources, where the largest variation is taken for each parameter. The uncertainty originating from the limited MC statistics in each region is also shown for comparison.

Source	SRIncl	WWCRIncl	TopCRIncl	$\alpha = N_{\text{SRIncl}}/N_{\text{topCRIncl}}$	$\beta = N_{\text{WWCRIncl}}/N_{\text{topCRIncl}}$
EG_RESOLUTION_ALL	+0.02 +0.01	+0.04 +0.03	+0.02 −0.00	+0.01 +0.02	+0.02 +0.03
EG_SCALE_ALLCORR	−0.06 +0.07	−0.07 +0.11	−0.06 +0.08	+0.00 −0.01	−0.01 +0.03
EG_SCALE_E4SCINTILLATOR	+0.00 +0.00	−0.00 +0.00	+0.00 +0.00	−0.00 −0.00	−0.00 −0.00
EG_SCALE_LARCALIB_EXTRA2015PRE	+0.00 +0.01	−0.02 −0.01	−0.01 +0.01	+0.01 −0.00	−0.01 −0.02
EG_SCALE_LARTEMPERATURE_EXTRA2015PRE	+0.00 +0.00	−0.00 −0.00	+0.00 +0.00	−0.00 −0.00	−0.00 −0.00
EG_SCALE_LARTEMPERATURE_EXTRA2016PRE	+0.00 +0.00	−0.00 −0.00	+0.00 +0.00	−0.00 −0.00	−0.00 −0.00
MUON_ID	+0.03 +0.02	−0.06 −0.09	+0.00 +0.03	+0.02 −0.01	−0.06 −0.12
MUON_MS	+0.01 +0.00	+0.01 −0.05	−0.01 +0.01	+0.02 −0.00	+0.02 −0.06
MUON_SCALE	+0.06 −0.06	+0.05 −0.11	+0.04 −0.04	+0.01 −0.01	+0.01 −0.07
JET_BJES_Response	+0.56 −0.01	+0.64 −0.07	+0.16 +0.01	+0.40 −0.01	+0.48 −0.08
JET_EffectiveNP_1	+1.88 −1.63	+1.88 −1.57	+0.77 −0.78	+1.11 −0.86	+1.11 −0.80
JET_EffectiveNP_2	−0.46 +0.46	−0.46 +0.55	−0.19 +0.23	−0.27 +0.23	−0.27 +0.33
JET_EffectiveNP_3	+0.09 −0.07	+0.06 −0.07	+0.04 −0.04	+0.04 −0.03	+0.01 −0.02
JET_EffectiveNP_4	−0.04 +0.07	−0.06 +0.06	−0.03 +0.03	−0.01 +0.04	−0.03 +0.04
JET_EffectiveNP_5	+0.05 −0.02	+0.04 −0.03	+0.02 −0.02	+0.03 −0.00	+0.02 −0.01
JET_EffectiveNP_6	−0.03 +0.02	−0.01 +0.01	−0.00 +0.01	−0.02 +0.01	−0.01 −0.00
JET_EffectiveNP_7	−0.03 +0.04	−0.04 +0.04	−0.02 +0.02	−0.01 +0.02	−0.02 +0.01
JET_EffectiveNP_8restTerm	+0.05 −0.03	+0.01 −0.04	+0.02 −0.02	+0.03 −0.01	−0.00 −0.02
JET_EtaIntercalibration_Modelling	+0.60 −0.67	+0.70 −0.62	+0.33 −0.31	+0.27 −0.36	+0.37 −0.31
JET_EtaIntercalibration_NonClosure	+0.03 −0.04	+0.10 −0.09	+0.04 −0.03	−0.01 −0.02	+0.06 −0.06
JET_EtaIntercalibration_TotalStat	+0.31 −0.28	+0.35 −0.29	+0.15 −0.15	+0.16 −0.13	+0.20 −0.14
JET_Flavor_Composition	+1.06 −2.50	+1.27 −2.65	+0.86 −1.28	+0.20 −1.24	+0.41 −1.39
JET_Flavor_Response	−0.79 +0.32	−0.80 +0.43	−0.36 +0.23	−0.43 +0.09	−0.44 +0.20
JET_JER_SINGLE_NP	+2.80	+2.68	+0.97	+1.81	+1.69
JET_Pileup_OffsetMu	−0.27 +0.22	−0.09 +0.15	−0.08 +0.09	−0.20 +0.13	−0.02 +0.05
JET_Pileup_OffsetNPV	+0.35 −0.21	+0.29 −0.08	+0.16 −0.14	+0.19 −0.07	+0.12 +0.06
JET_Pileup_PtTerm	−0.18 +0.19	−0.19 +0.11	−0.03 +0.05	−0.15 +0.14	−0.16 +0.06
JET_Pileup_RhoTopology	+2.75 −2.27	+2.86 −2.24	+1.16 −1.07	+1.57 −1.21	+1.68 −1.19
JET_PunchThrough_MC15	+0.00 +0.00	−0.00 +0.00	+0.00 +0.00	+0.00 −0.00	−0.00 +0.00
JET_RelativeNonClosure_MC15	+0.00 +0.00	−0.00 −0.00	+0.00 +0.00	−0.00 −0.00	−0.00 −0.00
JET_SingleParticle_HighPt	+0.00 +0.00	−0.00 −0.00	+0.00 +0.00	−0.00 −0.00	−0.00 −0.00
MET_JetTrk_Scale	+0.00 +0.00	−0.00 −0.00	+0.00 +0.00	−0.00 −0.00	−0.00 −0.00
MET_SoftTrk_ResoPara	−0.04	−0.11	−0.02	−0.02	−0.09
MET_SoftTrk_ResoPerp	+0.03	+0.06	+0.01	+0.02	+0.06
MET_SoftTrk_Scale	+0.03 −0.04	+0.05 −0.03	+0.01 −0.02	+0.02 −0.02	+0.04 −0.01
Total	±5.21	±5.30	±2.22	±3.03	±3.11
MC Stat.	±0.53	±1.14	±0.26	±0.59	±1.17

The shape uncertainties for the top quark background from the experimental

Table 8.4: Relative experimental uncertainties in % related to the lepton, jets and missing transverse energy scale and resolution on the top quark background in the VBF SRs (2nd and 3rd columns), the corresponding WW CR (4th column) and top-quark CR (5th column) and on the transfer factors from the top-quark CR to the SRs (6th and 7th columns) and from the top-quark CR to the WW CR (last column). The two uncertainty values in each column represent the up and down variations. The two uncertainty values in each column represent the up and down variations. The row labeled "Total" is the squared sum of all sources, where the largest variation is taken for each parameter. The uncertainty originating from the limited MC statistics in each region is also shown for comparison.

Source	SRVBF1J	SRVBF2J	WWCRVBF1J	TopCRVBF	α_VBF1J = $\frac{N_{\text{SRVBF1J}}}{N_{\text{TopCRVBF}}}$	α_VBF2J = $\frac{N_{\text{SRVBF2J}}}{N_{\text{TopCRVBF}}}$	$\beta = \frac{N_{\text{WWCRVBF1J}}}{N_{\text{TopCRVBF}}}$
EG_RESOLUTION_ALL	+0.11 −0.01	−0.47 +0.15	−0.56 +0.08	−0.03 −0.02	+0.15 +0.01	−0.43 +0.17	−0.53 +0.10
EG_SCALE_ALLCORR	−0.01 +0.00	−0.00 −0.04	−0.20 −0.07	−0.14 +0.08	+0.13 −0.07	+0.14 −0.12	−0.06 −0.15
EG_SCALE_E4SCINTILLATOR	+0.00 +0.00	−0.00 −0.00	+0.00 −0.00	−0.01 −0.00	+0.01 +0.00	+0.01 −0.00	+0.01 +0.00
EG_SCALE_LARCALIB_EXTRA2015PRE	−0.00 −0.01	+0.00 −0.00	+0.00 +0.07	−0.04 +0.01	+0.04 −0.02	+0.05 −0.01	+0.05 +0.05
EG_SCALE_LARTEMPERATURE_EXTRA2015PRE	+0.00 +0.00	−0.00 −0.00	−0.00 −0.00	−0.00 −0.00	+0.00 +0.00	−0.00 −0.00	+0.00 +0.00
EG_SCALE_LARTEMPERATURE_EXTRA2016PRE	+0.00 +0.00	−0.00 −0.00	−0.00 −0.00	−0.00 −0.00	+0.00 +0.00	−0.00 −0.00	+0.00 +0.00
MUON_ID	+0.11 +0.02	−0.09 −0.17	−0.31 −0.47	+0.01 −0.02	+0.10 +0.04	−0.09 −0.15	−0.32 −0.45
MUON_MS	+0.05 +0.02	+0.02 −0.28	−0.16 −0.23	+0.01 −0.04	+0.04 +0.07	+0.00 −0.24	−0.17 −0.18
MUON_SCALE	+0.00 −0.05	+0.09 −0.21	+0.22 −0.17	+0.02 −0.03	−0.02 −0.02	+0.07 −0.18	+0.20 −0.14
JET_BJES_Response	+1.48 −0.62	+0.97 +0.12	+1.74 −1.02	+0.49 −0.71	+0.98 +0.10	+0.48 +0.84	+1.25 −0.31
JET_EffectiveNP_1	+2.44 −1.58	−0.25 +0.50	+2.43 −3.43	−0.74 +0.76	+3.20 −2.32	+0.49 −0.26	+3.19 −4.16
JET_EffectiveNP_2	−0.29 +0.40	−0.07 +0.59	−0.74 +0.46	+0.03 −0.09	−0.32 +0.50	−0.10 +0.69	−0.77 +0.56
JET_EffectiveNP_3	+0.01 −0.16	−0.05 −0.13	+0.16 −0.26	+0.13 −0.08	−0.12 −0.08	−0.18 −0.05	+0.03 −0.18
JET_EffectiveNP_4	−0.10 −0.02	−0.19 −0.01	+0.03 −0.06	−0.10 +0.15	+0.00 −0.18	−0.09 −0.16	+0.13 −0.21
JET_EffectiveNP_5	−0.01 −0.05	+0.11 −0.15	−0.26 +0.06	+0.09 −0.10	−0.10 +0.04	+0.02 −0.05	−0.36 +0.16
JET_EffectiveNP_6	+0.13 +0.03	−0.04 +0.07	−0.12 −0.27	−0.05 +0.04	+0.17 −0.00	+0.00 +0.03	−0.07 −0.30
JET_EffectiveNP_7	−0.01 +0.01	−0.19 −0.03	−0.08 +0.01	−0.04 +0.05	+0.03 −0.04	−0.14 −0.08	−0.04 −0.05
JET_EffectiveNP_Rest Term	+0.06 −0.09	−0.12 −0.02	+0.16 −0.21	−0.06 +0.07	+0.13 −0.16	−0.06 −0.09	+0.23 −0.28
JET_EtaIntercalibration_Modelling	−3.40 +3.86	−5.09 +5.02	−1.99 +2.55	−4.52 +4.37	+1.17 −0.49	−0.60 +0.62	+2.64 −1.74
JET_EtaIntercalibration_NonClosure	−1.14 +1.79	−1.62 +1.65	−1.93 +1.57	−0.93 +0.93	−0.21 +0.85	−0.70 +0.71	−1.01 +0.63
JET_EtaIntercalibration_TotalStat	−0.15 +0.34	−0.54 +0.94	+0.64 +0.10	−0.68 +0.75	+0.54 −0.41	+0.14 +0.18	+1.33 −0.65
JET_Flavor_Composition	+0.12 −0.18	−6.43 +4.77	−1.51 −3.09	−5.18 +5.24	+5.59 −5.15	−1.32 −0.45	+3.86 −7.92
JET_Flavor_Response	+0.86 −0.50	+0.90 −2.19	−0.56 +0.33	+1.65 −1.67	−0.77 +1.19	−0.74 −0.53	−2.17 +2.03
JET_JER_SINGLE_NP	+6.47	+3.23	+6.22	+3.10	+3.27	+0.13	+3.03
JET_Pileup_OffsetMu	+2.06 +0.05	+0.53 −0.81	+0.10 +0.38	+0.75 −0.84	+1.30 +0.90	−0.21 +0.03	−0.64 +1.23
JET_Pileup_OffsetNPV	+1.25 +0.58	−0.58 +0.42	−0.67 −0.23	−0.36 +0.29	+1.62 +0.28	−0.22 +0.12	−0.31 −0.52
JET_Pileup_PtTerm	−0.50 +0.83	−1.61 +1.86	+0.32 +0.24	−1.37 +1.15	+0.88 −0.31	−0.24 +0.71	+1.72 −0.90
JET_Pileup_RhoTopology	+4.05 −2.33	−0.64 +0.96	+4.21 −4.61	−0.91 +0.77	+5.01 −3.07	+0.27 +0.19	+5.16 −5.34
JET_PunchThrough_MC15	+0.00 +0.00	+0.00 +0.00	−0.00 −0.00	−0.00 +0.01	+0.00 −0.01	+0.00 −0.01	+0.00 −0.01
JET_RelativeNonClosure_MC15	+0.00 +0.00	−0.00 −0.00	−0.00 −0.00	−0.00 −0.00	+0.00 +0.00	−0.00 −0.00	+0.00 +0.00
JET_SingleParticle_HighPt	+0.00 +0.00	−0.00 −0.00	−0.00 −0.00	−0.00 −0.00	+0.00 +0.00	−0.00 −0.00	+0.00 +0.00
MET_JetTrk_Scale	+0.00 +0.00	−0.00 −0.00	−0.00 −0.00	−0.00 −0.00	+0.00 +0.00	−0.00 −0.00	+0.00 +0.00
MET_SoftTrk_ResoPara	+0.13	−0.09	−0.00	−0.00	+0.13	−0.09	+0.00
MET_SoftTrk_ResoPerp	−0.10	−0.36	−0.00	−0.00	−0.10	−0.36	+0.00
MET_SoftTrk_Scale	+0.06 +0.10	+0.10 −0.10	−0.00 +0.00	−0.00 −0.00	+0.06 +0.10	+0.10 −0.10	+0.00 +0.00
Total	±9.60	±9.68	±9.87	±8.15	±9.36	±2.43	±11.83
MC Stat.	±2.83	±3.03	±4.50	±0.84	±2.96	±3.14	±4.58

Table 8.5: Relative experimental uncertainties in % related to efficiency corrections on the top quark background in the ggF quasi-inclusive SR (2nd column), the corresponding WW CR (3rd column) and top-quark CR (4th column) and on the transfer factors from the top-quark CR to the SR (5th column) and from the top-quark CR to the WW CR (last column). The two uncertainty values in each column represent the up and down variations. The row labeled "Total" is the squared sum of all sources, where the largest variation is taken for each parameter. The uncertainty originating from the limited MC statistics in each region is also shown for comparison.

Source	SRIncl	WWCRIncl	TopCRIncl	$\alpha = N_{\text{SRIncl}}/N_{\text{topCRIncl}}$	$\beta = N_{\text{WWCRIncl}}/N_{\text{topCRIncl}}$
EL_EFF_Reco_TOTAL_1NPCOR_PLUS_UNCOR	−0.14 +0.14	−0.14 +0.14	−0.14 +0.14	−0.01 +0.01	−0.01 +0.01
EL_EFF_Iso_TOTAL_1NPCOR_PLUS_UNCOR	−0.22 +0.22	−0.20 +0.20	−0.21 +0.21	−0.01 +0.01	+0.01 −0.01
EL_EFF_ID_CorrUncertaintyNP0	+0.00 +0.00	−0.00 −0.00	+0.00 +0.00	−0.00 −0.00	−0.00 −0.00
EL_EFF_ID_CorrUncertaintyNP1	+0.00 +0.00	−0.00 −0.00	+0.00 +0.00	−0.00 −0.00	−0.00 −0.00
EL_EFF_ID_CorrUncertaintyNP2	+0.00 +0.00	−0.00 −0.00	+0.00 +0.00	−0.00 −0.00	−0.00 −0.00
EL_EFF_ID_CorrUncertaintyNP3	+0.00 +0.00	−0.00 −0.00	+0.00 +0.00	−0.00 −0.00	−0.00 −0.00
EL_EFF_ID_CorrUncertaintyNP4	+0.00 +0.00	−0.00 −0.00	+0.00 +0.00	−0.00 −0.00	−0.00 −0.00
EL_EFF_ID_CorrUncertaintyNP5	−0.00 +0.00	−0.00 +0.00	−0.00 +0.00	−0.00 +0.00	−0.00 +0.00
EL_EFF_ID_CorrUncertaintyNP6	−0.00 +0.00	+0.00 −0.00	+0.00 +0.00	−0.00 +0.00	+0.00 −0.00
EL_EFF_ID_CorrUncertaintyNP7	−0.02 +0.02	−0.02 +0.02	−0.02 +0.02	−0.00 +0.00	−0.00 +0.00
EL_EFF_ID_CorrUncertaintyNP8	+0.02 −0.02	+0.03 −0.03	+0.02 −0.02	−0.00 +0.00	+0.01 −0.01
EL_EFF_ID_CorrUncertaintyNP9	−0.02 +0.02	−0.02 +0.02	−0.02 +0.02	−0.00 +0.00	−0.00 +0.00
EL_EFF_ID_CorrUncertaintyNP10	−0.03 +0.03	−0.03 +0.03	−0.03 +0.03	−0.00 +0.00	−0.00 +0.00
EL_EFF_ID_CorrUncertaintyNP11	−0.10 +0.10	−0.10 +0.10	−0.10 +0.10	−0.00 +0.00	−0.00 +0.00
EL_EFF_ID_CorrUncertaintyNP12	+0.00 −0.00	+0.00 −0.00	+0.00 −0.00	+0.00 −0.00	+0.00 −0.00
EL_EFF_ID_CorrUncertaintyNP13	−0.09 +0.09	−0.11 +0.11	−0.08 +0.08	−0.01 +0.01	−0.03 +0.03
EL_EFF_ID_CorrUncertaintyNP14	−0.25 +0.25	−0.26 +0.26	−0.24 +0.24	−0.01 +0.01	−0.02 +0.02
EL_EFF_ID_SIMPLIFIED_UncorrUncertaintyNP0	+0.00 +0.00	−0.00 −0.00	+0.00 +0.00	−0.00 −0.00	−0.00 −0.00
EL_EFF_ID_SIMPLIFIED_UncorrUncertaintyNP1	+0.00 +0.00	−0.00 −0.00	+0.00 +0.00	−0.00 −0.00	−0.00 −0.00
EL_EFF_ID_SIMPLIFIED_UncorrUncertaintyNP2	+0.00 +0.00	−0.00 −0.00	+0.00 +0.00	−0.00 −0.00	−0.00 −0.00
EL_EFF_ID_SIMPLIFIED_UncorrUncertaintyNP3	+0.00 +0.00	−0.00 −0.00	+0.00 +0.00	−0.00 −0.00	−0.00 −0.00
EL_EFF_ID_SIMPLIFIED_UncorrUncertaintyNP4	+0.00 +0.00	−0.00 −0.00	+0.00 +0.00	−0.00 −0.00	−0.00 −0.00
EL_EFF_ID_SIMPLIFIED_UncorrUncertaintyNP5	+0.00 +0.00	−0.00 −0.00	+0.00 +0.00	−0.00 −0.00	−0.00 −0.00
EL_EFF_ID_SIMPLIFIED_UncorrUncertaintyNP6	−0.05 +0.05	−0.04 +0.04	−0.05 +0.05	+0.01 −0.01	+0.01 −0.01
EL_EFF_ID_SIMPLIFIED_UncorrUncertaintyNP7	−0.04 +0.04	−0.03 +0.03	−0.04 +0.04	+0.00 −0.00	+0.01 −0.01
EL_EFF_ID_SIMPLIFIED_UncorrUncertaintyNP8	−0.14 +0.14	−0.11 +0.11	−0.14 +0.14	+0.00 −0.00	+0.04 −0.04
EL_EFF_ID_SIMPLIFIED_UncorrUncertaintyNP9	+0.00 +0.00	−0.00 −0.00	+0.00 +0.00	−0.00 −0.00	−0.00 −0.00
EL_EFF_ID_SIMPLIFIED_UncorrUncertaintyNP10	+0.00 +0.00	−0.00 −0.00	+0.00 +0.00	−0.00 −0.00	−0.00 −0.00
EL_EFF_ID_SIMPLIFIED_UncorrUncertaintyNP11	+0.00 +0.00	−0.00 −0.00	+0.00 +0.00	−0.00 −0.00	−0.00 −0.00
EL_EFF_ID_SIMPLIFIED_UncorrUncertaintyNP12	+0.00 +0.00	−0.00 −0.00	+0.00 +0.00	−0.00 −0.00	−0.00 −0.00
EL_EFF_ID_SIMPLIFIED_UncorrUncertaintyNP13	+0.00 +0.00	−0.00 −0.00	+0.00 +0.00	−0.00 −0.00	−0.00 −0.00
EL_EFF_ID_SIMPLIFIED_UncorrUncertaintyNP14	+0.00 +0.00	−0.00 −0.00	+0.00 +0.00	−0.00 −0.00	−0.00 −0.00
EL_EFF_ID_SIMPLIFIED_UncorrUncertaintyNP15	−0.03 +0.03	−0.05 +0.05	−0.02 +0.02	−0.01 +0.01	−0.02 +0.02
EL_EFF_Trigger_TOTAL_1NPCOR_PLUS_UNCOR	−0.07 +0.07	−0.07 +0.07	−0.07 +0.07	+0.00 −0.00	−0.00 +0.00
MUON_EFF_STAT	−0.19 +0.19	−0.18 +0.18	−0.19 +0.19	+0.00 −0.00	+0.01 −0.01
MUON_EFF_SYS	−0.78 +0.79	−0.80 +0.80	−0.77 +0.77	−0.02 +0.02	−0.03 +0.03
MUON_ISO_SYS	−0.20 +0.20	−0.20 +0.20	−0.20 +0.20	−0.00 +0.00	+0.00 −0.00
MUON_ISO_STAT	−0.02 +0.02	−0.02 +0.02	−0.02 +0.02	−0.00 +0.00	+0.00 −0.00
MUON_EFF_TrigStatUncertainty	−0.04 +0.04	−0.04 +0.04	−0.04 +0.04	+0.00 −0.00	−0.00 +0.00
MUON_EFF_TrigSystUncertainty	−0.07 +0.07	−0.07 +0.07	−0.07 +0.07	+0.00 −0.00	−0.01 +0.01
FT_EFF_Eigen_B_0	−15.20 +16.45	−15.88 +17.10	−4.35 +3.80	−11.34 +12.19	−12.05 +12.81
FT_EFF_Eigen_B_1	−2.78 +2.82	−2.71 +2.75	−0.70 +0.68	−2.10 +2.12	−2.03 +2.05
FT_EFF_Eigen_B_2	+1.78 −1.76	+1.84 −1.83	+0.39 −0.40	+1.38 −1.37	+1.44 −1.43
FT_EFF_Eigen_C_0	−0.44 +0.45	−0.44 +0.45	−0.28 +0.28	−0.17 +0.17	−0.16 +0.16
FT_EFF_Eigen_C_1	+0.04 −0.04	+0.05 −0.05	+0.02 −0.02	+0.02 −0.02	+0.04 −0.04
FT_EFF_Eigen_C_2	−0.02 +0.02	−0.02 +0.02	−0.02 +0.02	−0.00 +0.00	−0.00 +0.00
FT_EFF_Eigen_C_3	+0.00 −0.00	+0.00 −0.00	+0.00 −0.00	+0.00 −0.00	+0.00 −0.00
FT_EFF_Eigen_Light_0	−0.86 +0.87	−0.86 +0.87	−0.60 +0.61	−0.25 +0.26	−0.26 +0.26
FT_EFF_Eigen_Light_1	+0.08 −0.08	+0.08 −0.08	+0.03 −0.03	+0.04 −0.04	+0.05 −0.05
FT_EFF_Eigen_Light_2	+0.49 −0.49	+0.50 −0.50	+0.34 −0.33	+0.16 −0.16	+0.16 −0.16
FT_EFF_Eigen_Light_3	+0.20 −0.20	+0.21 −0.21	+0.11 −0.11	+0.09 −0.09	+0.10 −0.10
FT_EFF_Eigen_Light_4	−0.03 +0.03	−0.04 +0.04	−0.02 +0.02	−0.01 +0.01	−0.01 +0.01
FT_EFF_extrapolation	+0.03 −0.03	+0.03 −0.03	+0.02 −0.02	+0.01 −0.01	+0.01 −0.01
FT_EFF_extrapolation_from_charm	−0.00	−0.00	−0.00	−0.00	−0.00
JET_JvtEfficiency	−0.36 +0.36	−0.37 +0.37	−0.45 +0.46	+0.09 −0.09	+0.08 −0.08
PU_SF	+0.71 −1.01	+0.59 −0.61	+0.93 −1.28	−0.23 +0.27	−0.34 +0.69
Total	±16.89	±17.49	±4.78	±12.46	±13.07
MC Stat.	±0.53	±1.14	±0.26	±0.59	±1.17

Table 8.6: Relative experimental uncertainties in % related to efficiency corrections on the top quark background in the VBF $n_{\text{jet}} = 1$ SR (2nd column) and the corresponding WW CR (3rd column) and on the transfer factor from the CR to the SR (4th column) and in the VBF $n_{\text{jet}} \geq 2$ SR (last column). The two uncertainty values in each column represent the up and down variations. The row labeled "Total" is the squared sum of all sources, where the largest variation is taken for each parameter. The uncertainty originating from the limited MC statistics in each region is also shown for comparison.

Source	SRVBF1J	SRVBF2J	WWCRVBF1J	TopCRVBF	α_VBF1J = $\frac{N_{\text{SRVBF1J}}}{N_{\text{topCRVBF}}}$	α_VBF2J = $\frac{N_{\text{SRVBF2J}}}{N_{\text{topCRVBF}}}$	$\beta = \frac{N_{\text{WWCRVBF1J}}}{N_{\text{topCRVBF}}}$
EL_EFF_Reco_TOTAL_1NPCOR_PLUS_UNCOR	−0.14 +0.14	−0.15 +0.15	−0.17 +0.17	−0.15 +0.15	+0.01 −0.01	+0.00 −0.00	−0.01 +0.01
EL_EFF_Iso_TOTAL_1NPCOR_PLUS_UNCOR	−0.21 +0.21	−0.26 +0.26	−0.13 +0.13	−0.19 +0.19	−0.02 +0.02	−0.07 +0.07	+0.06 −0.06
EL_EFF_ID_CorrUncertaintyNP0	+0.00 +0.00	−0.00 −0.00	−0.00 −0.00	−0.00 −0.00	+0.00 +0.00	−0.00 −0.00	+0.00 +0.00
EL_EFF_ID_CorrUncertaintyNP1	+0.00 +0.00	−0.00 −0.00	−0.00 −0.00	−0.00 −0.00	+0.00 +0.00	−0.00 −0.00	+0.00 +0.00
EL_EFF_ID_CorrUncertaintyNP2	+0.00 +0.00	−0.00 −0.00	−0.00 −0.00	−0.00 −0.00	+0.00 +0.00	−0.00 −0.00	+0.00 +0.00
EL_EFF_ID_CorrUncertaintyNP3	+0.00 +0.00	−0.00 −0.00	−0.00 −0.00	−0.00 −0.00	+0.00 +0.00	−0.00 −0.00	+0.00 +0.00
EL_EFF_ID_CorrUncertaintyNP4	+0.00 +0.00	−0.00 −0.00	−0.00 −0.00	−0.00 −0.00	+0.00 +0.00	−0.00 −0.00	+0.00 +0.00
EL_EFF_ID_CorrUncertaintyNP5	−0.00 +0.00	−0.00 +0.00	−0.00 +0.00	−0.00 +0.00	−0.00 +0.00	−0.00 +0.00	+0.00 −0.00
EL_EFF_ID_CorrUncertaintyNP6	−0.00 +0.00	−0.00 +0.00	+0.00 −0.00	+0.00 −0.00	−0.00 +0.00	−0.00 +0.00	+0.00 −0.00
EL_EFF_ID_CorrUncertaintyNP7	−0.02 +0.02	−0.02 +0.02	−0.01 +0.01	−0.01 +0.01	−0.00 +0.00	−0.00 +0.00	+0.00 −0.00
EL_EFF_ID_CorrUncertaintyNP8	+0.01 −0.01	+0.02 −0.02	+0.02 −0.02	+0.02 −0.02	−0.01 +0.01	−0.00 +0.00	+0.00 −0.00
EL_EFF_ID_CorrUncertaintyNP9	−0.02 +0.02	−0.02 +0.02	+0.01 −0.01	−0.01 +0.01	−0.02 +0.02	−0.01 +0.01	+0.02 −0.02
EL_EFF_ID_CorrUncertaintyNP10	−0.02 +0.02	−0.03 +0.03	−0.03 +0.03	−0.02 +0.02	+0.00 −0.00	−0.00 +0.00	−0.00 +0.00
EL_EFF_ID_CorrUncertaintyNP11	−0.09 +0.09	−0.10 +0.10	−0.12 +0.12	−0.11 +0.11	+0.01 −0.01	+0.01 −0.01	−0.01 +0.01
EL_EFF_ID_CorrUncertaintyNP12	−0.00 +0.00	+0.00 −0.00	+0.01 −0.01	+0.00 −0.00	−0.01 +0.01	−0.00 +0.00	+0.00 −0.00
EL_EFF_ID_CorrUncertaintyNP13	−0.07 +0.07	−0.09 +0.09	−0.12 +0.12	−0.11 +0.11	+0.04 −0.04	+0.02 −0.02	−0.02 +0.02
EL_EFF_ID_CorrUncertaintyNP14	−0.26 +0.26	−0.24 +0.24	−0.38 +0.38	−0.31 +0.31	+0.05 −0.05	+0.07 −0.07	−0.07 +0.07
EL_EFF_ID_SIMPLIFIED_UncorrUncertaintyNP0	+0.00 +0.00	−0.00 −0.00	−0.00 −0.00	−0.00 −0.00	+0.00 +0.00	−0.00 −0.00	+0.00 +0.00
EL_EFF_ID_SIMPLIFIED_UncorrUncertaintyNP1	+0.00 +0.00	−0.00 −0.00	−0.00 −0.00	−0.00 −0.00	+0.00 +0.00	−0.00 −0.00	+0.00 +0.00
EL_EFF_ID_SIMPLIFIED_UncorrUncertaintyNP2	+0.00 +0.00	−0.00 −0.00	−0.00 −0.00	−0.00 −0.00	+0.00 +0.00	−0.00 −0.00	+0.00 +0.00
EL_EFF_ID_SIMPLIFIED_UncorrUncertaintyNP3	+0.00 +0.00	−0.00 −0.00	−0.00 −0.00	−0.00 −0.00	+0.00 +0.00	−0.00 −0.00	+0.00 +0.00
EL_EFF_ID_SIMPLIFIED_UncorrUncertaintyNP4	+0.00 +0.00	−0.00 −0.00	−0.00 −0.00	−0.00 −0.00	+0.00 +0.00	−0.00 −0.00	+0.00 +0.00
EL_EFF_ID_SIMPLIFIED_UncorrUncertaintyNP5	+0.00 +0.00	−0.00 −0.00	−0.04 +0.04	−0.02 +0.02	+0.02 −0.02	+0.02 −0.02	−0.02 +0.02
EL_EFF_ID_SIMPLIFIED_UncorrUncertaintyNP6	−0.05 +0.05	−0.04 +0.04	−0.07 +0.07	−0.05 +0.05	−0.00 +0.00	+0.01 −0.01	−0.02 +0.02
EL_EFF_ID_SIMPLIFIED_UncorrUncertaintyNP7	−0.05 +0.05	−0.04 +0.04	−0.03 +0.03	−0.04 +0.04	−0.01 +0.01	−0.00 +0.00	+0.01 −0.01
EL_EFF_ID_SIMPLIFIED_UncorrUncertaintyNP8	−0.17 +0.17	−0.15 +0.15	−0.05 +0.05	−0.11 +0.11	−0.06 +0.06	−0.05 +0.05	+0.06 −0.06
EL_EFF_ID_SIMPLIFIED_UncorrUncertaintyNP9	+0.00 +0.00	−0.00 −0.00	−0.00 −0.00	−0.00 −0.00	+0.00 +0.00	−0.00 −0.00	+0.00 +0.00
EL_EFF_ID_SIMPLIFIED_UncorrUncertaintyNP10	+0.00 +0.00	−0.00 −0.00	−0.00 −0.00	−0.00 −0.00	+0.00 +0.00	−0.00 −0.00	+0.00 +0.00
EL_EFF_ID_SIMPLIFIED_UncorrUncertaintyNP11	+0.00 +0.00	−0.00 −0.00	−0.00 −0.00	−0.00 −0.00	+0.00 +0.00	−0.00 −0.00	+0.00 +0.00
EL_EFF_ID_SIMPLIFIED_UncorrUncertaintyNP12	+0.00 +0.00	−0.00 −0.00	−0.00 −0.00	−0.00 −0.00	+0.00 +0.00	−0.00 −0.00	+0.00 +0.00
EL_EFF_ID_SIMPLIFIED_UncorrUncertaintyNP13	+0.00 +0.00	−0.00 −0.00	−0.00 −0.00	−0.00 −0.00	+0.00 +0.00	−0.00 −0.00	+0.00 +0.00
EL_EFF_ID_SIMPLIFIED_UncorrUncertaintyNP14	+0.00 +0.00	−0.00 −0.00	−0.01 +0.01	−0.01 +0.01	+0.01 −0.01	+0.01 −0.01	−0.01 +0.01
EL_EFF_ID_SIMPLIFIED_UncorrUncertaintyNP15	−0.01 +0.01	−0.03 +0.03	−0.03 +0.03	−0.03 +0.03	+0.02 −0.02	−0.00 +0.00	−0.00 +0.00
EL_EFF_Trigger_TOTAL_1NPCOR_PLUS_UNCOR	−0.07 +0.07	−0.07 +0.07	−0.09 +0.09	−0.08 +0.08	+0.01 −0.01	+0.01 −0.01	−0.01 +0.01
MUON_EFF_STAT	−0.20 +0.20	−0.19 +0.19	−0.19 +0.19	−0.19 +0.19	−0.01 +0.01	+0.00 −0.00	+0.00 −0.00
MUON_EFF_SYS	−0.78 +0.78	−0.80 +0.80	−0.72 +0.72	−0.74 +0.74	−0.04 +0.04	−0.06 +0.06	+0.03 −0.03
MUON_ISO_SYS	−0.20 +0.20	−0.21 +0.21	−0.21 +0.21	−0.21 +0.21	+0.00 −0.00	+0.00 −0.00	−0.00 +0.00
MUON_ISO_STAT	−0.02 +0.02	−0.02 +0.02	−0.02 +0.02	−0.02 +0.02	−0.00 +0.00	−0.00 +0.00	+0.00 −0.00
MUON_EFF_TrigStatUncertainty	−0.03 +0.03	−0.04 +0.03	−0.08 +0.08	−0.05 +0.05	+0.02 −0.02	+0.02 −0.02	−0.03 +0.03
MUON_EFF_TrigSystUncertainty	−0.06 +0.06	−0.07 +0.07	−0.16 +0.16	−0.10 +0.10	+0.04 −0.04	+0.04 −0.04	−0.06 +0.06
FT_EFF_Eigen_B_0	−7.26 +7.49	−12.80 +13.87	−7.64 +7.91	+3.15 −3.32	−10.09 +11.18	−15.47 +17.77	−10.47 +11.61
FT_EFF_Eigen_B_1	+0.45 −0.45	−1.88 +1.88	+0.43 −0.43	+0.24 −0.24	+0.21 −0.20	−2.11 +2.13	+0.19 −0.19
FT_EFF_Eigen_B_2	−0.08 +0.08	+1.28 −1.28	−0.06 +0.06	−0.22 +0.22	+0.14 −0.14	+1.51 −1.49	+0.16 −0.16
FT_EFF_Eigen_C_0	−0.21 +0.21	−0.51 +0.52	−0.13 +0.13	+0.12 −0.12	−0.33 +0.33	−0.63 +0.64	−0.25 +0.25
FT_EFF_Eigen_C_1	+0.10 −0.10	+0.06 −0.06	+0.06 −0.06	+0.01 −0.01	+0.09 −0.09	+0.05 −0.05	+0.05 −0.05
FT_EFF_Eigen_C_2	−0.04 +0.04	−0.01 +0.01	−0.02 +0.02	−0.00 +0.00	−0.04 +0.04	−0.00 +0.00	−0.02 +0.02
FT_EFF_Eigen_C_3	−0.01 +0.01	+0.00 −0.00	−0.00 +0.00	−0.01 +0.01	−0.00 +0.00	+0.01 −0.01	+0.00 −0.00
FT_EFF_Eigen_Light_0	−0.39 +0.39	−1.11 +1.13	−0.39 +0.39	+0.29 −0.30	−0.67 +0.69	−1.40 +1.43	−0.68 +0.69
FT_EFF_Eigen_Light_1	−0.08 +0.08	+0.05 −0.05	−0.09 +0.09	−0.04 +0.04	−0.04 +0.04	+0.09 −0.09	−0.06 +0.06
FT_EFF_Eigen_Light_2	+0.40 −0.40	+0.57 −0.57	+0.42 −0.42	−0.20 +0.20	+0.60 −0.59	+0.78 −0.77	+0.62 −0.62
FT_EFF_Eigen_Light_3	+0.16 −0.16	+0.15 −0.15	+0.16 −0.16	−0.13 +0.13	+0.30 −0.30	+0.28 −0.28	+0.29 −0.29
FT_EFF_Eigen_Light_4	−0.06 +0.06	−0.04 +0.04	−0.07 +0.07	+0.03 −0.03	−0.09 +0.09	−0.07 +0.07	−0.10 +0.10
FT_EFF_extrapolation	+0.00 +0.00	+0.02 −0.02	−0.00 −0.00	−0.00 +0.00	+0.00 −0.00	+0.03 −0.03	+0.00 −0.00
FT_EFF_extrapolation_from_charm	+0.00	−0.01	−0.00	+0.00	−0.00	−0.01	−0.00
JET_JvtEfficiency	−0.14 +0.14	−0.37 +0.38	−0.15 +0.15	−0.56 +0.56	+0.42 −0.42	+0.19 −0.19	+0.41 −0.41
PU_SF	−0.20 +1.79	−0.29 −1.07	+0.76 −2.18	+0.26 −0.03	−0.47 +1.82	−0.55 −1.04	+0.49 −2.15
Total	±7.80	±14.20	±8.29	±3.54	±11.38	±18.08	±11.86
MC Stat.	±2.83	±3.03	±4.50	±0.84	±2.96	±3.14	±4.58

sources are found to be insignificant with respect to the other uncertainty sources and therefore neglected in the analysis. This is also true for the other backgrounds and the signals.

8.3 Experimental uncertainties on WW background

As with the top quark background experimental uncertainties, the four-momentum experimental uncertainties for the WW background in the quasi-inclusive ggF category and VBF categories are presented in Tables 8.7 and 8.8, respectively. Similarly, the scale-factor experimental uncertainties are presented in Tables 8.9 and 8.10. The quantity α corresponds to the extrapolation uncertainties from the top or WW CR to the SR.

Table 8.7: Relative experimental uncertainties in % related to the lepton, jets and missing transverse energy scale and resolution on the WW background in the ggF quasi-inclusive SR (2nd column) and the corresponding WW CR (3rd column) and on the transfer factor from the CR to the SR (last column). The two uncertainty values in each column represent the up and down variations. The row labeled "Total" is the squared sum of all sources, where the largest variation is taken for each parameter. The uncertainty originating from the limited MC statistics in each region is also shown for comparison.

Source	SRIncl	WWCRIncl	$\alpha = N_{\text{SRIncl}}/N_{\text{WWCRIncl}}$
EG_RESOLUTION_ALL	−0.03 +0.01	+0.08 +0.03	−0.11 −0.02
EG_SCALE_ALLCORR	−0.13 +0.13	−0.13 +0.12	+0.01 +0.00
EG_SCALE_E4SCINTILLATOR	+0.00 +0.00	+0.00 +0.00	+0.00 −0.00
EG_SCALE_LARCALIB_EXTRA2015PRE	+0.00 −0.00	−0.01 +0.02	+0.01 −0.03
EG_SCALE_LARTEMPERATURE_EXTRA2015PRE	+0.00 +0.00	+0.00 +0.00	+0.00 +0.00
EG_SCALE_LARTEMPERATURE_EXTRA2016PRE	+0.00 +0.00	+0.00 +0.00	+0.00 +0.00
MUON_ID	+0.04 +0.01	+0.05 +0.04	−0.00 −0.02
MUON_MS	+0.03 +0.04	+0.07 +0.04	−0.04 −0.00
MUON_SCALE	+0.07 −0.07	+0.12 −0.05	−0.05 −0.02
JET_BJES_Response	+0.00 −0.00	+0.01 −0.00	−0.00 +0.00
JET_EffectiveNP_1	+0.33 −0.31	+0.31 −0.29	+0.02 −0.03
JET_EffectiveNP_2	−0.09 +0.09	−0.09 +0.09	−0.01 −0.00
JET_EffectiveNP_3	−0.00 −0.01	−0.02 +0.01	+0.02 −0.01
JET_EffectiveNP_4	−0.01 −0.00	+0.02 −0.03	−0.03 +0.03
JET_EffectiveNP_5	−0.00 −0.00	−0.02 +0.01	+0.02 −0.01
JET_EffectiveNP_6	+0.00 −0.00	−0.00 +0.01	+0.00 −0.01
JET_EffectiveNP_7	−0.01 −0.00	−0.01 −0.02	+0.00 +0.02
JET_EffectiveNP_8restTerm	+0.00 −0.00	−0.01 −0.01	+0.01 +0.01
JET_EtaIntercalibration_Modelling	+0.39 −0.40	+0.33 −0.40	+0.07 −0.01
JET_EtaIntercalibration_NonClosure	+0.19 −0.21	+0.16 −0.16	+0.03 −0.04
JET_EtaIntercalibration_TotalStat	+0.11 −0.13	+0.09 −0.12	+0.02 −0.01
JET_Flavor_Composition	+0.76 −0.71	+0.65 −0.64	+0.10 −0.07
JET_Flavor_Response	−0.25 +0.22	−0.16 +0.24	−0.09 −0.02
JET_JER_SINGLE_NP	−0.28	−0.12	−0.17
JET_Pileup_OffsetMu	−0.02 +0.04	−0.03 +0.01	+0.01 +0.03
JET_Pileup_OffsetNPV	+0.12 −0.13	+0.09 −0.07	+0.03 −0.06
JET_Pileup_PtTerm	+0.06 −0.01	+0.12 −0.08	−0.06 +0.08
JET_Pileup_RhoTopology	+0.52 −0.47	+0.46 −0.38	+0.06 −0.10
JET_PunchThrough_MC15	+0.00 −0.00	−0.00 +0.00	+0.00 −0.00
JET_RelativeNonClosure_MC15	+0.00 +0.00	+0.00 +0.00	+0.00 +0.00
JET_SingleParticle_HighPt	+0.00 +0.00	+0.00 +0.00	+0.00 +0.00
MET_JetTrk_Scale	+0.00 +0.00	+0.00 +0.00	+0.00 +0.00
MET_SoftTrk_ResoPara	−0.08	−0.03	−0.05
MET_SoftTrk_ResoPerp	−0.07	+0.04	−0.11
MET_SoftTrk_Scale	+0.08 −0.07	+0.08 +0.05	−0.00 −0.12
Total	±1.18	±1.05	±0.35
MC Stat.	±0.36	±0.82	±0.90

Table 8.8: Relative experimental uncertainties in % related to the lepton, jets and missing transverse energy scale and resolution on the WW background in the VBF $n_{\text{jet}} = 1$ SR (2nd column) and the corresponding WW CR (3rd column) and on the transfer factor from the CR to the SR (4th column) and in the VBF $n_{\text{jet}} \geq 2$ SR (last column). The two uncertainty values in each column represent the up and down variations. The row labeled "Total" is the squared sum of all sources, where the largest variation is taken for each parameter. The uncertainty originating from the limited MC statistics in each region is also shown for comparison.

Source	SRVBF1J	WWCRVBF1J	$\alpha = N_{\text{SRVBF1J}}/N_{\text{WWCRVBF1J}}$	SRVBF2J
EG_RESOLUTION_ALL	−0.00 −0.16	−0.07 −0.10	+0.07 −0.06	−0.14 −0.04
EG_SCALE_ALLCORR	−0.10 −0.00	−0.40 +0.05	+0.31 −0.05	−0.17 +0.04
EG_SCALE_E4SCINTILLATOR	−0.00 −0.01	−0.00 +0.00	−0.00 −0.01	−0.01 +0.00
EG_SCALE_LARCALIB_EXTRA2015PRE	−0.05 +0.00	−0.25 +0.03	+0.20 −0.02	−0.08 −0.04
EG_SCALE_LARTEMPERATURE_EXTRA2015PRE	−0.00 −0.00	−0.00 −0.00	−0.00 −0.00	+0.00 +0.00
EG_SCALE_LARTEMPERATURE_EXTRA2016PRE	−0.00 −0.00	−0.00 −0.00	−0.00 −0.00	+0.00 +0.00
MUON_ID	+0.11 +0.12	+0.18 +0.06	−0.07 +0.06	+0.04 +0.01
MUON_MS	+0.04 −0.17	+0.14 +0.16	−0.09 −0.33	−0.19 −0.07
MUON_SCALE	−0.01 −0.01	+0.13 +0.06	−0.14 −0.07	+0.02 −0.09
JET_BJES_Response	+0.02 +0.02	−0.00 +0.02	+0.02 +0.00	+0.02 +0.01
JET_EffectiveNP_1	−2.55 +3.11	−2.60 +1.93	+0.05 +1.17	−2.86 +3.41
JET_EffectiveNP_2	+0.23 −0.57	+0.66 −0.77	−0.42 +0.20	+0.70 −0.76
JET_EffectiveNP_3	+0.05 −0.16	−0.10 +0.07	+0.15 −0.23	−0.02 −0.00
JET_EffectiveNP_4	+0.07 −0.14	−0.08 +0.05	+0.15 −0.18	−0.16 +0.08
JET_EffectiveNP_5	−0.15 −0.06	+0.16 −0.20	−0.31 +0.14	+0.28 −0.30
JET_EffectiveNP_6	+0.03 −0.13	−0.23 +0.18	+0.25 −0.31	−0.33 +0.26
JET_EffectiveNP_7	+0.07 +0.00	−0.01 +0.07	+0.08 −0.07	−0.02 +0.02
JET_EffectiveNP_8restTerm	−0.04 −0.10	−0.14 +0.06	+0.11 −0.16	−0.17 +0.14
JET_EtaIntercalibration_Modelling	−7.25 +7.44	−5.64 +7.81	−1.71 −0.34	−6.09 +7.53
JET_EtaIntercalibration_NonClosure	−3.37 +4.28	−3.20 +2.86	−0.17 +1.38	−1.72 +2.59
JET_EtaIntercalibration_TotalStat	−1.41 +1.24	−1.33 +1.23	−0.09 +0.00	−1.67 +1.71
JET_Flavor_Composition	−7.64 +7.77	−5.35 +7.62	−2.43 +0.14	−8.95 +10.40
JET_Flavor_Response	+3.21 −2.66	+1.65 −2.37	+1.54 −0.30	+3.42 −2.58
JET_JER_SINGLE_NP	+11.03	+9.58	+1.32	+9.65
JET_Pileup_OffsetMu	+0.32 −0.91	+1.49 −1.08	−1.15 +0.17	+1.41 −1.33
JET_Pileup_OffsetNPV	−1.46 +1.00	−0.43 +0.54	−1.03 +0.46	−0.43 +1.44
JET_Pileup_PtTerm	−1.34 +0.73	−0.90 +0.90	−0.44 −0.17	−1.68 +1.47
JET_Pileup_RhoTopology	−3.59 +4.13	−2.88 +2.14	−0.73 +1.95	−3.76 +3.93
JET_PunchThrough_MC15	−0.00 −0.00	−0.00 −0.00	−0.00 −0.00	+0.00 −0.01
JET_RelativeNonClosure_MC15	−0.00 −0.00	−0.00 −0.00	−0.00 −0.00	+0.00 +0.00
JET_SingleParticle_HighPt	−0.00 −0.00	−0.00 −0.00	−0.00 −0.00	+0.00 +0.00
MET_JetTrk_Scale	−0.00 −0.00	−0.00 −0.00	−0.00 −0.00	+0.00 +0.00
MET_SoftTrk_ResoPara	−0.29	+0.00	−0.29	−0.22
MET_SoftTrk_ResoPerp	−0.04	−0.00	−0.04	+0.08
MET_SoftTrk_Scale	+0.06 −0.31	+0.00 +0.00	+0.06 −0.31	−0.14 −0.16
Total	±17.33	±15.74	±4.85	±17.73
MC Stat.	±2.00	±2.18	±2.96	±2.40

Table 8.9: Relative experimental uncertainties in % related to efficiency corrections on the WW background in the ggF quasi-inclusive SR (2nd column) and the corresponding WW CR (3rd column) and on the transfer factor from the CR to the SR (last column). The two uncertainty values in each column represent the up and down variations. The row labeled "Total" is the squared sum of all sources, where the largest variation is taken for each parameter. The uncertainty originating from the limited MC statistics in each region is also shown for comparison.

Source	SRIncl	WWCRIncl	$\alpha = N_{\text{SRIncl}}/N_{\text{WWCRIncl}}$
EL_EFF_Reco_TOTAL_1NPCOR_PLUS_UNCOR	−0.14 +0.14	−0.14 +0.14	−0.00 +0.00
EL_EFF_Iso_TOTAL_1NPCOR_PLUS_UNCOR	−0.22 +0.22	−0.19 +0.19	−0.03 +0.03
EL_EFF_ID_CorrUncertaintyNP0	+0.00 +0.00	+0.00 +0.00	+0.00 +0.00
EL_EFF_ID_CorrUncertaintyNP1	+0.00 +0.00	+0.00 +0.00	+0.00 +0.00
EL_EFF_ID_CorrUncertaintyNP2	+0.00 +0.00	+0.00 +0.00	+0.00 +0.00
EL_EFF_ID_CorrUncertaintyNP3	+0.00 +0.00	+0.00 +0.00	+0.00 +0.00
EL_EFF_ID_CorrUncertaintyNP4	+0.00 +0.00	+0.00 +0.00	+0.00 +0.00
EL_EFF_ID_CorrUncertaintyNP5	−0.00 +0.00	−0.00 +0.00	+0.00 −0.00
EL_EFF_ID_CorrUncertaintyNP6	+0.00 −0.00	+0.00 −0.00	−0.00 +0.00
EL_EFF_ID_CorrUncertaintyNP7	−0.02 +0.02	−0.02 +0.02	+0.00 −0.00
EL_EFF_ID_CorrUncertaintyNP8	+0.02 −0.02	+0.03 −0.03	−0.01 +0.01
EL_EFF_ID_CorrUncertaintyNP9	−0.02 +0.02	−0.02 +0.03	+0.00 −0.00
EL_EFF_ID_CorrUncertaintyNP10	−0.03 +0.03	−0.04 +0.04	+0.01 −0.01
EL_EFF_ID_CorrUncertaintyNP11	−0.10 +0.10	−0.10 +0.10	+0.01 −0.01
EL_EFF_ID_CorrUncertaintyNP12	+0.00 −0.00	+0.00 −0.00	+0.00 −0.00
EL_EFF_ID_CorrUncertaintyNP13	−0.10 +0.10	−0.12 +0.12	+0.02 −0.02
EL_EFF_ID_CorrUncertaintyNP14	−0.23 +0.23	−0.24 +0.24	+0.01 −0.01
EL_EFF_ID_SIMPLIFIED_UncorrUncertaintyNP0	+0.00 +0.00	+0.00 +0.00	+0.00 +0.00
EL_EFF_ID_SIMPLIFIED_UncorrUncertaintyNP1	+0.00 +0.00	+0.00 +0.00	+0.00 +0.00
EL_EFF_ID_SIMPLIFIED_UncorrUncertaintyNP2	+0.00 +0.00	+0.00 +0.00	+0.00 +0.00
EL_EFF_ID_SIMPLIFIED_UncorrUncertaintyNP3	+0.00 +0.00	+0.00 +0.00	+0.00 +0.00
EL_EFF_ID_SIMPLIFIED_UncorrUncertaintyNP4	+0.00 +0.00	+0.00 +0.00	+0.00 +0.00
EL_EFF_ID_SIMPLIFIED_UncorrUncertaintyNP5	+0.00 +0.00	+0.00 +0.00	+0.00 +0.00
EL_EFF_ID_SIMPLIFIED_UncorrUncertaintyNP6	−0.05 +0.05	−0.05 +0.05	−0.00 +0.00
EL_EFF_ID_SIMPLIFIED_UncorrUncertaintyNP7	−0.04 +0.04	−0.03 +0.03	−0.01 +0.01
EL_EFF_ID_SIMPLIFIED_UncorrUncertaintyNP8	−0.11 +0.11	−0.08 +0.08	−0.04 +0.04
EL_EFF_ID_SIMPLIFIED_UncorrUncertaintyNP9	+0.00 +0.00	+0.00 +0.00	+0.00 +0.00
EL_EFF_ID_SIMPLIFIED_UncorrUncertaintyNP10	+0.00 +0.00	+0.00 +0.00	+0.00 +0.00
EL_EFF_ID_SIMPLIFIED_UncorrUncertaintyNP11	+0.00 +0.00	+0.00 +0.00	+0.00 +0.00
EL_EFF_ID_SIMPLIFIED_UncorrUncertaintyNP12	+0.00 +0.00	+0.00 +0.00	+0.00 +0.00
EL_EFF_ID_SIMPLIFIED_UncorrUncertaintyNP13	+0.00 +0.00	+0.00 +0.00	+0.00 +0.00
EL_EFF_ID_SIMPLIFIED_UncorrUncertaintyNP14	+0.00 +0.00	+0.00 +0.00	+0.00 +0.00
EL_EFF_ID_SIMPLIFIED_UncorrUncertaintyNP15	−0.04 +0.04	−0.06 +0.06	+0.02 −0.02
EL_EFF_Trigger_TOTAL_1NPCOR_PLUS_UNCOR	−0.07 +0.07	−0.08 +0.08	+0.01 −0.01
MUON_EFF_STAT	−0.19 +0.19	−0.19 +0.19	−0.00 +0.00
MUON_EFF_SYS	−0.78 +0.78	−0.79 +0.79	+0.01 −0.01
MUON_ISO_SYS	−0.21 +0.21	−0.20 +0.20	−0.00 +0.00
MUON_ISO_STAT	−0.02 +0.02	−0.02 +0.02	−0.00 +0.00
MUON_EFF_TrigStatUncertainty	−0.04 +0.04	−0.04 +0.04	+0.00 −0.00
MUON_EFF_TrigSystUncertainty	−0.07 +0.07	−0.08 +0.08	+0.01 −0.01
FT_EFF_Eigen_B_0	−0.06 +0.06	−0.05 +0.05	−0.01 +0.01
FT_EFF_Eigen_B_1	−0.00 +0.00	−0.00 +0.00	−0.00 +0.00
FT_EFF_Eigen_B_2	+0.00 −0.00	+0.00 −0.00	+0.00 −0.00
FT_EFF_Eigen_C_0	−0.43 +0.44	−0.34 +0.35	−0.09 +0.09
FT_EFF_Eigen_C_1	+0.00 −0.00	+0.01 −0.01	−0.01 +0.01
FT_EFF_Eigen_C_2	−0.02 +0.02	−0.02 +0.02	−0.00 +0.00
FT_EFF_Eigen_C_3	+0.01 −0.01	+0.01 −0.01	+0.00 −0.00
FT_EFF_Eigen_Light_0	−0.67 +0.68	−0.60 +0.61	−0.07 +0.07
FT_EFF_Eigen_Light_1	+0.06 −0.06	+0.05 −0.05	+0.01 −0.01
FT_EFF_Eigen_Light_2	+0.34 −0.34	+0.35 −0.34	−0.00 +0.00
FT_EFF_Eigen_Light_3	+0.14 −0.14	+0.13 −0.13	+0.00 −0.00
FT_EFF_Eigen_Light_4	−0.03 +0.03	−0.03 +0.03	−0.00 +0.00
FT_EFF_extrapolation	+0.01 −0.01	+0.00 −0.00	+0.00 −0.00
FT_EFF_extrapolation_from_charm	−0.00	−0.00	+0.00
JET_JvtEfficiency	−0.18 +0.18	−0.17 +0.17	−0.01 +0.01
PU_SF	+1.02 −1.17	+0.83 −1.36	+0.19 +0.19
Total	±1.75	±1.84	±0.24
MC Stat.	±0.36	±0.82	±0.90

Table 8.10: Relative experimental uncertainties in % related to efficiency corrections on the WW background in the VBF $n_{\text{jet}} = 1$ SR (2nd column) and the corresponding WW CR (3rd column) and on the transfer factor from the CR to the SR (4th column) and in the VBF $n_{\text{jet}} \geq 2$ SR (last column). The two uncertainty values in each column represent the up and down variations. The row labeled "Total" is the squared sum of all sources, where the largest variation is taken for each parameter. The uncertainty originating from the limited MC statistics in each region is also shown for comparison.

Source	SRVBF1J	WWCRVBF1J	$\alpha = N_{\text{SRVBF1J}}/N_{\text{WWCRVBF1J}}$	SRVBF2J
EL_EFF_Reco_TOTAL_1NPCOR_PLUS_UNCOR	−0.13 +0.13	−0.16 +0.16	+0.03 −0.03	−0.15 +0.15
EL_EFF_Iso_TOTAL_1NPCOR_PLUS_UNCOR	−0.19 +0.19	−0.14 +0.14	−0.06 +0.06	−0.30 +0.30
EL_EFF_ID_CorrUncertaintyNP0	−0.00 −0.00	−0.00 −0.00	−0.00 −0.00	+0.00 +0.00
EL_EFF_ID_CorrUncertaintyNP1	−0.00 −0.00	−0.00 −0.00	−0.00 −0.00	+0.00 +0.00
EL_EFF_ID_CorrUncertaintyNP2	−0.00 −0.00	−0.00 −0.00	−0.00 −0.00	+0.00 +0.00
EL_EFF_ID_CorrUncertaintyNP3	−0.00 −0.00	−0.00 −0.00	−0.00 −0.00	+0.00 +0.00
EL_EFF_ID_CorrUncertaintyNP4	−0.00 −0.00	−0.00 −0.00	−0.00 −0.00	+0.00 +0.00
EL_EFF_ID_CorrUncertaintyNP5	−0.00 +0.00	−0.00 +0.00	−0.00 +0.00	−0.00 +0.00
EL_EFF_ID_CorrUncertaintyNP6	−0.00 +0.00	+0.00 −0.00	−0.00 +0.00	+0.00 −0.00
EL_EFF_ID_CorrUncertaintyNP7	−0.02 +0.02	−0.01 +0.01	−0.01 +0.01	−0.02 +0.02
EL_EFF_ID_CorrUncertaintyNP8	+0.02 −0.02	+0.03 −0.03	−0.01 +0.01	+0.02 −0.02
EL_EFF_ID_CorrUncertaintyNP9	−0.02 +0.02	+0.01 −0.01	−0.03 +0.03	−0.03 +0.03
EL_EFF_ID_CorrUncertaintyNP10	−0.03 +0.03	−0.03 +0.03	−0.01 +0.01	−0.02 +0.02
EL_EFF_ID_CorrUncertaintyNP11	−0.10 +0.10	−0.12 +0.12	+0.02 −0.02	−0.09 +0.09
EL_EFF_ID_CorrUncertaintyNP12	−0.00 +0.00	+0.00 −0.00	−0.01 +0.01	−0.00 +0.00
EL_EFF_ID_CorrUncertaintyNP13	−0.08 +0.08	−0.14 +0.14	+0.06 −0.06	−0.10 +0.10
EL_EFF_ID_CorrUncertaintyNP14	−0.22 +0.22	−0.36 +0.36	+0.15 −0.15	−0.24 +0.24
EL_EFF_ID_SIMPLIFIED_UncorrUncertaintyNP0	−0.00 −0.00	−0.00 −0.00	−0.00 −0.00	+0.00 +0.00
EL_EFF_ID_SIMPLIFIED_UncorrUncertaintyNP1	−0.00 −0.00	−0.00 −0.00	−0.00 −0.00	+0.00 +0.00
EL_EFF_ID_SIMPLIFIED_UncorrUncertaintyNP2	−0.00 −0.00	−0.00 −0.00	−0.00 −0.00	+0.00 +0.00
EL_EFF_ID_SIMPLIFIED_UncorrUncertaintyNP3	−0.00 −0.00	−0.00 −0.00	−0.00 −0.00	+0.00 +0.00
EL_EFF_ID_SIMPLIFIED_UncorrUncertaintyNP4	−0.00 −0.00	−0.00 −0.00	−0.00 −0.00	+0.00 +0.00
EL_EFF_ID_SIMPLIFIED_UncorrUncertaintyNP5	−0.00 −0.00	−0.04 +0.04	+0.04 −0.04	+0.00 +0.00
EL_EFF_ID_SIMPLIFIED_UncorrUncertaintyNP6	−0.06 +0.06	−0.07 +0.07	+0.01 −0.01	−0.04 +0.04
EL_EFF_ID_SIMPLIFIED_UncorrUncertaintyNP7	−0.04 +0.04	−0.02 +0.02	−0.03 +0.03	−0.03 +0.03
EL_EFF_ID_SIMPLIFIED_UncorrUncertaintyNP8	−0.11 +0.11	−0.03 +0.03	−0.08 +0.08	−0.16 +0.16
EL_EFF_ID_SIMPLIFIED_UncorrUncertaintyNP9	−0.00 −0.00	−0.00 −0.00	−0.00 −0.00	+0.00 +0.00
EL_EFF_ID_SIMPLIFIED_UncorrUncertaintyNP10	−0.00 −0.00	−0.00 −0.00	−0.00 −0.00	+0.00 +0.00
EL_EFF_ID_SIMPLIFIED_UncorrUncertaintyNP11	−0.00 −0.00	−0.00 −0.00	−0.00 −0.00	+0.00 +0.00
EL_EFF_ID_SIMPLIFIED_UncorrUncertaintyNP12	−0.00 −0.00	−0.00 −0.00	−0.00 −0.00	+0.00 +0.00
EL_EFF_ID_SIMPLIFIED_UncorrUncertaintyNP13	−0.00 −0.00	−0.00 −0.00	−0.00 −0.00	+0.00 +0.00
EL_EFF_ID_SIMPLIFIED_UncorrUncertaintyNP14	−0.00 −0.00	−0.02 +0.02	+0.02 −0.02	+0.00 +0.00
EL_EFF_ID_SIMPLIFIED_UncorrUncertaintyNP15	−0.02 +0.02	−0.04 +0.04	+0.02 −0.02	−0.03 +0.03
EL_EFF_Trigger_TOTAL_1NPCOR_PLUS_UNCOR	−0.07 +0.07	−0.10 +0.10	+0.03 −0.03	−0.07 +0.07
MUON_EFF_STAT	−0.19 +0.19	−0.19 +0.19	−0.00 +0.00	−0.18 +0.18
MUON_EFF_SYS	−0.74 +0.74	−0.70 +0.70	−0.04 +0.04	−0.82 +0.82
MUON_ISO_SYS	−0.21 +0.21	−0.21 +0.21	+0.00 −0.00	−0.21 +0.21
MUON_ISO_STAT	−0.02 +0.02	−0.02 +0.02	−0.00 +0.00	−0.02 +0.02
MUON_EFF_TrigStatUncertainty	−0.04 +0.04	−0.08 +0.08	+0.04 −0.04	−0.04 +0.04
MUON_EFF_TrigSystUncertainty	−0.07 +0.08	−0.16 +0.17	+0.09 −0.09	−0.07 +0.07
FT_EFF_Eigen_B_0	−0.01 +0.02	−0.02 +0.02	+0.02 −0.01	−0.10 +0.10
FT_EFF_Eigen_B_1	+0.00 −0.00	+0.00 −0.00	−0.00 +0.00	+0.00 −0.00
FT_EFF_Eigen_B_2	−0.00 +0.00	−0.00 +0.00	−0.00 +0.00	+0.00 −0.00
FT_EFF_Eigen_C_0	−0.13 +0.14	−0.13 +0.13	−0.01 +0.01	−0.77 +0.79
FT_EFF_Eigen_C_1	+0.06 −0.06	+0.06 −0.06	+0.00 −0.00	−0.01 +0.01
FT_EFF_Eigen_C_2	−0.02 +0.02	−0.02 +0.02	+0.00 −0.00	−0.04 +0.04
FT_EFF_Eigen_C_3	−0.00 +0.00	−0.00 +0.00	+0.00 −0.00	+0.01 −0.01
FT_EFF_Eigen_Light_0	−0.33 +0.33	−0.31 +0.32	−0.01 +0.01	−1.32 +1.34
FT_EFF_Eigen_Light_1	−0.08 +0.08	−0.06 +0.06	−0.02 +0.02	+0.08 −0.08
FT_EFF_Eigen_Light_2	+0.34 −0.34	+0.33 −0.33	+0.01 −0.01	+0.53 −0.53
FT_EFF_Eigen_Light_3	+0.10 −0.10	+0.13 −0.13	−0.03 +0.03	+0.11 −0.11
FT_EFF_Eigen_Light_4	−0.04 +0.04	−0.05 +0.05	+0.01 −0.01	−0.04 +0.04
FT_EFF_extrapolation	+0.00 −0.00	+0.00 −0.00	−0.00 +0.00	+0.01 −0.01
FT_EFF_extrapolation_from_charm	−0.00	−0.00	−0.00	+0.00
JET_JvtEfficiency	−0.08 +0.08	−0.08 +0.08	−0.00 +0.00	−0.30 +0.30
PU_SF	−1.19 +2.55	−2.72 +4.37	+1.57 −1.74	−2.23 +2.37
Total	±2.75	±4.49	±1.75	±3.07
MC Stat.	±2.00	±2.18	±2.96	±2.40

8.4 Experimental uncertainties on signals

As with the top quark background experimental uncertainties, the four-momentum experimental uncertainties for the NWA ggF and VBF signals with a mass of 700 GeV, as an example, in the SRs are presented in Tables 8.11 and 8.12, respectively. Similarly, the scale-factor experimental uncertainties are presented in Tables 8.13 and 8.14.

Table 8.11: Relative experimental uncertainties in % related to the lepton, jets and missing transverse energy scale and resolution on the NWA ggF signal with mass 700 GeV in the signal regions. The two uncertainty values in each column represent the up and down variations. The row labeled "Total" is the squared sum of all sources, where the largest variation is taken for each parameter. The uncertainty originating from the limited MC statistics in each region is also shown for comparison.

Source	SRIncl	SRVBF1J	SRVBF2J
EG_RESOLUTION_ALL	+0.00 −0.02	−0.14 +0.00	−0.00 +0.00
EG_SCALE_ALLCORR	−0.03 +0.02	−0.10 +0.00	+0.00 −0.00
EG_SCALE_E4SCINTILLATOR	−0.00 +0.00	+0.00 +0.00	+0.00 +0.00
EG_SCALE_LARCALIB_EXTRA2015PRE	−0.01 −0.00	+0.00 −0.05	−0.00 +0.00
EG_SCALE_LARTEMPERATURE_EXTRA2015PRE	+0.00 +0.00	+0.00 +0.00	+0.00 +0.00
EG_SCALE_LARTEMPERATURE_EXTRA2016PRE	+0.00 +0.00	+0.00 +0.00	+0.00 +0.00
MUON_ID	+0.01 +0.02	+0.05 +0.00	−0.00 +0.10
MUON_MS	+0.01 +0.01	−0.06 −0.05	+0.00 −0.10
MUON_SCALE	+0.02 −0.01	−0.00 −0.00	+0.00 −0.10
JET_BJES_Response	+0.00 −0.00	+0.00 −0.00	+0.00 −0.00
JET_EffectiveNP_1	+0.55 −0.58	+0.06 −0.22	−1.74 +0.95
JET_EffectiveNP_2	−0.14 +0.09	+0.14 +0.10	+0.04 +0.03
JET_EffectiveNP_3	+0.02 −0.03	+0.00 +0.04	+0.10 −0.01
JET_EffectiveNP_4	−0.03 +0.01	−0.00 +0.05	−0.01 +0.10
JET_EffectiveNP_5	+0.01 −0.03	+0.01 −0.00	+0.19 −0.01
JET_EffectiveNP_6	−0.02 +0.00	−0.00 +0.00	−0.01 +0.19
JET_EffectiveNP_7	−0.03 +0.01	−0.00 +0.00	−0.01 +0.10
JET_EffectiveNP_8restTerm	+0.01 −0.02	+0.00 +0.05	+0.10 −0.00
JET_EtaIntercalibration_Modelling	+0.54 −0.56	−2.18 +2.07	−4.91 +4.28
JET_EtaIntercalibration_NonClosure	+0.12 −0.13	−1.03 +1.16	−0.90 +0.77
JET_EtaIntercalibration_TotalStat	+0.11 −0.14	−0.23 +0.31	−0.77 +0.58
JET_Flavor_Composition	+1.17 −1.20	−0.78 +1.26	−6.71 +5.67
JET_Flavor_Response	−0.29 +0.24	+0.23 −0.08	+1.19 −1.96
JET_JER_SINGLE_NP	+0.04	−0.19	+3.03
JET_Pileup_OffsetMu	−0.19 +0.07	+0.80 −0.40	+0.58 −0.83
JET_Pileup_OffsetNPV	+0.14 −0.19	+0.24 +0.11	−1.42 +0.04
JET_Pileup_PtTerm	−0.03 −0.06	−0.35 +0.55	−0.37 +0.86
JET_Pileup_RhoTopology	+0.78 −0.87	+0.13 +0.09	−2.55 +1.81
JET_PunchThrough_MC15	+0.00 −0.00	+0.00 +0.00	+0.00 +0.00
JET_RelativeNonClosure_MC15	+0.00 +0.00	+0.00 +0.00	+0.00 +0.00
JET_SingleParticle_HighPt	+0.00 +0.00	+0.00 +0.00	+0.00 +0.00
MET_JetTrk_Scale	+0.00 +0.00	+0.00 +0.00	+0.00 +0.00
MET_SoftTrk_ResoPara	−0.01	+0.00	+0.10
MET_SoftTrk_ResoPerp	+0.02	−0.10	−0.09
MET_SoftTrk_Scale	−0.01 +0.01	−0.04 −0.05	−0.09 +0.00
Total	±1.75	±3.00	±9.84
MC Stat.	±0.87	±3.05	±3.90

Table 8.12: Relative experimental uncertainties in % related to the lepton, jets and missing transverse energy scale and resolution on the NWA VBF signal with mass 700 GeV in the signal regions. The two uncertainty values in each column represent the up and down variations. The row labeled "Total" is the squared sum of all sources, where the largest variation is taken for each parameter. The uncertainty originating from the limited MC statistics in each region is also shown for comparison.

Source	SRIncl	SRVBF1J	SRVBF2J
EG_RESOLUTION_ALL	−0.05 −0.02	+0.15 +0.04	−0.05 +0.00
EG_SCALE_ALLCORR	−0.26 −0.02	+0.14 +0.08	−0.00 −0.02
EG_SCALE_E4SCINTILLATOR	−0.00 −0.00	+0.00 +0.00	+0.00 +0.00
EG_SCALE_LARCALIB_EXTRA2015PRE	−0.02 −0.26	+0.04 +0.05	+0.00 −0.00
EG_SCALE_LARTEMPERATURE_EXTRA2015PRE	+0.00 +0.00	+0.00 +0.00	+0.00 +0.00
EG_SCALE_LARTEMPERATURE_EXTRA2016PRE	+0.00 +0.00	+0.00 +0.00	+0.00 +0.00
MUON_ID	+0.02 +0.05	+0.05 +0.04	−0.04 +0.00
MUON_MS	−0.00 +0.00	+0.09 +0.05	−0.03 +0.02
MUON_SCALE	+0.02 −0.00	+0.05 +0.05	+0.00 −0.00
JET_BJES_Response	+0.10 −0.00	+0.00 +0.00	+0.00 +0.00
JET_EffectiveNP_1	+1.21 −1.01	+1.16 −1.39	−0.97 +1.00
JET_EffectiveNP_2	−0.21 +0.17	−0.82 +0.28	+0.40 −0.20
JET_EffectiveNP_3	−0.02 −0.07	+0.14 −0.05	−0.02 +0.04
JET_EffectiveNP_4	−0.03 −0.02	+0.05 −0.00	−0.04 +0.04
JET_EffectiveNP_5	+0.04 −0.01	−0.40 +0.17	+0.17 −0.09
JET_EffectiveNP_6	+0.01 +0.03	+0.12 −0.40	−0.07 +0.17
JET_EffectiveNP_7	−0.00 +0.00	+0.00 −0.05	−0.00 +0.02
JET_EffectiveNP_8restTerm	−0.03 −0.03	+0.19 −0.25	−0.07 +0.17
JET_EtaIntercalibration_Modelling	+1.98 −2.06	+2.13 −1.48	−2.50 +2.29
JET_EtaIntercalibration_NonClosure	+0.59 −0.90	+0.55 −0.71	−0.66 +1.00
JET_EtaIntercalibration_TotalStat	+0.41 −0.48	+0.18 −0.96	−0.40 +0.78
JET_Flavor_Composition	+2.22 −2.63	+3.86 −2.63	−2.95 +2.62
JET_Flavor_Response	−0.95 +0.98	−1.08 +0.68	+1.08 −0.97
JET_JER_SINGLE_NP	+0.46	−0.60	+0.45
JET_Pileup_OffsetMu	−0.22 +0.45	−0.47 +0.43	+0.62 −0.58
JET_Pileup_OffsetNPV	+0.31 −0.05	−0.22 −0.90	−0.00 +0.31
JET_Pileup_PtTerm	+0.16 −0.29	−0.05 −0.40	−0.23 +0.55
JET_Pileup_RhoTopology	+1.29 −1.42	+1.53 −1.57	−1.00 +1.11
JET_PunchThrough_MC15	+0.00 +0.00	+0.00 +0.00	−0.00 +0.00
JET_RelativeNonClosure_MC15	+0.00 +0.00	+0.00 +0.00	+0.00 +0.00
JET_SingleParticle_HighPt	+0.00 +0.00	+0.00 +0.00	+0.00 +0.00
MET_JetTrk_Scale	+0.00 +0.00	+0.00 +0.00	+0.00 +0.00
MET_SoftTrk_ResoPara	+0.05	+0.05	−0.00
MET_SoftTrk_ResoPerp	−0.20	+0.09	+0.02
MET_SoftTrk_Scale	+0.00 −0.23	+0.05 +0.14	+0.00 −0.02
Total	±4.19	±5.39	±4.60
MC Stat.	±2.01	±2.87	±1.78

Table 8.13: Relative experimental uncertainties in % related to efficiency corrections on the NWA ggF signal with mass 700 GeV in the signal regions. The two uncertainty values in each column represent the up and down variations. The row labeled "Total" is the squared sum of all sources, where the largest variation is taken for each parameter. The uncertainty originating from the limited MC statistics in each region is also shown for comparison.

Source	SRIncl	SRVBF1J	SRVBF2J
EL_EFF_Reco_TOTAL_1NPCOR_PLUS_UNCOR	−0.19 +0.19	−0.18 +0.18	−0.18 +0.18
EL_EFF_Iso_TOTAL_1NPCOR_PLUS_UNCOR	−1.10 +1.10	−1.12 +1.12	−1.03 +1.03
EL_EFF_ID_CorrUncertaintyNP0	+0.00 +0.00	+0.00 +0.00	+0.00 +0.00
EL_EFF_ID_CorrUncertaintyNP1	+0.00 +0.00	+0.00 +0.00	+0.00 +0.00
EL_EFF_ID_CorrUncertaintyNP2	+0.00 +0.00	+0.00 +0.00	+0.00 +0.00
EL_EFF_ID_CorrUncertaintyNP3	+0.00 +0.00	+0.00 +0.00	+0.00 +0.00
EL_EFF_ID_CorrUncertaintyNP4	+0.00 +0.00	+0.00 +0.00	+0.00 +0.00
EL_EFF_ID_CorrUncertaintyNP5	−0.00 +0.00	−0.00 +0.00	−0.00 +0.00
EL_EFF_ID_CorrUncertaintyNP6	−0.00 +0.00	−0.00 +0.00	−0.00 +0.00
EL_EFF_ID_CorrUncertaintyNP7	−0.01 +0.01	−0.01 +0.01	−0.01 +0.01
EL_EFF_ID_CorrUncertaintyNP8	−0.01 +0.01	−0.02 +0.02	−0.01 +0.01
EL_EFF_ID_CorrUncertaintyNP9	−0.04 +0.04	−0.05 +0.05	−0.05 +0.05
EL_EFF_ID_CorrUncertaintyNP10	−0.01 +0.01	−0.02 +0.02	+0.00 −0.00
EL_EFF_ID_CorrUncertaintyNP11	−0.05 +0.05	−0.05 +0.05	−0.05 +0.05
EL_EFF_ID_CorrUncertaintyNP12	+0.01 −0.01	+0.01 −0.01	+0.01 −0.01
EL_EFF_ID_CorrUncertaintyNP13	−0.07 +0.07	−0.06 +0.06	−0.06 +0.06
EL_EFF_ID_CorrUncertaintyNP14	−0.17 +0.17	−0.17 +0.17	−0.19 +0.19
EL_EFF_ID_SIMPLIFIED_UncorrUncertaintyNP0	+0.00 +0.00	+0.00 +0.00	+0.00 +0.00
EL_EFF_ID_SIMPLIFIED_UncorrUncertaintyNP1	+0.00 +0.00	+0.00 +0.00	+0.00 +0.00
EL_EFF_ID_SIMPLIFIED_UncorrUncertaintyNP2	+0.00 +0.00	+0.00 +0.00	+0.00 +0.00
EL_EFF_ID_SIMPLIFIED_UncorrUncertaintyNP3	+0.00 +0.00	+0.00 +0.00	+0.00 +0.00
EL_EFF_ID_SIMPLIFIED_UncorrUncertaintyNP4	+0.00 +0.00	+0.00 +0.00	+0.00 +0.00
EL_EFF_ID_SIMPLIFIED_UncorrUncertaintyNP5	+0.00 +0.00	+0.00 +0.00	+0.00 +0.00
EL_EFF_ID_SIMPLIFIED_UncorrUncertaintyNP6	−0.01 +0.01	−0.01 +0.01	−0.01 +0.01
EL_EFF_ID_SIMPLIFIED_UncorrUncertaintyNP7	−0.02 +0.02	−0.02 +0.02	−0.02 +0.02
EL_EFF_ID_SIMPLIFIED_UncorrUncertaintyNP8	−0.56 +0.56	−0.61 +0.61	−0.57 +0.57
EL_EFF_ID_SIMPLIFIED_UncorrUncertaintyNP9	+0.00 +0.00	+0.00 +0.00	+0.00 +0.00
EL_EFF_ID_SIMPLIFIED_UncorrUncertaintyNP10	+0.00 +0.00	+0.00 +0.00	+0.00 +0.00
EL_EFF_ID_SIMPLIFIED_UncorrUncertaintyNP11	+0.00 +0.00	+0.00 +0.00	+0.00 +0.00
EL_EFF_ID_SIMPLIFIED_UncorrUncertaintyNP12	+0.00 +0.00	+0.00 +0.00	+0.00 +0.00
EL_EFF_ID_SIMPLIFIED_UncorrUncertaintyNP13	+0.00 +0.00	+0.00 +0.00	+0.00 +0.00
EL_EFF_ID_SIMPLIFIED_UncorrUncertaintyNP14	+0.00 +0.00	+0.00 +0.00	+0.00 +0.00
EL_EFF_ID_SIMPLIFIED_UncorrUncertaintyNP15	−0.00 +0.00	−0.00 +0.00	−0.00 +0.00
EL_EFF_Trigger_TOTAL_1NPCOR_PLUS_UNCOR	−0.07 +0.07	−0.07 +0.07	−0.06 +0.06
MUON_EFF_STAT	−0.20 +0.20	−0.21 +0.21	−0.19 +0.19
MUON_EFF_SYS	−1.28 +1.29	−1.29 +1.30	−1.25 +1.25
MUON_ISO_SYS	−0.22 +0.22	−0.22 +0.22	−0.22 +0.22
MUON_ISO_STAT	−0.05 +0.05	−0.05 +0.05	−0.05 +0.05
MUON_EFF_TrigStatUncertainty	−0.02 +0.02	−0.02 +0.01	−0.02 +0.02
MUON_EFF_TrigSystUncertainty	−0.03 +0.03	−0.03 +0.03	−0.03 +0.03
FT_EFF_Eigen_B_0	−0.11 +0.12	−0.08 +0.08	−0.04 +0.04
FT_EFF_Eigen_B_1	−0.01 +0.01	+0.00 −0.00	+0.00 −0.00
FT_EFF_Eigen_B_2	+0.00 −0.00	−0.00 +0.00	−0.00 +0.00
FT_EFF_Eigen_C_0	−0.45 +0.46	−0.09 +0.09	−0.44 +0.44
FT_EFF_Eigen_C_1	+0.01 −0.01	+0.04 −0.04	−0.03 +0.03
FT_EFF_Eigen_C_2	−0.03 +0.03	−0.02 +0.02	−0.03 +0.03
FT_EFF_Eigen_C_3	+0.01 −0.01	−0.00 +0.00	+0.01 −0.01
FT_EFF_Eigen_Light_0	−0.97 +0.98	−0.33 +0.33	−1.23 +1.25
FT_EFF_Eigen_Light_1	+0.09 −0.09	−0.08 +0.08	+0.03 −0.03
FT_EFF_Eigen_Light_2	+0.44 −0.44	+0.34 −0.33	+0.48 −0.47
FT_EFF_Eigen_Light_3	+0.15 −0.15	+0.12 −0.12	+0.04 −0.04
FT_EFF_Eigen_Light_4	−0.03 +0.03	−0.05 +0.05	−0.03 +0.03
FT_EFF_extrapolation	+0.01 −0.01	+0.00 −0.00	+0.01 −0.01
FT_EFF_extrapolation_from_charm	+0.00	+0.00	+0.00
JET_JvtEfficiency	−0.25 +0.25	−0.08 +0.08	−0.25 +0.25
PU_SF	+0.58 −1.07	−1.35 +2.10	−2.08 +1.39
Total	±2.44	±2.85	±3.08
MC Stat.	±0.87	±3.05	±3.90

Table 8.14: Relative experimental uncertainties in % related to efficiency corrections on the NWA VBF signal with mass 700 GeV in the signal regions. The two uncertainty values in each column represent the up and down variations. The row labeled "Total" is the squared sum of all sources, where the largest variation is taken for each parameter. The uncertainty originating from the limited MC statistics in each region is also shown for comparison.

Source	SRIncl	SRVBF1J	SRVBF2J
EL_EFF_Reco_TOTAL_1NPCOR_PLUS_UNCOR	−0.19 +0.19	−0.19 +0.19	−0.19 +0.19
EL_EFF_Iso_TOTAL_1NPCOR_PLUS_UNCOR	−1.09 +1.09	−1.11 +1.11	−1.11 +1.11
EL_EFF_ID_CorrUncertaintyNP0	+0.00 +0.00	+0.00 +0.00	+0.00 +0.00
EL_EFF_ID_CorrUncertaintyNP1	+0.00 +0.00	+0.00 +0.00	+0.00 +0.00
EL_EFF_ID_CorrUncertaintyNP2	+0.00 +0.00	+0.00 +0.00	+0.00 +0.00
EL_EFF_ID_CorrUncertaintyNP3	+0.00 +0.00	+0.00 +0.00	+0.00 +0.00
EL_EFF_ID_CorrUncertaintyNP4	+0.00 +0.00	+0.00 +0.00	+0.00 +0.00
EL_EFF_ID_CorrUncertaintyNP5	−0.00 +0.00	−0.00 +0.00	−0.00 +0.00
EL_EFF_ID_CorrUncertaintyNP6	−0.00 +0.00	−0.00 +0.00	−0.00 +0.00
EL_EFF_ID_CorrUncertaintyNP7	−0.01 +0.01	−0.01 +0.01	−0.02 +0.02
EL_EFF_ID_CorrUncertaintyNP8	−0.02 +0.02	−0.01 +0.01	−0.02 +0.02
EL_EFF_ID_CorrUncertaintyNP9	−0.04 +0.04	−0.05 +0.05	−0.05 +0.05
EL_EFF_ID_CorrUncertaintyNP10	−0.02 +0.02	−0.01 +0.01	−0.02 +0.02
EL_EFF_ID_CorrUncertaintyNP11	−0.05 +0.05	−0.04 +0.04	−0.05 +0.05
EL_EFF_ID_CorrUncertaintyNP12	+0.01 −0.01	+0.01 −0.01	+0.01 −0.01
EL_EFF_ID_CorrUncertaintyNP13	−0.07 +0.07	−0.08 +0.08	−0.07 +0.07
EL_EFF_ID_CorrUncertaintyNP14	−0.18 +0.18	−0.15 +0.15	−0.17 +0.17
EL_EFF_ID_SIMPLIFIED_UncorrUncertaintyNP0	+0.00 +0.00	+0.00 +0.00	+0.00 +0.00
EL_EFF_ID_SIMPLIFIED_UncorrUncertaintyNP1	+0.00 +0.00	+0.00 +0.00	+0.00 +0.00
EL_EFF_ID_SIMPLIFIED_UncorrUncertaintyNP2	+0.00 +0.00	+0.00 +0.00	+0.00 +0.00
EL_EFF_ID_SIMPLIFIED_UncorrUncertaintyNP3	+0.00 +0.00	+0.00 +0.00	+0.00 +0.00
EL_EFF_ID_SIMPLIFIED_UncorrUncertaintyNP4	+0.00 +0.00	+0.00 +0.00	+0.00 +0.00
EL_EFF_ID_SIMPLIFIED_UncorrUncertaintyNP5	+0.00 +0.00	+0.00 +0.00	+0.00 +0.00
EL_EFF_ID_SIMPLIFIED_UncorrUncertaintyNP6	−0.01 +0.01	−0.01 +0.01	−0.01 +0.01
EL_EFF_ID_SIMPLIFIED_UncorrUncertaintyNP7	−0.02 +0.02	−0.02 +0.02	−0.01 +0.01
EL_EFF_ID_SIMPLIFIED_UncorrUncertaintyNP8	−0.56 +0.56	−0.61 +0.61	−0.61 +0.61
EL_EFF_ID_SIMPLIFIED_UncorrUncertaintyNP9	+0.00 +0.00	+0.00 +0.00	+0.00 +0.00
EL_EFF_ID_SIMPLIFIED_UncorrUncertaintyNP10	+0.00 +0.00	+0.00 +0.00	+0.00 +0.00
EL_EFF_ID_SIMPLIFIED_UncorrUncertaintyNP11	+0.00 +0.00	+0.00 +0.00	+0.00 +0.00
EL_EFF_ID_SIMPLIFIED_UncorrUncertaintyNP12	+0.00 +0.00	+0.00 +0.00	+0.00 +0.00
EL_EFF_ID_SIMPLIFIED_UncorrUncertaintyNP13	+0.00 +0.00	+0.00 +0.00	+0.00 +0.00
EL_EFF_ID_SIMPLIFIED_UncorrUncertaintyNP14	+0.00 +0.00	+0.00 +0.00	+0.00 +0.00
EL_EFF_ID_SIMPLIFIED_UncorrUncertaintyNP15	−0.00 +0.00	−0.00 +0.00	−0.00 +0.00
EL_EFF_Trigger_TOTAL_1NPCOR_PLUS_UNCOR	−0.07 +0.07	−0.07 +0.07	−0.07 +0.07
MUON_EFF_STAT	−0.20 +0.20	−0.20 +0.20	−0.20 +0.20
MUON_EFF_SYS	−1.28 +1.29	−1.24 +1.24	−1.27 +1.27
MUON_ISO_SYS	−0.22 +0.22	−0.21 +0.21	−0.22 +0.22
MUON_ISO_STAT	−0.05 +0.05	−0.05 +0.05	−0.05 +0.05
MUON_EFF_TrigStatUncertainty	−0.02 +0.02	−0.02 +0.02	−0.02 +0.02
MUON_EFF_TrigSystUncertainty	−0.03 +0.03	−0.03 +0.03	−0.03 +0.03
FT_EFF_Eigen_B_0	−0.06 +0.06	+0.00 +0.00	−0.01 +0.01
FT_EFF_Eigen_B_1	−0.01 +0.01	+0.00 +0.00	−0.00 +0.00
FT_EFF_Eigen_B_2	+0.00 −0.00	+0.00 +0.00	−0.00 +0.00
FT_EFF_Eigen_C_0	−0.79 +0.79	−0.11 +0.11	−0.42 +0.42
FT_EFF_Eigen_C_1	−0.06 +0.06	+0.04 −0.04	−0.08 +0.08
FT_EFF_Eigen_C_2	−0.04 +0.04	−0.02 +0.02	−0.02 +0.02
FT_EFF_Eigen_C_3	+0.01 −0.01	−0.00 +0.00	+0.01 −0.01
FT_EFF_Eigen_Light_0	−0.91 +0.92	−0.16 +0.16	−0.71 +0.71
FT_EFF_Eigen_Light_1	+0.03 −0.03	−0.05 +0.05	+0.01 −0.01
FT_EFF_Eigen_Light_2	+0.25 −0.25	+0.14 −0.14	+0.17 −0.17
FT_EFF_Eigen_Light_3	−0.01 +0.01	+0.01 −0.01	−0.03 +0.03
FT_EFF_Eigen_Light_4	−0.01 +0.01	−0.01 +0.01	−0.02 +0.02
FT_EFF_extrapolation	+0.01 −0.01	+0.00 +0.00	+0.01 −0.01
FT_EFF_extrapolation_from_charm	+0.00	+0.00	+0.00
JET_JvtEfficiency	−0.15 +0.15	−0.02 +0.02	−0.08 +0.08
PU_SF	+1.14 −1.18	+0.28 −0.38	+1.83 −2.08
Total	±2.51	±1.88	±2.91
MC Stat.	±2.01	±2.87	±1.78

8.5 Theoretical uncertainties on top quark background

The theoretical uncertainties for the top-quark background in the ggF and VBF categories are shown in Table 8.15 (a) and (b), respectively. Apart from those already mentioned previously, the "Radiation" in the tables corresponds to the "Scale" uncertainty, as defined in Section 8.1. Besides, the $t\bar{t}$ process and the dominant single top-quark process Wt share the same final state and interference effects between the two processes are expected. A large part of the effects is removed when generating the Wt events separately from the $t\bar{t}$ events by using the diagram removal (DR) scheme which simply removes all diagrams in the NLO Wt amplitudes that are doubly resonant or the diagram subtraction (DS) scheme which modified the NLO Wt cross section by implementing a subtraction term designed to cancel locally the $t\bar{t}$ contributions [133]. The "$Wt - t\bar{t}$ interference" uncertainty in the tables represents a comparison between two difference schemes. The quantity α corresponds to the extrapolation uncertainties from the top or WW CR to the SR, while β corresponds to the extrapolation from the top CR to the WW CR.

The PDF uncertainties shown in the tables are actually only normalisation uncertainties, which are used only in the CRs. In the SRs, the PDF uncertainties are estimated to be m_{T}-dependent and shown in Figure 8.1, where "NNPDF total" corresponds to the uncertainties of the NNPDF set, the differences between the NNPDF and the other PDF sets are shown by the other curves and the "Total" corresponds to the envelope of all the uncertainties (see Section 8.1).

As mentioned in Section 8.1, two shape uncertainties are considered for the top-quark background (except for the m_{T}-dependent PDF uncertainties discussed above), one being the Scale uncertainty, and the other being the leading lepton p_{T} reweighting uncertainty. These shape uncertainties are shown in Figure 8.2 (left). To avoid the statistical fluctuation, the uncertainties are fitted with the polynomial function. The better one between the 1st and 2nd order functions is chosen. This is also shown in Figure 8.2 (right), taking the fit result of one of the shape uncertainties as an example. The uncertainties are considered only in the quasi-inclusive ggF SR. For the VBF SRs, there is no significant shape uncertainties observed considering the lower statistics and number of bins in the m_{T} distributions. The number of m_{T} bins that are used to estimate the shape uncertainties corresponds to those used in the statistics fit.

Table 8.15: Relative theoretical uncertainties in % of the top-quark background in (a) the ggF SR (2nd column), WW CR (3rd column), top CR (4th column) and of the transform factor from the top CR to the ggF SR (α, 5th column) and from the top CR to the WW CR (β, last column); in (b) the VBF1J SR (2nd column), VBF2J SR (3rd column), VBF1J WW CR (4th column), VBF top CR (5th column) and of the transform factor from the VBF top CR to the VBF1J SR (α_{VBF1J}, 6th column), to the VBF2J SR (α_{VBF2J}, 7th column) and to the VBF1J WW CR (β, last column).

(a) Uncertainties in the ggF category

Error source	SRIncl	WWCRIncl	topCRIncl	$\alpha = N_{\text{SRIncl}}/N_{\text{topCRIncl}}$	$\beta = N_{\text{WWCRIncl}}/N_{\text{topCRIncl}}$
ME+PS(Sherpa)	$\mp 1.3 \pm 0.7$	$\pm 1.1 \pm 1.6$	$\mp 0.34 \pm 0.35$	$\mp 0.99 \pm 0.75\,[0.20, 0.73]$	$\pm 1.4 \pm 1.7\,[0.4, 1.6]$
Radiation	$\pm 3.0 \pm 0.3$	$\pm 6.3 \pm 0.5$	$\mp 0.21 \pm 0.13$	$\pm 3.2 \pm 0.3\,[0.2, 0.2]$	$\pm 6.5 \pm 0.6\,[0.4, 0.4]$
$Wt - t\bar{t}$ interference	$\mp 0.42 \pm 0.25$	$\mp 1.6 \pm 0.5$	$\mp 0.66 \pm 0.13$	$\pm 0.24 \pm 0.28\,[0.20, 0.20]$	$\mp 0.99 \pm 0.56\,[0.39, 0.40]$
Relative variation of $\sigma_{\text{st}}(\pm 20)$	∓ 4.2	∓ 4.0	∓ 2.6	∓ 1.3	∓ 1.4
PDF (up/down)	± 2.5	± 3.2	± 3.0	± 0.86	± 0.55

(b) Uncertainties in the VBF categories

Error source	SRVBF1J	SRVBF2J	WWCRVBF1J	topCRVBF	$\alpha_{\text{VBF1J}} = \frac{N_{\text{SRVBF1J}}}{N_{\text{topCRVBF}}}$	$\alpha_{\text{VBF2J}} = \frac{N_{\text{SRVBF2J}}}{N_{\text{topCRVBF}}}$	$\beta = \frac{N_{\text{WWCRVBF1J}}}{N_{\text{topCRVBF}}}$
ME+PS(Sherpa)	$\mp 1.0 \pm 4.0$	$\pm 9.5 \pm 4.7$	$\pm 9.4 \pm 6.1$	$\pm 10 \pm 1$	$\mp 10 \pm 4\,[1, 4]$	$\mp 0.7 \pm 4.4\,[1.1, 4.3]$	$\mp 0.8 \pm 5.7\,[1.6, 5.5]$
Radiation	$\mp 1.6 \pm 1.5$	$\pm 5.0 \pm 1.6$	$\mp 3.9 \pm 2.3$	$\pm 1.5 \pm 0.5$	$\mp 3.0 \pm 1.5\,[1.1, 1.1]$	$\pm 3.4 \pm 1.7\,[1.2, 1.2]$	$\mp 5.3 \pm 2.3\,[1.7, 1.5]$
$Wt - t\bar{t}$ interference	$\mp 0.2 \pm 1.5$	$\mp 1.2 \pm 1.5$	$\pm 1.1 \pm 2.3$	$\mp 0.44 \pm 0.42$	$\pm 0.27 \pm 1.6\,[1.1, 1.1]$	$\mp 0.80 \pm 1.6\,[1.1, 1.1]$	$\pm 1.5 \pm 2.3\,[1.6, 1.6]$
Relative variation of $\sigma_{\text{st}}(\pm 20)$	± 5.9	± 2.1	± 5.3	± 1.3	± 4.6	± 0.83	± 4.0
PDF (up/down)	± 2.6	± 3.4	± 2.7	± 3.7	± 2.0	± 1.6	± 1.7

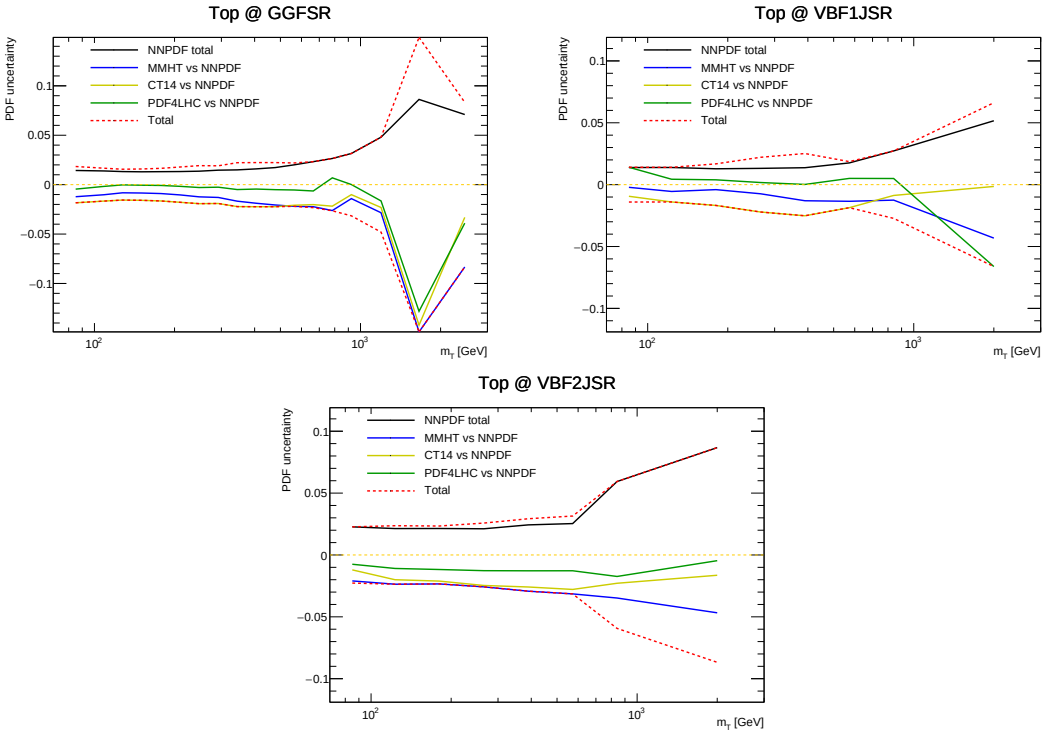

Figure 8.1: PDF uncertainties as a function of m_{T} for the ggF quasi-inclusive SR (top left), VBF $n_{\mathrm{jet}} = 1$ (top right) and $n_{\mathrm{jet}} \geq 2$ (bottom) SRs for the top-quark process, where "NNPDF total" corresponds to the uncertainties of the NNPDF set, the difference between the NNPDF and the other PDF sets are shown by the other curves and the "Total" used in the analysis corresponds to the envelope of all the uncertainties.

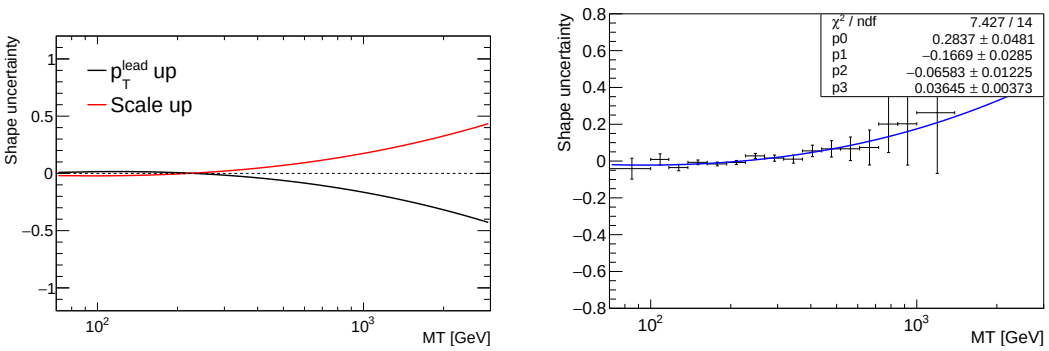

Figure 8.2: Comparison of fitted shape uncertainties of the considered sources for the top-quark background (left). Shape uncertainty on m_{T} for a selected example for the top-quark background (right). Some of the error sources have up and down variations, one of them are shown here for clarity.

8.6 Theoretical uncertainties on WW background

The theoretical uncertainties for the WW background in the ggF and VBF categories are shown in Tables 8.16 and 8.17, respectively. Apart from those already mentioned previously, the "Qsf" represents the resummation scale uncertainty which has been varied up and down by a factor of 2. The "CKKW" corresponds to the Catani-Krauss-Kuhn-Webber (CKKW) [134] matching scale uncertainty, that is varied between 15 GeV and 30 GeV from the nominal scale of 20 GeV. The "CSS" corresponds to the Catani-Seymour Scheme (CSS) uncertainty on the parton shower scheme, which is estimated by comparing the default scheme (CSS_KIN_SCHEME=0) with the alternative scheme (CSS_KIN_SCHEME=1). The quantity α corresponds to the extrapolation uncertainties from the top or WW CR to the SR.

Table 8.16: Relative theoretical uncertainties in % of the WW background in the ggF quasi-inclusive SR (2nd column), the corresponding WW CR (3rd column) and on the transfer factor from the CR to the SR (last column). The two numbers in the brackets show the uncertainty contributions from the nominal and alternative sample, respectively.

Error source	SRIncl	WWCRIncl	$\alpha = N_{\text{SRIncl}}/N_{\text{WWCRIncl}}$
ME+PS(PowPy8)	$\mp 2.4 \pm 0.3$	$\pm 2.6 \pm 0.6$	$\mp 4.9 \pm 0.6\,[0.6, 0.3]$
Renormalisation scale	∓ 1.7	∓ 0.95	∓ 0.75
Factorisation scale	∓ 0.16	∓ 0.04	∓ 0.12
Qsf	$\mp 3.1 \pm 0.3$	$\mp 2.9 \pm 0.5$	$\mp 0.26 \pm 0.58\,[0.42, 0.40]$
CKKW	$\mp 0.89 \pm 0.28$	$\mp 0.73 \pm 0.56$	$\mp 0.15 \pm 0.63\,[0.43, 0.45]$
CSS	$\mp 0.45 \pm 0.40$	$\pm 0.09 \pm 0.83$	$\mp 0.54 \pm 0.92\,[0.50, 0.77]$
PDF(up/down)	± 2.7	± 3.6	± 1.1

Table 8.17: Relative theoretical uncertainties in % of the WW background in the VBF $N_{\text{jet}} = 1$ SR (2nd column), the corresponding WW CR (3rd column), on the transfer factor from the CR to the SR (4th column) and in the VBF $N_{\text{jet}} \geq 2$ SR (last column). The two numbers in the brackets show the uncertainty contributions from the nominal and alternative sample, respectively.

Error source	SRVBF1J	WWCRVBF1J	$\alpha = N_{\text{SRVBF1J}}/N_{\text{WWCRVBF1J}}$	SRVBF2J
ME+PS(PowPy8)	$\mp 11 \pm 2$	$\mp 12 \pm 2$	$\pm 1.1 \pm 2.8\,[2.5, 1.3]$	$\mp 38 \pm 1$
Renormalisation scale	∓ 7.3	∓ 11	± 4.0	∓ 18
Factorisation scale	∓ 0.48	± 1.3	∓ 1.8	∓ 1.6
Qsf	$\mp 5.0 \pm 1.6$	$\mp 2.3 \pm 2.0$	$\mp 2.7 \pm 2.6\,[1.9, 1.7]$	$\mp 1.4 \pm 2.3$
CKKW	$\pm 0.6 \pm 1.7$	$\mp 1.7 \pm 2.4$	$\pm 2.3 \pm 3.0\,[2.2, 2.0]$	$\mp 11 \pm 3$
CSS	$\mp 3.8 \pm 2.8$	$\mp 0.5 \pm 4.5$	$\mp 3.3 \pm 5.2\,[2.1, 4.8]$	$\mp 5 \pm 4$
PDF(up/down)	± 2.3	± 2.8	± 0.76	± 2.1

As with the top quark background, the PDF uncertainties for the WW background shown in the tables are also only normalisation uncertainties, which are used only in the CRs. In the SRs, the PDF uncertainties are estimated to be m_{T}-dependent and shown in Figure 8.3, which are treated in the same way as that for the top quark background.

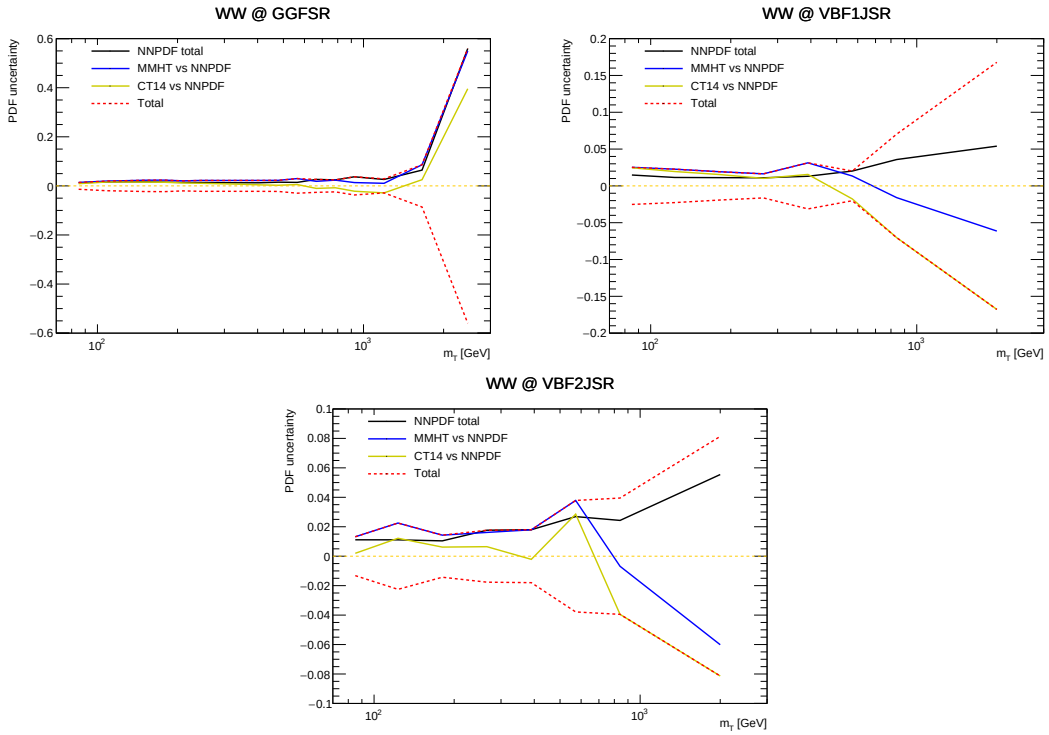

Figure 8.3: PDF uncertainties as a function of m_{T} for the ggF quasi-inclusive SR (top left), VBF $n_{\mathrm{jet}} = 1$ (top right) and $n_{\mathrm{jet}} \geq 2$ (bottom) SRs for the WW process, where "NNPDF total" corresponds to the uncertainties of the NNPDF set, the difference between the NNPDF and the other PDF sets are shown by the other curves and the "Total" used in the analysis corresponds to the envelope of all the uncertainties.

As mentioned in Section 8.1, two shape uncertainties are considered for the WW background (except for the m_{T}-dependent PDF uncertainties discussed above), one being the ME+PS uncertainty, and the other being the $q\bar{q} \to WW$ Sherpa NNLO QCD + NLO EW reweighting uncertainty. These shape uncertainties are shown in Figure 8.4 (left), where the latter uncertainty actually includes also the normalisation uncertainty. To avoid the statistical fluctuation, the uncertainties are fitted with the polynomial function. The better one between the 1st and 2nd order functions is chosen. This is also shown in Figure 8.4 (right), taking the fit result of one of the shape uncertainties as an example. The uncertainties are considered only in the quasi-inclusive ggF SR. For the VBF SRs, there is no significant shape uncertainties observed considering the lower statistics and

number of bins in the m_{T} distributions. The number of m_{T} bins that are used to estimate the shape uncertainties corresponds to those used in the statistics fit.

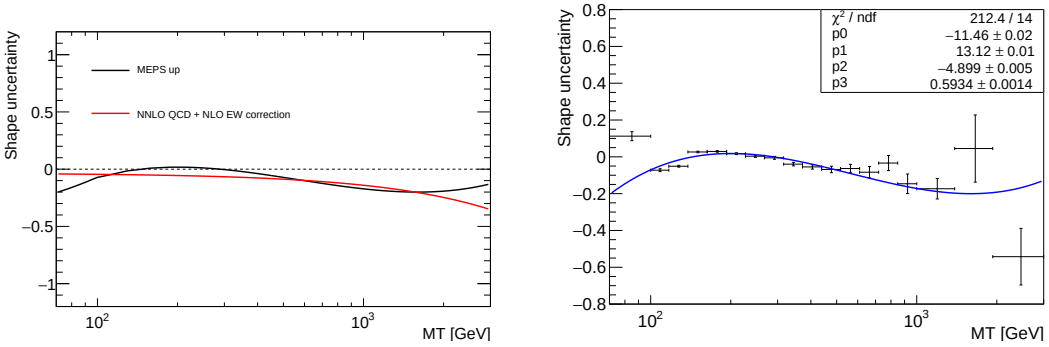

Figure 8.4: Comparison of fitted shape uncertainties of the considered sources for the WW background (left). Shape uncertainty on m_{T} for a selected example for the WW background (right). The uncertainty on the NNLO QCD + NLO EW correction contains not only the shape uncertainty but also a normalisation uncertainty. Some of the error sources have up and down variations, one of them are shown here for clarity.

8.7 Theoretical uncertainties on signals

The theoretical uncertainties for the signals were briefly mentioned in Section 8.1 with overall results. However, technically, those uncertainties have some dependences on the masses of the signals, and this is presented in this section.

The QCD renormalisation and factorisation scales uncertainties for the ggF and VBF signals are shown in Figures 8.5 and 8.6, respectively. For the ggF signals in the quasi-inclusive ggF category, the uncertainties are found to be negligibly small and thus not shown.

The PDF uncertainties for the ggF and VBF signals are shown in Figure 8.7 (a,c,e) and (b,d,f), respectively.

The parton shower (model and tune) uncertainties for the ggF and VBF signals are shown in Figure 8.8 (a,c,e) and (b,d,f), respectively.

The event category migration uncertainties are further discussed in Appendix H.

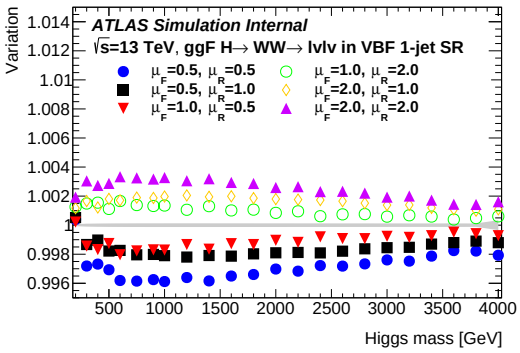

(a) Scale uncertainties ($N_{\text{jet}} = 1$ VBF)

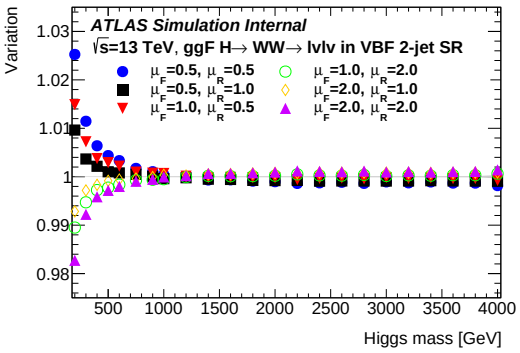

(b) Scale uncertainties ($N_{\text{jet}} = 2$ VBF)

Figure 8.5: Variations of the scale uncertainties on the selection efficiency as a function of the resonance mass for ggF production. This uncertainty is presented separately for $N_{\text{jet}} = 1$ VBF (left) and ≥ 2 VBF (right).

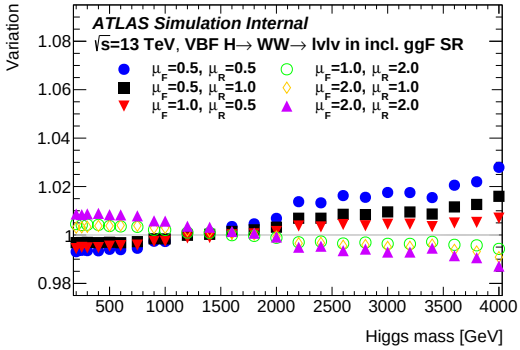

(a) Scale uncertainties (ggF inclusive)

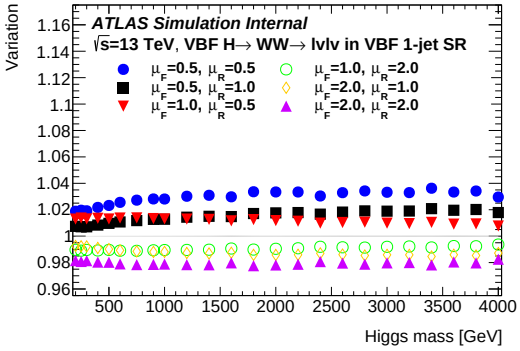

(b) Scale uncertainties ($N_{\text{jet}} = 1$ VBF)

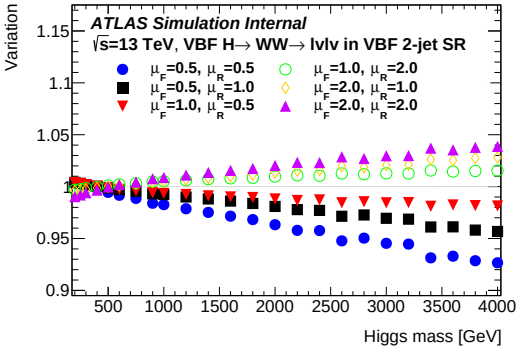

(c) Scale uncertainties ($N_{\text{jet}} = 2$ VBF)

Figure 8.6: Variations of the scale uncertainties on the selection efficiency as a function of the resonance mass for VBF produced Higgs-like particles. This uncertainty is presented separately for ggF inclusive (top), $N_{\text{jet}} = 1$ VBF (bottom left) and ≥ 2 VBF (bottom right).

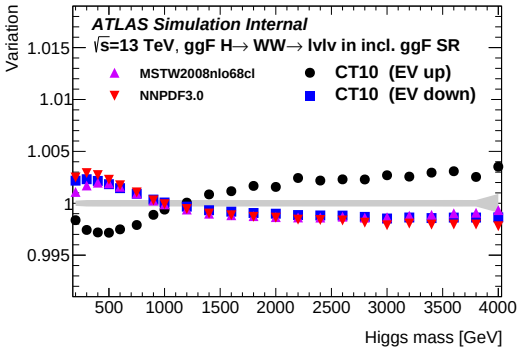

(a) PDF uncertainties for ggF signals (ggF inclusive)

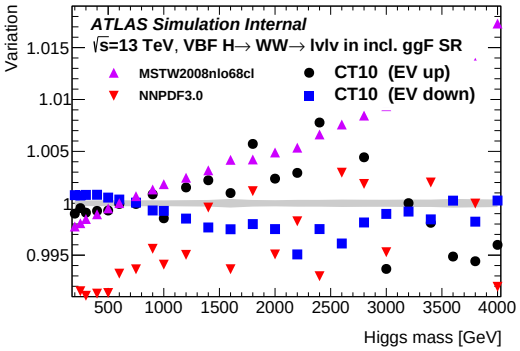

(b) PDF uncertainties for VBF signals (ggF inclusive)

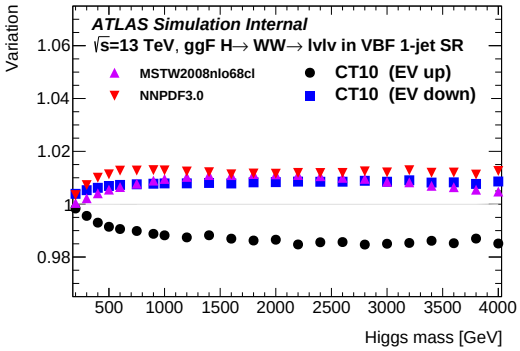

(c) PDF uncertainties for ggF signals ($N_{\text{jet}} = 1$ VBF)

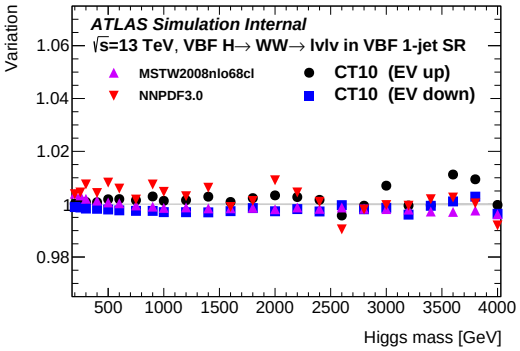

(d) PDF uncertainties for VBF signals ($N_{\text{jet}} = 1$ VBF)

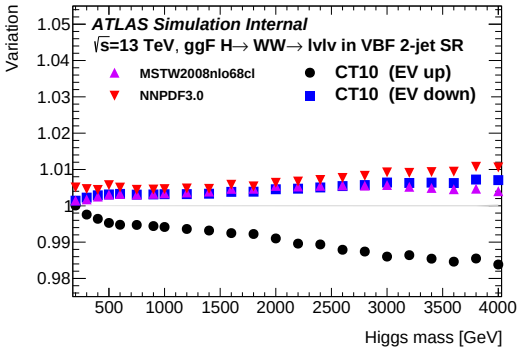

(e) PDF uncertainties for ggF signals ($N_{\text{jet}} \geq 2$ VBF)

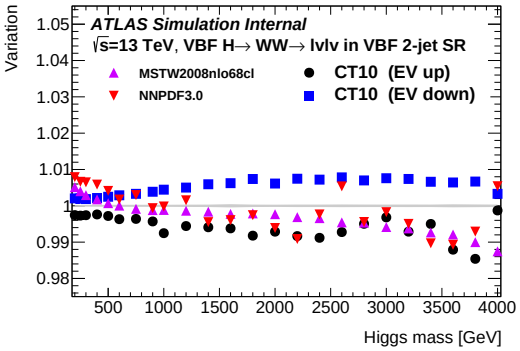

(f) PDF uncertainties for VBF signals ($N_{\text{jet}} \geq 2$ VBF)

Figure 8.7: Variations of the PDF uncertainties for ggF (left column) and VBF (right column) signals on the selection efficiency as a function of the resonance mass, where EV stands for envelope and EV1, EV2, FSR and MPI are different sets of parton shower parameters. These two uncertainties are presented separately for ggF inclusive (top row), $N_{\text{jet}} = 1$ VBF (middle row) and ≥ 2 VBF (bottom row).

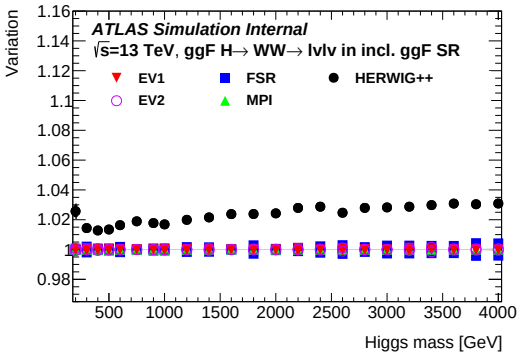

(a) PS uncertainties for ggF signals (ggF inclusive)

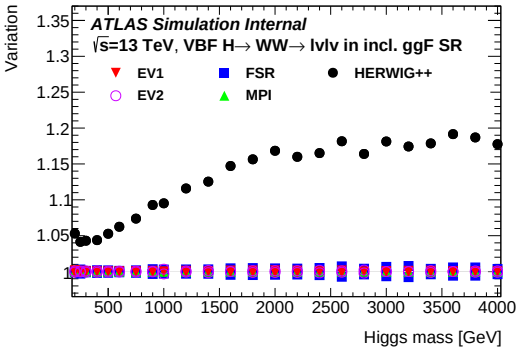

(b) PS uncertainties for VBF signals (ggF inclusive)

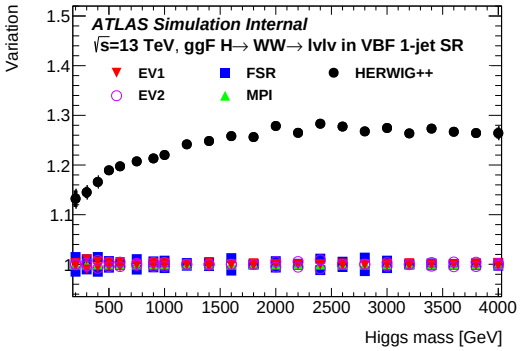

(c) PS uncertainties for ggF signals ($N_{\text{jet}} = 1$ VBF)

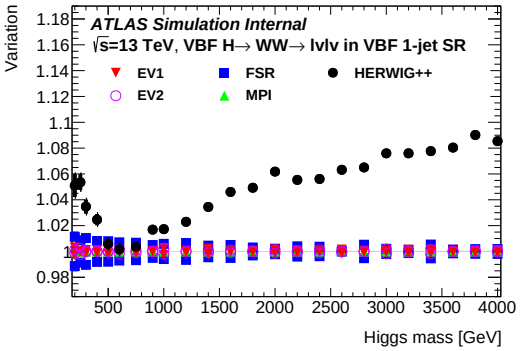

(d) PS uncertainties for VBF signals ($N_{\text{jet}} = 1$ VBF)

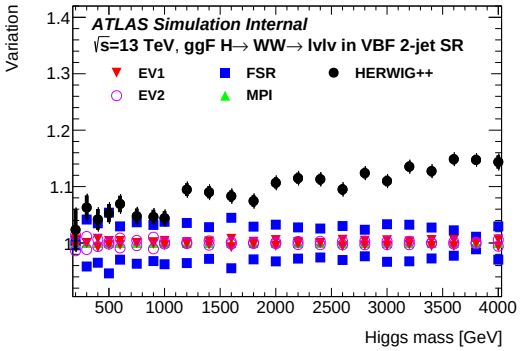

(e) PS uncertainties for ggF signals ($N_{\text{jet}} \geq 2$ VBF)

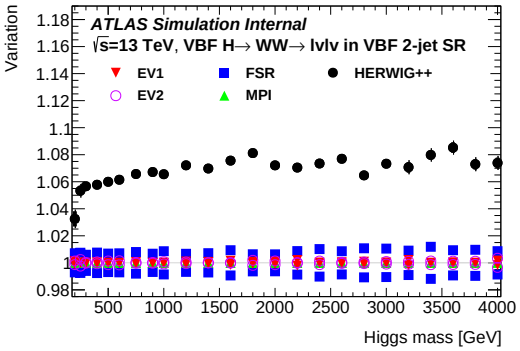

(f) PS uncertainties for VBF signals ($N_{\text{jet}} \geq 2$ VBF)

Figure 8.8: Variations of the parton shower model and tune uncertainties for ggF (left column) and VBF (right column) signals on the selection efficiency as a function of the resonance mass, where EV stands for envelope and EV1, EV2, FSR and MPI are different sets of parton shower parameters. These two uncertainties are presented separately for ggF inclusive (top row), $N_{\text{jet}} = 1$ VBF (middle row) and ≥ 2 VBF (bottom row).

8.8 Systematic uncertainties on the W+jets background

The systematic errors associated with the fake factor evaluation can be found in Table 8.18 and consist of several contributions.

Table 8.18: Relative systematic uncertainties (in %) associated with the fake factor evaluation at the pre-selection level. The column labeled "Total" is the squared sum of all sources.

Kinematic region ($\|\eta\|$ and p_{T} range)	Flavour composition	EW subtraction	p_{T} dependence	Statistics	Total
Muon:					
$0 < \|\eta\| < 1.1$					
$15 - 20$ GeV	39	1	–	1	39
$20 - 25$ GeV	39	2	–	3	39
$1.1 < \|\eta\| < 2.5$					
$15 - 20$ GeV	39	1	–	1	39
$20 - 25$ GeV	39	3	–	2	39
$0 < \|\eta\| < 2.5$					
$25 - 1000$ GeV	39	21	11	3	46
Electron:					
$0 < \|\eta\| < 1.5$					
$15 - 20$ GeV	36	1	–	2	36
$20 - 25$ GeV	36	2	–	4	37
$25 - 35$ GeV	36	4	¡1	4	37
$35 - 1000$ GeV	36	14	13	8	42
$1.5 < \|\eta\| < 2.5$					
$15 - 20$ GeV	36	1	–	3	36
$20 - 25$ GeV	36	1	–	4	37
$25 - 35$ GeV	36	3	1	4	37
$35 - 1000$ GeV	36	7	10	7	39

Apart from those uncertainties mentioned in Section 8.1, an addtional p_{T} dependence uncertainty is introduced. At large p_{T}, the number of fake lepton events is limited in particular for muons. For this reason, the fake-factors are determined for a single bin covering a large p_{T} range and combining the central and forward regions. Its potential p_{T} dependence is studied by fitting the nominal fake-factors determined in finer p_{T} bins by a first-order polynomial function (see Figure 8.9). The difference, between using the nominal fake-factor and using a fake-factor based on the fit at a p_{T} value corresponding to the mean p_{T} value of the W+jets control sample in the relevant large p_{T} bin, is assigned as an additional systematic uncertainty associated with the potential p_{T} dependence of the fake-factors.

Propagated uncertainties of the nominal and triggered fake-factors are shown for different SRs and CRs in Tables 8.19 and 8.20, respectively. The systematic uncertainty of the EW background subtraction in the W+jets control sample is

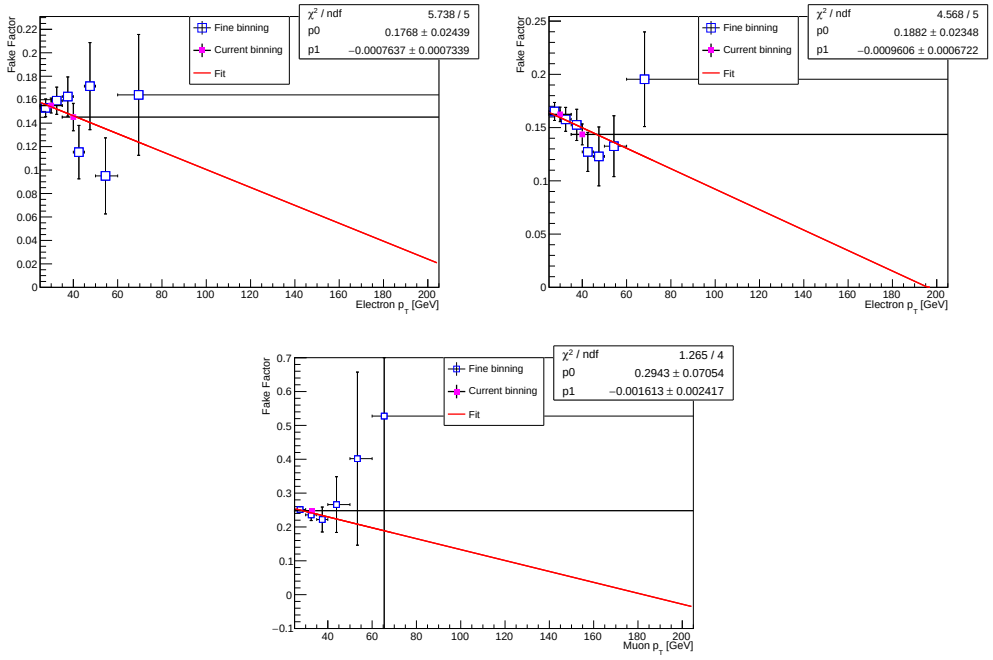

Figure 8.9: Comparison of nominal fake-factors determined with finer p_{T} bins from di-jet samples in data (blue open squares) and the default one (magenta solid squares) for electrons (top) and muons (bottom) and in central (left) and forward (right) regions. The error bars show the statistical uncertainties. The red curve corresponds to a fit with the first order polynomial function to the fake-factors in the finer p_{T} bins.

neglected since it is estimated to be smaller than the uncertainties of the fake-factors and the statistical uncertainty of the W+jets control sample. This is a conservative approach considering this uncertainty of the dominant EW background (top-quark and WW) may be correlated with that of the same background processes in the SR.

Table 8.19: Systematic uncertainties associated with the fake-factor evaluation in the signal regions. The first two rows correspond to the uncertainty of the EW background subtraction, the 3rd and 4th rows correspond to the p_{T} dependent uncertainties, the 5th and 6th rows correspond to the uncertainties of the flavour composition and the other rows are due to the data statistics of the di-jet samples used to determine the nominal and triggered fake-factors, with the last two indices standing for the p_{T} and η bins (when the two η bins are combined it is shown as 1.2), respectively. The two uncertainty values in each column represent the up and down variations. The row labeled "Total" is the squared sum of all sources, where the largest variation is taken for each parameter. The last row shows the statistical uncertainty of the W+jets control sample (both data and the subtracted EW MC samples).

Source	SRIncl	SRVBF1J	SRVBF2J
elFF_EWSUBTR	−9.45 +9.45	−7.01 +7.01	−12.27 +12.27
muFF_EWSUBTR	−6.75 +6.75	−9.15 +9.15	−7.84 +7.84
elFF_PtDepen	−10.76 +10.76	−9.24 +9.24	−12.70 +12.70
muFF_PtDepen	−6.44 +6.44	−8.76 +8.76	−6.75 +6.75
elFF_SAMPLECOMPOSITION	−25.91 +25.91	−22.28 +22.28	−25.44 +25.44
muFF_SAMPLECOMPOSITION	−10.93 +10.93	−14.86 +14.86	−11.44 +11.44
elFF_STAT_combined_1_1	−0.00 −0.00	−0.00 −0.00	−0.00 −0.00
elFF_STAT_combined_1_2	−0.00 −0.00	−0.00 −0.00	−0.00 −0.00
elFF_STAT_combined_2_1	−0.00 −0.00	−0.00 −0.00	−0.00 −0.00
elFF_STAT_combined_2_2	−0.00 −0.00	−0.00 −0.00	−0.00 −0.00
elFF_STAT_combined_3_1	−0.26 +0.26	−0.35 +0.35	−0.37 +0.37
elFF_STAT_combined_3_2	−0.16 +0.16	−0.08 +0.08	−0.34 +0.34
elFF_STAT_combined_4_1	−2.06 +2.06	−2.33 +2.33	−4.35 +4.35
elFF_STAT_combined_4_2	−0.99 +0.99	−0.84 +0.84	+0.58 −0.58
elFF_STAT_2015_3_1	−0.00 +0.00	−0.00 −0.00	−0.00 −0.00
elFF_STAT_2015_3_2	−0.00 +0.00	+0.00 −0.00	−0.00 −0.00
elFF_STAT_2015_4_1	−0.05 +0.05	−0.05 +0.05	+0.01 −0.01
elFF_STAT_2015_4_2	−0.01 +0.01	−0.02 +0.02	+0.04 −0.04
elFF_STAT_2016_3_1	+0.00 −0.00	+0.00 −0.00	−0.00 −0.00
elFF_STAT_2016_3_2	−0.00 +0.00	−0.00 −0.00	−0.00 −0.00
elFF_STAT_2016_4_1	−0.08 +0.08	+0.01 −0.01	−0.49 +0.49
elFF_STAT_2016_4_2	−0.02 +0.02	+0.00 −0.00	+0.01 −0.01
elFF_STAT_2016D_3_1	−0.00 +0.00	+0.01 −0.01	+0.02 −0.02
elFF_STAT_2016D_3_2	+0.00 −0.00	+0.00 −0.00	+0.01 −0.01
elFF_STAT_2016D_4_1	−0.21 +0.21	−0.07 +0.07	−0.12 +0.12
elFF_STAT_2016D_4_2	−0.05 +0.05	−0.05 +0.05	+0.04 −0.04
muFF_STAT_combined_1_1	−0.00 −0.00	−0.00 −0.00	−0.00 −0.00
muFF_STAT_combined_1_2	−0.00 −0.00	−0.00 −0.00	−0.00 −0.00
muFF_STAT_combined_2_1	−0.00 −0.00	−0.00 −0.00	−0.00 −0.00
muFF_STAT_combined_2_2	−0.00 −0.00	−0.00 −0.00	−0.00 −0.00
muFF_STAT_combined_3_1.2	−0.55 +0.55	−0.72 +0.72	−0.86 +0.86
muFF_STAT_2015_2_1	−0.00 −0.00	−0.00 −0.00	−0.00 −0.00
muFF_STAT_2015_2_2	−0.00 −0.00	−0.00 −0.00	−0.00 −0.00
muFF_STAT_2015_3_1.2	−0.01 +0.01	−0.00 −0.00	+0.35 −0.35
muFF_STAT_2016_3_1.2	−0.04 +0.04	−0.09 +0.09	−0.10 +0.10
muFF_STAT_2016D_3_1.2	−0.16 +0.16	−0.20 +0.20	−0.22 +0.22
Total	±33.00	±31.93	±34.90
MC Stat.	±3.50	±11.74	±46.45

Table 8.20: Systematic uncertainties associated with the fake factor evaluation in the control regions. The first two rows correspond to the uncertainty of the EW background subtraction, the 3rd and 4th rows correspond to the p_{T} dependent uncertainties, the 5th and 6th rows correspond to the uncertainties of the flavour composition and the other rows are due to the data statistics of the di-jet samples used to determine the nominal and triggered fake-factors, with the last two indices standing for the p_{T} and η bins (when the two η bins are combined it is shown as 1.2), respectively. The two uncertainty values in each column represent the up and down variations. The row labeled "Total" is the squared sum of all sources, where the largest variation is taken for each parameter. The last row shows the statistical uncertainty of the W+jets control sample (both data and the subtracted EW MC samples).

Source	TopCRIncl	TopCRVBF	WWCRIncl	WWCRVBF1J
elFF_EWSUBTR	−10.58 +10.58	−8.26 +8.26	−9.04 +9.04	−4.56 +4.56
muFF_EWSUBTR	−9.03 +9.03	−10.72 +10.72	−5.68 +5.68	−9.31 +9.31
elFF_PtDepen	−9.70 +9.70	−7.55 +7.55	−10.68 +10.68	−3.51 +3.51
muFF_PtDepen	−9.03 +9.03	−10.51 +10.51	−5.84 +5.84	−8.38 +8.38
elFF_SAMPLECOMPOSITION	−21.86 +21.86	−19.56 +19.56	−26.86 +26.86	−22.88 +22.88
muFF_SAMPLECOMPOSITION	−15.32 +15.32	−17.81 +17.81	−9.90 +9.90	−14.21 +14.21
elFF_STAT_combined_1_1	−0.00 −0.00	−0.00 −0.00	+0.00 +0.00	−0.00 −0.00
elFF_STAT_combined_1_2	−0.00 −0.00	−0.00 −0.00	+0.00 +0.00	−0.00 −0.00
elFF_STAT_combined_2_1	−0.00 −0.00	−0.00 −0.00	+0.00 +0.00	−0.00 −0.00
elFF_STAT_combined_2_2	−0.00 −0.00	−0.00 −0.00	+0.00 +0.00	−0.00 −0.00
elFF_STAT_combined_3_1	−0.12 +0.12	−0.24 +0.24	−0.25 +0.25	−1.02 +1.02
elFF_STAT_combined_3_2	−0.05 +0.05	−0.04 +0.04	−0.23 +0.23	−0.34 +0.34
elFF_STAT_combined_4_1	−1.23 +1.23	−0.75 +0.75	−1.95 +1.95	−0.78 +0.78
elFF_STAT_combined_4_2	−0.42 +0.42	−0.39 +0.39	−1.22 +1.22	−0.24 +0.24
elFF_STAT_2015_3_1	−0.00 +0.00	+0.00 −0.00	−0.00 +0.00	−0.01 +0.01
elFF_STAT_2015_3_2	−0.00 +0.00	+0.00 −0.00	−0.01 +0.01	+0.00 −0.00
elFF_STAT_2015_4_1	−0.05 +0.05	−0.00 +0.00	−0.00 +0.00	−0.08 +0.08
elFF_STAT_2015_4_2	−0.01 +0.01	−0.02 +0.02	−0.00 +0.00	−0.03 +0.03
elFF_STAT_2016_3_1	−0.00 +0.00	−0.01 +0.01	+0.00 −0.00	−0.03 +0.03
elFF_STAT_2016_3_2	+0.00 −0.00	−0.02 +0.02	+0.00 −0.00	−0.01 +0.01
elFF_STAT_2016_4_1	−0.08 +0.08	−0.34 +0.34	−0.10 +0.10	+0.05 −0.05
elFF_STAT_2016_4_2	−0.01 +0.01	−0.01 +0.01	−0.01 +0.01	+0.00 −0.00
elFF_STAT_2016D_3_1	−0.02 +0.02	−0.01 +0.01	−0.00 +0.00	−0.04 +0.04
elFF_STAT_2016D_3_2	−0.00 +0.00	+0.00 −0.00	+0.00 −0.00	−0.01 +0.01
elFF_STAT_2016D_4_1	−0.42 +0.42	−0.17 +0.17	−0.16 +0.16	−0.03 +0.03
elFF_STAT_2016D_4_2	−0.06 +0.06	−0.07 +0.07	−0.08 +0.08	−0.02 +0.02
muFF_STAT_combined_1_1	−0.00 −0.00	−0.00 −0.00	+0.00 +0.00	−0.00 −0.00
muFF_STAT_combined_1_2	−0.00 −0.00	−0.00 −0.00	+0.00 +0.00	−0.00 −0.00
muFF_STAT_combined_2_1	−0.00 −0.00	−0.00 −0.00	+0.00 +0.00	−0.00 −0.00
muFF_STAT_combined_2_2	−0.00 −0.00	−0.00 −0.00	+0.00 +0.00	−0.00 −0.00
muFF_STAT_combined_3_1.2	−0.94 +0.94	−0.92 +0.92	−0.59 +0.59	−0.53 +0.53
muFF_STAT_2015_2_1	−0.00 −0.00	−0.00 −0.00	+0.00 +0.00	−0.00 −0.00
muFF_STAT_2015_2_2	−0.00 −0.00	−0.00 −0.00	+0.00 +0.00	−0.00 −0.00
muFF_STAT_2015_3_1.2	−0.01 +0.01	+0.00 −0.00	−0.01 +0.01	−0.03 +0.03
muFF_STAT_2016_3_1.2	−0.04 +0.04	−0.12 +0.12	−0.06 +0.06	−0.04 +0.04
muFF_STAT_2016D_3_1.2	−0.15 +0.15	−0.20 +0.20	−0.07 +0.07	−0.30 +0.30
Total	±32.93	±32.43	±32.98	±30.29
MC Stat.	±5.56	±16.75	±5.88	±21.48

Chapter 9

Results

In this section, the results are presented. This includes a brief description of the statistics method used in this analysis (Section 9.1), the pre-fit and post-fit results in the SRs (Sections 9.2 and 9.3) and the upper limits (Section 9.4). "Pre-fit" and "post-fit" correspond to the results before and after the simultaneous fit (see Chapter 7 and Section 9.1), respectively. The effect of the interference between signal and backgrounds is studied and discussed in Appendix G.

9.1 General statistics methodology

The statistical method used in this analysis to interpret the results is same as that used in Ref. [135]. A likelihood function $\mathcal{L}$ is defined as the product of Poisson probabilities associated with the number of events in bins of the m_{T} distributions in the signal regions and of the total yields in the control regions. The m_{T} distributions in the SRs use the same binnings as described in Appendix D. Each source of systematic uncertainty is parameterised by a corresponding nuisance parameter θ constrained by a Gaussian function.

The likelihood function can be expressed in the following formula:

$$\mathcal{L}(\mu, \mu_b) = P(N|\mu s + \mu_b b_{\mathrm{SR}}^{\mathrm{exp}}) \times P(M|\mu_b b_{\mathrm{CR}}^{\mathrm{exp}}) \tag{9.1}$$

where N and M are the number of data events in the signal and control regions respectively, s is the expected signal yield in the signal region, $b_{\mathrm{SR}}^{\mathrm{exp}}$ and $b_{\mathrm{CR}}^{\mathrm{exp}}$ are expected background yields in the signal and control regions respectively, μ is the signal strength parameter, defined as the ratio of the measured $\sigma_H \times \mathrm{BR}(H \to WW)$ to that predicted [9] , and μ_b is the strength parameter for background b.

[9]The SM cross-section prediction is used to define μ for the NWA and LWA scenarios.

The backgrounds treated this way are the WW background in the inclusive ggF and $N_{\text{jet}} = 1$ VBF categories, and the top-quark background in the inclusive ggF and $N_{\text{jet}} \geq 2$ VBF categories.

The full likelihood includes a product over m_{T} bins and over lepton and jet final states:

$$\mathcal{L}(\mu, \vec{\theta}) = \left\{ \prod_{j=0}^{N_{\text{category}}} \prod_{i=1}^{N_{\text{bins}}} P(N_{ij} | \mu s_{ij} + \sum_{m}^{N_{\text{bkg}}} b_{ijm}) \right\} \times \prod_{i=1}^{N_\theta} N(\tilde{\theta}|\theta) \tag{9.2}$$

where the vector $\vec{\theta}$ represents the nuisance parameters and the $N(\tilde{\theta}|\theta)$ are auxiliary measurements that constrain $\vec{\theta}$. Nuisance parameters corresponding to the various systematic uncertainties and background determinations in the analysis can broadly be divided into four types:

Type I: Systematics that do not change the m_{T} shape (flat systematics) take the form $\nu_{\text{flat}}(\theta) = \kappa^\theta$, where κ is determined by measuring ν_{flat} at $\theta = \pm 1$. In this case, the constraint term on θ that is present in the likelihood is a unit Gaussian, and κ^θ is log-normally distributed to prevent predicted event yields from taking unphysical values.

Type II: In the case that a systematic can affect the shape, the shape variation is first separated into a flat component and a pure shape component, such that varying the pure shape component has no effect on the expected rate. The flat component is treated as described above. The pure shape component uses vertical linear interpolation to estimate the variation, and so is distributed as a truncated Gaussian. Explicitly, $\nu_{\text{shape}}(\theta) = 1 + \epsilon\theta$, where ϵ is again determined by measuring ν_{shape} at $\theta = \pm 1$ and the constraint is a unit Gaussian. The truncation is imposed such that $\nu_{\text{shape}}(\theta < \frac{-1}{\epsilon}) = 0$. Systematic sources can have both a normalisation (type I) and shape component. In such cases, the same θ is shared between both functions $\nu_{\text{flat}}(\theta)$ and $\nu_{\text{shape}}(\theta)$.

Type III: The third type pertains to the treatment of purely statistical uncertainties, i.e., uncertainties from MC statistics or data-driven methods. The constraint represents an auxiliary measured number of events $\tilde{\theta}$ with an expected number $\theta\lambda$. In other words, it is the Poisson probability $P(\tilde{\theta}|\theta\lambda) = \frac{(\theta\lambda)^{\tilde{\theta}} e^{\theta\lambda}}{\tilde{\theta}!}$. For an uncertainty σ_b on an expectation b_0, $\tilde{\theta} = \lambda = \frac{b_0^2}{\sigma_{b_0}^2}$, and $\nu_{\text{stat}}(\theta) = \theta$.

Type IV: The final type arises when a high-statistics data control region is used to constrain the normalisation of a background. This is similar to the third type. The constraint is the Poisson probability $P(\tilde{\theta}|\lambda(\theta)) = \frac{(\theta\lambda(\theta))^{\tilde{\theta}}e^{\lambda(\theta)}}{\tilde{\theta}!}$, $\tilde{\theta}$ being the observed events in the CR. The expected number of events is $\lambda = \mu s + \theta b_{\text{target}} + \sum_i^{N_{\text{bkg}}-1} b_i$, where b_{target} is the background targeted by the CR. This treatment properly takes into account the contamination in the CR due to both the signal and other backgrounds. The background strength parameters multiply expected backgrounds anywhere that the respective backgrounds are present.

It is possible for a single nuisance parameter to affect multiple signal and background rates in a correlated manner, while other nuisance parameters can pertain to specific physics processes. Shape systematics are considered only for shape variations that are statistically significant given the size of MC samples (see Figure 8.2 and 8.4). For a given systematic source, spurious variations of the m_{T} shape can arise from poor MC statistics, leading to fit convergence problems if that systematic is used as a shape variation as well as a normalisation variation. The m_{T} shape variation of the total background is dominated by the normalisation variations of individual backgrounds. Since individual backgrounds are not equally distributed across the m_{T} spectrum, systematics that lead to normalisation variations of individual backgrounds result in variations in the m_{T} shape of the total background.

The analysis has signal regions optimised for the ggF and VBF signal production modes, but the presence of both signal processes is accounted for in all signal regions. Limits are obtained separately for ggF and VBF production in all interpretations. To derive the expected limits on the ggF production mode, the VBF production cross section is set to zero, so that the expected limits correspond to the background-only hypothesis. To derive the observed limits on the ggF (VBF) production mode, the VBF (ggF) production cross section is treated as a nuisance parameter in the fit and profiled using a flat prior, as is used for the normalisation of backgrounds using CRs. This approach avoids making any assumption on the presence or absence of the signal in other production modes, by using the signal regions themselves to set the normalisation of the production mode not being tested.

The modified frequentist method known as CL_s, combined with asymptotic approximation, is used to compute 95% CL upper limits. The method uses a test

statistic q_μ, a function of the signal strength μ. The test statistic is defined as:

$$q_\mu = -2 \ln \left(\frac{\mathcal{L}(\mu; \hat{\theta}_\mu)}{\mathcal{L}(\hat{\mu}; \hat{\theta})} \right) . \tag{9.3}$$

The denominator does not depend on μ. The quantities $\hat{\mu}$ and $\hat{\theta}$ are values of μ and θ, respectively, that unconditionally maximise $\mathcal{L}$. The numerator depends on the values $\hat{\theta}_\mu$ that maximise $\mathcal{L}$ for a given value of μ.

Type III (statistical) uncertainties are applicable to each m_{T} bin in each signal and control region in the analysis. The applicability of uncertainties of types I and II depends on the estimation method of particular backgrounds, as discussed below.

Continuum WW: Systematic uncertainties of types I and II are applicable. Most of the experimental uncertainties are common between the control and signal regions, and thus largely cancel out. In the $N_{\mathrm{jet}} \geq 2$ VBF category, the normalisation is taken from MC prediction, so that uncertainties of types I and II are applicable.

$t\bar{t}$+ single top: In the inclusive ggF and $N_{\mathrm{jet}} \geq 2$ VBF categories, the normalisation is constrained from control regions, so that uncertainties of types I and II are applicable, but again most experimental systematic uncertainties cancel out in the extrapolation.

W+ jets: A data-driven method is used to determine both the normalisation and the shape. There is a systematic uncertainty on the fake rate, so that uncertainties of types I are applicable.

Z/γ^*+ jets, $WZ/ZZ/W\gamma$: These (generally small) backgrounds are estimated purely using MC, so that uncertainties of type I are applicable.

Finally, the signal prediction is estimated from MC, and uncertainties of types I and II are applicable.

9.2 Pre-fit results

The cutflow of the pre-fit event yields in the SRs is shown in Table 9.1. The pre-fit normalisation factors are applied to the dominant top and WW backgrounds, while the other backgrounds that have small contributions use predictions from MC simulation.

Table 9.1: Cutflow table for signal and background channels in signal regions. The ggF and VBF heavy Higgs signal at 700 GeV is based on NWA samples. The quoted errors are statistical only. The normalisation factors (NFs) stand for the pre-fit background normalisation factors and have been applied accordingly to the relevant background processes (i.e. the entries of the following rows in the same column). The 1st, 2nd, 3rd, 5th and 6th blocks correspond to the pre-selection level, W+jets CR, ggF SR, VBF 1J SR and VBF 2J SR, respectively. The ggF and VBF signals at 700 GeV are normalised to their expected limits, respectively.

$\sqrt{s} = 13TeV$, $\mathcal{L} = 36.1fb^{-1}$,	H GGF [NWA, 700]	H VBF [NWA, 700]	VBF [125]	WW	Other VV	$t\bar{t}$	Single Top	Z/γ^*	W+jet (DD)	Total Bkg.	Data	Data/Bkg
Channel Selection	199.42 ± 1.31	58.38 ± 0.56	285.72 ± 1.45	48387.68 ± 84.54	42788.27 ± 192.89	401839.07 ± 396.52	39675.82 ± 84.28	211415.91 ± 1511.11	785026.10 ± 2617.52	1529418.56 ± 3056.73	1088505	0.71 ± 0.00
W+jets flavour split muon	199.42 ± 1.31	58.38 ± 0.56	285.72 ± 1.45	48387.68 ± 84.54	42788.27 ± 192.89	401839.07 ± 396.52	39675.82 ± 84.28	211415.91 ± 1511.11	785026.10 ± 2617.52	1529418.56 ± 3056.73	1088505	0.71 ± 0.00
W+jets flavour split electron	199.42 ± 1.31	58.38 ± 0.56	285.72 ± 1.45	48387.68 ± 84.54	42788.27 ± 192.89	401839.07 ± 396.52	39675.82 ± 84.28	211415.91 ± 1511.11	785026.10 ± 2617.52	1529418.56 ± 3056.73	1088505	0.71 ± 0.00
LWA width reweight	199.42 ± 1.31	58.38 ± 0.56	285.72 ± 1.45	48387.68 ± 84.54	42788.27 ± 192.89	401839.07 ± 396.52	39675.82 ± 84.28	211415.91 ± 1511.11	785026.10 ± 2617.52	1529418.56 ± 3056.73	1088505	0.71 ± 0.00
GRL Selection	199.42 ± 1.31	58.38 ± 0.56	285.72 ± 1.45	48387.68 ± 84.54	42788.27 ± 192.89	401839.07 ± 396.52	39675.82 ± 84.28	211415.91 ± 1511.11	718498.10 ± 2604.79	1462890.56 ± 3045.82	1048583	0.72 ± 0.00
Jet Cleaning	196.77 ± 1.30	54.88 ± 0.54	283.45 ± 1.44	48290.46 ± 84.45	42650.20 ± 192.63	400634.92 ± 395.79	39563.01 ± 84.13	210942.02 ± 1509.76	712868.94 ± 2601.39	1455233.00 ± 3042.14	1043528	0.72 ± 0.00
Trigger Selection	193.59 ± 1.29	53.96 ± 0.54	241.85 ± 1.33	43729.27 ± 80.64	31958.57 ± 151.18	367952.99 ± 379.65	36185.36 ± 79.87	141122.92 ± 1201.48	407049.03 ± 1900.74	1028239.98 ± 2288.28	817002	0.79 ± 0.00
Trigger Matching	193.34 ± 1.29	53.93 ± 0.54	236.09 ± 1.32	43004.35 ± 80.05	29352.51 ± 144.53	363150.32 ± 377.33	35754.50 ± 79.34	128716.72 ± 1143.61	380541.96 ± 1810.05	980756.44 ± 2181.77	785246	0.80 ± 0.00
Only two Leptons	192.91 ± 1.29	53.90 ± 0.54	235.86 ± 1.31	42985.95 ± 80.03	19839.36 ± 132.47	360563.79 ± 375.99	35594.88 ± 79.18	119262.41 ± 1090.70	382403.89 ± 1722.81	960886.14 ± 2080.70	763184	0.79 ± 0.00
$p_t^{lead} > 25$ GeV	192.91 ± 1.29	53.90 ± 0.54	235.40 ± 1.31	42935.05 ± 79.99	19738.74 ± 131.87	360328.44 ± 375.87	35571.78 ± 79.15	118306.69 ± 1086.41	378132.67 ± 1716.05	955248.76 ± 2072.79	760135	0.80 ± 0.00
$p_t^{sublead} > 25$	182.73 ± 1.26	50.89 ± 0.52	123.34 ± 0.96	30631.32 ± 67.61	8730.99 ± 78.07	258912.17 ± 320.60	24968.63 ± 65.19	36372.94 ± 610.20	84618.26 ± 1093.80	444357.64 ± 1298.63	392573	0.88 ± 0.00
OS Leptons	180.32 ± 1.25	50.31 ± 0.52	122.52 ± 0.96	30201.11 ± 67.25	4476.03 ± 54.36	256343.61 ± 319.06	24622.68 ± 64.60	34871.49 ± 589.51	58364.09 ± 1034.35	409001.53 ± 1237.28	373427	0.91 ± 0.00
$M_{\ell\ell} > 10$ GeV	180.31 ± 1.25	50.31 ± 0.52	116.93 ± 0.93	30092.49 ± 67.17	4300.75 ± 52.85	255439.64 ± 318.51	24529.93 ± 64.46	34692.01 ± 586.43	50614.23 ± 1027.02	399785.98 ± 1229.47	368496	0.92 ± 0.00
Leptons ID, W+jets 1 anti-ID,1 ID	173.62 ± 1.23	48.66 ± 0.51	101.38 ± 0.86	27434.53 ± 64.02	3308.03 ± 47.54	228933.97 ± 300.75	21992.93 ± 60.47	29779.70 ± 529.26	31476.19 ± 553.59	343026.74 ± 828.88	320763	0.94 ± 0.00
Apply fake factor	173.62 ± 1.23	48.66 ± 0.51	101.38 ± 0.86	27434.53 ± 64.02	3308.03 ± 47.54	228933.97 ± 300.75	21992.93 ± 60.47	29779.70 ± 529.26	8333.05 ± 207.81	319883.60 ± 650.98	320763	1.00 ± 0.00
Scale factors				NF $= 1.15 \pm 0.03$		NF $= 0.99 \pm 0.01$	NF $= 0.99 \pm 0.01$					
VBFVeto	153.62 ± 1.15	18.35 ± 0.31	59.70 ± 0.66	29935.97 ± 71.58	3123.23 ± 45.83	220580.16 ± 293.88	21119.92 ± 59.03	28521.37 ± 520.28	8043.56 ± 205.06	311383.91 ± 640.17	310937	1.00 ± 0.00
VBFVeto: b-veto	137.81 ± 1.08	16.57 ± 0.30	50.80 ± 0.61	28065.56 ± 69.76	2806.99 ± 43.56	16342.90 ± 76.49	4197.91 ± 25.41	26804.10 ± 509.08	4248.78 ± 177.06	82517.03 ± 551.16	79955	0.97 ± 0.01
Incl. SR: $\Delta\eta_{ll} < 1.8$	111.38 ± 0.96	13.44 ± 0.27	50.79 ± 0.61	22537.65 ± 61.09	2326.83 ± 39.75	13365.73 ± 69.14	3515.05 ± 23.20	26527.52 ± 506.53	3454.57 ± 174.86	71778.13 ± 545.69	69086	0.96 ± 0.01
Incl. SR: $M_{ll} > 55$ GeV	111.36 ± 0.96	13.44 ± 0.27	9.64 ± 0.26	19313.64 ± 57.30	1841.77 ± 31.69	11513.98 ± 64.62	3051.72 ± 21.76	24112.22 ± 497.76	3025.07 ± 170.03	62868.05 ± 534.43	60254	0.96 ± 0.01
Incl. SR: $p_T^{lead} > 45$ GeV	111.06 ± 0.96	13.41 ± 0.27	6.50 ± 0.22	15555.92 ± 50.86	1187.47 ± 23.73	10561.90 ± 61.96	2806.06 ± 20.89	4036.13 ± 200.46	1799.30 ± 107.91	35953.28 ± 243.43	35037	0.97 ± 0.01
Incl. SR: $p_T^{sub-lead} > 30$ GeV	108.67 ± 0.95	13.18 ± 0.26	5.06 ± 0.19	13912.70 ± 48.32	984.60 ± 20.79	9423.29 ± 58.61	2502.16 ± 19.82	2687.82 ± 174.38	1411.37 ± 56.42	30926.98 ± 200.47	29980	0.97 ± 0.01
Incl. SR: $max(M_{\mathrm{T}}^{\ell}) > 50$ GeV	108.17 ± 0.94	13.12 ± 0.26	3.68 ± 0.17	11641.69 ± 41.99	846.62 ± 19.49	8920.43 ± 56.60	2372.81 ± 19.22	1361.62 ± 126.48	1286.38 ± 45.06	26433.22 ± 154.09	26739	1.01 ± 0.01
Scale factors						NF $= 0.98 \pm 0.02$	NF $= 0.98 \pm 0.02$					
VBFLike	20.00 ± 0.43	30.31 ± 0.40	41.68 ± 0.55	1312.40 ± 14.06	184.80 ± 12.66	6260.59 ± 49.39	671.00 ± 10.23	1258.34 ± 97.08	289.49 ± 33.70	10018.28 ± 116.03	9826	0.98 ± 0.02
VBFLike: b-veto	18.70 ± 0.41	28.72 ± 0.39	38.29 ± 0.52	1243.51 ± 13.77	165.65 ± 11.10	1066.57 ± 19.41	273.18 ± 6.42	1191.30 ± 94.60	191.41 ± 29.29	4169.92 ± 102.66	3937	0.94 ± 0.03
Scale factors				NF $= 0.92 \pm 0.13$		NF $= 0.98 \pm 0.02$	NF $= 0.98 \pm 0.02$					
VBFLike: $n_{jets} = 1$	12.54 ± 0.35	9.04 ± 0.23	9.44 ± 0.26	894.61 ± 11.94	117.11 ± 9.68	428.67 ± 12.43	191.88 ± 5.48	984.39 ± 90.59	143.77 ± 26.06	2769.88 ± 96.47	2649	0.96 ± 0.04
VBF SR 1J: $\Delta\eta_{ll} < 1.8$	11.03 ± 0.33	7.72 ± 0.22	9.42 ± 0.26	750.54 ± 11.00	91.46 ± 7.21	369.92 ± 11.43	168.92 ± 5.12	973.56 ± 90.32	111.85 ± 25.62	2475.67 ± 95.62	2351	0.95 ± 0.04
VBF SR 1J: $M_{ll} > 55$ GeV	11.03 ± 0.33	7.71 ± 0.22	1.76 ± 0.11	621.02 ± 10.34	76.41 ± 6.62	325.23 ± 10.82	146.25 ± 4.74	908.16 ± 86.94	97.05 ± 24.05	2175.88 ± 91.80	2055	0.94 ± 0.04
VBF SR 1J: $p_T^{lead} > 45$ GeV	11.01 ± 0.33	7.70 ± 0.22	1.04 ± 0.08	483.52 ± 9.00	42.99 ± 4.39	298.20 ± 10.45	133.48 ± 4.56	175.68 ± 36.56	74.80 ± 11.04	1209.71 ± 41.09	1275	1.05 ± 0.05
VBF SR 1J: $p_T^{sub-lead} > 30$ GeV	10.83 ± 0.33	7.52 ± 0.22	0.76 ± 0.07	434.64 ± 8.51	34.27 ± 3.73	261.89 ± 9.72	119.04 ± 4.30	114.39 ± 29.51	54.87 ± 7.30	1019.85 ± 33.52	1069	1.05 ± 0.05
VBF SR 1J: $max(M_{\mathrm{T}}^{\ell}) > 50$ GeV	10.78 ± 0.33	7.47 ± 0.21	0.58 ± 0.06	412.73 ± 8.25	32.53 ± 3.68	251.69 ± 9.52	115.90 ± 4.24	73.27 ± 26.43	56.82 ± 6.67	943.52 ± 30.55	978	1.04 ± 0.05
VBFLike: $n_{jets} \geq 2$	6.16 ± 0.22	19.68 ± 0.31	28.86 ± 0.45	276.30 ± 4.77	48.54 ± 5.43	637.90 ± 14.90	81.29 ± 3.34	206.91 ± 27.26	47.64 ± 13.37	1327.44 ± 34.75	1288	0.97 ± 0.04
VBF SR 2J: $\Delta\eta_{ll} < 1.8$	5.14 ± 0.20	15.79 ± 0.28	28.83 ± 0.45	236.16 ± 4.36	40.22 ± 4.55	482.59 ± 13.07	67.20 ± 3.05	206.04 ± 27.25	34.25 ± 12.75	1095.29 ± 33.55	1019	0.93 ± 0.04
VBF SR 2J: $M_{ll} > 55$ GeV	5.13 ± 0.20	15.79 ± 0.28	4.66 ± 0.18	190.43 ± 4.01	27.35 ± 2.84	416.41 ± 12.26	59.23 ± 2.88	130.44 ± 23.42	15.30 ± 11.70	843.82 ± 29.46	817	0.97 ± 0.05
VBF SR 2J: $p_T^{lead} > 45$ GeV	5.12 ± 0.20	15.72 ± 0.28	3.66 ± 0.16	172.10 ± 3.77	21.64 ± 2.49	390.38 ± 11.94	54.15 ± 2.75	64.88 ± 14.46	16.32 ± 5.90	723.12 ± 20.36	700	0.97 ± 0.05
VBF SR 2J: $p_T^{sub-lead} > 30$ GeV	5.05 ± 0.20	15.33 ± 0.27	3.00 ± 0.14	152.28 ± 3.52	18.59 ± 2.31	352.48 ± 11.51	47.40 ± 2.57	38.07 ± 10.39	11.68 ± 5.06	623.50 ± 17.04	616	0.99 ± 0.05
VBF SR 2J: $max(M_{\mathrm{T}}^{\ell}) > 50$ GeV	5.04 ± 0.20	15.26 ± 0.27	2.12 ± 0.12	143.16 ± 3.44	17.22 ± 2.25	338.02 ± 11.32	44.88 ± 2.52	27.56 ± 9.76	9.77 ± 4.54	582.73 ± 16.35	560	0.96 ± 0.05

The distributions of the common variables used in the selection of the SRs are shown in Figures 9.1-9.3 for ggF, VBF $N_{\text{jet}} = 1$ and ≥ 2 categories, respectively, where one of the cuts is removed while all other cuts are applied (the N-1 plots). Similar comparisons for m_{jj} and Δy_{jj} are shown in Figure 9.4. Overall good agreement is observed in all the distributions shown for all the jet categories except for some deficit in data at values of m_{T} around 200 GeV in the $N_{\text{jet}} = 1$ category. Extensive checks have been performed and no strong discrepency found between data and MC predictions in those distributions.

The pre-fit m_{T} distributions of the SRs in the ggF, VBF $N_{\text{jet}} = 1$ and ≥ 2 categories are shown in Figure 9.5.

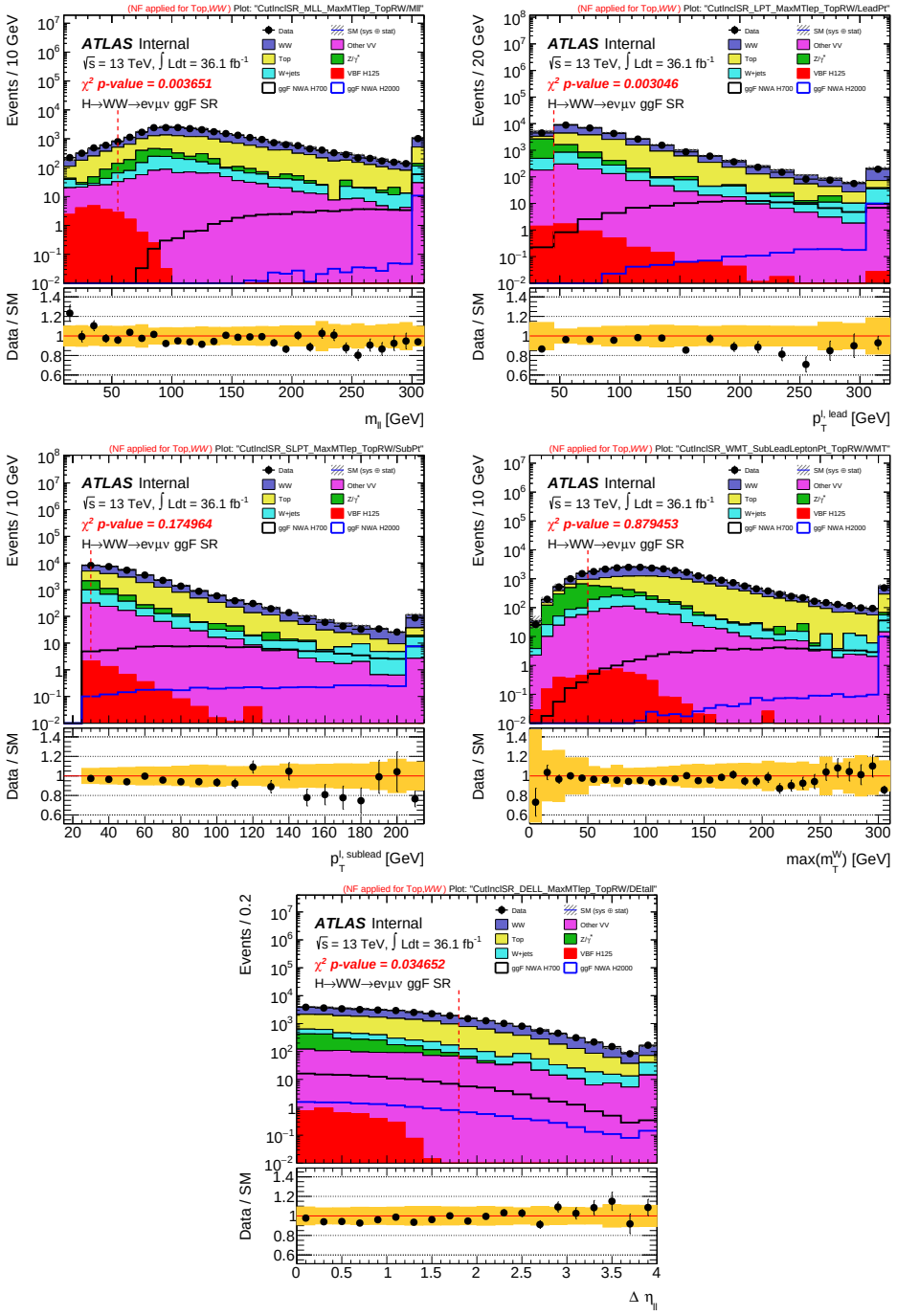

Figure 9.1: Distribution of $m_{\ell\ell}$ (upper left), $p_{\mathrm{T}}^{\ell,\mathrm{lead}}$ (upper right), $p_{\mathrm{T}}^{\ell,\mathrm{sublead}}$ (middle left), $\max(m_{\mathrm{T}}^{W})$ (middle right) and $\Delta\eta_{\ell\ell}$ (bottom) when the corresponding cut is removed while all other cuts are applied in the selection of the SR for the ggF category. The hatched band in the upper panel and the shaded band in the lower panel show the combined statistical and experimental uncertainties on the predictions. The last bin contains the overflow. The pre-fit normalisation factors obtained from a comparison of data and predictions in different control regions have been applied in these figures. The ggF and VBF signals at 700 GeV and 2 TeV are normalised to the expected limits. The red dashed vertical line indicates the cut value.

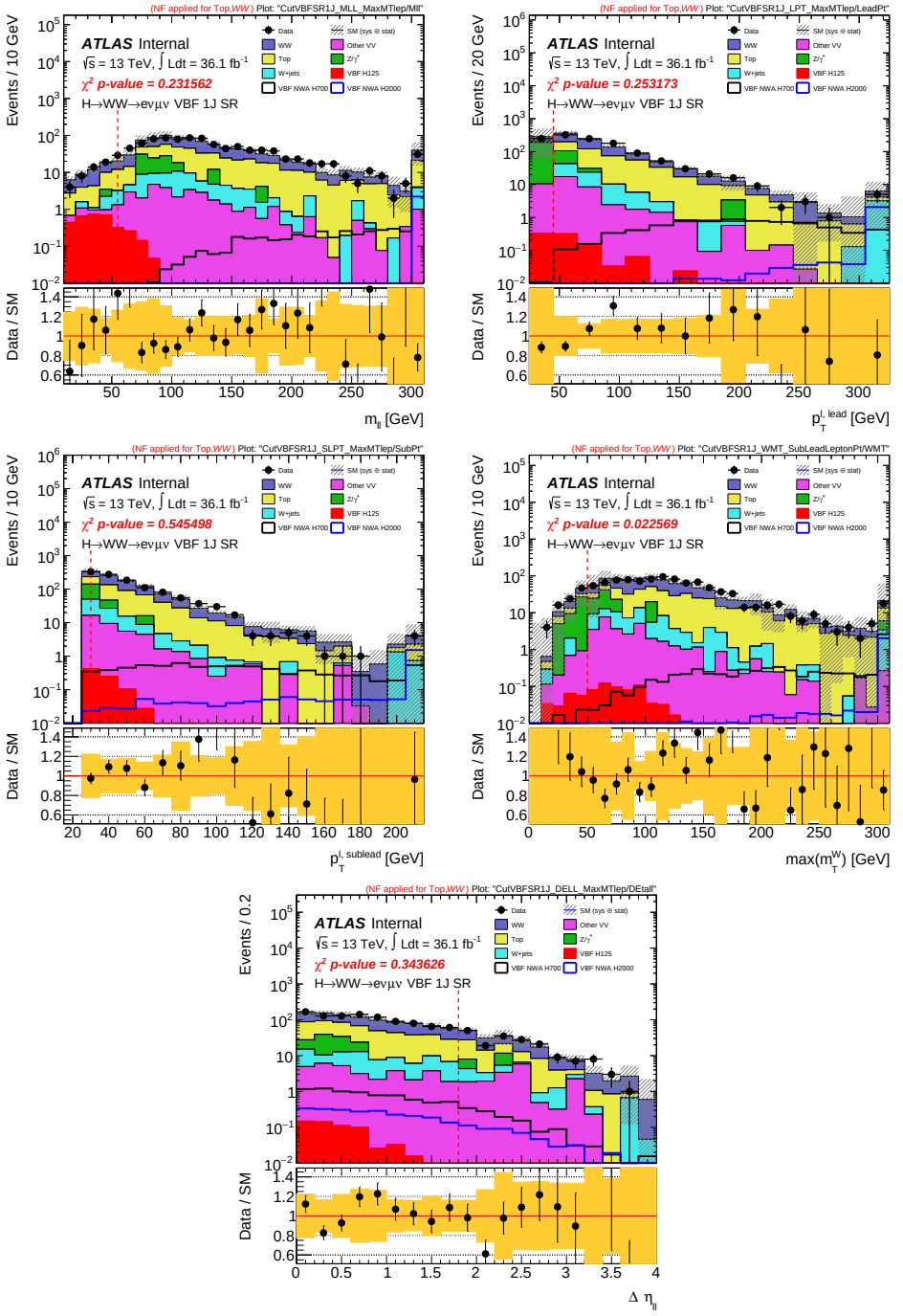

Figure 9.2: Distribution of $m_{\ell\ell}$ (upper left), $p_{\mathrm{T}}^{\ell,\mathrm{lead}}$ (upper right), $p_{\mathrm{T}}^{\ell,\mathrm{sublead}}$ (middle left), $\max(m_{\mathrm{T}}^{W})$ (middle right) and $\Delta\eta_{\ell\ell}$ (bottom) when the corresponding cut is removed while all other cuts are applied in the selection of the SR for the VBF $N_{\mathrm{jet}} = 1$ category. The hatched band in the upper panel and the shaded band in the lower panel show the combined statistical and experimental uncertainties on the predictions. The last bin contains the overflow. The pre-fit normalisation factors obtained from a comparison of data and predictions in different control regions have been applied in these figures. The ggF and VBF signals at 700 GeV and 2 TeV are normalised to the expected limits. The red dashed vertical line indicates the cut value.

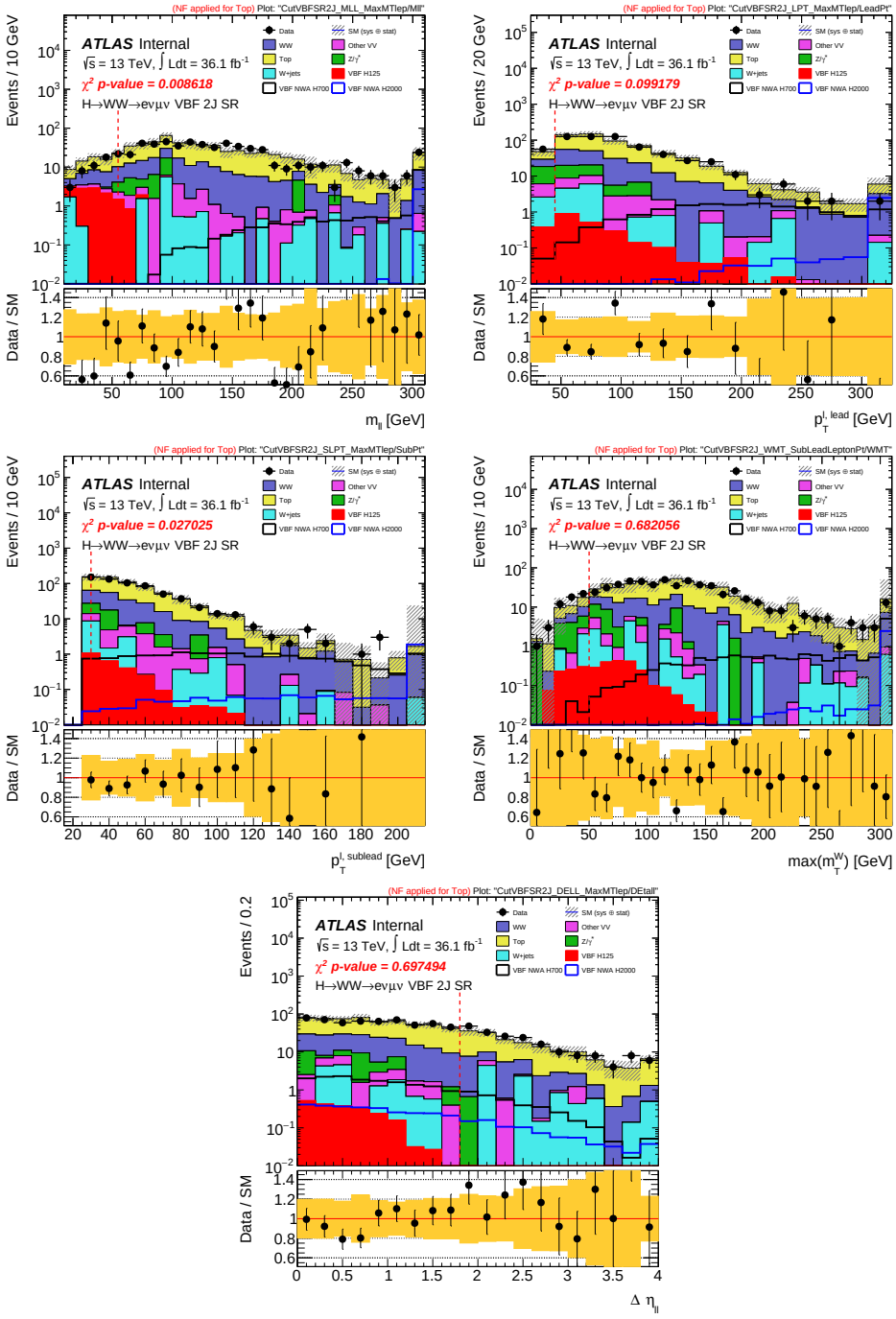

Figure 9.3: Distribution of $m_{\ell\ell}$ (upper left), $p_{\mathrm{T}}^{\ell,\mathrm{lead}}$ (upper right), $p_{\mathrm{T}}^{\ell,\mathrm{sublead}}$ (middle left), $\max(m_{\mathrm{T}}^{W})$ (middle right) and $\Delta\eta_{\ell\ell}$ (bottom) when the corresponding cut is removed while all other cuts are applied in the selection of the SR for the VBF $N_{\mathrm{jet}} \geq 2$ category. The hatched band in the upper panel and the shaded band in the lower panel show the combined statistical and experimental uncertainties on the predictions. The last bin contains the overflow. The pre-fit normalisation factors obtained from a comparison of data and predictions in different control regions have been applied in these figures. The ggF and VBF signals at 700 GeV and 2 TeV are normalised to the expected limits. The red dashed vertical line indicates the cut value.

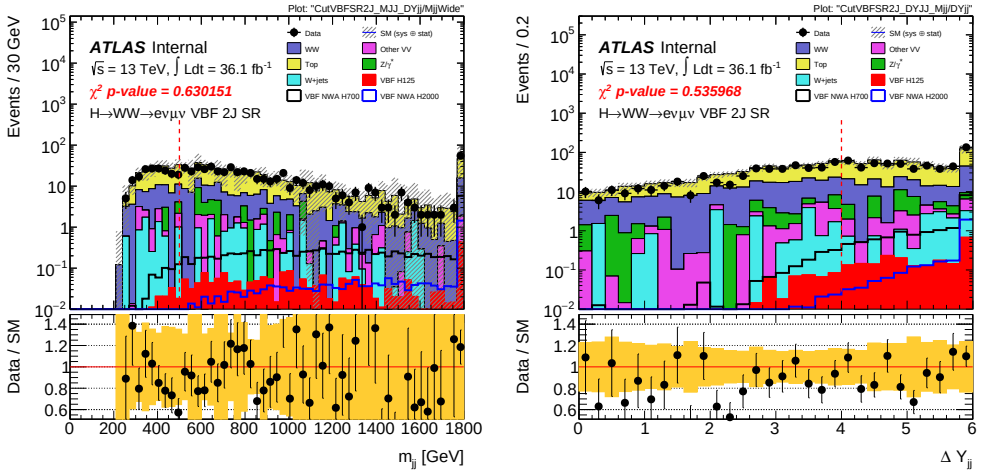

Figure 9.4: Comparison of data and MC in the VBF 2-jet SR when one of the cuts is removed from the selection: m_{jj} (left) and Δy_{jj}. The hatched band in the upper panel and the shaded band in the lower panel show the combined statistical and experimental uncertainties on the predictions. The last bin contains the overflow. The pre-fit normalisation factors obtained from a comparison of data and predictions have been applied in these figures. The red dashed vertical line indicates the cut value.

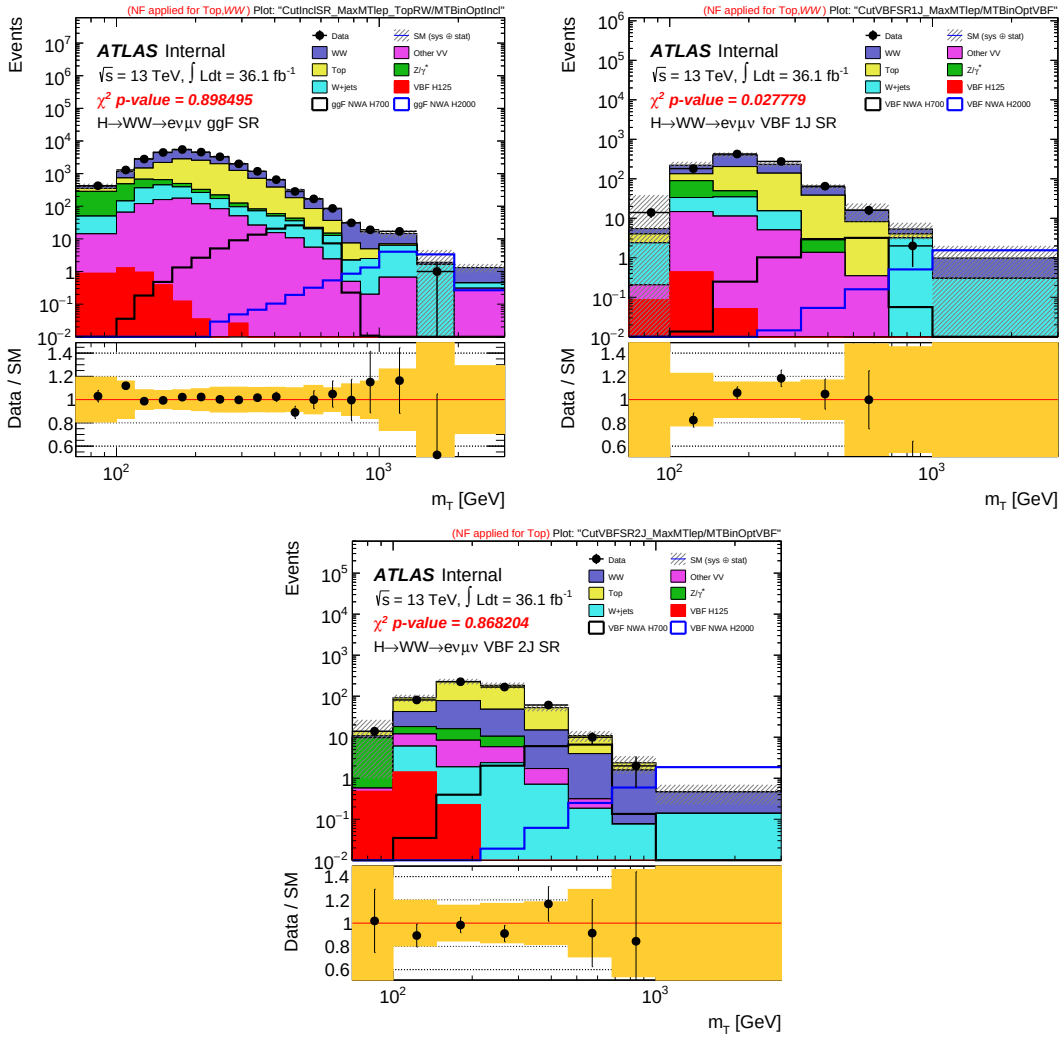

Figure 9.5: Distributions of the transverse mass m_{T} of the SR in the ggF (top left), VBF $N_{\mathrm{jet}} = 1$ (top right) and ≥ 2 (bottom) categories. The hatched band in the upper panel and the shaded band in the lower panel show the statistical uncertainties on the predictions. The pre-fit normalisation factors obtained from a comparison of data and predictions in different control regions have been applied in these figures. The ggF and VBF signals at 700 GeV and 2 TeV are normalised to the expected limits.

9.3 Post-fit results

The number of events that is predicted and observed in the SRs and CRs is shown in Tables 9.2 and 9.3, corresponding to, respectively, the quasi-inclusive ggF categories and the VBF $N_{\text{jet}} = 1$ and ≥ 2 categories. These event yields are obtained from a simultaneous fit of MC samples to the data in all the SRs and the CRs. The event yields of signals obtained from the fit are consistent with zero. The different background compositions are varied largely in different categories: the event yields of the top-quark and WW processes are comparable in SR_{ggF} and SR_{VBF1J}, whilst the top-quark events have the dominant contribution in SR_{VBF2J}. There is a large reduction in the total uncertainty of the backgrounds, which is actually due to the fact that there are very strong anti-correlations between the different uncertainty sources of the top-quark and WW backgrounds. The distributions of m_{T} in SR_{ggF}, SR_{VBF1J} and SR_{VBF2J} are shown in Figure 9.6. As there is no significant excess of data over the background prediction observed, upper limits at 95% CL are thus set on the production cross section times the branching fraction, $\sigma_X \times B(X \to WW)$, for each signal model.

Table 9.2: Event yields of data and backgrounds in the quasi-inclusive ggF category. The yields and uncertainties for the backgrounds are obtained from the simultaneous fit. The uncertainty includes both statistical and systematic uncertainties. "VV" represents non-WW weak diboson backgrounds. The PDG rounding rule [136] has been applied to all background event yields.

	SR_{ggF}	Top CR_{ggF}	WW CR_{ggF}
WW	11 500 ± 800	820 ± 120	3 360 ± 220
Top quark	11 800 ± 600	52 550 ± 330	2 610 ± 180
Z/γ^*	1 420 ± 110	111 ± 20	20.9 ± 2.0
W+jets	1 180 ± 320	710 ± 190	280 ± 70
VV	866 ± 34	101 ± 12	250 ± 11
Background	26 740 ± 170	54 290 ± 250	6 510 ± 80
Data	26 739	54 295	6 515

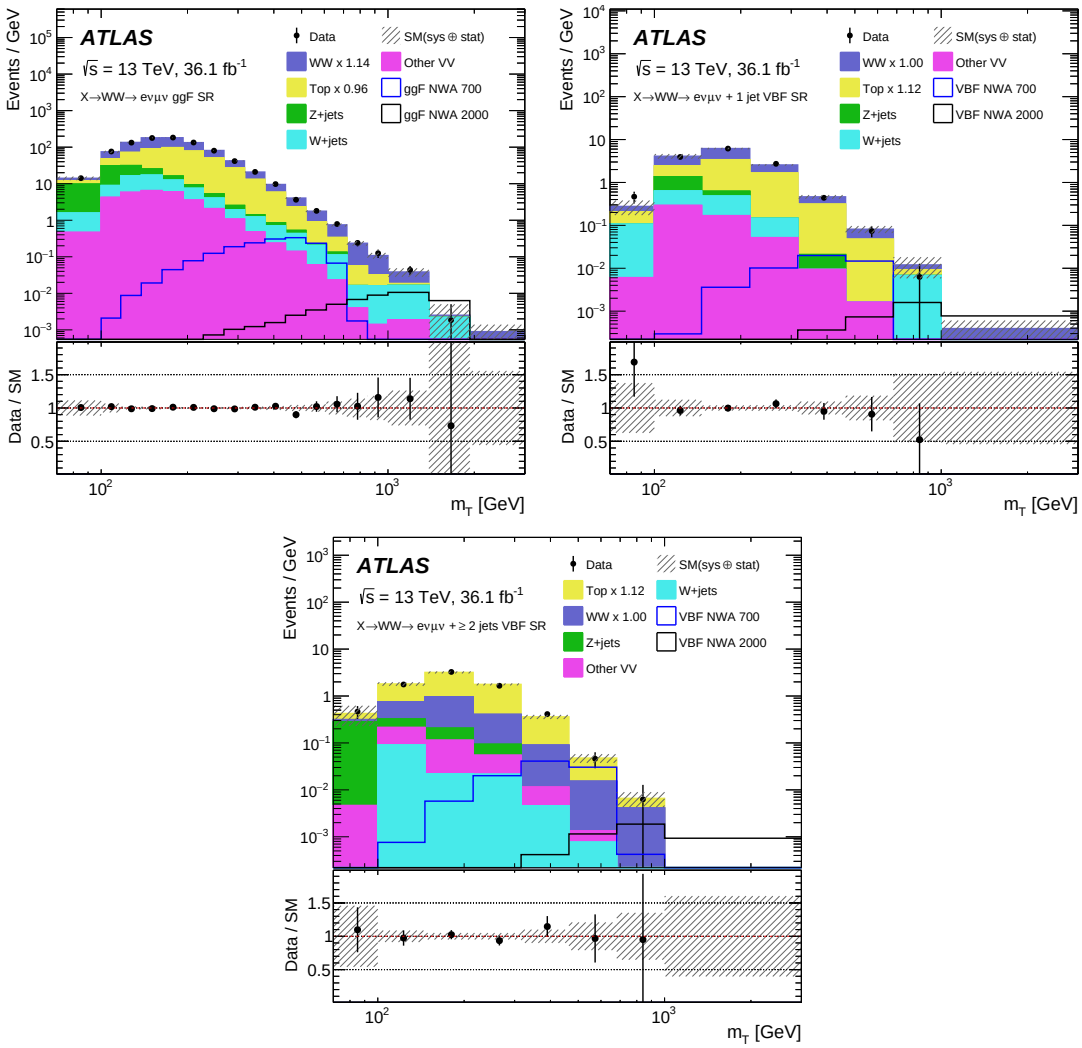

Figure 9.6: Post-fit m_{T} distributions in the $\mathrm{SR}_{\mathrm{ggF}}$ (top left), $\mathrm{SR}_{\mathrm{VBF1J}}$ (top right) and $\mathrm{SR}_{\mathrm{VBF2J}}$ (bottom) categories. In each plot, the last bin contains the overflow. The hatched band in the upper and lower panels shows the combined statistical, experimental and theoretical uncertainties in the predictions. The top and WW backgrounds are scaled by the indicated normalisation factors that are determined from the corresponding CRs. The yields of signal events, which are normalised to the expected limits on $\sigma_H \times B(H \to WW)$, are shown for masses of 700 GeV and 2000 GeV in the NWA scenario.

Table 9.3: Event yields of data and backgrounds in the $N_{\text{jet}} = 1$ and ≥ 2 VBF categories. The yields and uncertainties for the backgrounds are obtained from the simultaneous fit. The uncertainty includes both statistical and systematic uncertainties. "VV" represents non-WW weak diboson backgrounds. The PDG rounding rule [136] has been applied to all background event yields.

	SR_{VBF1J}	SR_{VBF2J}	Top CR_{VBF}	WW CR_{VBF1J}
WW	390 ± 50	120 ± 26	61 ± 11	265 ± 32
Top quark	450 ± 50	391 ± 24	5 650 ± 90	167 ± 18
Z/γ^*	45 ± 11	24 ± 6	68 ± 19	74 ± 12
W+jets	52 ± 13	8.9 ± 2.5	91 ± 24	43 ± 11
VV	32 ± 7	16.6 ± 1.9	20 ± 9	38 ± 4
Background	972 ± 29	563 ± 22	5 890 ± 80	596 ± 22
Data	978	560	5 889	594

9.4 Upper limits

Figure 9.7 presents the upper limits at 95% CL on $\sigma_H \times B(H \to WW)$ as a function of the Higgs mass in the mass range 200 GeV $\leq m_H \leq$ 4 TeV for a Higgs boson in the NWA scenario. Values above 6.4 pb (1.3 pb) at $m_H = 200$ GeV and above 0.008 pb (0.006 pb) at 4 TeV (3 TeV) are excluded at 95% CL for NWA signals in the ggF (VBF) production mode. The main systematic uncertainties that affect the limits are associated to the leading lepton p_{T} correction for the top-quark background, the scale variations of the top-quark background, the generator parton shower modelling for the WW background, and the jet energy scale and resolution. Limits are consistent with those expected in the absence of a signal over the investigated mass range. The observed limits are more stringent than the expected limits for mass values beyond 2 TeV. This can be explained by the deficit in data at the high m_{T} tails in Figure 9.6. The limits are extracted using the asymptotic approximation. The accuracy is verified using pseudo-experiments and found to be consistent within about 5% at 800 GeV and less than 20% at 2 TeV and beyond.

The analysis is extended to a more general case where the relative fraction of the ggF production cross section varies over the total cross section of the ggF and VBF productions. The corresponding 95% CL upper exclusion limits for a signal with mass at 800 GeV are shown in Figure 9.8. The dependence of the limits on the ggF fraction for other masses is very similar but becomes slightly stronger for lower masses. The limit values for a ggF fraction of 0 or 1 are comparable with the VBF or ggF limits, correspondingly, and shown in Figure 9.7 at the same mass

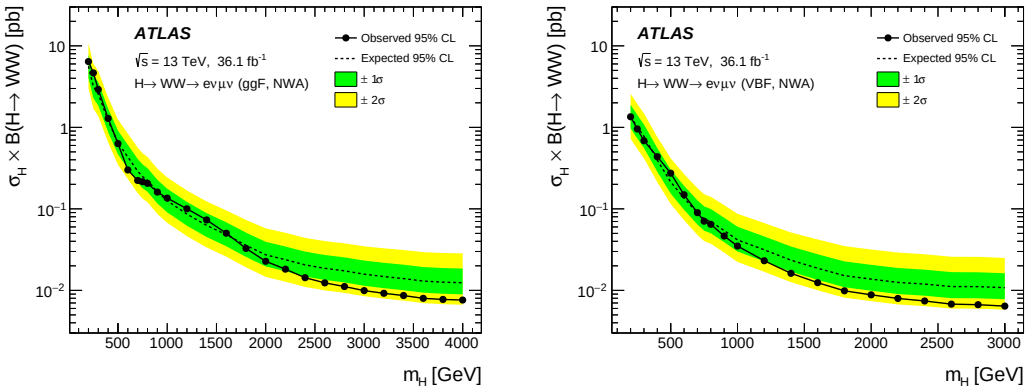

Figure 9.7: Upper limits at 95% CL on the Higgs production cross section times branching fraction $\sigma_H \times B(H \to WW)$ in the $e\nu\mu\nu$ channel, for ggF (left) and VBF (right) signals with narrow-width lineshape as a function of the signal mass. The inner and outer bands show the $\pm 1\sigma$ and $\pm 2\sigma$ uncertainties on the expected limit.

point. The limits for VBF are tighter than ggF since the VBF $N_{\text{jet}} \geq 2$ SR has the smallest background contribution and thus is the most sensitive SR.

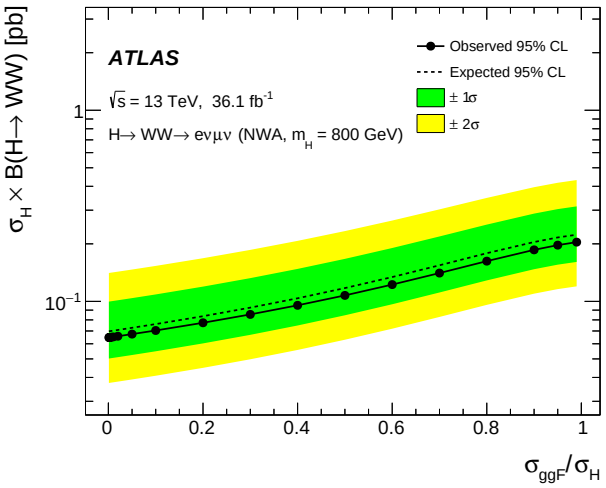

Figure 9.8: Upper limits at 95% CL on the total ggF and VBF Higgs production cross section times branching fraction $\sigma_H \times B(H \to WW)$ in the $e\nu\mu\nu$ channel, for a signal at 800 GeV as a function of the ggF cross section over the combined ggF and VBF production cross section. The inner and outer bands show the $\pm 1\sigma$ and $\pm 2\sigma$ uncertainties on the expected limit.

The NWA exclusion limit shown above is further translated to exclusion contours in the 2HDM in the phase space where the narrow-width approximation is valid. The exclusion contours at 95% CL for Type I and Type II in the plane of $\tan\beta$ and $\cos(\beta - \alpha)$ are shown in Figure 9.9, for three mass values: 200 GeV, 300 GeV and 500 GeV. For a fixed value of $\cos(\beta - \alpha) = -0.1$, exclusion limits at

95% CL on $\tan\beta$ as a function of the mass of the heavy Higgs boson are shown in Figure 9.10.

For the LWA scenario, the impact on the limits of the interference effects among the heavy Higgs boson, the SM WW continuum background and the light Higgs boson at 125 GeV, have been studied and found to be negligible. The upper limits at 95% CL are shown in Figure 9.11. The limits for signal widths of 5%, 10% and 15% are comparable with the limits from the NWA scenario for the VBF signals, while for the ggF signals, the limits degrade slightly at high masses as the width increases. For the LWA signal with a 15% width, the upper exclusion limit ranges between 5.2 pb (1.3 pb) at $m_H = 200$ GeV to 0.02 pb (0.006 pb) at 4 TeV (3 TeV) for the ggF (VBF) signals.

Figure 9.12 shows the limits on the resonance production cross section times branching fraction $\sigma_X \times B(X \to WW)$ and $\sin\theta_H$ for a scalar GM signal with masses between 200 GeV and 1 TeV. At the observed limit, the width is narrower than the experimental resolution [67]. The current sensitivity is not sufficient to exclude the benchmark model with $\sin\theta_H = 0.4$.

For the qqA and VBF HVT signals, limits are derived in the mass range from 250 GeV to 5 TeV and from 300 GeV to 1 TeV, respectively, as shown in Figure 9.13. For the qqA production, signals below about 1.3 TeV are excluded at 95% CL. For the VBF production in the benchmark model assuming a coupling strength to gauge bosons of $g_V = 1$ and a coupling to fermions of $c_F = 0$, no limits can be set. The model has an intrinsic width much narrower than the detector resolution.

Figure 9.14 shows the limits on a $G_{\mathrm{KK}} \to WW$ signal for two different couplings: $k/\bar{M}_{\mathrm{Pl}} = 1$ and $k/\bar{M}_{\mathrm{Pl}} = 0.5$, for masses between 200 GeV and 5 TeV, and for an ELM spin-2 VBF signal for masses between 200 GeV and 1 TeV. A KK graviton signal lighter than 1.1 TeV (750 GeV) with the higher (lower) coupling is excluded by the observed limits, while the current sensitivity is not sufficient to exclude the ELM spin-2 VBF signal.

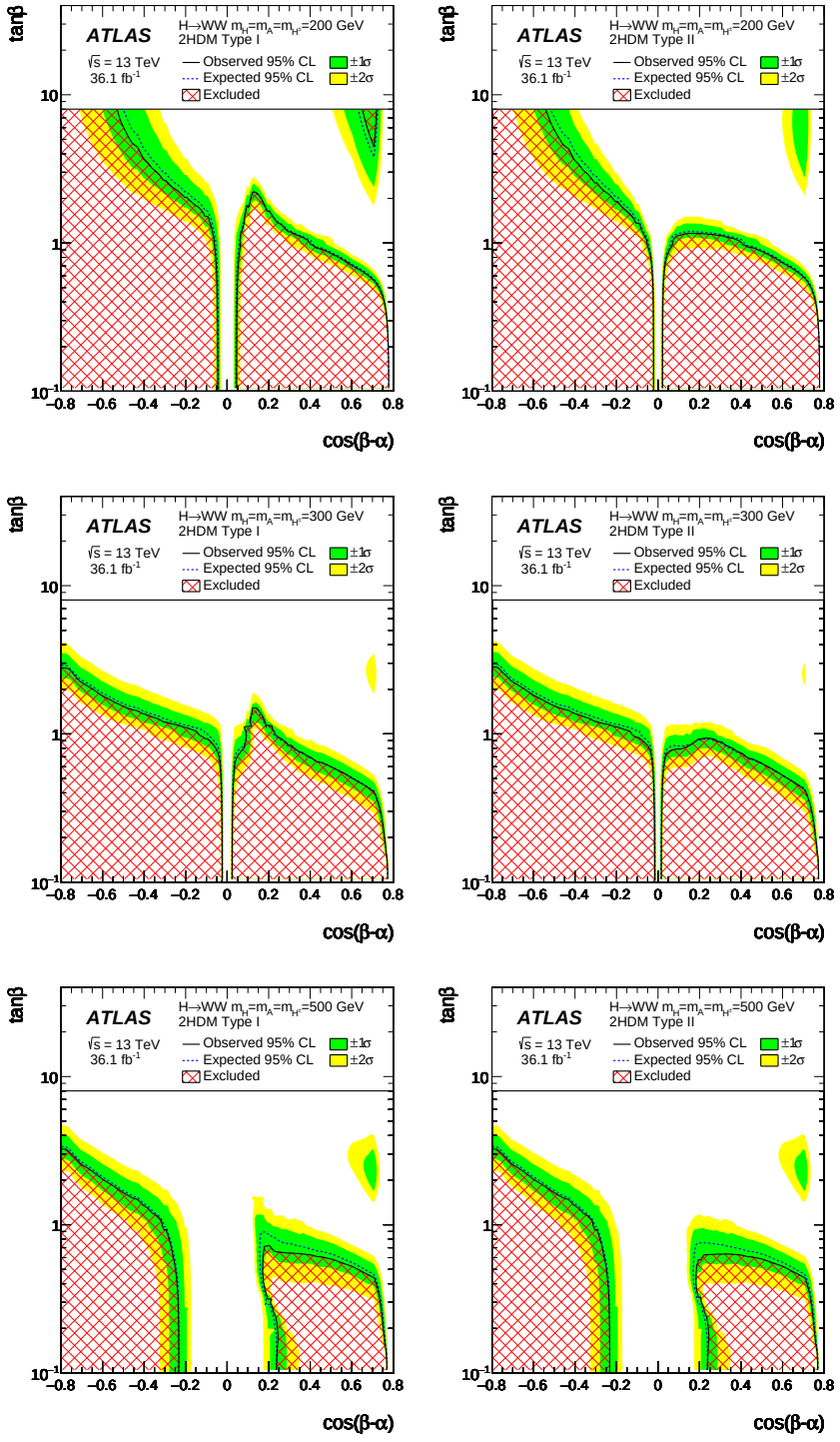

Figure 9.9: Exclusion contours at 95% CL in the plane of $\tan\beta$ and $\cos(\beta-\alpha)$ for three mass values of 200 GeV (top), 300 GeV (middle) and 500 GeV (bottom) for Type I (left) and Type II (right) 2HDM signals. The inner and outer bands show the $\pm1\sigma$ and $\pm2\sigma$ uncertainties on the expected limit and the hatched regions are excluded.

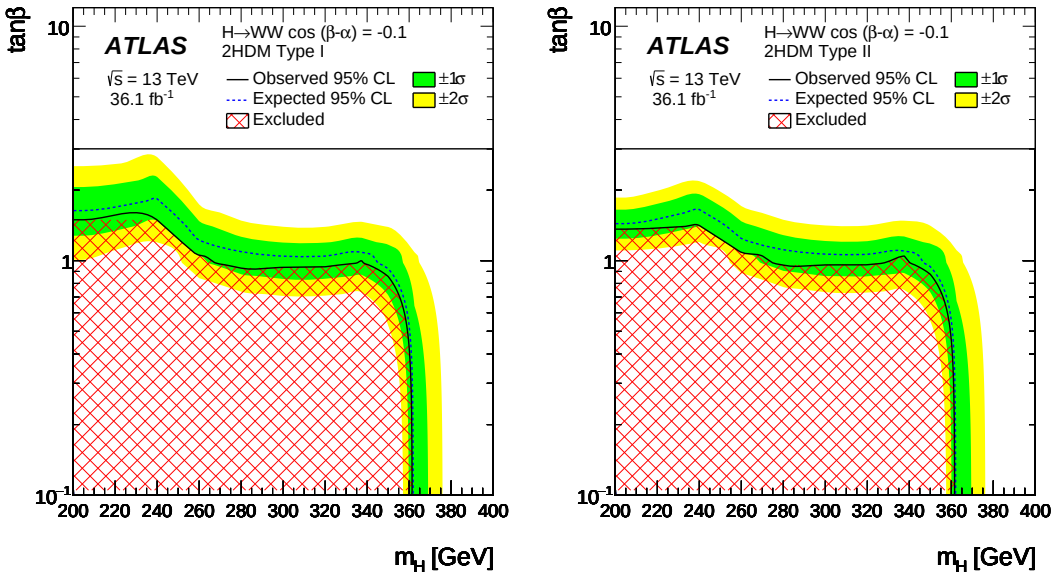

Figure 9.10: Exclusion contours at 95% CL in the plane of $\tan\beta$ and m_H for $\cos(\beta-\alpha) = -0.1$ for Type I (left) and Type II (right) 2HDM signals. The inner and outer bands show the $\pm1\sigma$ and $\pm2\sigma$ uncertainties on the expected limit and the hatched regions are excluded. The other heavy Higgs boson states A and $H^{\pm}$ are assumed to have the same mass as H.

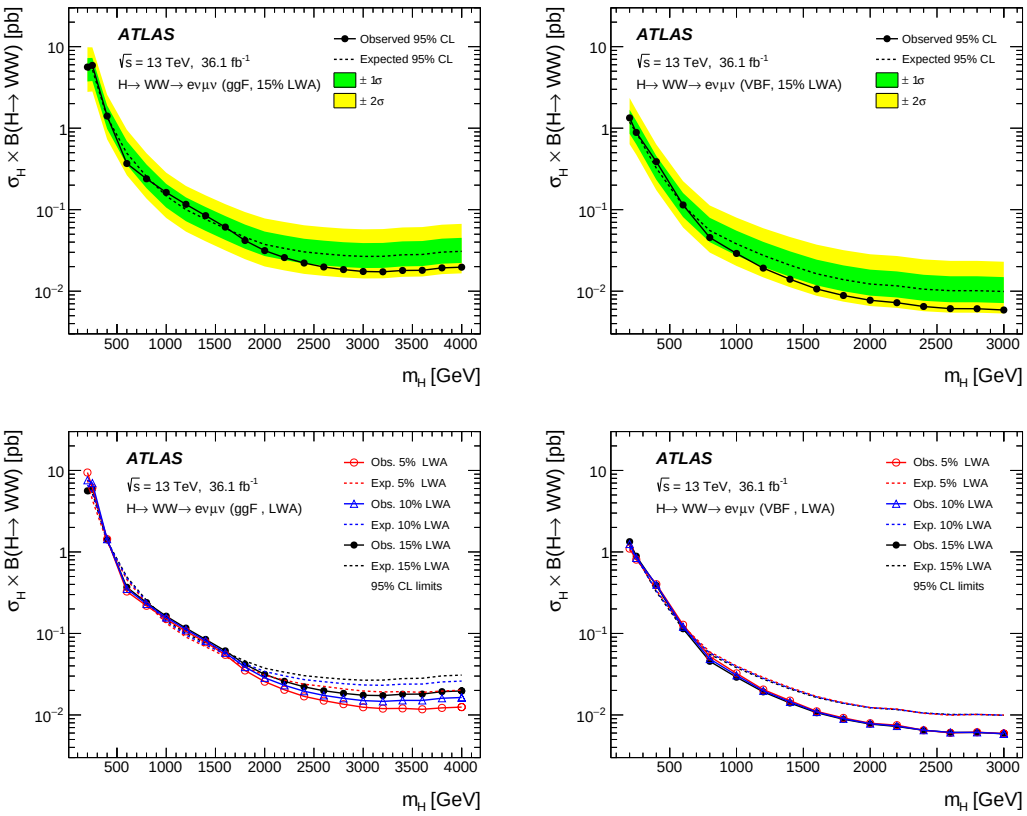

Figure 9.11: Upper limits at 95% CL on the Higgs production cross section times branching fraction $\sigma_H \times B(H \to WW)$ in the $e\nu\mu\nu$ channel, for a signal with a width of 15% of the mass (top) and the comparison of three different widths (bottom) for the ggF (left) and VBF (right) production. The inner and outer bands show the $\pm 1\sigma$ and $\pm 2\sigma$ uncertainties on the expected limit.

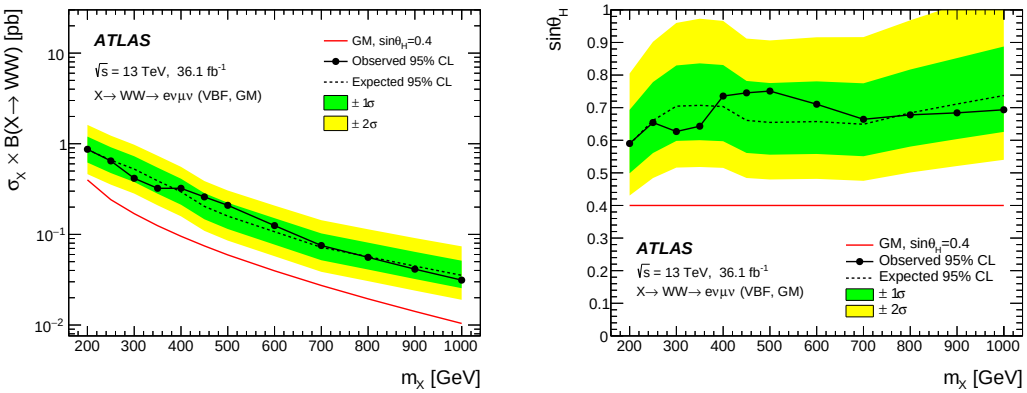

Figure 9.12: Upper limits at 95% CL on the resonance production cross section times branching fraction $\sigma_X \times B(X \to WW)$ (left) and on $\sin\theta_H$ (right) in the $e\nu\mu\nu$ channel, for an GM signal. The inner and outer bands show the $\pm 1\sigma$ and $\pm 2\sigma$ uncertainties on the expected limit. The red curves correspond to the predicted theoretical cross section and the model parameter used in the benchmark model, respectively.

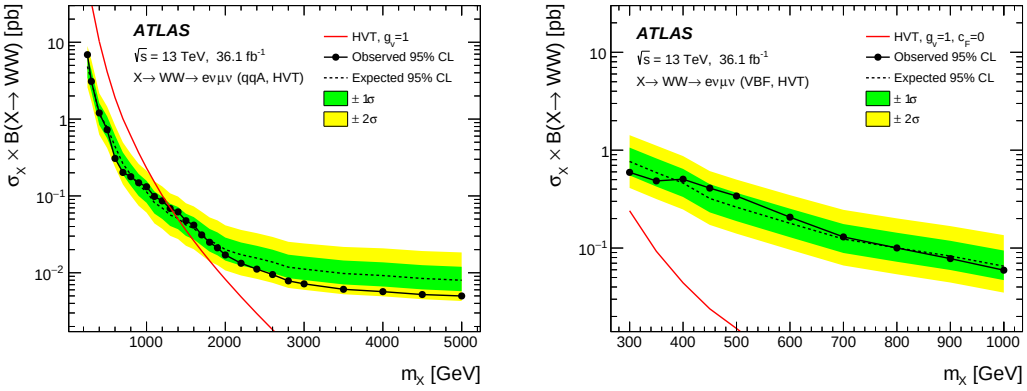

Figure 9.13: Upper limits at 95% CL on the resonance production cross section times branching faction $\sigma_X \times B(X \to WW)$ in the $e\nu\mu\nu$ channel, for HVT qqA (left) and VBF (right) signals. The inner and outer bands show the $\pm 1\sigma$ and $\pm 2\sigma$ ranges around the expected limit. The full curves without dots correspond to the predicted theoretical cross sections.

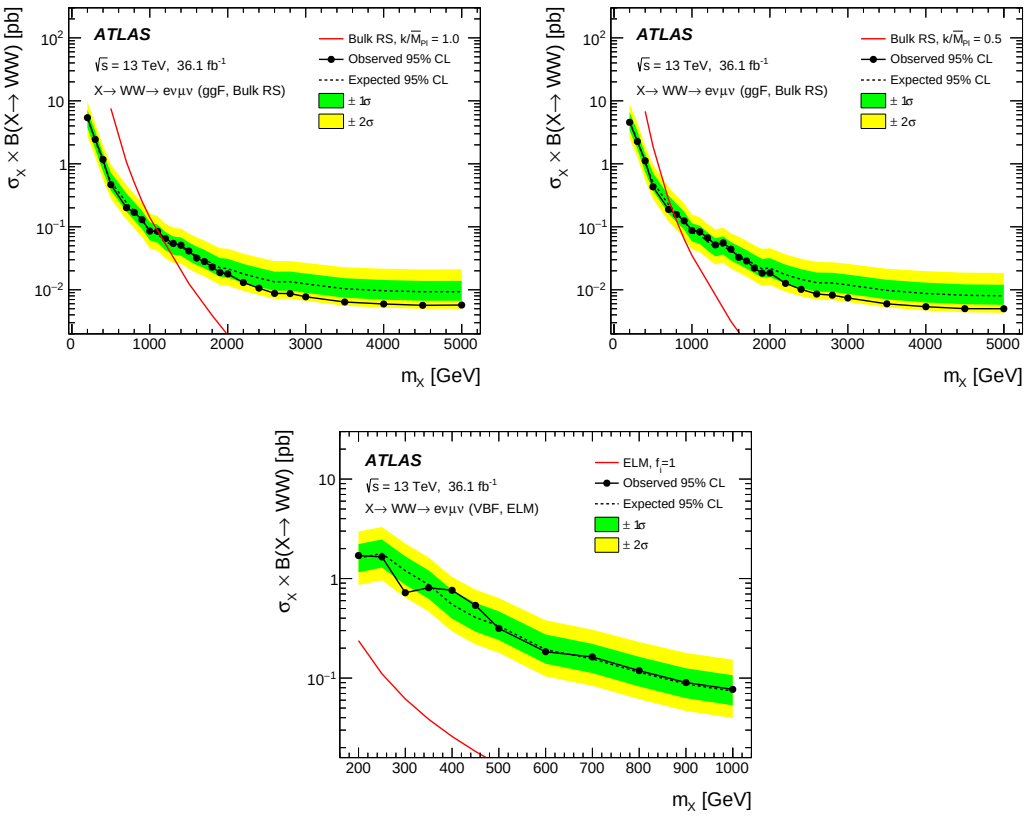

Figure 9.14: Upper limits at 95% CL on the resonance production cross section times branching fraction $\sigma_X \times B(X \to WW)$ in the $e\nu\mu\nu$ channel, for a graviton signal with two different couplings of $k/\bar{M}_{\mathrm{Pl}} = 1$ (left) and $k/\bar{M}_{\mathrm{Pl}} = 0.5$ (right), and for an ELM spin-2 VBF signal (bottom). The inner and outer bands show the $\pm 1\sigma$ and $\pm 2\sigma$ ranges around the expected limit. The full curves without dots correspond to the predicted theoretical cross sections.

Chapter 10

Conclusion and outlook

A search for heavy neutral resonances that decay into a WW boson pair in the $e\nu\mu\nu$ final state is performed by the ATLAS Collaboration and presented in this thesis. The search uses proton-proton collision data collected by the ATLAS detector at the LHC at the centre-of-mass energy of 13 TeV corresponding to an integrated luminosity of 36.1 fb^{-1}. My personal contributions to this analysis cover several parts, including mainly the optimisation of the event selection in signal regions and the binning of transverse mass distributions for the statistical analysis, the estimation experimental systematic and theoretical uncertainties for the main backgrounds, data analysis and the production of the input for the statistical analysis.

No significant excess of events beyond the Standard Model background prediction is observed in the mass range between 200 GeV and up to 5 TeV. Therefore, upper limits are set on the product of the production cross section and the $X \to WW$ branching fraction in several scenarios: a high-mass Higgs boson with a narrow width or with intermediate widths (of 5%,10%,15% of the heavy Higgs boson mass), as well as other scalar, vector and spin-2 signals. For the narrow-width heavy Higgs boson signals, values above 6.4 pb (1.3 pb) at $m_H = 200$ GeV and above 0.008 pb (0.005 pb) at 4 TeV are excluded at 95% confidence level for the gluon-gluon fusion (vector-boson fusion) production mode. For the signals of heavy vector triplet model A, described in Chapter 4, produced by quark-antiquark annihilation, mass values below 1.3 TeV are excluded. While for the signals of Randall-Sundrum graviton model with $k/\bar{M}_{\text{Pl}} = 1(0.5)$, mass values below 1.1 TeV (750 GeV) are excluded.

For some of the specific models considered in this thesis, the current exclusion limits are still above the corresponding model predictions. Therefore there is a good prospect for future improvements. At low masses or low m_{T} where the SM

background contribution is important, the main improvement should come from further suppressed background contribution with reduced systematic uncertainties. At higher masses where the current sensitivity is statistically limited, the expected large increase in the integrated luminosity of the future data taking at the LHC will greatly improve the search sensitivity.

Appendices

A Trigger efficiency

This study is aimed to estimate the trigger efficiency in the analysis. The *trigger efficiency* is computed to be $\frac{N'}{N''}$, and the *trigger and trigger matching efficiency* is computed to be $\frac{N}{N''}$, where N is the number of events passing all selection criteria (as described in Section 6.2), N' is the number of events passing all selection criteria except for the trigger matching cut, and N'' is the number of events passing all selection criteria except for the trigger cut and the trigger matching cut (as described in Chapter 4).

The efficiencies for the 3 SRs are listed in Table A.1 and they are all above 99%.

Table A.1: Efficiencies of *trigger* and *trigger and trigger matching* computed for the 3 SRs in the analysis.

Region	Trigger efficiency [%]	Trigger and trigger matching efficiency [%]
Inclusive ggF SR	99.44 ± 0.05	99.40 ± 0.05
VBF 1-jet SR	99.2 ± 0.3	99.2 ± 0.3
VBF 2-jet SR	$99.5^{+0.3}_{-0.4}$	$99.5^{+0.3}_{-0.4}$

A potential dependence on lepton p_{T} and η was also checked. Figure A.1 shows the efficiencies for the combination of the $e\mu$ and μe channels as a function of leading and subleading lepton p_{T}. The structure observed for the efficiencies as a function of leading lepton p_{T} in the top right plot of Figure A.1 is further investigated in Figure A.2 separately for leading electrons and muons, but no clear effect can be seen in those plots. The dependence on η of the leptons is shown in Figure A.3.

Two-dimensional $\eta - p_{\mathrm{T}}$ maps of the trigger efficiency are shown in Figure A.4 for the three signal regions. They are provided to be able to spot any possible regions of the phase space to be responsible for some of the $\leq 99\%$ efficiencies shown in Figures A.1 and A.3. Efficiencies were also computed separately for the

two lepton flavours, shown in Figures A.5-A.7, but none of the plots show any particular trigger efficiency dependence on η or p_{T}.

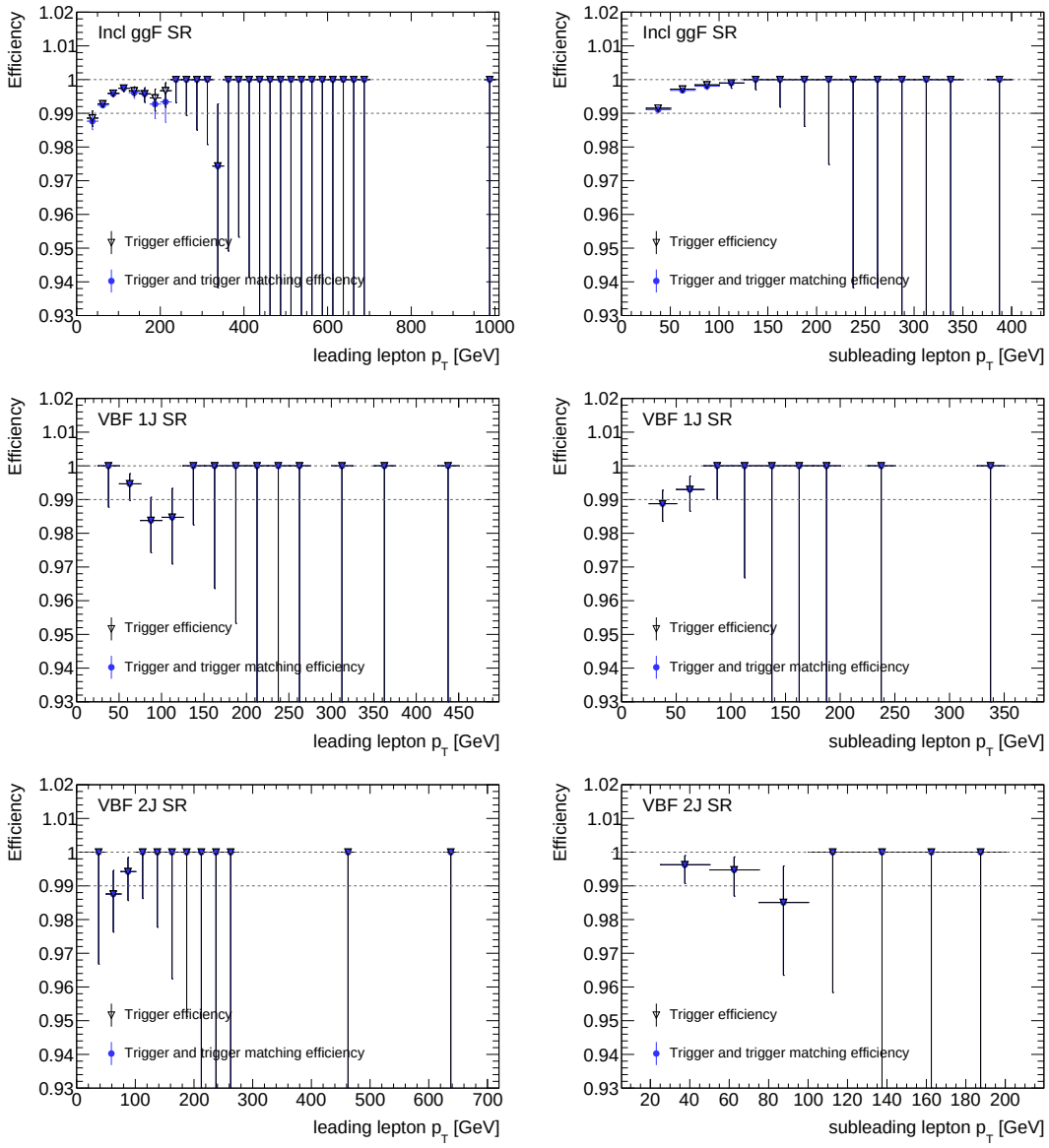

Figure A.1: Trigger efficiency (black) and trigger and trigger matching efficiency (blue) as a function of the leading (left) and subleading (right) lepton p_{T} for the Inclusive ggF signal region (top), VBF 1-jet signal region (middle) and VBF 2-jet signal region (bottom).

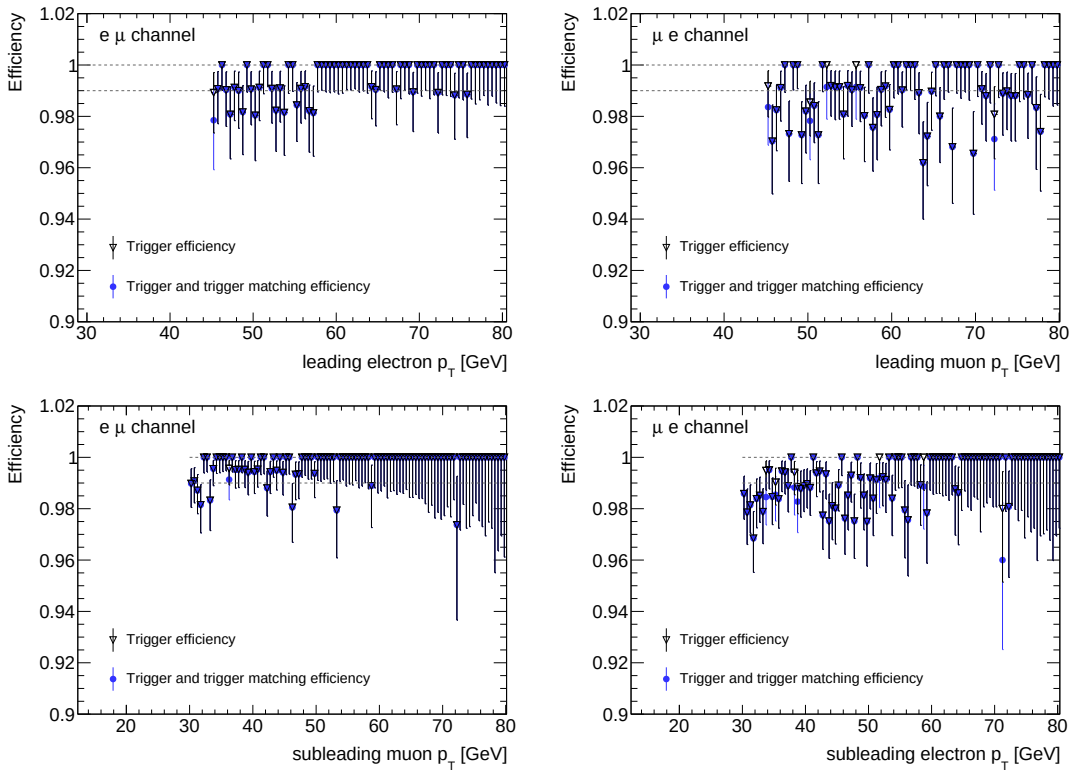

Figure A.2: Trigger efficiency (black) and trigger and trigger matching efficiency (blue) as a function of the leading electron (top left), leading muon (top right), subleading muon (bottom left) and subleading electron (bottom right) p_{T} for the Inclusive ggF signal region.

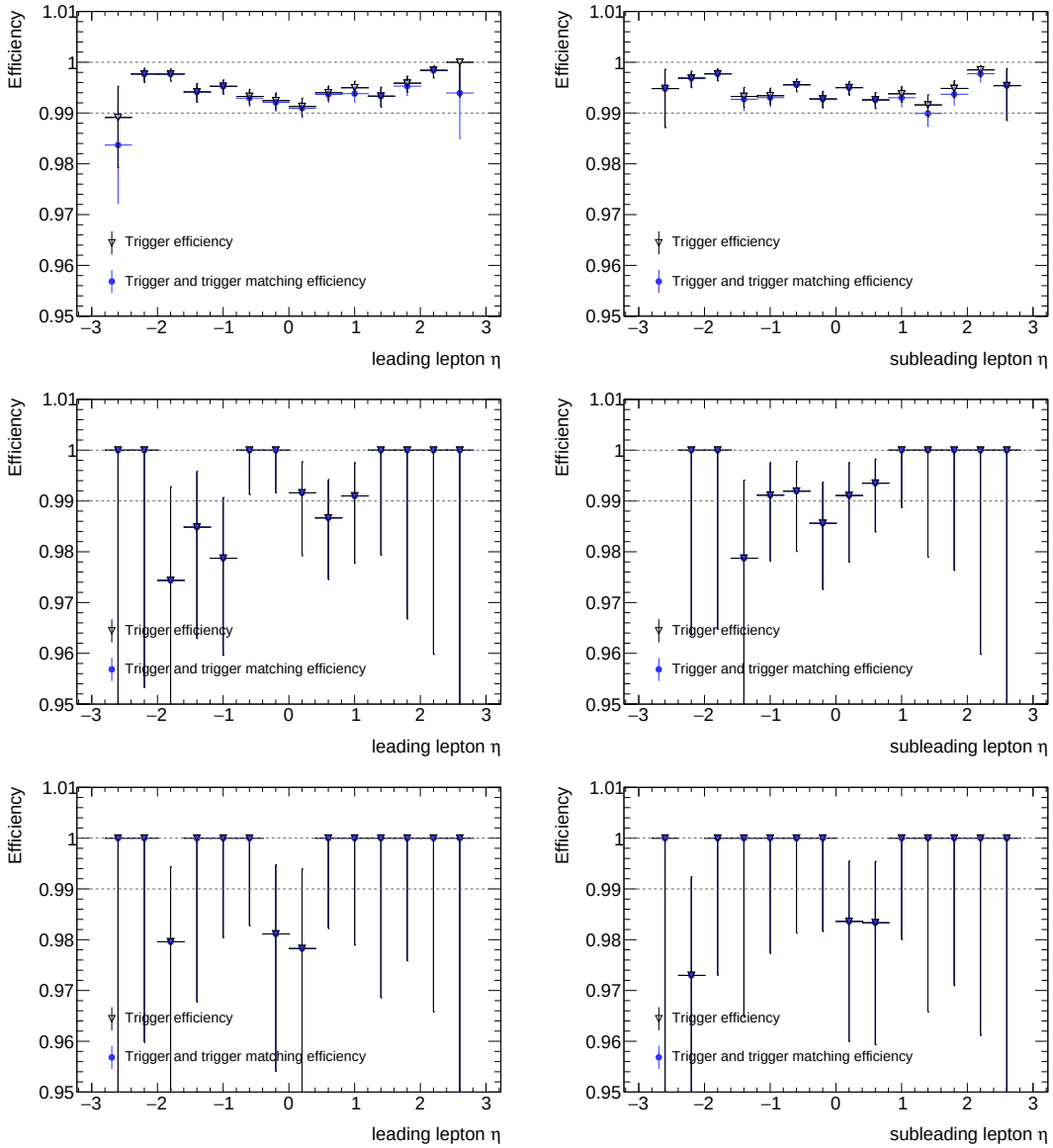

Figure A.3: Trigger efficiency (black) and trigger and trigger matching efficiency (blue) as a function of the leading (left) and subleading (right) lepton η for the Inclusive ggF signal region (top), VBF 1-jet signal region (middle) and VBF 2-jet signal region (bottom).

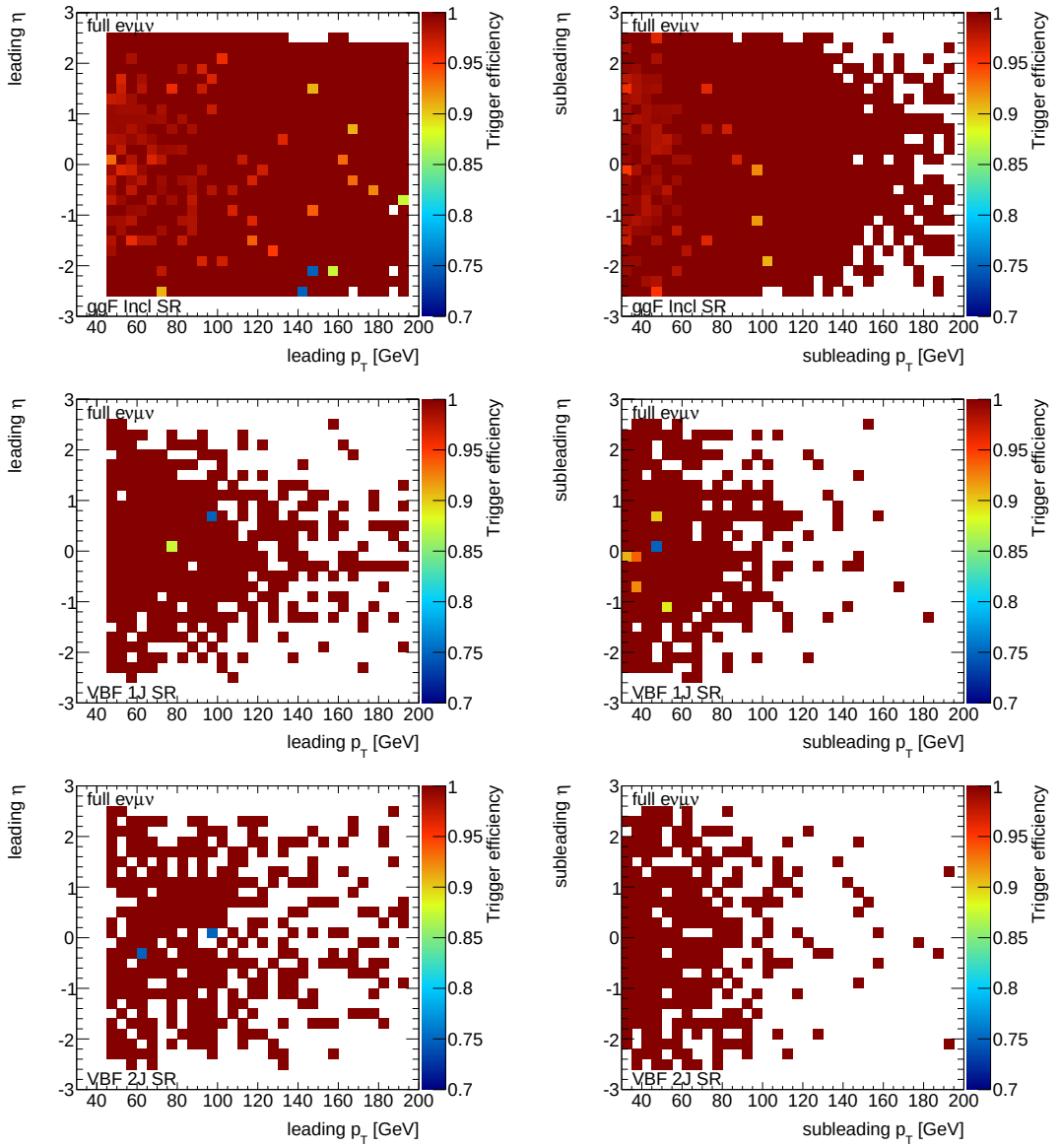

Figure A.4: Trigger efficiency as a function of the leading (left) and subleading (right) lepton p_{T} and η for the Inclusive ggF signal region (top), VBF 1-jet signal region (middle) and VBF 2-jet signal region (bottom).

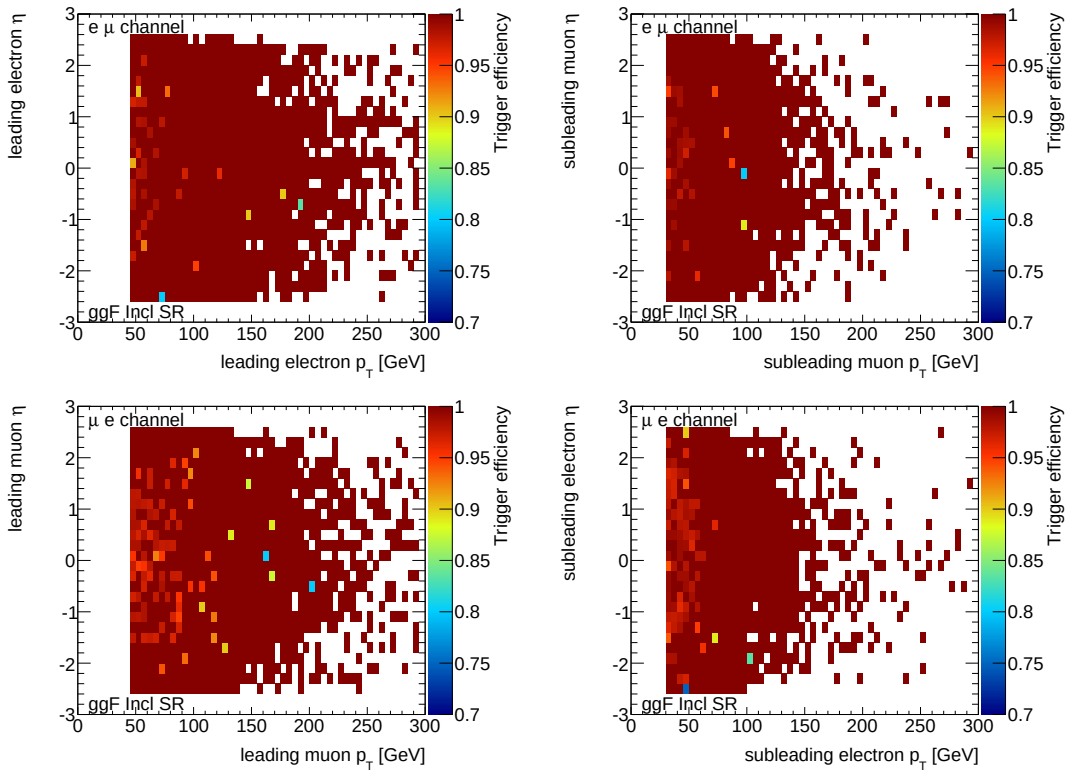

Figure A.5: Trigger efficiency as a function of the leading electron (top left), subleading muon (bottom left), leading muon (top right) and subleading electron (bottom right) p_{T} and η for the Inclusive ggF signal region.

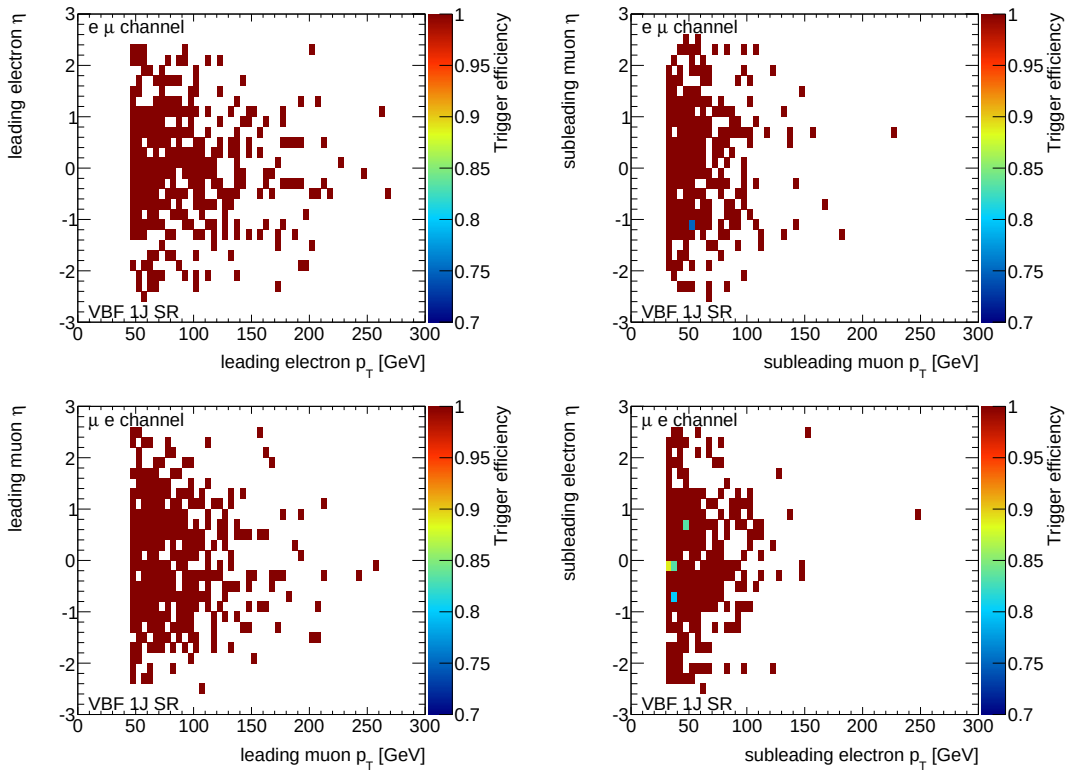

Figure A.6: Trigger efficiency as a function of the leading electron (top left), subleading muon (bottom left), leading muon (top right) and subleading electron (bottom right) p_{T} and η for the VBF 1-jet signal region.

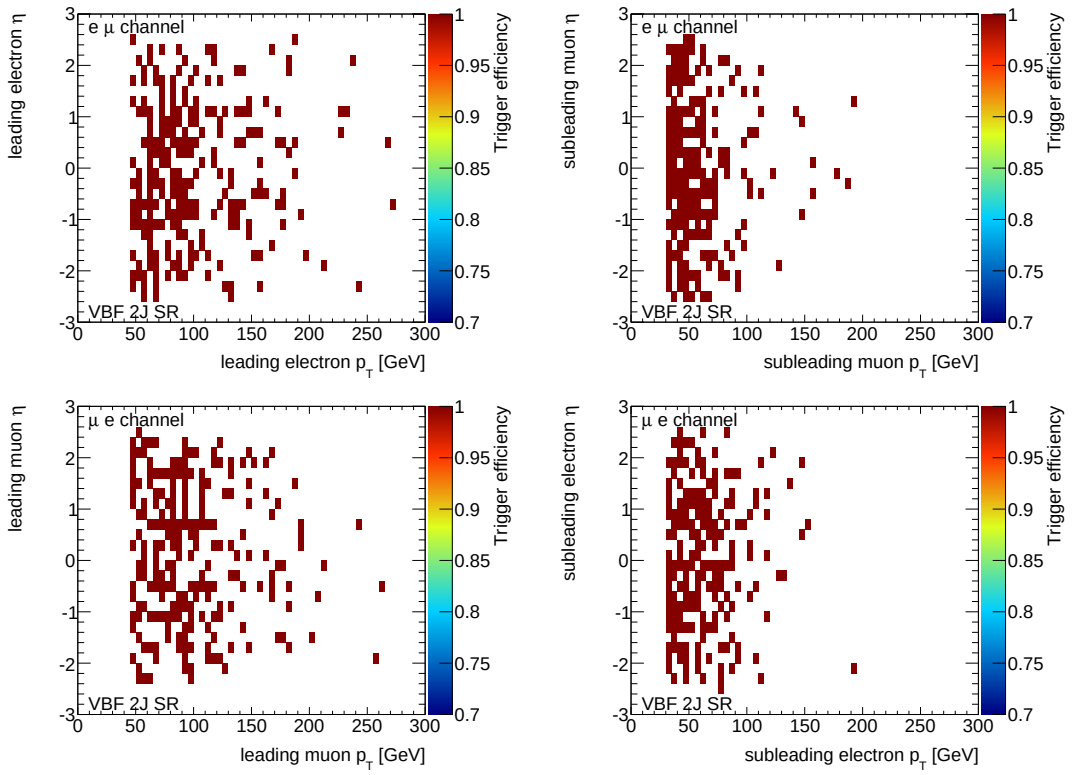

Figure A.7: Trigger efficiency as a function of the leading electron (top left), subleading muon (bottom left), leading muon (top right) and subleading electron (bottom right) p_{T} and η for the VBF 2-jet signal region.

B Powheg-to-MadGraph reweighting

The POWHEG generator version that was used to simulate the NWA signal samples is only capable of producing maximal one jet in association to a ggF induced Higgs-like resonance in the matrix element, while further jets are emulated by the parton shower generator, PYTHIA8. As a consequence, the contribution of the ggF signal topology in the $N_{\text{jet}} \geq 2$ VBF event category is assumed to be insufficiently described. However, a more realistic modelling of higher jet-multiplicities is provided using the MADGRAPH5_AMC@NLO [83] generator in order to simulate $gg \to H$ events in association with up to two jets in the matrix element. Here, the overlap between identical final states generated at the matrix element and the parton shower stage is removed using the FxFx merging [84].

Thus the expected mismodelling in the $N_{\text{jet}} \geq 2$ VBF event category corresponding to the predictions of the POWHEG generator are corrected by dedicated scale factors. These scale factors are determined as the double ratios

$$k = \frac{N^{\text{2-jet VBF}}_{\text{MADGRAPH5}} / N^{\text{inclusive ggF}}_{\text{MADGRAPH5}}}{N^{\text{2-jet VBF}}_{\text{POWHEG}} / N^{\text{inclusive ggF}}_{\text{POWHEG}}} \ , \tag{1}$$

in which $N^{\text{2-jet VBF}}_{\text{MADGRAPH5}}$ and $N^{\text{inclusive ggF}}_{\text{MADGRAPH5}}$ are the event yields in the $N_{\text{jet}} \geq 2$ VBF and inclusive ggF event categories respectively (obtained using the event selection at generator level), as predicted by the MADGRAPH5 generator. The parameters $N^{\text{2-jet VBF}}_{\text{POWHEG}}$ and $N^{\text{inclusive ggF}}_{\text{POWHEG}}$ are the corresponding event yields as predicted by POWHEG.

These scale factors are calculated for several hypothetical heavy-Higgs masses and the corresponding results are presented in Table B.1. According to these findings, the lowest considered mass values, 0.2 TeV, correspond to the largest k-factor value, 1.136. The size of the k-factor decreases continuously with increasing resonance mass and reaches finally a value of 0.843 for the 4.0 TeV mass point.

In addition, POWHEG-to-MADGRAPH scale factors are also calculated for the $N_{\text{jet}} = 1$ VBF category, as the gluon fusion induced production of heavy Higgs-like particles is not yet intensively studied within such phase space regions using LHC data. The corresponding k-factors range from 0.905 for the lowest considered resonance mass to 0.729 for the largest considered mass value. As for the k-factors corresponding to the ratio of event yields in the $N_{\text{jet}} \geq 2$ VBF and the inclusive ggF category, the size of the scale factors decreases with increasing resonance mass. The full set of k-factors is shown in Table B.2.

An extrapolation is applied separately on both sets of k-factors using second

order polynomials in order to obtain k-factors for other Higgs mass values as well. In case the k-factors corresponding to the comparison of the event yields in the $N_{\text{jet}} \geq 2$ VBF and the inclusive ggF category are considered, the extrapolation function is obtained to be

$$1.726 \cdot 10^{-8} \times m_H^2/\,\text{GeV}^2 - 1.323 \cdot 10^{-4} \times m_H/\,\text{GeV} + 1.130\,, \tag{2}$$

while the extrapolation function obtained after fitting the set of k-factors that corresponds to the use of the $N_{\text{jet}} = 1$ VBF category is given by

$$3.593 \cdot 10^{-8} \times m_H^2/\,\text{GeV}^2 - 1.880 \cdot 10^{-4} \times m_H/\,\text{GeV} + 0.918\,. \tag{3}$$

The curves of these two extrapolation functions are presented in Figure B.1 together with the two sets of k-factors.

Table B.1: POWHEG-to-MADGRAPH scale factors for various resonance mass points using the ratio of the number of events in the $N_{\text{jet}} \geq 2$ VBF category to the number of events in the inclusive ggF category.

Mass point [GeV]	$r_{\text{2-jet VBF, ggF}}$ (MADGRAPH5)	$r_{\text{2-jet VBF, ggF}}$ (POWHEG)	scale factor k
200	0.017	0.015	1.136
300	0.020	0.019	1.071
400	0.025	0.022	1.107
600	0.032	0.031	1.041
1000	0.043	0.042	1.013
1200	0.044	0.046	0.956
1400	0.048	0.050	0.973
1600	0.050	0.053	0.950
1800	0.052	0.055	0.956
2400	0.056	0.060	0.938
3000	0.057	0.063	0.902
3400	0.058	0.064	0.901
4000	0.056	0.065	0.851

Table B.2: POWHEG-to-MADGRAPH scale factors for various resonance mass points using the ratio of the number of events in the $N_{\text{jet}} = 1$ VBF category to the number of events in the inclusive ggF category.

Mass point [GeV]	$r_{\text{1-jet VBF, ggF}}$ (MADGRAPH5)	$r_{\text{1-jet VBF, ggF}}$ (POWHEG)	scale factor k
200	0.053	0.059	0.905
300	0.058	0.065	0.894
400	0.059	0.070	0.845
600	0.057	0.074	0.766
1000	0.055	0.075	0.726
1200	0.058	0.075	0.771
1400	0.053	0.074	0.717
1600	0.053	0.073	0.724
1800	0.050	0.072	0.692
2400	0.049	0.069	0.703
3000	0.043	0.066	0.648
3400	0.047	0.065	0.722
4000	0.045	0.062	0.727

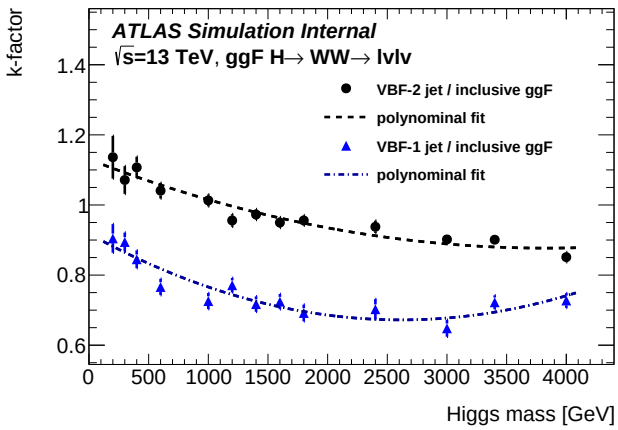

Figure B.1: Distribution of the two sets of POWHEG-to-MADGRAPH scale factors displayed for various resonance mass values. These scale factors are represented as black dots for the ratio of event yields in the $N_{\text{jet}} \geq 2$ VBF and the inclusive ggF categories and as blue triangles for the ratio of event yields in the $N_{\text{jet}} = 1$ VBF and the inclusive ggF categories. The two second order polynomials, which are used as extrapolation functions are shown in addition as a black and a blue dashed lines.

C Study of High-p_{T} muons

The current analysis selects muons with the "Medium" working point[10]. This selection is of course valid in the full momentum range but may not provide the best momentum resolution. This study is aimed to check the impact of using the "High-p_{T} muons" working point is checked.

Figure C.1 shows a comparison for the distributions of the leading muons passing the pre-selection with that passing addtionally the major "High-p_{T}" cuts. The discrepancy in slope is believed to be due to the mismodelling of the top-

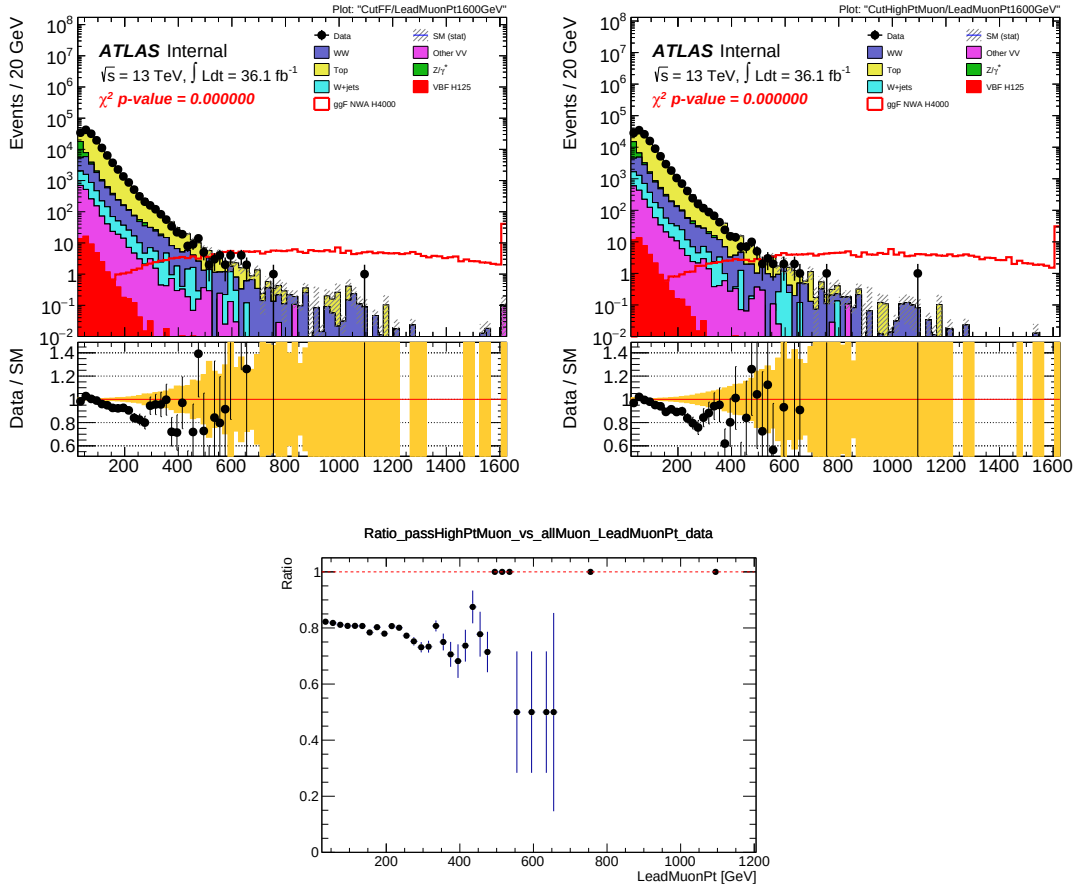

Figure C.1: Distributions of p_{T} of all selected leading muons in the preselected sample (left) and of those passing the major "High-p_{T}" cuts (right) and their ratio (bottom). The hatched band in the upper panel and the shaded band in the lower panel show the statistical uncertainty only on the predictions. The last bin contains the overflow. The 4 TeV signal is normalised to $\sigma_H \times \mathrm{BR}(H \to WW) = 1\,\mathrm{pb}$.

quark background (see Section 7.1). The different slopes between the left and right plots are thought to be a reflection that different scale factors are needed for

[10]The major reason is that the "High-p_{T}" working point is not available in the samples used in the analysis from the group production.

the "Medium" and "High-p_{T}" selections. And the ratio plot shows the "High-p_{T}" selection seems to be a subset ($\sim 80\%$) of the "Medium" selection.

The p_{T} distribution of the leading muons (Figure C.1 (left) is also compared with the corresponding distribution of the leading electrons (Figure C.2 (left)). Their ratio for data is shown in Figure C.2 (right). With limited data statistics, there is no indication that the leading muons differ from the leading electrons for $p_{\mathrm{T}} \gtrsim 300\,\mathrm{GeV}$.

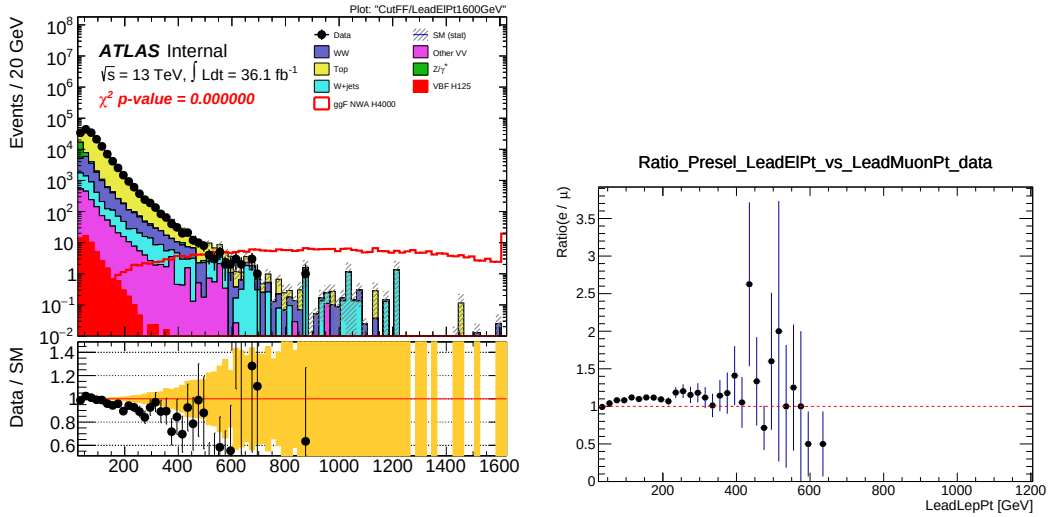

Figure C.2: Distributions of p_{T} of all selected leading electrons in the preselected sample (left) and the ratio of electron p_{T} over muon p_{T} in data (right). The hatched band in the upper panel and the shaded band in the lower panel show the statistical uncertainty only on the predictions. The last bin contains the overflow. The 4 TeV signal is normalised to $\sigma_H \times \mathrm{BR}(H \to WW) = 1\,\mathrm{pb}$.

To further explain and understand the mismodelling of top that leads to the sloping discrepency in Figure C.1 (left), the leading muon p_{T} distribution (in the quasi-inclusive ggF top-quark CR) is shown in Figure C.3 before the p_{T} correction (left) and after the correction (right) with a p_{T} range of up to 800 GeV.

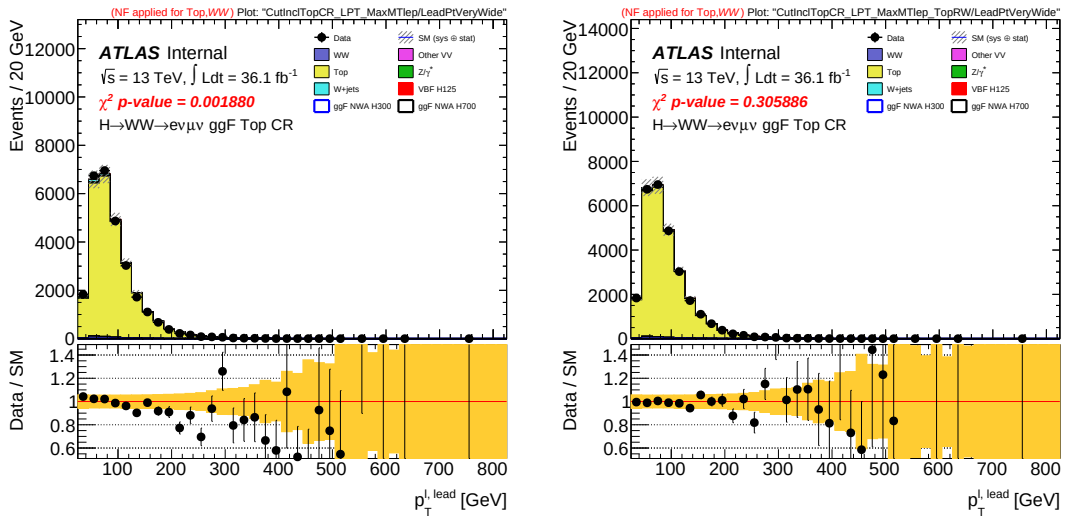

Figure C.3: Distributions of p_{T} of the leading muons in the quasi-inclusive ggF top-quark control region before the leading p_{T} correction (left) and after the correction (right). The hatched band in the upper panel and the shaded band in the lower panel show the statistical uncertainty only on the predictions.

D The optimisation of the m_{T} binning

In this section, the optimisation method for the binning of the m_{T} distribution is discussed. As with the event selection optimisation, the optimisation of the m_{T} binning is also very important to improve the signal sensitivity in the statistical fit. A preliminary optimisation strategy is first proposed to get the optimised binning from a scan on a fine-binned m_{T} distribution by requiring a maximum significance. However, as a result, the m_{T} distributions look quite fluctuating. Some bins have too small bin size and very large statistical uncertainties on the backgrounds. Nevertheless, the optimised binning is found to have some tendency that it is regularly divided in logarithmic scale (log-scale). This is adopted by the improved optimisation strategy, which has been developed to improve the optimisation. Finally the results for the optimised binning are also shown in this section.

Preliminary optimisation strategy

Similar to the event selection optimisation method in Section 6.1, significance is a very important quantity which will be required to be at the maximum value with the optimised binning, and it has been defined earlier as in Equation 6.1. However, this is a general definition of significance. To take the binning information into account, it is still necessary to extend the significance definition over the m_{T} distribution, as defined in Equation 6.2.

The first step is to do a mass dependent binning optimisation. For each mass point of signal, a scan on every m_{T} bin is performed. During the scan, when a bin, bin i, satisfies $s_{i-1}^2 + s_i^2 < s_{i-1,i}^2$, it will be merged with the previous bin, bin $i-1$. s_{i-1} and s_i are the significance values for bins $i-1$ and i, respectively, while $s_{i-1,i}$ is the significance value for a merged bin from bin $i-1$ and bin i. If a bin has negative number of events of signal or backgrounds, it will also be merged with the previous bin. In the optimisation, the last bin will always include overflow events. At the end of this step, it is supposed to get an optimised binning for each mass point of signal. However, a mass dependent binning makes the analysis much more complicated. For such a search analysis, it is necessary to further simplify the binning. This will be done in the second step.

The second step requires also a scan on the mass points. For each mass point of signal, significance as well as the uncertainty of it will be calculated for all the optimised binning that is obtained from the first step. By a visual comparison of all these significance values and uncertainties in each signal region, a binning that

gives a large significance but small uncertainty will be chosen to be the optimised binning for all signals. As with the event selection optimisation, the binning optimisation is done with the NWA signals.

The optimised binning gives much improved upper limits than the binning with a constant bin size. However, the m_{T} distributions with the new binnings are found to be fluctuating dramatically in some bins. An example in the quasi-inclusive signal region with the optimised m_{T} binning is shown in Figure D.1. For a better display, the distribution with a binning in log-scale is also shown.

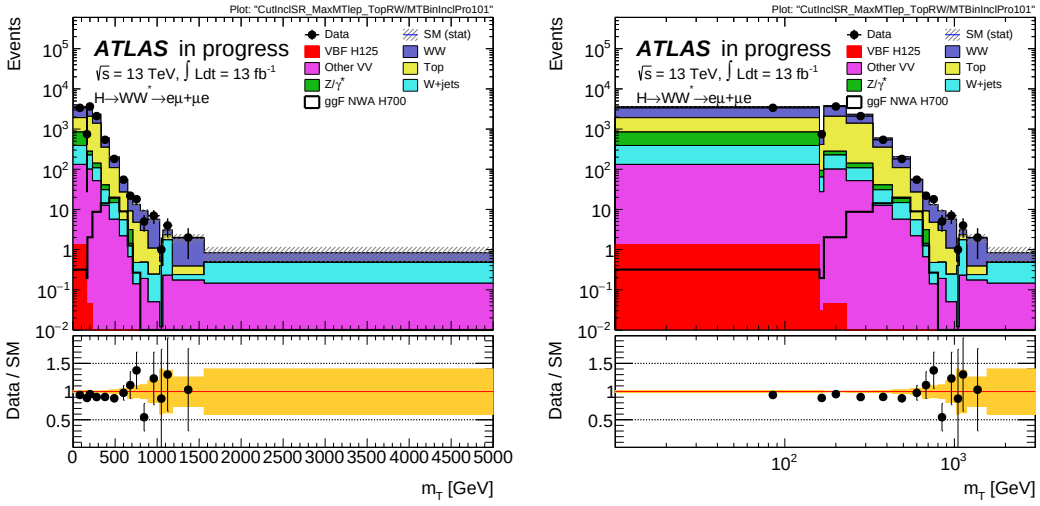

Figure D.1: m_{T} distribution with the preliminary optimised binning in the quasi-inclusive SR. The binning is shown in both linear scale (left) and log-scale (right).

Improved optimisation strategy

To avoid the fluctuation mentioned above, an improved optimisation strategy is needed. Despite some bins are fluctuating and have very irregular bin sizes, the bin size appears to be regular and roughly equal when the binning is shown in log-scale, especially in the middle range of m_{T} where staistics are high enough compared with the tails.

Therefore the improved strategy is based on the distribution of $\log m_{\mathrm{T}}$. Given that the distributions of signals are always changing from one mass point to another but the backgrounds are always the same, the distribution of backgrounds is always the main consideration in the optimisation. The first bin is always fixed to 70–100 GeV, due to the fact that there are not much statistics of backgrounds in this range and no events selected below $m_{\mathrm{T}} = 70$ GeV. In the middle range, 100–1000 GeV, where the backgrounds are mainly distributed, the binning is divided

into N bins with a constant $\log m_{\mathrm{T}}$ bin size: $\frac{\log 1000 - \log 100}{N} = \frac{1}{N}$. At the high m_{T} tail, 1000–3000 GeV, the binning is required to have a bin size that is two times larger ($\frac{2}{N}$ in log-scale) than that in the middle range. N is the parameter to be optimised and is supposed to give the maximum significance.

To get the optimised N, a scan is performed on it from a small integer ($\sim$ 5) to a large integer ($\sim$ 60) with a step of unit. The optimised N is found to be 14 for the ggF SR, and 6 for the VBF 1-jet and 2-jet SRs. Therefore, finally, the m_{T} distributions in the signal regions are divided into 18 (8) bins for the ggF quasi-inclusive ($N_{\mathrm{jet}} = 1$ and ≥ 2 VBF) categories.

Optimised binning

The m_{T} distributions with optimised binnings can be found in Sections 9.2 (Figure 9.5) and 9.3 (Figure 9.6). The bin boundaries are summarised in Table D.1.

Table D.1: Bin boundaries in log [linear] scale of the m_{T} distributions used in the fit for the three signal regions are shown.

Inclusive ggF SR									
$\sim$ 1.8 [70]	2.0 [100]	2.07 [120]	2.14 [140]	2.21 [160]	2.28 [190]	2.36 [230]	2.43 [270]	2.5 [315]	2.57 [370]
2.64 [440]	2.71 [510]	2.78 [600]	2.86 [725]	2.93 [850]	3.0 [1000]	3.14 [1380]	3.28 [1900]	3.48 [3000]	
$N_{\mathrm{jet}} = 1$ and ≥ 2 VBF SRs									
$\sim$ 1.8 [70]	2.0 [100]	2.17 [150]	2.33 [215]	2.5 [315]	2.67 [470]	2.83 [680]	3.0 [1000]	3.48 [3000]	

E Sherpa $q\bar{q} \to WW$ correction

As briefly discussed in Section 7.2, the correction applied to the $q\bar{q} \to WW$ process is studied in detail in this section. The generator for the nominal samples for this process is SHERPA 2.2.1, which has NLO precision for events with up to one parton. In order to have a prediction as precise as we can, the SHERPA samples are thus corrected (at truth or generator level) to a combination of MATRIX NNLO QCD calculation [118] and NLO EW correction [119] (see Figure E.1), to give a better MC prediction.

The correction is aimed at and only applied to the quasi-inclusive ggF SR and WW CR, since for the VBF categories the MC samples are already approaching NNLO considering the requirements on the number of jets in the VBF phase spaces. And in the top CRs, the WW background has too small contributions, therefore the correction is also not needed.

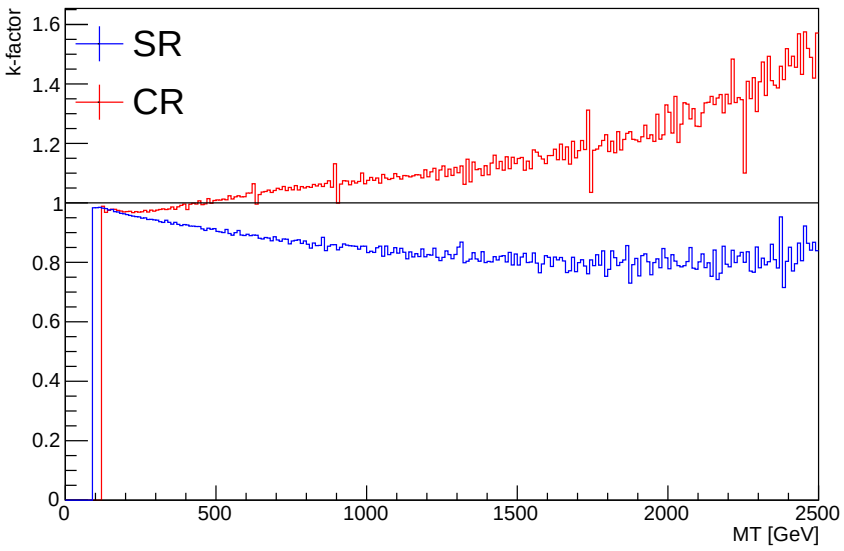

Figure E.1: NLO EW corrections as a function of m_{T} in the quasi-inclusive ggF SR and WW CR.

To apply such a correction, a k-factor as a function of m_{T} is used to reweight the SHERPA samples. To avoid bias due to statistical fluctuation, several polynomial fit functions are tried to get a smooth extrapolation of the k-factor, but finally only one function is selected to be used in the analysis. This is shown in Figure E.2. The uncertainty band indicates the total systematic uncertainty on the correction, and corresponds to 100% of the correction (half-to-half scaled up and down). And it properly covers most of the differences due to different fit functions.

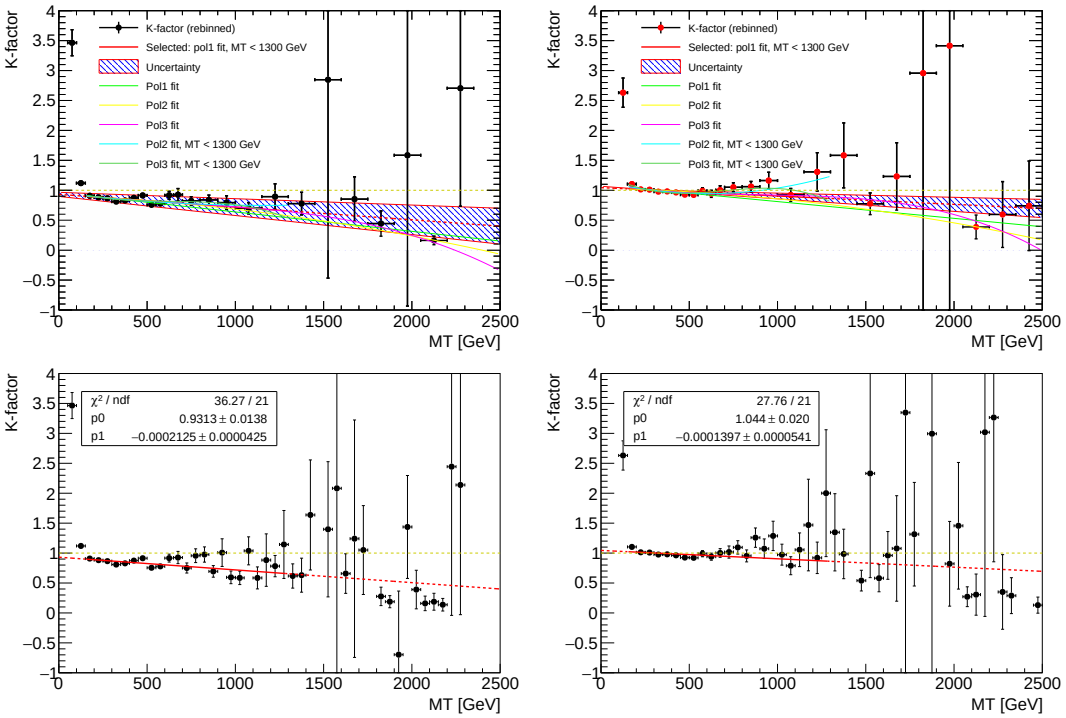

Figure E.2: K-factor as a function of m_{T} and extrapolations in the quasi-inclusive ggF SR (left) and WW CR (right). The selected fit functions are shown in the bottom plots. The solid curves indicate the m_{T} range where the functions are fit to the k-factor, while the dashed curves are simply extensions of the fit functions.

F Sources of experimental systematics

The systematic uncertainty on the energy (for electrons) or momentum (for muons) scale or resolution is calculated by shifting the energy or momentum by scale factor before selecting the events and by observing the effect of this scale factor on the number of events in the final state. The shifting procedure is done for a nominal scaling value and scaling values with $\pm 1\sigma$.

The systematic uncertainties are calculated using the recommendations from the ATLAS Combined Performance (CP) groups. The standard set of experimental systematics is made of many nuisance parameters:

Trigger efficiency uncertainty: three nuisance parameters are considered, one for electron (*EL_EFF_Trigger_Total_1NPCOR_PLUS_UNCOR*) and two for muons (*MUON_EFF_TrigStatUncertainty, MUON_EFF_TrigSystUncertainty*).

Electron reconstruction and identification: four nuisance parameters, EL_EFF_Reco_TOTAL_1NPCOR_PLUS_UNCOR and EL_EFF_ID_CorrUncertaintyNP0 (0 to 14), EL_EFF_ID_SIMPLIFIED_UncorrUncertaintyNP0 (0 to 15), are considered for the systematic uncertainties of the electron reconstruction efficiency and identification efficiencies.

Electron energy scale and resolution: the standard set for the systematic uncertainties of the electron energy scale and resolution is made of EG_RESOLUTION_ALL, EG_SCALE_ALLCORR, EG_SCALE_E4SCINTILLATOR, EG_SCALE_LARTEMPERATURE_EXTRA2015PRE, EG_SCALE_LARTEMPERATURE_EXTRA2016PRE and EG_SCALE_LARCALIB_EXTRA2015PRE.

Muon reconstruction and identification: two nuisance parameters, MUON_EFF_STAT, MUON_EFF_SYS are considered for the systematic uncertainties of the muon reconstruction and identification efficiency.

Muon momentum scale and resolution: three nuisance parameters, MUONS_SCALE, MUONS_ID and MUONS_MS are considered for the systematic uncertainties of muon momentum scale and resolution. Muon momentum resolution systematics are separated into the ID part and the MS part.

Muon track-to-vertex-association (TTVA): two nuisance parameters, MUON_TTVA_STAT and MUON_TTVA_SYS, are considered for the systematic uncertainty of an additional correction for the efficiency of the muon track-to-vertex association (TTVA) cuts ($|d_0^{sig}| < 3$ and $|\Delta z_0 \sin\theta| < 0.5$/,mm).

Isolation: three nuisance parameters, EL_EFF_Iso_TOTAL_1NPCOR_PLUS_UNCOR, MUON_ISO_STAT and MUON_ISO_SYS, are considered for the systematic uncertainty of electron and muon isolation. Muon isolation systematics are separated into the statistical part and systematic part.

Jet energy scale: the jet energy scale nuisance parameter set is formed by JET_EtaIntercalibration_Modelling, JET_EtaIntercalibration_TotalStat, JET_EtaIntercalibration_NonClosure, JET_PunchThrough_MC15, JET_EffectiveNP1 (1 to 8), JET_SingleParticle_HighPt, JET_RelativeNonClosure_MC15, JET_BJES_Response, JET_Flavor_Composition and JET_Flavor_Response.

Jet energy resolution: one nuisance parameter, JET_JER_SINGLE_NP, is considered for jet energy resolution systematics. This nuisance parameter is one-direction variation (1up).

Flavour tagging: the flavour tagging efficiencies systematics are considered using FT_EFF_Eigen_B0 (0 to 2), FT_EFF_Eigen_C0 (0 to 3), FT_EFF_Eigen_Light0 (0 to 4), FT_EFF_extrapolation and FT_EFF_extrapolation_ from_charm.

Pileup mu value rescaling and pileup rejection: the default value of the data scale factor for the pileup $\langle\mu\rangle$ value rescaling is 1.0/1.09. To evaluate the systematics of the pileup $\langle\mu\rangle$ value rescaling, the data scale factor are varied upward (1.0/1.0) and downward (1.0/1.18). The nuisance parameter ATLAS_PRW_DATASF is used to account for this uncertainty. The pileup jet rejection tool efficiency is also considered in the systematics through JET_JvtEfficiency, JET_Pileup_OffsetMu, JET_Pileup_OffsetNPV, JET_Pileup_PtTerm and JET_Pileup_RhoTopology variations.

MET: the MET computation is assigned four nuisance parameters: MET_JetTrk_Scale, MET_SoftTrk_ResoPara, MET_SoftTrk_ResoPerp, MET_SoftTrk_Scale.

Integrated luminosity: the final value of the uncertainty on the integrated luminosity is ±2.1% for the 2015 dataset and ±2.2% for the 2016 dataset, resulting in a ±2.1% uncertainty for the overall 13 TeV *pp* collisions.

G Interference effects

The interference effects between a heavy resonance and the SM WW continuum and the SM Higgs boson at 125 GeV are important in particular when the decay width or the mass of the heavy resonance is large. This is illustrated in Figure G.1 for two selected mass values at 1 TeV and 3 TeV and three width values of 5%, 10% and 15% of the mass. The invariant mass distributions, normalised to the integrated luminosity of the data 2015 and 2016, are obtained with generator gg2VV [137]. Its lineshape has been compared with MadGraph5_aMC@NLO [83] for a SM-like heavy Higgs boson and good agreement has been observed.

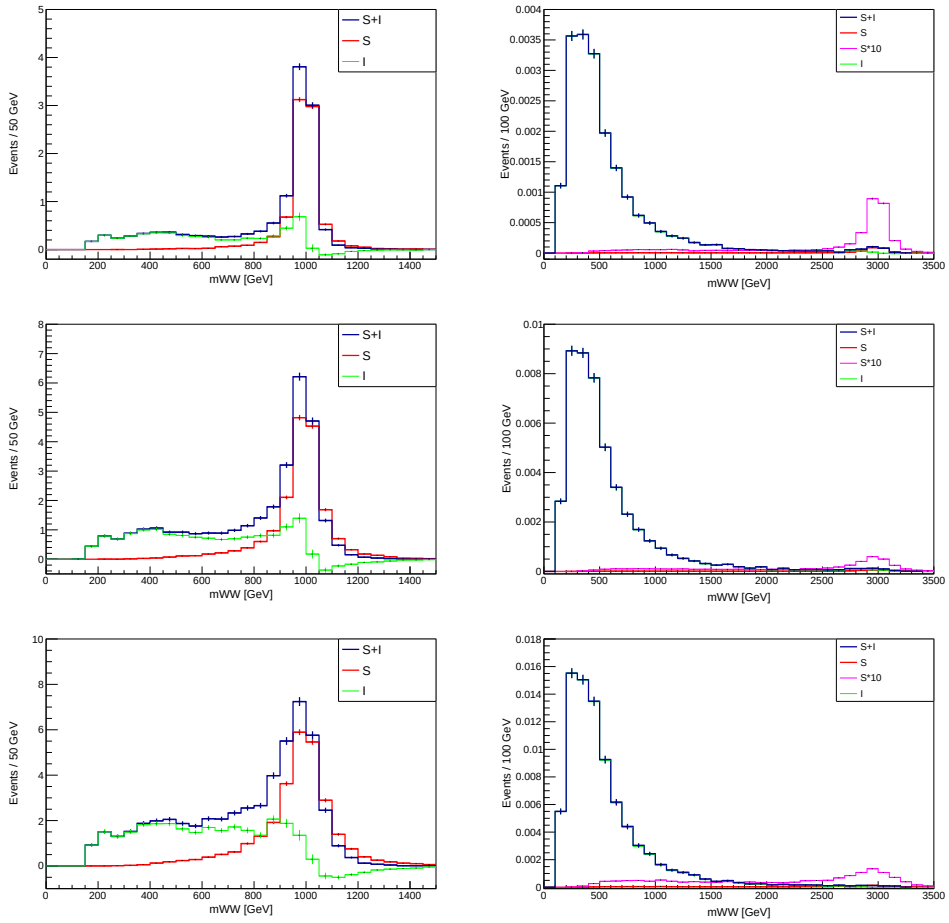

Figure G.1: Invariant WW mass distributions obtained with gg2VV for $gg \to WW \to e\nu\mu\nu$ for a heavy Higgs boson (S, red curve) at 1 TeV (left) and 3 TeV (right) with a width of 5% (top), 10% (middle) and 15% (bottom) of its mass. The interference effects (I) between the heavy Higgs boson with the SM Higgs boson at 125 GeV and the SM WW continuum are shown with the green curve and $S + I$ in blue curve. The y axis corresponds to the number of events normalised to the integrated luminosity of the 2015+2016 data.

Given that we do not have a MC sample which has the full interference effects included, a reweighting technique is applied to derive the interference contribution to the m_{T} distribution in the following way:

$$I^{\mathrm{derived}} = I^{\mathrm{truth}}_{\mathrm{gg2VV}} \times \frac{S^{\mathrm{rec}}_{\mathrm{LWA}}}{S^{\mathrm{truth}}_{\mathrm{gg2VV}}} \tag{4}$$

where $I^{\mathrm{truth}}_{\mathrm{gg2VV}}$ and $S^{\mathrm{truth}}_{\mathrm{gg2VV}}$ are the m_{T} distributions at truth level from gg2VV of the interference and signal at a given signal mass, and $S^{\mathrm{rec}}_{\mathrm{LWA}}$ is the reconstructed m_{T} distribution of a LWA signal at the same mass. A closure test has been successfully performed by applying the reweighting technique to a NWA signal.

In the statistic analysis, the relevant part has been modified from

$$\mu S + B \tag{5}$$

to

$$\mu S + \sqrt{\mu} I + B \tag{6}$$

where μ the signal strength parameter, S, I and B stand for the heavy resonance signal, interference and continuum background, respectively.

We have checked the impact of the interference effects on the expected limits for four mass points for the LWA signal with a width of 15% of its mass. The results are shown in Table G.1. The impact is found to be negligible and can be safely neglected. The same is true for the VBF signals.

Table G.1: Impact of the interference effects on the expected limits for four mass points of the LWA signal.

m_H [GeV]	600	1 000	2 000	3 000
Without interference	0.485	0.151	0.0383	0.0283
With interference	0.488	0.149	0.0383	0.0282

In addition to the missing interference effects, potential effects from a missing t-channel contribution in the VBF mode are also studied (see Appendix I). The latter effects are found to be much smaller than the interference effects and can be neglected for this analysis.

H Event category uncertainty

As this analysis is carried out in several orthogonal event categories, whose definition partially depend on the number of jets in the final state, the perturbative uncertainties on the theory predictions have to be calculated separately in each of these event categories. In addition, the correlation between the predicted cross sections and their corresponding uncertainties have to be taken into account, when combining the results of these exclusive event categories.

One of the approaches used in ATLAS to take into account the requirements that were stated above was developed by Stewart and Tackmann [132]. The main idea of this method is to first determine the uncertainties on inclusive N-jet cross sections $\sigma_{\geq N}$ and use them to calculate uncertainties on the exclusive N-jet cross section σ_N using the relation

$$\sigma_N = \sigma_{\geq N} - \sigma_{\geq N+1}\,.$$

Here, the inclusive jet-bin cross sections $\sigma_{\geq N}$ and $\sigma_{\geq N+1}$ are assumed to be uncorrelated. Thus the uncertaintiies on the exclusive jet-bin cross section σ_N can simply be determined via

$$\Delta\sigma_N = \sqrt{\Delta\sigma^2_{\geq N} + \Delta\sigma^2_{\geq N+1}}\,.$$

Following the example given in Ref. [138], nuisance parameters are defined (in Table H.1) corresponding to the average upward and downward variation κ_i of the calculated exclusive cross section uncertainties for a log-normal distribution. These up and down variations are calculated by varying the QCD factorisation and normalisation scales in the ranges

$$\frac{1}{2} \leq \frac{\mu_F}{m_H/2} \leq 2 \text{ and } \frac{1}{2} \leq \frac{\mu_R}{m_H/2} \leq 2\,.$$

For the definition of the nuisance parameters, the exclusive jet-bin fractions $f_0 = \sigma_0/\sigma_{\geq 0}$, $f_1 = \sigma_1/\sigma_{\geq 0}$, and $f_2 = \sigma_2/\sigma_{\geq 0}$ are used as well. The total inclusive production cross section $\sigma_{\geq 0}$ and their corresponding scale uncertainties are calculated at next-to-next-to-leading order QCD using the parton-level fixed-order program HNNLO (v1.3), while the inclusive 1- and 2-jet bin cross sections $\sigma_{\geq 1}$ and $\sigma_{\geq 2}$ as well as their corresponding QCD scale uncertainties are calculated at NLO and LO precision respectively using the program MCFM (v8.0). Jets are defined in these calculations as objects having a transverse momentum

of at least 30 GeV and an absolute pseudo-rapidity value of at least 2.4. This of course leads to the problem that the definition of the $N_{\text{jet}} \geq 2$ category used in this approach to calculate the jet bin migration uncertainties is different from the VBF $N_{\text{jet}} \geq 2$ category used in this analysis. Thus the standard procedure of the Stewart-Tackman method is slightly adjusted in the following: the cross section $\sigma_{\geq 2}$ (calculated considering only jets with $|\eta| > 2.4$) will be used to calculate the migration uncertainties related to the VBF $N_{\text{jet}} = 1$ category but not for those of the VBF $N_{\text{jet}} \geq 2$ category. The corresponding uncertainties for the VBF $N_{\text{jet}} \geq 2$ category are then simply determined separately using the largest of the two considered QCD scale variations on the production cross section predicted by the NLO generator MG5_aMC@NLO (simulating the gluon-fusion induced production of Higgs bosons in association with up to two jets in the matrix element). As the overlap between the definition of the VBF $N_{\text{jet}} \geq 2$ phase space and the definition of the phase space used to calculate $\sigma_{\geq 2}$ is relative small, potential correlations between the nuisance parameter of the VBF $N_{\text{jet}} \geq 2$ category $S_{\text{VBF 2-jet}}$ and those for the inclusive ggF S^0_{ggF} and S^1_{ggF} as well as the VBF $N_{\text{jet}} = 1$ region $S^1_{\text{VBF 1-jet}}$ and $S^2_{\text{VBF 1-jet}}$ are neglected in the following.

Table H.1: Definition of nuisance parameters used to describe the uncertainties based on the migration between event categories [132].

ggF inclusive category	VBF $N_{\text{jet}} = 1$ category	VBF $N_{\text{jet}} \geq 2$ category
$S^0_{\text{ggF}} = (\kappa_{\geq 0})^{\frac{1}{f_0}}$	–	–
$S^1_{\text{ggF}} = (\kappa_{\geq 1})^{-\frac{f_1+f_2}{f_0}}$	$S^1_{\text{VBF 1-jet}} = (\kappa_{\geq 1})^{\frac{f_1+f_2}{f_1}}$	–
–	$S^2_{\text{VBF 1-jet}} = (\kappa_{\geq 2})^{-\frac{f_2}{f_1}}$	$S_{\text{VBF 2-jet}} = \kappa_{\geq 2}$

The distributions of the four nuisance parameters obtained via the Stewart-Tackmann method are shown as a function of the resonance mass in Figure H.1. All four parameters show a small mass dependence. The parameter S^0_{ggF} increases from 1.027 for the lowest resonance mass up to a value of 1.064 for a resonance mass of 3 TeV, while S^1_{ggF} varies between 0.958 and 0.919. The nuisance parameters for the VBF $N_{\text{jet}} = 1$ category $S^1_{\text{VBF 1-jet}}$ and $S^2_{\text{VBF 1-jet}}$ are 1.299 and 0.968 for a resonance mass of 200 GeV and decrease to values of 1.260 and 0.963 respectively for a resonance mass of 3 TeV. In the VBF $N_{\text{jet}} \geq 2$ category the normalisation uncertainties due to the QCD scale choice have been calculated to be +30.2% (−26.8%) for a resonance mass of 200 GeV. These uncertainties increase for increasing resonance masses and reach values of +58.2% and −37.0% for a resonance

mass of 4 TeV. The exact uncertainty values for all considered mass points are shown in Table H.2, while Table H.3 shows the exclusive jet-bin fractions and the corresponding κ_i values, i.e. the input quantities used to calculate these nuisance parameters. The distribution of the exclusive jet-bin fractions is also shown as a function of the resonance mass in Figure H.2.

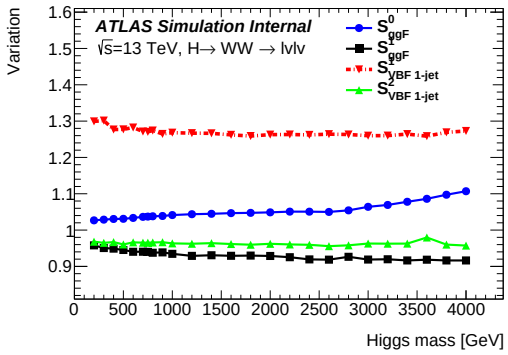

Figure H.1: Distribution of the nuisance parameters, which describe the uncertainties arising due to the migration between event categories.

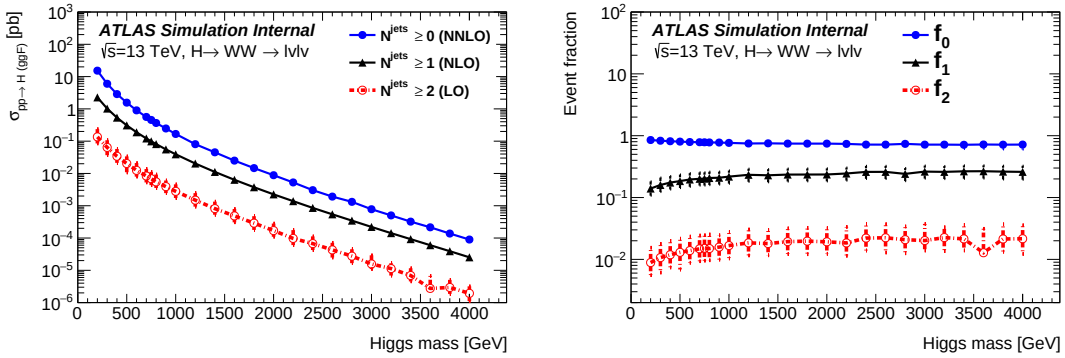

Figure H.2: Inclusive cross sections per event category and relative event fractions displayed as a function of the resonance mass.

Table H.2: Nuisance parameters describing the jet bin migration uncertainties as calculated with the Stewart-Tackmann method for various resonance mass point.

Mass point [GeV]	S^0_{ggF}	S^1_{ggF}	$S^1_{\text{VBF 1-jet}}$	$S^2_{\text{VBF 1-jet}}$	$S_{\text{VBF} \geq \text{2-jets}}$
200	1.027	0.958	1.299	0.968	1.302/0.732
300	1.029	0.951	1.301	0.965	1.285/0.738
400	1.031	0.949	1.277	0.967	1.269/0.739
500	1.031	0.945	1.277	0.960	– – –
600	1.033	0.940	1.282	0.966	1.306/0.728
700	1.036	0.940	1.271	0.965	– – –
750	1.037	0.940	1.270	0.965	– – –
800	1.038	0.938	1.274	0.966	– – –
900	1.039	0.939	1.265	0.967	– – –
1000	1.041	0.935	1.268	0.963	1.352/0.711
1200	1.044	0.929	1.267	0.962	1.342/0.711
1400	1.045	0.931	1.266	0.964	1.394/0.696
1600	1.047	0.929	1.262	0.962	1.366/0.701
1800	1.047	0.930	1.259	0.960	1.430/0.683
2000	1.049	0.929	1.263	0.962	– – –
2200	1.051	0.925	1.263	0.960	– – –
2400	1.051	0.919	1.262	0.959	1.440/0.676
2600	1.050	0.919	1.264	0.956	– – –
2800	1.054	0.926	1.263	0.958	– – –
3000	1.064	0.919	1.260	0.963	1.484/0.659
3200	1.069	0.920	1.260	0.963	– – –
3400	1.078	0.916	1.264	0.963	1.530/0.645
3600	1.086	0.918	1.259	0.980	– – –
3800	1.097	0.916	1.269	0.960	– – –
4000	1.107	0.916	1.273	0.957	1.578/0.631

Table H.3: Exclusive jet bin fractions and κ_i values for various resonance mass points.

Mass point [GeV]	f_0	f_1	f_2	$\kappa_{\geq 0}$	$\kappa_{\geq 1}$	$\kappa_{\geq 2}$
200	0.851	0.14	0.0089	1.023	1.279	1.667
300	0.83	0.16	0.0107	1.024	1.28	1.705
400	0.814	0.175	0.0119	1.025	1.257	1.641
500	0.802	0.185	0.013	1.025	1.257	1.773
600	0.79	0.196	0.0139	1.026	1.261	1.625
700	0.784	0.201	0.0148	1.028	1.25	1.614
750	0.783	0.202	0.0151	1.029	1.249	1.605
800	0.778	0.207	0.015	1.029	1.253	1.616
900	0.775	0.209	0.0158	1.03	1.244	1.569
1000	0.765	0.218	0.0167	1.031	1.247	1.626
1200	0.748	0.233	0.0185	1.033	1.245	1.621
1400	0.753	0.229	0.018	1.034	1.245	1.594
1600	0.746	0.235	0.0194	1.035	1.24	1.609
1800	0.745	0.235	0.0197	1.035	1.237	1.634
2000	0.745	0.236	0.0192	1.036	1.241	1.605
2200	0.737	0.245	0.0184	1.037	1.243	1.707
2400	0.718	0.260	0.0221	1.036	1.239	1.626
2600	0.718	0.260	0.0223	1.036	1.241	1.694
2800	0.738	0.241	0.0208	1.040	1.240	1.644
3000	0.717	0.263	0.0202	1.046	1.239	1.636

I The contribution of the t-channel to the VBF production mode

The various VBF signal samples that are used for the studies presented in this note are simulated for each mass point hypothesis separately from the background. Thus both interference effects but also the non-resonant t-channel contribution of the searched resonance are not taken into account when comparing the sum of the background predictions and the signal hypothesis to the observations in data. This section focuses on a quantification of the missing t-channel contribution, while details on the interference effects between the signal and the diboson WW background were already described in Appendix G. For this study, only processes that correspond to an electroweak production of W^+W^-jj final states are considered.

Due to technical reasons, the estimation of the missing t-channel contribution, requires the generation of three Monte-Carlo samples (per mass point) in addition to the background only hypothesis. These samples contain:

1. s-channel production of a heavy resonance (with the resonance decaying via $H \to W^+W^-$).

2. Simultaneous production of the signal and background (includes interference effects and the t-channel contribution).

3. Non-resonant W^+W^-jj production (only t-channel and background).

These samples are generated at leading order QCD using MadGraph5_aMC@NLO v2.3.2 and assuming SM-like couplings between the heavy scalar and vector bosons. Contributions of diagrams that correspond to a non pure electroweak production of the W^+W^-jj final state are removed and do not enter the cross section calculations nor the spectrum of the invariant diboson mass m_{WW} or the transverse diboson mass m_{T} (Figures I.1 and I.2).

Cross section values for the various W^+W^-jj production modes that include a contribution of a heavy scalar are presented in Table I.1 for resonance masses m_H of 300 GeV, 1.5 TeV and 3 TeV. At the same time, the width of these resonances is set for every mass point to $0.15m_H$. The cross section of the background only hypothesis is $\sigma_B = 0.7650 \pm 0.0003$ pb. Here, the cross section of the resonant s-channel production is referred to as σ_S, while the cross sections for the simultaneous production of the scalar and the background including (excluding) a resonant W^+W^- production are denoted as σ_{S+B} ($\sigma_{B+t\text{-chan}}$). In addition, the t-channel cross section, which is estimated via $\sigma_{B+t\text{-chan}} - \sigma_B$, is listed as well.

For a mass of 300 GeV, the t-channel contribution is predicted to increase the non-resonant W^+W^-jj production cross section by approximately 1.0% and for a resonance mass of 1.5 TeV the increase would be about 0.2%. For a mass of 3 TeV, the t-channel contribution is compatible with zero considering the statistical uncertainties on the cross section calculations. Therefore, a missing of the t-channel contribution to the the background process is significantly smaller than the theoretical uncertainties on the background cross section. In addition, the contribution of the t-channel is shown in Figure I.1 as a function of the invariant diboson mass m_{WW} and in Figure I.2 as a function of the transverse diboson mass m_{T}. Their distribution is shown together with the cross section modulation obtained when considering interference effects between the resonant and non-resonant W^+W^-jj production modes.

Table I.1: Cross sections for resonant and non-resonant W^+W^-jj production.

Mass point	σ_S [pb]	σ_{S+B} [pb]	$\sigma_{B+t\text{-chan}}$ [pb]	$\sigma_{B+t\text{-chan}} - \sigma_B$ [pb]
300 GeV	0.1423 ± 0.0001	0.8577 ± 0.0004	0.7732 ± 0.0003	0.0082 ± 0.0004
1.5 TeV	0.06901 ± 0.00003	0.8426 ± 0.0004	0.7662 ± 0.0003	0.0012 ± 0.0004
3 TeV	0.009744 ± 0.000004	0.7804 ± 0.0003	0.7647 ± 0.0003	-0.0003 ± 0.0004

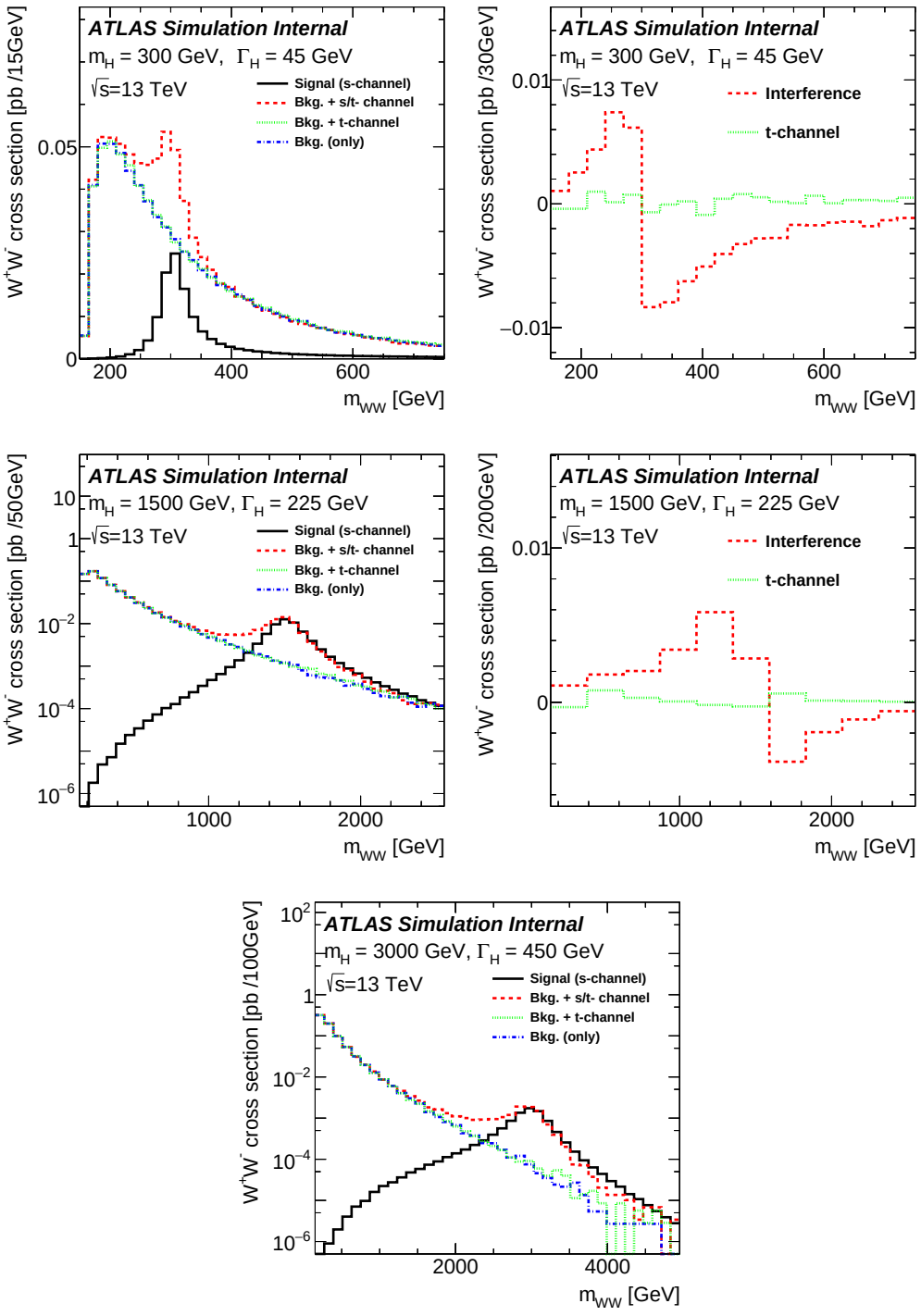

Figure I.1: Cross section for resonant and non-resonant W^+W^-jj production modes as a function of the m_{WW} shown in addition to their interference and the contribution of the missing t-channel.

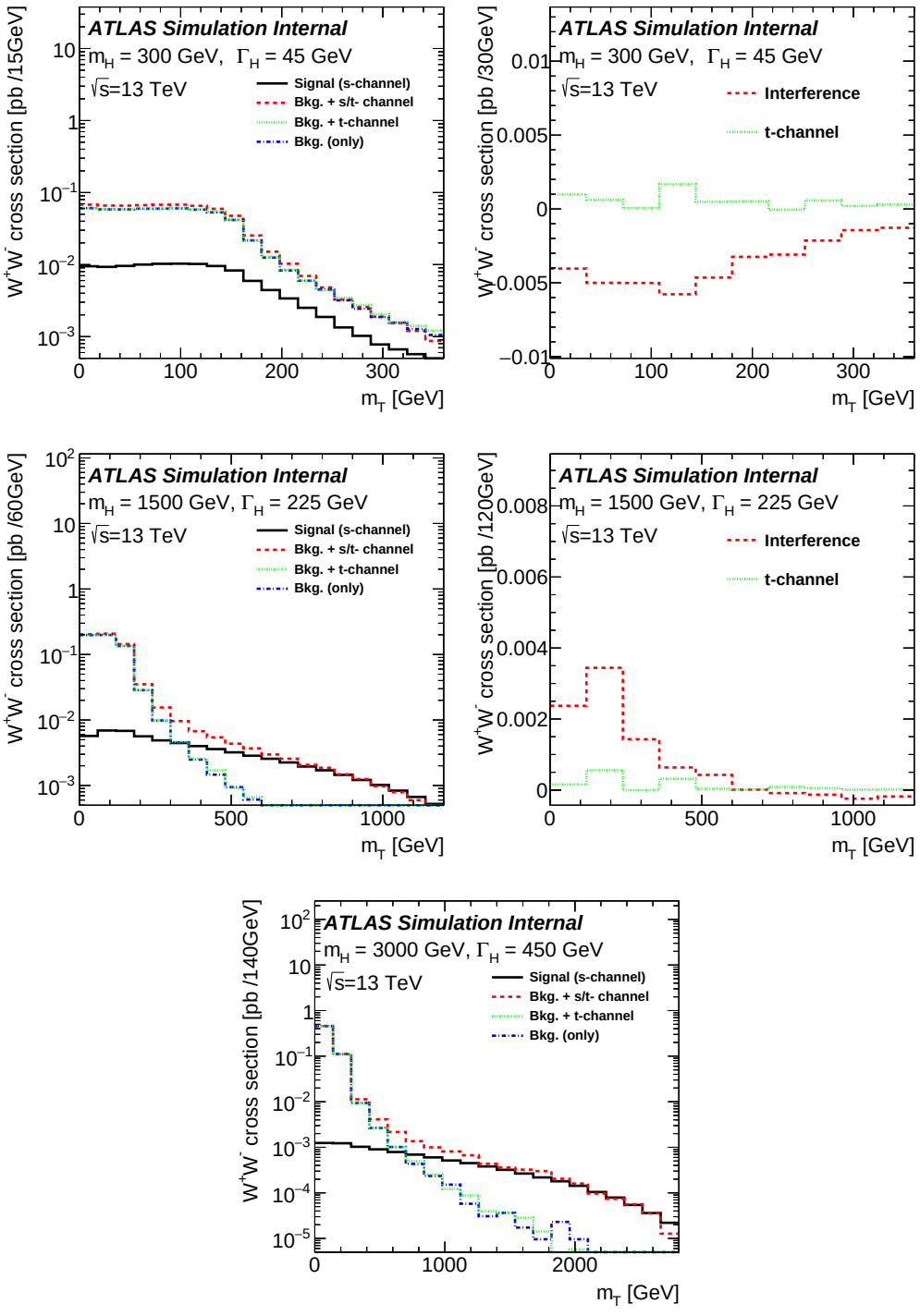

Figure I.2: Cross section for resonant and non-resonant W^+W^-jj production modes as a function of the m_{T} shown in addition to their interference and the contribution of the missing t-channel.

References

[1] ATLAS Collaboration, "Observation of a new particle in the search for the Standard Model Higgs boson with the ATLAS detector at the LHC", in: *Phys. Lett. B* 716 (2012), p. 1, DOI: 10.1016/j.physletb.2012.08.020, arXiv: 1207.7214 [hep-ex].

[2] CMS Collaboration, "Observation of a new boson at a mass of 125 GeV with the CMS experiment at the LHC", in: *Phys. Lett. B* 716 (2012), pp. 30–61, DOI: 10.1016/j.physletb.2012.08.021, arXiv: 1207.7235 [hep-ex].

[3] ATLAS Collaboration, "Measurements of the Higgs boson production and decay rates and coupling strengths using pp collision data at $\sqrt{s} = 7$ and 8 TeV in the ATLAS experiment", in: *Eur. Phys. J. C* 76.1 (2016), p. 6, DOI: 10.1140/epjc/s10052-015-3769-y, arXiv: 1507.04548 [hep-ex].

[4] ATLAS Collaboration, "Study of the spin and parity of the Higgs boson in diboson decays with the ATLAS detector", in: *Eur. Phys. J. C* 75 (2015), p. 476, DOI: 10.1140/epjc/s10052-015-3685-1, arXiv: 1506.05669 [hep-ex].

[5] CMS Collaboration, "Precise determination of the mass of the Higgs boson and tests of compatibility of its couplings with the standard model predictions using proton collisions at 7 and 8 TeV", in: *Eur. Phys. J. C* 75 (2015), p. 212, DOI: 10.1140/epjc/s10052-015-3351-7, arXiv: 1412.8662 [hep-ex].

[6] ATLAS and CMS Collaborations, "Measurements of the Higgs boson production and decay rates and constraints on its couplings from a combined ATLAS and CMS analysis of the LHC pp collision data at $\sqrt{s} = 7$ and 8 TeV", in: *JHEP* 08 (2016), p. 045, DOI: 10.1007/JHEP08(2016)045, arXiv: 1606.02266 [hep-ex].

[7] D. de Florian et al., *Handbook of LHC Higgs cross sections: 4. Deciphering the nature of the Higgs sector*, 2016, arXiv: 1610.07922 [hep-ph].

[8] Igor P. Ivanov, "Building and testing models with extended Higgs sectors", in: *Prog. Part. Nucl. Phys.* 95 (2017), pp. 160–208, DOI: 10.1016/j.ppnp.2017.03.001, arXiv: 1702.03776 [hep-ph].

[9] Kaustubh Agashe, Roberto Contino, and Alex Pomarol, "The minimal composite Higgs model", in: *Nucl. Phys. B* 719 (2005), pp. 165–187, DOI: 10.1016/j.nuclphysb.2005.04.035, arXiv: hep-ph/0412089.

[10] G.F. Giudice et al., "The strongly-interacting light Higgs", in: *JHEP* 06 (2007), p. 045, DOI: 10.1088/1126-6708/2007/06/045, arXiv: hep-ph/0703164.

[11] Lisa Randall and Raman Sundrum, "A large mass hierarchy from a small extra dimension", in: *Phys. Rev. Lett.* 83 (1999), pp. 3370–3373, DOI: 10.1103/PhysRevLett.83.3370, arXiv: hep-ph/9905221.

[12] Kaustubh Agashe et al., "Warped gravitons at the LHC and beyond", in: *Phys. Rev. D* 76 (2007), p. 036006, DOI: 10.1103/PhysRevD.76.036006, arXiv: hep-ph/0701186.

[13] Oleg Antipin, David Atwood, and Amarjit Soni, "Search for RS gravitons via W_LW_L decays", in: *Phys. Lett. B* 666 (2008), pp. 155–161, DOI: 10.1016/j.physletb.2008.07.009, arXiv: 0711.3175 [hep-ph].

[14] Oleg Antipin and Amarjit Soni, "Towards establishing the spin of warped gravitons", in: *JHEP* 10 (2008), p. 018, DOI: 10.1088/1126-6708/2008/10/018, arXiv: 0806.3427 [hep-ph].

[15] ATLAS Collaboration, "Search for a high-mass Higgs boson decaying to a W boson pair in pp collisions at $\sqrt{s} = 8\,\text{TeV}$ with the ATLAS detector", in: *JHEP* 01 (2016), p. 032, DOI: 10.1007/JHEP01(2016)032, arXiv: 1509.00389 [hep-ex].

[16] CMS Collaboration, "Search for a Higgs boson in the mass range from 145 to 1000 GeV decaying to a pair of W or Z bosons", in: *JHEP* 10 (2015), p. 144, DOI: 10.1007/JHEP10(2015)144, arXiv: 1504.00936 [hep-ex].

[17] ATLAS Collaboration, "Search for new phenomena in the $WW \to \ell\nu\ell'\nu'$ final state in pp collisions at $\sqrt{s} = 7\,\text{TeV}$ with the ATLAS detector", in: *Phys. Lett. B* 718 (2013), p. 860, DOI: 10.1016/j.physletb.2012.11.040, arXiv: 1208.2880 [hep-ex].

[18] CMS Collaboration, "Search for massive resonances in dijet systems containing jets tagged as W or Z boson decays in pp collisions at $\sqrt{s} = 8\,\text{TeV}$", in: *JHEP* 08 (2014), p. 173, DOI: 10.1007/JHEP08(2014)173, arXiv: 1405.1994 [hep-ex].

[19] CMS Collaboration, "Search for massive resonances decaying into pairs of boosted bosons in semi-leptonic final states at $\sqrt{s} = 8\,\text{TeV}$", in: *JHEP* 08 (2014), p. 174, DOI: 10.1007/JHEP08(2014)174, arXiv: 1405.3447 [hep-ex].

[20] ATLAS Collaboration, "Search for WZ resonances in the fully leptonic channel using pp collisions at $\sqrt{s} = 8\,\text{TeV}$ with the ATLAS detector", in: *Phys. Lett. B* 737 (2014), pp. 223–243, DOI: 10.1016/j.physletb.2014.08.039, arXiv: 1406.4456 [hep-ex].

[21] CMS Collaboration, "Search for new resonances decaying via WZ to leptons in proton-proton collisions at $\sqrt{s} = 8\,\text{TeV}$", in: *Phys. Lett. B* 740 (2015), pp. 83–104, DOI: 10.1016/j.physletb.2014.11.026, arXiv: 1407.3476 [hep-ex].

[22] ATLAS Collaboration, "Search for production of WW/WZ resonances decaying to a lepton, neutrino and jets in pp collisions at $\sqrt{s} = 8\,\text{TeV}$ with the ATLAS detector", in: *Eur. Phys. J. C* 75.5 (2015), Erratum: Eur. Phys. J. C **75** (2015) 370, p. 209, DOI: 10.1140/epjc/s10052-015-3593-4,10.1140/epjc/s10052-015-3425-6, arXiv: 1503.04677 [hep-ex].

[23] ATLAS Collaboration, "Search for high-mass diboson resonances with boson-tagged jets in proton-proton collisions at $\sqrt{s} = 8\,\text{TeV}$ with the ATLAS detector", in: *JHEP* 12 (2015), p. 055, DOI: 10.1007/JHEP12(2015)055, arXiv: 1506.00962 [hep-ex].

[24] ATLAS Collaboration, "Combination of searches for WW, WZ, and ZZ resonances in pp collisions at $\sqrt{s} = 8\,\text{TeV}$ with the ATLAS detector", in: *Phys. Lett. B* 755 (2016), p. 285, DOI: 10.1016/j.physletb.2016.02.015, arXiv: 1512.05099 [hep-ex].

[25] ATLAS Collaboration, "Searches for heavy diboson resonances in pp collisions at $\sqrt{s} = 13\,\text{TeV}$ with the ATLAS detector", in: *JHEP* 09 (2016), p. 173, DOI: 10.1007/JHEP09(2016)173, arXiv: 1606.04833 [hep-ex].

[26] CMS Collaboration, "Search for massive resonances decaying into WW, WZ or ZZ bosons in proton-proton collisions at $\sqrt{s} = 13\,\text{TeV}$", in: *JHEP* 03 (2017), p. 162, DOI: 10.1007/JHEP03(2017)162, arXiv: 1612.09159 [hep-ex].

[27] CMS Collaboration, "Combination of searches for heavy resonances decaying to WW, WZ, ZZ, WH, and ZH boson pairs in proton-proton collisions at $\sqrt{s} = 8$ and $13\,\text{TeV}$", in: *Phys. Lett. B* 774 (2017), p. 533, DOI: 10.1016/j.physletb.2017.09.083, arXiv: 1705.09171 [hep-ex].

[28] W. N. Cottingham and D. A. Greenwood, *An introduction to the Standard Model of particle physics*, University of Bristol, UK: Cambridge University Press, 2007.

[29] W. N. Cottingham and D. A. Greenwood, *An introduction to nuclear physics*, University of Bristol, UK: Cambridge University Press, 1986.

[30] Walter Greiner, Stefan Schramm, and Eckart Stein, *Quantum Chromodynamics*, Heidelberg, Germany: Springer Berlin Heidelberg, 2007.

[31] Massimiliano Grazzini, "Higgs cross sections: A Brief overview", in: *EPJ Web Conf.* 28 (2012), p. 07001, DOI: 10.1051/epjconf/20122807001, arXiv: 1202.3927 [hep-ph].

[32] S. Dawson, "Introduction to electroweak symmetry breaking", in: *Proceedings, Summer School in High-energy physics and cosmology: Trieste, Italy, June 29-July 17, 1998*, 1998, pp. 1–83, arXiv: hep-ph/9901280 [hep-ph].

[33] V. Andreev et al., "Determination of the strong coupling constant $\alpha_s(m_Z)$ in next-to-next-to-leading order QCD using H1 jet cross section measurements", in: *Eur. Phys. J.* C77.11 (2017), p. 791, DOI: 10.1140/epjc/s10052-017-5314-7, arXiv: 1709.07251 [hep-ex].

[34] Wim Beenakker et al., "NLO+NLL squark and gluino production cross-sections with threshold-improved parton distributions", in: *Eur. Phys. J.* C76.2 (2016), p. 53, DOI: 10.1140/epjc/s10052-016-3892-4, arXiv: 1510.00375 [hep-ph].

[35] Hung-Liang Lai et al., "New parton distributions for collider physics", in: *Phys. Rev. D* 82 (2010), p. 074024, DOI: 10.1103/PhysRevD.82.074024, arXiv: 1007.2241 [hep-ph].

[36] Sayipjamal Dulat et al., "New parton distribution functions from a global analysis of quantum chromodynamics", in: *Phys. Rev. D* 93.3 (2016), p. 033006, DOI: 10.1103/PhysRevD.93.033006, arXiv: 1506.07443 [hep-ph].

[37] Richard D. Ball et al., "Parton distributions for the LHC Run II", in: *JHEP* 04 (2015), p. 040, DOI: 10.1007/JHEP04(2015)040, arXiv: 1410.8849 [hep-ph].

[38] L. A. Harland-Lang et al., "Parton distributions in the LHC era: MMHT 2014 PDFs", in: *Eur. Phys. J. C* 75.5 (2015), p. 204, DOI: 10.1140/epjc/s10052-015-3397-6, arXiv: 1412.3989 [hep-ph].

[39] Jon Butterworth et al., "PDF4LHC recommendations for LHC Run II", in: *J. Phys.* G43 (2016), p. 023001, DOI: 10.1088/0954-3899/43/2/023001, arXiv: 1510.03865 [hep-ph].

[40] G. Watt and R. S. Thorne, "Study of Monte Carlo approach to experimental uncertainty propagation with MSTW 2008 PDFs", in: *JHEP* 08 (2012), p. 052, DOI: 10.1007/JHEP08(2012)052, arXiv: 1205.4024 [hep-ph].

[41] Jun Gao and Pavel Nadolsky, "A meta-analysis of parton distribution functions", in: *JHEP* 07 (2014), p. 035, DOI: 10.1007/JHEP07(2014)035, arXiv: 1401.0013 [hep-ph].

[42] Stefano Carrazza et al., "An Unbiased Hessian Representation for Monte Carlo PDFs", in: *Eur. Phys. J.* C75.8 (2015), p. 369, DOI: 10.1140/epjc/s10052-015-3590-7, arXiv: 1505.06736 [hep-ph].

[43] Stefano Carrazza et al., "A compression algorithm for the combination of PDF sets", in: *Eur. Phys. J.* C75 (2015), p. 474, DOI: 10.1140/epjc/s10052-015-3703-3, arXiv: 1504.06469 [hep-ph].

[44] Alan S. Cornell, "Some theories beyond the Standard Model", in: *J. Phys. Conf. Ser.* 645.1 (2015), p. 012002, DOI: 10.1088/1742-6596/645/1/012002, arXiv: 1506.05602 [hep-ph].

[45] Michael J. Dugan, Howard Georgi, and David B. Kaplan, "Anatomy of a Composite Higgs Model", in: *Nucl. Phys.* B254 (1985), pp. 299–326, DOI: 10.1016/0550-3213(85)90221-4.

[46] Kaustubh Agashe, Roberto Contino, and Alex Pomarol, "The minimal composite Higgs model", in: *Nuclear Physics B* 719.1 (2005), pp. 165–187, ISSN: 0550-3213, DOI: https://doi.org/10.1016/j.nuclphysb.2005.04.035, URL: http://www.sciencedirect.com/science/article/pii/S0550321305003445.

[47] Lisa Randall and Raman Sundrum, "Large Mass Hierarchy from a Small Extra Dimension", in: *Phys. Rev. Lett.* 83 (17 Oct. 1999), pp. 3370–3373, DOI: 10.1103/PhysRevLett.83.3370, URL: https://link.aps.org/doi/10.1103/PhysRevLett.83.3370.

[48] Lisa Randall and Raman Sundrum, "An Alternative to Compactification", in: *Phys. Rev. Lett.* 83 (23 Dec. 1999), pp. 4690–4693, DOI: 10.1103/PhysRevLett.83.4690, URL: https://link.aps.org/doi/10.1103/PhysRevLett.83.4690.

[49] H. Davoudiasl, J. L. Hewett, and T. G. Rizzo, "Experimental probes of localized gravity: On and off the wall", in: *Phys. Rev. D* 63 (7 Mar. 2001), p. 075004, DOI: 10.1103/PhysRevD.63.075004, URL: https://link.aps.org/doi/10.1103/PhysRevD.63.075004.

[50] Tao Han, Joseph D. Lykken, and Ren-Jie Zhang, "On Kaluza-Klein states from large extra dimensions", in: *Phys. Rev. D* 59 (1999), p. 105006, DOI: 10.1103/PhysRevD.59.105006, arXiv: hep-ph/9811350.

[51] Maxime Gabella, *The Randall-Sundrum Model*, 2006.

[52] Jogesh C. Pati and Abdus Salam, "Lepton number as the fourth "color"", in: *Phys. Rev. D* 10 (1 July 1974), pp. 275–289, DOI: 10.1103/PhysRevD.10.275, URL: https://link.aps.org/doi/10.1103/PhysRevD.10.275.

[53] Howard Georgi and S. L. Glashow, "Unity of All Elementary-Particle Forces", in: *Phys. Rev. Lett.* 32 (8 Feb. 1974), pp. 438–441, DOI: 10.1103/PhysRevLett.32.438, URL: https://link.aps.org/doi/10.1103/PhysRevLett.32.438.

[54] Howard Georgi, "The State of the ArtGauge Theories", in: *AIP Conference Proceedings* 23.1 (1975), pp. 575–582, DOI: 10.1063/1.2947450, eprint: https://aip.scitation.org/doi/pdf/10.1063/1.2947450, URL: https://aip.scitation.org/doi/abs/10.1063/1.2947450.

[55] Harald Fritzsch and Peter Minkowski, "Unified interactions of leptons and hadrons", in: *Annals of Physics* 93.1 (1975), pp. 193–266, ISSN: 0003-4916, DOI: https://doi.org/10.1016/0003-4916(75)90211-0, URL: http://www.sciencedirect.com/science/article/pii/0003491675902110.

[56] ATLAS Collaboration, "Constraints on new phenomena via Higgs boson couplings and invisible decays with the ATLAS detector", in: *JHEP* 11 (2015), p. 206, DOI: 10.1007/JHEP11(2015)206, arXiv: 1509.00672 [hep-ex].

[57] G.C. Branco et al., "Theory and phenomenology of two-Higgs-doublet models", in: *Phys. Rept.* 516 (2012), pp. 1–102, DOI: 10.1016/j.physrep.2012.02.002, arXiv: 1106.0034 [hep-ph].

[58] Robert V. Harlander, Stefan Liebler, and Hendrik Mantler, "SusHi: a program for the calculation of Higgs production in gluon fusion and bottom-quark annihilation in the Standard Model and the MSSM", in: *Comput. Phys. Commun.* 184 (2013), p. 1605, DOI: 10.1016/j.cpc.2013.02.006, arXiv: 1212.3249 [hep-ph].

[59] David Eriksson, Johan Rathsman, and Oscar Stal, "2HDMC: Two-Higgs-doublet model calculator", in: *Comput. Phys. Commun.* 181 (2010), Erratum: Comput. Phys. Commun. **181** (2010) 985, p. 189, DOI: 10.1016/j.cpc.2009.09.011, arXiv: 0902.0851 [hep-ph].

[60] Howard Georgi and Marie Machacek, "Doubly charged Higgs bosons", in: *Nucl. Phys. B* 262 (1985), pp. 463–477, DOI: 10.1016/0550-3213(85)90325-6.

[61] Michael S. Chanowitz and Mitchell Golden, "Higgs boson triplets with $M_W = M_Z \cos\theta_W$", in: *Phys. Lett. B* 165 (1985), pp. 105–108, DOI: 10.1016/0370-2693(85)90700-2.

[62] Cline Degrande et al., "Automatic predictions in the Georgi-Machacek model at next-to-leading order accuracy", in: *Phys. Rev. D* 93.3 (2016), p. 035004, DOI: 10.1103/PhysRevD.93.035004, arXiv: 1512.01243 [hep-ph].

[63] Stephen Godfrey and Ken Moats, "Exploring Higgs triplet models via vector boson scattering at the LHC", in: *Phys. Rev. D* 81 (2010), p. 075026, DOI: 10.1103/PhysRevD.81.075026, arXiv: 1003.3033 [hep-ph].

[64] N. Arkani-Hamed et al., "The littlest Higgs", in: *JHEP* 07 (2002), p. 034, DOI: 10.1088/1126-6708/2002/07/034, arXiv: hep-ph/0206021.

[65] J. F. Gunion et al., "Higgs bosons in left-right symmetric models", in: *Phys. Rev. D* 40 (1989), p. 1546, DOI: 10.1103/PhysRevD.40.1546.

[66] Katy Hartling, Kunal Kumar, and Heather E. Logan, *GMCALC: a calculator for the Georgi-Machacek model*, 2014, arXiv: 1412.7387 [hep-ph].

[67] Marco Zaro and Heather Logan, *Recommendations for the interpretation of LHC searches for H_5^0, $H_5^\pm$, and $H_5^{\pm\pm}$ in vector boson fusion with decays to vector boson pairs*, LHC Higgs Cross Section Working Group, LHCHXSWG-2015-001, URL: https://cds.cern.ch/record/2002500.

[68] J. de Blas, J. M. Lizana, and M. Perez-Victoria, "Combining searches of Z' and W' bosons", in: *JHEP* 01 (2013), p. 166, DOI: 10.1007/JHEP01(2013)166, arXiv: 1211.2229 [hep-ph].

[69] Duccio Pappadopulo et al., "Heavy vector triplets: bridging theory and data", in: *JHEP* 09 (2014), p. 060, DOI: 10.1007/JHEP09(2014)060, arXiv: 1402.4431 [hep-ph].

[70] Jessica Frank, Michael Rauch, and Dieter Zeppenfeld, "Spin-2 resonances in vector-boson-fusion processes at next-to-leading order QCD", in: *Phys. Rev. D* 87.5 (2013), p. 055020, DOI: 10.1103/PhysRevD.87.055020, arXiv: 1211.3658 [hep-ph].

[71] Lyndon Evans and Philip Bryant, "LHC Machine", in: *JINST* 3 (2008), S08001, DOI: 10.1088/1748-0221/3/08/S08001.

[72] ATLAS Collaboration, "The ATLAS Experiment at the CERN Large Hadron Collider", in: *JINST* 3 (2008), S08003, DOI: 10.1088/1748-0221/3/08/S08003.

[73] M. Aaboud et al., "Performance of the ATLAS Track Reconstruction Algorithms in Dense Environments in LHC Run 2", in: *Eur. Phys. J.* C77.10 (2017), p. 673, DOI: 10.1140/epjc/s10052-017-5225-7, arXiv: 1704.07983 [hep-ex].

[74] Georges Aad et al., "Electron and photon energy calibration with the ATLAS detector using LHC Run 1 data", in: *Eur. Phys. J.* C74.10 (2014), p. 3071, DOI: 10.1140/epjc/s10052-014-3071-4, arXiv: 1407.5063 [hep-ex].

[75] ATLAS Collaboration, "Performance of the ATLAS Trigger System in 2015", in: *Eur. Phys. J. C* 77 (2017), p. 317, DOI: 10.1140/epjc/s10052-017-4852-3, arXiv: 1611.09661 [hep-ex].

[76] Paolo Nason, "A new method for combining NLO QCD with shower Monte Carlo algorithms", in: *JHEP* 11 (2004), p. 040, DOI: 10.1088/1126-6708/2004/11/040, arXiv: hep-ph/0409146.

[77] Stefano Frixione, Paolo Nason, and Carlo Oleari, "Matching NLO QCD computations with parton shower simulations: the POWHEG method", in: *JHEP* 11 (2007), p. 070, DOI: 10.1088/1126-6708/2007/11/070, arXiv: 0709.2092 [hep-ph].

[78] Simone Alioli et al., "A general framework for implementing NLO calculations in shower Monte Carlo programs: the POWHEG BOX", in: *JHEP* 06 (2010), p. 043, DOI: 10.1007/JHEP06(2010)043, arXiv: 1002.2581 [hep-ph].

[79] S. Alioli et al., "NLO Higgs boson production via gluon fusion matched with shower in POWHEG", in: *JHEP* 04 (2009), p. 002, DOI: 10.1088/1126-6708/2009/04/002, arXiv: 0812.0578 [hep-ph].

[80] P. Nason and C. Oleari, "NLO Higgs boson production via vector-boson fusion matched with shower in POWHEG", in: *JHEP* 02 (2010), p. 037, DOI: 10.1007/JHEP02(2010)037, arXiv: 0911.5299 [hep-ph].

[81] Torbjorn Sjöstrand, Stephen Mrenna, and Peter Z. Skands, "A brief Introduction to PYTHIA 8.1", in: *Comput. Phys. Commun.* 178 (2008), pp. 852–867, DOI: 10.1016/j.cpc.2008.01.036, arXiv: 0710.3820 [hep-ph].

[82] ATLAS Collaboration, "Measurement of the Z/γ^* boson transverse momentum distribution in pp collisions at $\sqrt{s} = 7\,\text{TeV}$ with the ATLAS detector", in: *JHEP* 09 (2014), p. 145, DOI: 10.1007/JHEP09(2014)145, arXiv: 1406.3660 [hep-ex].

[83] J. Alwall et al., "The automated computation of tree-level and next-to-leading order differential cross sections, and their matching to parton shower simulations", in: *JHEP* 07 (2014), p. 079, DOI: 10.1007/JHEP07(2014)079, arXiv: 1405.0301 [hep-ph].

[84] Rikkert Frederix and Stefano Frixione, "Merging meets matching in MC@NLO", in: *JHEP* 12 (2012), p. 061, DOI: 10.1007/JHEP12(2012)061, arXiv: 1209.6215 [hep-ph].

[85] Stefano Carrazza, Stefano Forte, and Juan Rojo, *Parton distributions and event generators*, 2013, arXiv: 1311.5887 [hep-ph].

[86] ATLAS Collaboration, *ATLAS* Pythia *8 tunes to 7 TeV data*, ATL-PHYS-PUB-2014-021, 2014, URL: https://cds.cern.ch/record/1966419.

[87] J. Baglio et al., *Release note - VBFNLO 2.7.0*, 2014, arXiv: 1404.3940 [hep-ph].

[88] Simone Alioli et al., "NLO single-top production matched with shower in Powheg: s- and t-channel contributions", in: *JHEP* 09 (2009), Erratum: JHEP **02** (2010) 011, p. 111, DOI: 10.1007/JHEP02(2010)011,10.1088/1126-6708/2009/09/111, arXiv: 0907.4076 [hep-ph].

[89] Emanuele Re, "Single-top Wt-channel production matched with parton showers using the Powheg method", in: *Eur. Phys. J. C* 71 (2011), p. 1547, DOI: 10.1140/epjc/s10052-011-1547-z, arXiv: 1009.2450 [hep-ph].

[90] Torbjorn Sjöstrand, Stephen Mrenna, and Peter Z. Skands, "Pythia 6.4 physics and manual", in: *JHEP* 05 (2006), p. 026, DOI: 10.1088/1126-6708/2006/05/026, arXiv: hep-ph/0603175.

[91] Peter Zeiler Skands, "Tuning Monte Carlo generators: The Perugia tunes", in: *Phys. Rev. D* 82 (2010), p. 074018, DOI: 10.1103/PhysRevD.82.074018, arXiv: 1005.3457 [hep-ph].

[92] J. Pumplin et al., "New generation of parton distributions with uncertainties from global QCD analysis", in: *JHEP* 07 (2002), p. 012, DOI: 10.1088/1126-6708/2002/07/012, arXiv: hep-ph/0201195.

[93] Simone Alioli, Sven-Olaf Moch, and Peter Uwer, "Hadronic top-quark pair-production with one jet and parton showering", in: *JHEP* 01 (2012), p. 137, DOI: 10.1007/JHEP01(2012)137, arXiv: 1110.5251 [hep-ph].

[94] D. J. Lange, "The EvtGen particle decay simulation package", in: *Nucl. Instrum. Meth. A* 462 (2001), pp. 152–155, DOI: 10.1016/S0168-9002(01)00089-4.

[95] T. Gleisberg et al., "Event generation with Sherpa 1.1", in: *JHEP* 02 (2009), p. 007, DOI: 10.1088/1126-6708/2009/02/007, arXiv: 0811.4622 [hep-ph].

[96] T. Gleisberg and S. Höche, "Comix, a new matrix element generator", in: *JHEP* 12 (2008), p. 039, DOI: 10.1088/1126-6708/2008/12/039, arXiv: 0808.3674 [hep-ph].

[97] Fabio Cascioli, Philipp Maierhofer, and Stefano Pozzorini, "Scattering amplitudes with open loops", in: *Phys. Rev. Lett.* 108 (2012), p. 111601, DOI: 10.1103/PhysRevLett.108.111601, arXiv: 1111.5206 [hep-ph].

[98] Steffen Schumann and Frank Krauss, "A Parton shower algorithm based on Catani-Seymour dipole factorisation", in: *JHEP* 03 (2008), p. 038, DOI: 10.1088/1126-6708/2008/03/038, arXiv: 0709.1027 [hep-ph].

[99] Stefan Höche et al., "QCD matrix elements + parton showers: The NLO case", in: *JHEP* 04 (2013), p. 027, DOI: 10.1007/JHEP04(2013)027, arXiv: 1207.5030 [hep-ph].

[100] S. Agostinelli et al., "GEANT4: a simulation toolkit", in: *Nucl. Instrum. Meth. A* 506 (2003), pp. 250–303, DOI: 10.1016/S0168-9002(03)01368-8.

[101] ATLAS Collaboration, "The ATLAS simulation infrastructure", in: *Eur. Phys. J. C* 70 (2010), pp. 823–874, DOI: 10.1140/epjc/s10052-010-1429-9, arXiv: 1005.4568 [physics.ins-det].

[102] W. Lampl et al., "Calorimeter clustering algorithms: Description and performance", in: (2008).

[103] Morad Aaboud et al., "Electron efficiency measurements with the ATLAS detector using 2012 LHC protonproton collision data", in: *Eur. Phys. J.* C77.3 (2017), p. 195, DOI: 10.1140/epjc/s10052-017-4756-2, arXiv: 1612.01456 [hep-ex].

[104] Andreas Hoecker et al., *TMVA: Toolkit for multivariate data analysis*, 2007, arXiv: physics/0703039.

[105] *Electron efficiency measurements with the ATLAS detector using the 2015 LHC proton-proton collision data*, tech. rep. ATLAS-CONF-2016-024, Geneva: CERN, June 2016, URL: https://cds.cern.ch/record/2157687.

[106] ATLAS Collaboration, "Muon reconstruction performance of the ATLAS detector in proton-proton collision data at $\sqrt{s} = 13\,\text{TeV}$", in: *Eur. Phys. J. C* 76.5 (2016), p. 292, DOI: 10.1140/epjc/s10052-016-4120-y, arXiv: 1603.05598 [hep-ex].

[107] Matteo Cacciari, Gavin P. Salam, and Gregory Soyez, "The anti-k_t jet clustering algorithm", in: *JHEP* 04 (2008), p. 063, DOI: 10.1088/1126-6708/2008/04/063, arXiv: 0802.1189 [hep-ph].

[108] Matteo Cacciari and Gavin P. Salam, "Pileup subtraction using jet areas", in: *Phys. Lett. B* 659 (2008), p. 119, DOI: 10.1016/j.physletb.2007.09.077.

[109] ATLAS Collaboration, "Jet energy scale measurements and their systematic uncertainties in proton-proton collisions at $\sqrt{s} = 13\,\text{TeV}$ with the ATLAS detector", in: *Phys. Rev. D* 96 (2017), DOI: 10.1103/PhysRevD.96.072002, arXiv: 1703.09665 [hep-ex].

[110] ATLAS Collaboration, *Tagging and suppression of pileup jets with the ATLAS detector*, ATLAS-CONF-2014-018, 2014, URL: https://cds.cern.ch/record/1700870.

[111] ATLAS Collaboration, "Performance of b-jet identification in the ATLAS experiment", in: *JINST* 11.04 (2016), P04008, DOI: 10.1088/1748-0221/11/04/P04008, arXiv: 1512.01094 [hep-ex].

[112] ATLAS Collaboration, *Optimisation of the ATLAS b-tagging performance for the 2016 LHC run*, ATL-PHYS-PUB-2016-012, 2016, URL: https://cds.cern.ch/record/2160731.

[113] Matteo Cacciari, Gavin P. Salam, and Gregory Soyez, "FastJet user manual", in: *Eur. Phys. J. C* 72 (2012), p. 1896, DOI: 10.1140/epjc/s10052-012-1896-2, arXiv: 1111.6097 [hep-ph].

[114] ATLAS Collaboration, *Performance of missing transverse momentum reconstruction with the ATLAS detector in the first proton-proton collisions at $\sqrt{s} = 13\,TeV$*, ATL-PHYS-PUB-2015-027, 2015, URL: https://cds.cern.ch/record/2037904.

[115] Glen Cowan et al., "Asymptotic formulae for likelihood-based tests of new physics", in: *Eur. Phys. J. C* 71 (2011), Erratum: Eur. Phys. J. C **73** (2013) 2501, p. 1554, DOI: 10.1140/epjc/s10052-011-1554-0, arXiv: 1007.1727 [physics.data-an].

[116] ATLAS Collaboration, "Observation and measurement of Higgs boson decays to WW* with the ATLAS detector", in: *Phys. Rev. D* 92.1 (2015), p. 012006, DOI: 10.1103/PhysRevD.92.012006, arXiv: 1412.2641 [hep-ex].

[117] K. Melnikov and F. Petriello, "Electroweak gauge boson production at hadron colliders through $\mathcal{O}(\alpha_s^2)$", in: *Phys. Rev. D* 74 (2006), p. 114017, DOI: 10.1103/PhysRevD.74.114017, arXiv: hep-ph/0609070.

[118] Massimiliano Grazzini et al., "W^+W^- production at the LHC: fiducial cross sections and distributions in NNLO QCD", in: *JHEP* 08 (2016), p. 140, DOI: 10.1007/JHEP08(2016)140, arXiv: 1605.02716 [hep-ph].

[119] Benedikt Biedermann et al., "Next-to-leading-order electroweak corrections to $pp \to W^+W^- \to 4$ leptons at the LHC", in: *JHEP* 06 (2016), p. 065, DOI: 10.1007/JHEP06(2016)065, arXiv: 1605.03419 [hep-ph].

[120] Kirill Melnikov and Matthew Dowling, "Production of two Z-bosons in gluon fusion in the heavy top quark approximation", in: *Phys. Lett. B* 744 (2015), pp. 43–47, DOI: 10.1016/j.physletb.2015.03.030, arXiv: 1503.01274 [hep-ph].

[121] Fabrizio Caola et al., "QCD corrections to W^+W^- production through gluon fusion", in: *Phys. Lett. B* 754 (2016), pp. 275–280, DOI: 10.1016/j.physletb.2016.01.046, arXiv: 1511.08617 [hep-ph].

[122] Marco Bonvini et al., "Signal-background interference effects for $gg \to H \to W^+W^-$ beyond leading order", in: *Phys. Rev. D* 88.3 (2013), p. 034032, DOI: 10.1103/PhysRevD.88.034032, arXiv: 1304.3053 [hep-ph].

[123] Chong Sheng Li et al., "Soft gluon resummation in the signal-background interference process of gg(h*) ZZ", in: *JHEP* 08 (2015), p. 065, DOI: 10.1007/JHEP08(2015)065, arXiv: 1504.02388 [hep-ph].

[124] Christian Gutschow et al., *Multi-Boson Simulation for 13 TeV ATLAS Analyses*, tech. rep. ATL-COM-PHYS-2015-1499, Geneva: CERN, Dec. 2015, URL: https://cds.cern.ch/record/2113154.

[125] ATLAS Collaboration, "Luminosity determination in pp collisions at $\sqrt{s} = 8\,\text{TeV}$ using the ATLAS detector at the LHC", in: *Eur. Phys. J. C* 76 (2016), p. 653, DOI: 10.1140/epjc/s10052-016-4466-1, arXiv: 1608.03953 [hep-ex].

[126] ATLAS Collaboration, *Electron efficiency measurements with the ATLAS detector using the 2015 LHC proton–proton collision data*, ATLAS-CONF-2016-024, 2016, URL: https://cds.cern.ch/record/2157687.

[127] ATLAS Collaboration, "Measurement of the inelastic proton-proton cross section at $\sqrt{s} = 13\,\text{TeV}$ with the ATLAS detector at the LHC", in: *Phys. Rev. Lett.* 117 (2016), p. 182002, DOI: 10.1103/PhysRevLett.117.182002, arXiv: 1606.02625 [hep-ex].

[128] ATLAS Collaboration, "Measurement of the production cross-section of a single top quark in association with a W boson at 8 TeV with the ATLAS experiment", in: *JHEP* 01 (2016), p. 064, DOI: 10.1007/JHEP01(2016)064, arXiv: 1510.03752 [hep-ex].

[129] ATLAS Collaboration, "Measurement of the cross-section for producing a W boson in association with a single top quark in pp collisions at $\sqrt{s} = 13$ TeV with ATLAS", in: (2016), arXiv: 1612.07231 [hep-ex].

[130] M. Bahr et al., "HERWIG++ physics and manual", in: *Eur. Phys. J. C* 58 (2008), pp. 639–707, DOI: 10.1140/epjc/s10052-008-0798-9, arXiv: 0803.0883 [hep-ph].

[131] J. Bellm et al., *HERWIG++ 2.7 release note*, 2013, arXiv: 1310.6877 [hep-ph].

[132] I. Stewart and F. Tackmann, "Theory uncertainties for Higgs mass and other searches using jet bins", in: *Phys. Rev. D* 85 (2012), p. 034011, DOI: 10.1103/PhysRevD.85.034011, arXiv: 1107.2117 [hep-ph].

[133] Stefano Frixione et al., "Single-top hadroproduction in association with a W boson", in: *JHEP* 07 (2008), p. 029, DOI: 10.1088/1126-6708/2008/07/029, arXiv: 0805.3067 [hep-ph].

[134] S. Catani et al., "QCD matrix elements + parton showers", in: *JHEP* 11 (2001), p. 063, DOI: 10.1088/1126-6708/2001/11/063, arXiv: hep-ph/0109231 [hep-ph].

[135] ATLAS Collaboration, "Combined search for the Standard Model Higgs boson in pp collisions at $\sqrt{s} = 7$ TeV with the ATLAS detector", in: *Phys. Rev. D* 86 (2012), p. 032003, DOI: 10.1103/PhysRevD.86.032003, arXiv: 1207.0319 [hep-ex].

[136] H Abramowicz et al., *Rounding - ATLAS Recommendations*, tech. rep. ATL-COM-GEN-2014-006, Geneva: CERN, Mar. 2014, URL: https://cds.cern.ch/record/1668799.

[137] Nikolas Kauer and Claire O'Brien, "Heavy Higgs signal-background interference in $gg \to VV$ in the Standard Model plus real singlet", in: *Eur. Phys. J.* C75 (2015), p. 374, DOI: 10.1140/epjc/s10052-015-3586-3, arXiv: 1502.04113 [hep-ph].

[138] ATLAS and CMS Collaborations, "Procedure for the LHC Higgs boson search combination in summer 2011", in: *ATL-PHYS-PUB-2011-011, CMS-NOTE-2011-005* (2011), https://cdsweb.cern.ch/record/1375842.

université PARIS-SACLAY | ÉCOLE DOCTORALE PHENIICS

Titre : Recherche d'une résonance lourde dans le canal $X \rightarrow WW \rightarrow e\nu\mu\nu$ avec le détecteur ATLAS au LHC

Mots clés : Résonance lourde; WW; boson de Higgs; au-delà du Modèle Standard

Résumé : Une recherche de résonance neutre et lourde X est effectuée dans le canal $X \rightarrow WW \rightarrow e\nu\mu\nu$ en utilisant les données en collision pp correspondant à une luminosit é intégrée d'environ 36,1 fb^{-1}, prises à une énergie dans le centre-de-masse de 13 TeV par le détecteur ATLAS au LHC. La résonance peut être soit un boson de Higgs scalaire lourd soit d'autres résonances lourdes aux spins différents. Deux scénarios de largeur sont étudis pour un boson de Higgs lourd dans les modes de fusion gluon-gluon et de fusion vecteur-boson; une largeur soit étroite soit grande. Plusieurs hypothèses sont utilisées pour rechercher d'autres résonances, comme le modèle avec deux doublets de Higgs, le modèle de Georgi-Machacek, le modèle avec un triplet vectoriel en mode d'annihilation quark-antiquark, le modèle de Randall-Sundrum avec un graviton de spin 2 correspondant à un paramètre d'échelle de courbure $k/\overline{M}_{\mathrm{Pl}}$ de 1 ou 0,5 et un signal de spin 2 dans le mode de fusion vecteur-boson. Trois catégories d'événements indépendantes sont définies dans l'analyse: une catégorie inclusive où les espaces de phase en fusion vecteurboson sont exclus et deux autres catégories qui sont optimisées pour les signaux produits en mode de fusion vecteur-boson avec un jet ou au moins deux jets. Aucun excès significatif d'événements au-delà de la prédiction du bruit de fond du Modèle Standard ne se trouve dans la gamme de masse comprise entre 200 GeV et 5 TeV. Les limites supérieures sont obtenues sur le produit de la section efficace de la production de la résonance et du rapport de branchement $X \rightarrow WW$. Pour les signaux de bosons de Higgs lourds, les valeurs supérieures à 6,4 pb et 1,3 pb à m_{H} = 200 GeV et supérieures à 0,008 pb et 0,005 pb à 4 TeV sont exclues à un niveau de confiance de 95% pour la fusion gluon-gluon et la fusion vecteur-boson, respectivement. Pour les signaux prédits par le modèle avec un triplet vectoriel, les valeurs de masse inférieures à 1,3 TeV sont exclues. De la même manière, pour les signaux prédits par le modèle de Randall-Sundrum, les valeurs de masse inférieures à 1,1 TeV et 850 GeV sont exclues pour $k/\overline{M}_{\mathrm{Pl}} = 1$ et $k/\overline{M}_{\mathrm{Pl}} = 0.5$, respectivement.

Université Paris-Saclay
Espace Technologique / Immeuble Discovery
Route de l'Orme aux Merisiers RD 128 / 91190 Saint-Aubin, France

université PARIS-SACLAY | ÉCOLE DOCTORALE PHENIICS

Title : Search for heavy resonances in the $X \rightarrow WW \rightarrow e\nu\mu\nu$ channel with the ATLAS detector at the LHC

Keywords : Heavy resonance; WW; Higgs boson; beyond the Standard Model

Abstract : A search for a heavy neutral resonance X is performed in the $X \rightarrow WW \rightarrow e\nu\mu\nu$ decay channel using pp collision data corresponding to an integrated luminosity of 36.1 fb^{-1}, collected at a centre-of-mass energy of 13 TeV by the ATLAS detector at the Large Hadron Collider. The resonance can be either a heavy scalar Higgs boson or other heavy resonances with different spins. Two scenarios are considered for the heavy Higgs boson hypothese with different decay widths in both the gluon-gluon fusion and the vector-boson fusion production modes, namely a narrow-width approximation and a large width assumption. Several hypotheses are used for the interpretation to search for other resonances, like two Higgs doublet models, Georgi-Machacek model, heavy vector triplet model in the quark-antiquark annihilation mode, a bulk Randall-Sundrum graviton model with a spin-2 Graviton with a curvature scale parameter $k/\overline{M}_{\mathrm{Pl}}$ of either 1 or 0.5 and a spin-2 signal in the vector-boson fusion mode. Three orthogonal event categories are defined in the analysis: two vector-boson fusion categories which are optimised for the signals produced in the vector-boson fusion mode with one jet or at least two jets and one quasi-inclusive gluon-gluon fusion category where the vectorboson fusion phase spaces defined by the two vector-boson fusion categories are excluded. No significant excess of events beyond the Standard Model background prediction is found in the mass range between 200 GeV and up to 5 TeV. Upper limits are set on the product of the production cross section of the resonance and the $X \rightarrow WW$ branching fraction. For heavy Higgs boson signals, values above 6.4 pb and 1.3 pb at $m_{\mathrm{H}} = 200$ GeV and above 0.008 pb and 0.005 pb at 4 TeV are excluded at 95% confidence level for the gluon-gluon fusion and the vector-boson fusion production modes, respectively. For signals predicted by the heavy vector triplet model, mass values below 1.3 TeV are excluded. Similarly, for signals predicted by the bulk Randall-Sundrum graviton model, mass values below 1.1 TeV and 850 GeV are excluded for $k/\overline{M}_{\mathrm{Pl}} = 1$ and $k/\overline{M}_{\mathrm{Pl}} = 0.5$, respectively.

Université Paris-Saclay
Espace Technologique / Immeuble Discovery
Route de l'Orme aux Merisiers RD 128 / 91190 Saint-Aubin, France